Università degli Studi di Ferrara

UCA Universidad de Cádiz

International Ph.D. Course
in
Earth and Marine Sciences (EMAS)

CYCLE XXXII

COORDINATOR Prof. COLTORTI MASSIMO

Taphonomy, sclerochronology and palaeoecology of Lower Jurassic lithiotid bivalves from the Trento Platform (Italy)

Scientific/Disciplinary Sector (SDS) GEO/O1

Candidate
Dott. Brandolese Valentina

Supervisor
Prof. Posenato Renato

Co-Supervisors
Prof. Bassi Davide
Dott. Takayanagi Hideko

Years 2016/2019

“You don't have to see the whole staircase,

just take the first step.”

(Martin Luther King Jr.)

ABSTRACT

The Lower Jurassic lithiotid bivalves are mostly represented by the larger, gregarious and monospecific genera *Lithiotis*, *Cochlearites* and *Lithioperna*. These formed large shell accumulations in the shallow-water carbonate settings of the Tethyan and Panthalassa margins.

This thesis analyses the lithiotid accumulations occurring in the Trento Platform (Southern Alps) through the study of a) the taphonomy of the accumulations; b) the skeletal and non-skeletal components along with pyrite forms of the bivalve accumulations to evaluate the microbial role in the shell accumulation geometry and to assess the redox conditions during the lithiotid accumulation growth; c) the shell growth pattern and stable isotope ($\delta^{13}C$ and $\delta^{18}O$) variations as proxy of paleoecological limiting factors.

The taphonomical analysis of lithiotid accumulations distinguished autochthonous, parautochthonous and allochthonous lithiotids in the accumulation core and flanks. Shell accumulation characteristics and taphonomic attributes, quantitatively analysed in the core and flanks (i.e., shell cover, shell density, percentage of articulated and complete shells), vary according to the dominating lithiotid bivalve. This quantitative approach is potentially useful as proxies for distinguishing core or flanks when the accumulation does not crop out as a whole.

The occurrence of bacteria-like features along with calcareous green algae (*Thaumatoporella parvovesiculifera*), from thin section observations, could contribute to stabilise the soft muddy substrate on which the lithiotids grew and to produce carbonate mud. This is evident in *Lithiotis*- and *Cochlearites*-dominated accumulations, characterised by larger dimensions. On contrary, *Lithioperna* generated tabular bodies. The relative increase in occurrence of bacteria-like features and calcareous green algae (i.e., *Palaedasycladus* sp., *Thaumatoporella parvovesiculifera*) upwardly in the Rotzo Formation points to a general decrease in water runoff and an increase in marine water carbonate saturation state.

Pyrite framboids, observed by SEM, locally registered lower dysoxic conditions in *Cochlearites* accumulation core and in both *Lithiotis* and *Cochlearites* accumulation flanks whilst *Lithiotis* core grew in fully oxic setting. The deposits overlying the lithiotid accumulations formed under oxic conditions.

High resolution stable isotope ($\delta^{13}C$ and $\delta^{18}O$) and shell growth pattern were investigated on well preserved lithiotid shells of *Lithiotis*, *Cochlearites* and *Lithioperna*. Shells of *Opisoma excavatum* and *Pachyrisma* (*Durga*) *crassa*, two bivalve species widespread in the Rotzo Formation, have been also analysed. Shell preservation was assessed by three different screening techniques (SEM, XRD and cathodoluminescence analyses). Finding of well-preserved and articulated specimens of *Lithiotis* clarifies the occurrence and structure of the outer calcitic layer in this species and the free valve morphology.

In all the studied bivalves, daily growth increments were grouped in fortnightly bundles suggesting a tidal influence even in subtidal settings. This study confirms the long life of some individuals (e.g., up to ca. 40 years old for *Cochlearites*) which distinguished this aberrant-bivalve group.

The $\delta^{18}O$ and $\delta^{13}C$ variations in the analysed bivalves respond to a complex of ecological conditions, mostly involving the effects of temperature, salinity and primary productivity. *Lithioperna*, *Opisoma* and *Pachyrisma*, which thrived in restricted environmental conditions with a reduced water circulation, could be influenced by water salinity. Their stable isotope profiles suggest higher riverine input and strong seasonal algal blooms. On contrary, *Lithiotis* and *Cochlearites* stable isotope profiles indicate a decrease of riverine input influence and more stable conditions. The inter-annual variability was probably related to inter-annual changes in rainy and dry seasons in a tropical climate.

TABLE OF CONTENTS

Chapter 1

Introduction

The Early Jurassic (201.3–174.1 Ma) is a period of fundamental changes in global climate and palaeogeography occurred between the end-Triassic mass extinction and the greenhouse warming corresponding to the Toarcian Oceanic Anoxic Event (T-OAE; e.g., Korte et al., 2015).

The Lower Jurassic shallow-water carbonate platforms are characterized by the lithiotids, a group of larger aberrant gregarious bivalves (e.g., Broglio Loriga and Neri, 1976). Appeared in the early Pliensbachian, they proliferated in upper Pliensbachian tropical lagoons, where they built tabular and dome-shaped sedimentary bodies known as bivalve-mound (e.g., Posenato and Masetti, 2012). As reported by Brame et al. (2019), the half Pliensbachian reefs (53% of reefs recorded in the PaleoReefs database; Kiessling et al., 2003) was made up of lithiotids. Their spread during the Lower Jurassic "reef gap" was considered an example of a failed succession (Fraser et al., 2004). Lithiotid bivalves would have filled ecological niche of corals, which had not yet fully recovered from the end-Triassic extinction (Nauss and Smith, 1988; Fraser et al., 2004; Franceschi et al., 2014a).

The spread of lithiotid bivalves along with Cretaceous rudists represents one of the two Mesozoic evolutionary phases in which constratal-growth bivalves (*sensu* Skelton et al., 1995) became globally widespread and played an essential role in tropical Tethyan and Panthalassa carbonate platform dynamics (e.g., Bosellini, 1972; Broglio Loriga and Neri, 1976; Geyer, 1977; Nauss and Smith, 1988; Leinfelder et al., 2002; Fraser et al., 2004; Posenato and Masetti, 2012).

The term lithiotid, commonly used in literature, has no systematic value since these bivalves belong to different taxonomic groups (e.g., Accorsi Benini and Broglio Loriga, 1977; Accorsi Benini, 1979). Lithiotid is essentially referred to three monospecific bivalve genera represented by the species: *Cochlearites loppianus* (Tausch, 1890), *Lithioperna scutata* (Dubar, 1948), and *Lithiotis problematica* Gümbel, 1871 (e.g., Debeljak and Buser, 1998; Posenato et al., 2018; Brame et al., 2019). Some authors have included in the lithiotids also the bivalves *Gervilleioperna* sp. Krumbeck, 1923, *Opisoma excavatum* Boehm, 1884, and *Pachyrisma* (*Durga*) *crassa* Boehm, 1884 (e.g., Fraser et al., 2004; Posenato and Masetti, 2012). These last three species show different stratigraphic distribution and their abundance in the tropical lagoon is less important.

Lithiotids thrived along the Tethyan and Panthalassa margins from northern Africa, through southeast Asia to western America (e.g., Bosellini, 1972; Broglio Loriga and Neri, 1976; Geyer, 1977; Nauss and Smith, 1988; Leinfelder et al., 2002; Fraser et al., 2004; Posenato and Masetti, 2012). Their geographic distribution took place after the Sinemurian–Pliensbachian eutrophic, poorly oxygenated water phase (Franceschi et al., 2014a).

The lithiotid success seems to have been interrupted by the reef crisis occurred during the Pliensbachian/Toarcian boundary and with the onset of the T-OAE. This period constitutes one of the most significant reef collapses of the Phanerozoic (Kiessling and Simpson, 2011). In the Trento Platform, the stratigraphic location of the Pliensbachian/Toarcian stage boundary is unclear (e.g., Posenato and Masetti, 2012), therefore the occurrence of lithiotid accumulations in the lower Toarcian is doubtful. The lithiotid stratigraphic distribution is more continuous in the Southern Apennines (Trecalli et al., 2012; Posenato et al., 2018) and Morocco (Brame et al., 2019), where the lithiotids pass the Pliensbachian/Toarcian boundary and reach the T-OAE when they become extinct.

Previous studies on lithiotids have been focused mostly on systematics (Accorsi Benini and Broglio Loriga, 1977; Accorsi Benini, 1979), functional morphology (i.e., Chinzei, 1982; Accorsi Benini and Broglio Loriga, 1982; Seilacher, 1984; Accorsi Benini, 1985; Broglio Loriga and Posenato, 1996; Savazzi, 1996) and paleobiogeography (Broglio Loriga and Neri, 1976; Fraser et al., 2004). Few works described the lithiotid accumulations in detail (Bosellini, 1972; Posenato and Masetti, 2012; Bassi et al., 2015; Posenato et al., 2018).

This thesis aims to examine the palaeoecological and paleoclimatic evidences recorded by the lithiotids (i.e., sclerochronology and shell accumulations) during the evolution of the Lower Jurassic lithiotid-bearing sedimentary succession of the Trento Platform (Southern Alps). In this area, lithiotids occur in the Pliensbachian part of the Rotzo Formation, which is included in the Calcari Grigi Group, a thick shallow-water carbonate succession. *Lithiotis* and *Cochlearites* were described here for the first time (e.g., Gümbel, 1871; Tausch, 1890; Böhm, 1891; Reis, 1903). This area is well known in literature for widespread and highly preserved outcrops which allow to analyse lithiotid accumulation geometries (e.g., Bosellini, 1972; Posenato et al., 2000; Posenato and Masetti, 2005; Posenato and Masetti, 2012).

The research deals with: a) the taphonomic signatures of the lithiotid shells in the accumulations; b) the skeletal and non-skeletal components along with pyrite forms in different accumulations; c) a geochemical-sclerochronological approach to provide information on the lithiotid growth strategies as proxy of palaeoecological limiting factors.

These points constitute the chapters of the thesis which is furtherly upheld by appendixes and plates. Each chapter is organized as a peer-review manuscript, being a single scientific contribution.

1.1. Thesis outlines

To assess the paleoenvironmental and paleoclimatic constrains on the lithiotid ecology, this thesis is divided into six chapters.

Chapter 2 presents the geological and stratigraphic setting of the studied area (Trento Platform, Southern Alps).

Chapter 3 evaluates the distribution of autochthonous, parautochthonous and allochthonous lithiotids in the accumulation core and flanks. Various representative accumulations are characterized with respect to systematic content, shell cover, shell density, disarticulation, shell fragmentation and orientation of individual shells. The analysis was carried by quantitative methods.

Chapter 4 verifies the occurrence of bacteria-like features and pyrite shapes to evaluate the microbial role and the redox conditions in the lithiotid accumulations.

Chapter 5 presents a sclerochronological and stable isotope study ($\delta^{13}C$ and $\delta^{18}O$) on some well-preserved lithiotid bivalves collected from the Lessini Mts. (Trento Platform). The $\delta^{13}C$ and $\delta^{18}O$ variations along with growth pattern investigations provide information on paleoenvironment and paleoclimatic changes recorded in the Pliensbachian part of the Rotzo Formation.

Finally, **Chapter 6** provides a summary of the conclusions achieved in this work.

The results and discussions of these Chapters are based on materials (e.g., specimens, thin sections) and data described and illustrated in Appendixes.

Chapter 2

Geological and stratigraphic setting

The Jurassic Trento Platform (Southern Alps) is a palaeogeographic unit inherited from the rifting associated with the opening of central North Atlantic Ocean (e.g., Winterer and Bosellini, 1981; Masetti et al., 1996; Masetti et al., 1998; Avanzini et al., 2006). In the Trento Platform, the Hettangian–Pliensbachian interval is represented by the Calcari Grigi Group, a thick carbonate shallow-water succession (Figs. 2.1, 2.2).

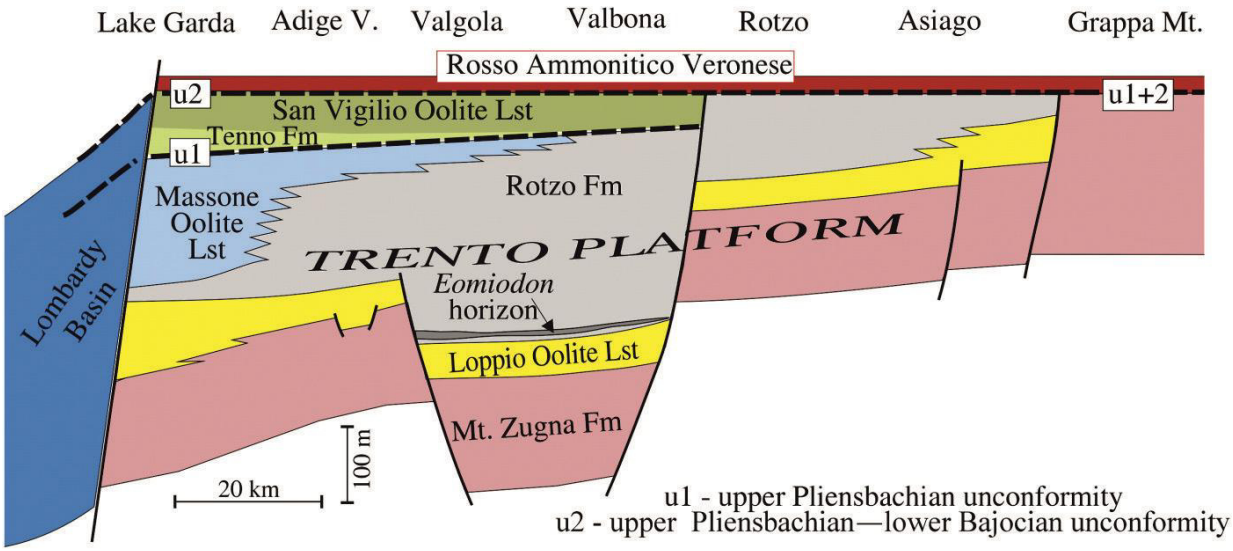

Figure 2.1. Stratigraphic relationship of the Lower Jurassic sedimentary successions along a W–E oriented transect of the Trento Platform (Early–Mid Jurassic) (from Posenato and Masetti, 2012, modified).

The Calcari Grigi Group, overlying the Dolomia Principale (a carbonate platform succession with peritidal cycles) is composed of (in stratigraphic order): Monte Zugna Formation (carbonate mudstones organized in peritidal cycles), Loppio Oolite Limestone (oolitic grainstones), Rotzo Formation (marlstones and bioclastic limestones) and Massone Oolite Limestone (oolitic grainstones) (e.g., Masetti et al., 1998; Castellarin et al., 2005; Fig. 2.1). The demise of the Trento Platform has been related to possible different events: a prolongated emersion (Sturani, 1971), a drowning below the photic zone (Winterer and Bosellini, 1981) or a combination of eustatic sea-level rise and environmental change (Zempolich, 1993).

Lithiotids occur in the upper Sinemurian–Pliensbachian Rotzo Formation, which extends from the Adige Valley to the Asiago area with the maximum thickness (~250 m) in the depocentre (Altopiano di Tonezza-Folgaria; Fig. 2.1). Masetti et al. (2012) and Franceschi et al. (2014b) suggested that the sharp thickness variations in the Rotzo Fm are a consequence of

an active syn-sedimentary tectonics. A hiatus of variable entity (u1 in Fig. 2.1) has been recognized between the Rotzo Fm and the Loppio Oolitic Limestone (Romano et al., 2005; Masetti et al., 2012). An unconformity surface (u2 in Fig. 2.1), corresponding to a temporal hiatus, truncates at various levels the Calcari Grigi Group (Masetti et al., 1998; Romano et al., 2005). The Rotzo Fm is overlain or laterally replaced by several formations (Figs. 2.1, 2.3) such as the Massone Oolite (Pliensbachian), the Tenno Formation (lower Toarcian) and the San Vigilio Oolite (upper Toarcian–Aalenian; Figs. 2.1, 2.3). Towards the east (Rotzo and Asiago area), where the thickness is less than 100 m, the Rotzo Fm is directly overlain by the pelagic and condensed succession of the Rosso Ammonitico (Aalenian–Tithonian; e.g., Masetti et al., 1998).

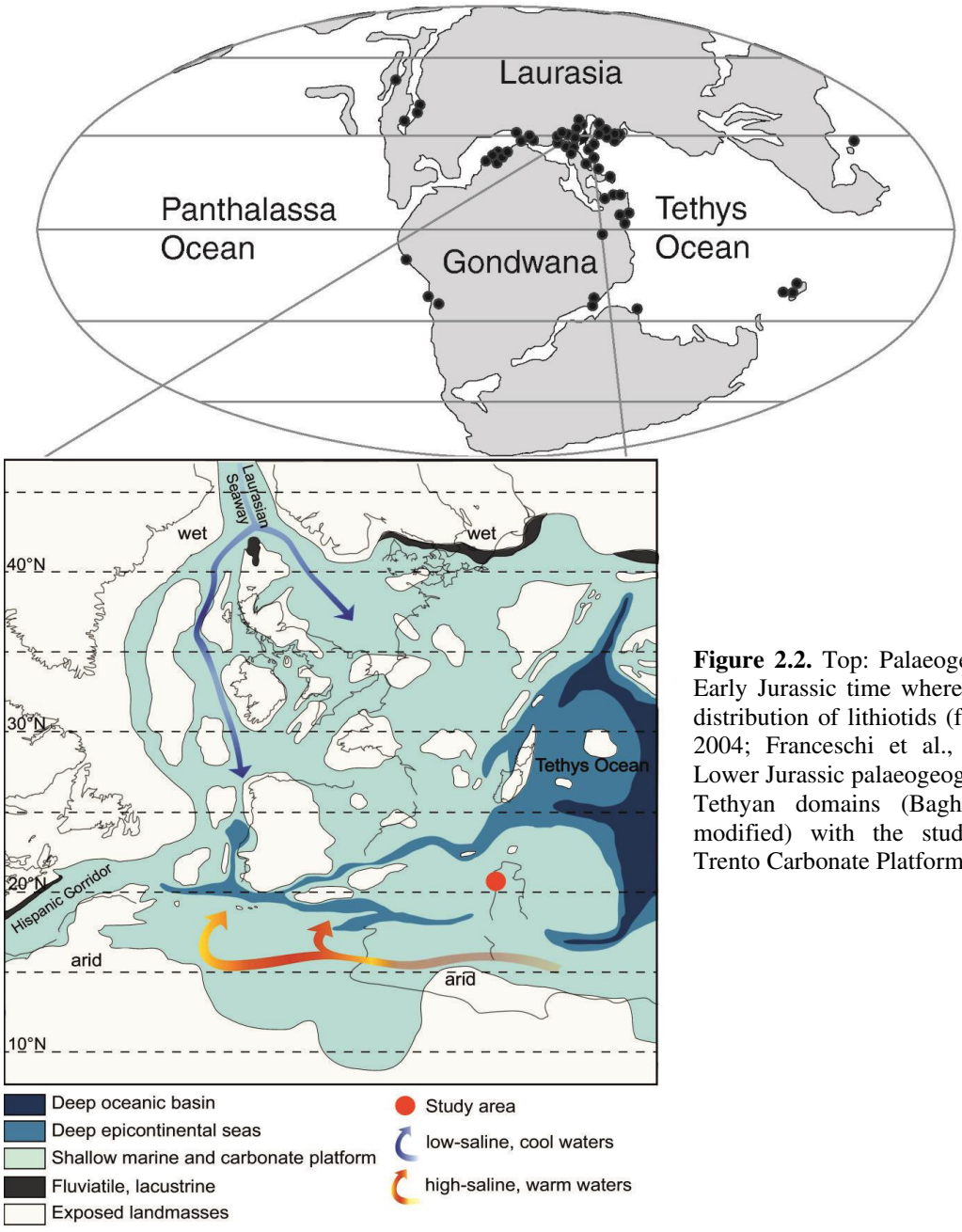

Figure 2.2. Top: Palaeogeographic map of Early Jurassic time where black dots show distribution of lithiotids (from Fraser et al., 2004; Franceschi et al., 2014a). Bottom: Lower Jurassic palaeogeography of the peri-Tethyan domains (Baghli et al., 2019, modified) with the studied area of the Trento Carbonate Platform.

The Rotzo Fm records a tropical lagoon protected from the open sea (Belluno Basin at east and Lombardian Basin at west) by oolitic shoals and from the land (probably towards south) by marshes (Bosellini and Broglio Loriga, 1971; Clari, 1975). The Rotzo Fm would represent a ramp-lagoon shielded towards the western Trento Platform (Monte Baldo area) by a distal littoral complex identifiable with the Massone Oolite limestone (Masetti et al., 1998; Masetti, 2002).

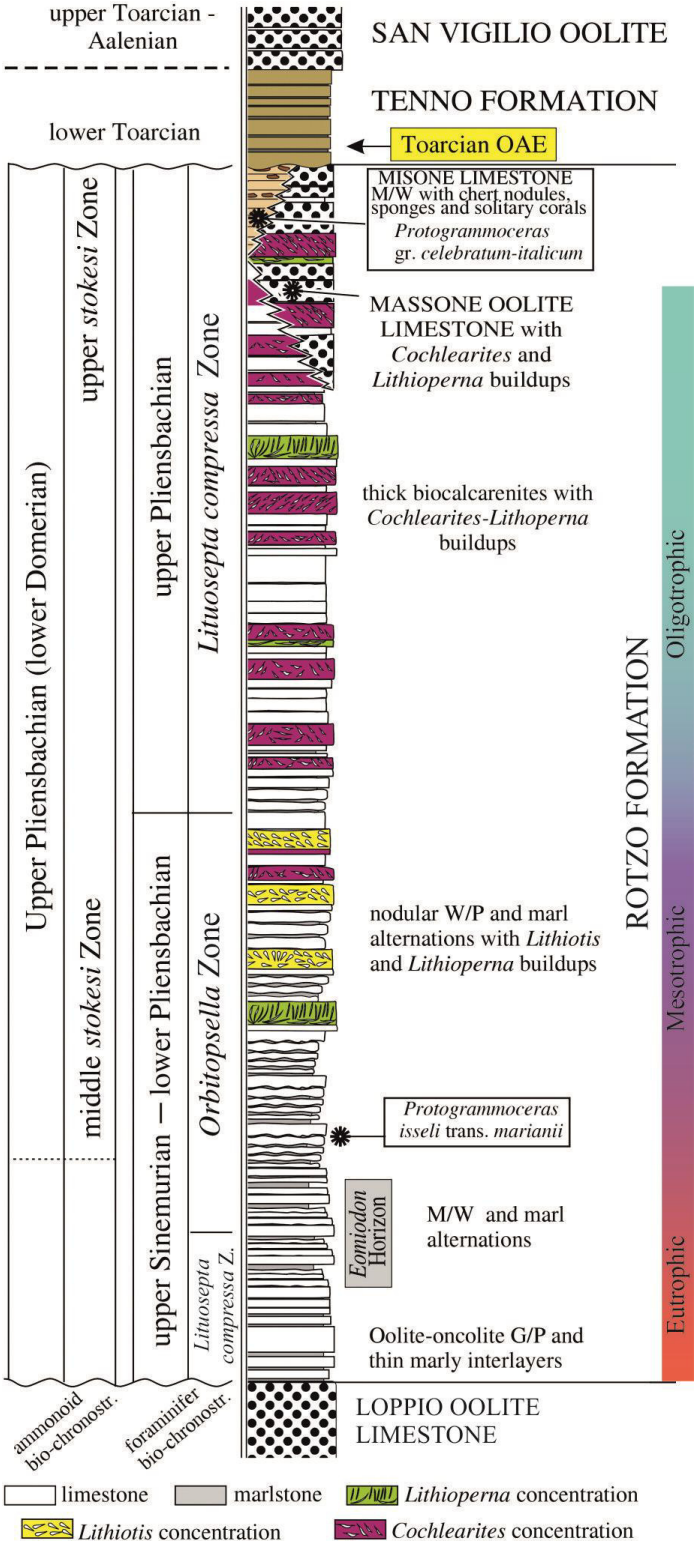

Figure 2.3. Schematic stratigraphic column and trophic regimes of the Rotzo Formation occurring in the depocenter (north-western area) of the Trento Platform (Posenato and Masetti, 2012, modified). Foraminiferal bio-chronostratigraphy and trophic regimes from Fugagnoli (2004). Z., Zone.

The Rotzo Fm contains rich micro- and macro-benthic associations including bivalves, gastropods, brachiopods, larger and small benthic foraminifera, calcareous algae, solitary corals, echinoderms and plant remains (e.g., De Zigno, 1856–1885; Tausch, 1890; Accorsi Benini and Broglio Loriga, 1977; Accorsi Benini, 1979; Fugagnoli, 2004). Fossil traces are also abundant (Monaco and Giannetti, 2001; 2002).

The lower part of the Formation consists of limestone and marlstone alternations with frequent organic-rich beds containing *Eomiodon* bivalve pavements. *Eomiodon* is an opportunistic veneroid bivalve, typical of stressed and low-salinity environments (Posenato et al., 2013b, and references therein). The *Eomiodon* beds deposited within a brackish and restricted lagoon with seasonal freshwater and nutrient inputs (Bassi et al., 1999; 2008; Boomer et al., 2001; Posenato et al., 2013b).

The middle and upper part of the Rotzo Fm consist of limestone-marlstone alternations and calcarenites. The marlstones decrease while calcarenites become more frequent and thicker upwards. In the depocenter of the Formation, the lithiotid accumulations appear in the middle part and flourish in the upper one (Fig. 2.3; Masetti, 2002; Masetti et al., 1998; Franceschi et al., 2014a). Limestone-marlstone alternations include decimeter-thick peloidal packstone/wackestone and thin marlstone, commonly with a thickening-upward trend (Fig. 2.3; e.g., Posenato and Masetti, 2012). The calcarenitic beds consist of packstone/grainstone with peloids, bioclasts or coated grains recording an increase in wave energy according to a shallowing-upward cycle evolution (e.g., Posenato and Masetti, 2012).

Because the rarity of ammonoids, the bio-chronostratigraphy of the Rotzo Fm has been essentially based on benthic foraminifera (e.g., Bosellini and Broglio Loriga, 1971; Fugagnoli and Loriga Broglio, 1998; Fugagnoli, 2004). The Rotzo Fm is divided into the following three foraminiferal biostratigraphic units (in stratigraphical order): *Lituosepta recoarensis* Zone, *Orbitopsella* Zone and *Lituosepta compressa* Zone.

The foraminiferal bio-chronostratigraphy suggested a late Sinemurian–late Pliensbachian age (*Orbitopsella* Zone and *Lituosepta compressa* Zone).

This dating has a low biostratigraphic accuracy because these foraminiferal zones have a strong environmental control and the correlation with the Lower Jurassic ammonoid biozones was proposed in Morocco where the foraminifera have a stratigraphic distribution sometimes different from that of the Trento Platform (e.g., Septfontaine, 1988; Fugagnoli and Loriga Broglio, 1998).

The single *in situ* ammonoid specimen "*Protogrammoceras isseli* trans. *marianii*" was collected from the *Orbitopsella* Zone of the Adige Valley (Sarti and Ferrari, 1999). This taxon is indicative of the middle *Stokesi* Subzone (lower *Margaritatus* Zone) and is early late

Pliensbachian in age (Sarti and Ferrari, 1999). Another ammonoid determined as "*Protogrammoceras* gr. *celebratum-italicum*" was collected from the debris of Rust Mt. (Lavarone; Sarti, 1981). It was referred to the upper *Stokesi* Subzone (lower *Margaritatus* Zone; Sarti and Ferrari, 1999). Based on these two findings, the *Orbitopsella* Zone in the Trento Platform seems to be mostly late Pliensbachian in age (Fig. 2.3; Posenato and Masetti, 2012), as suggested in the past (e.g., Cita, 1959). As resulted by ammonoid distribution and cyclostratigraphic analyses (Masetti et al., 1998) the most part of the Rotzo Fm deposited during a short time interval, restricted to the lower *Margaritatus* Zone (late Pliensbachian; Posenato and Masetti, 2012).

Data on isotope stratigraphy seem to confirm the chronostratigraphic framework so far proposed by mean of foraminifera. $^{87}Sr/^{86}Sr$ from the Madonna della Corona section (Woodfine et al., 2008) and $\delta^{13}C$ anomalies (Franceschi et al., 2014a) suggest that Rotzo Fm would range from the latest Sinemurian to the late Pliensbachian (Fig. 2.4).

2.1. Palaeoecological setting of the lithiotids: historical background

In the Rotzo Formation succession, three trophic intervals have been recognized (Fugagnoli, 2004). The lower part (*L. recoarensis* Zone and lower *Orbitopsella* Zone; Fig. 2.3) contains the *Eomiodon* horizon and corresponds to a eutrophic regime. The middle and upper part of the *Orbitopsella* Zone record mesotrophic conditions.

In this latter interval the lithiotid accumulations are sparse. The oligotrophic regime occurs in the *L. compressa* Zone. This interval is distinguished by a great abundance of lithiotid accumulations.

Franceschi et al. (2014a) correlated the spread of the lithiotids in the Trento Platform to the end of negative $\delta^{13}C$ perturbations, which characterized the lower Pliensbachian eutrophic phase. These perturbations, starting in the uppermost Loppio Oolitic Limestone and continuing into the base of the Rotzo Fm, have been correlated with the onset of the Sinemurian–Pliensbachian boundary Event (S–P Event; Franceschi et al., 2014a). The onset of more stable, meso-oligotrophic marine conditions is supported by the recovery of stenotopic marine benthonic biota (e.g., larger foraminifera, calcareous sponges, solitary corals, brachiopods, crinoids, photosymbiotic bivalves) and the simultaneous appearance of lithiotid bivalves (Fugagnoli, 2004). The acme of lithiotid accumulations is registered in the same period in other shallow-water carbonate platforms both in the tropical Tethyan and Panthalassa localities (Franceschi et al., 2014a, and references therein).

The stratigraphic and geographic distribution of the lithiotids was environmentally controlled although their limiting factors are still not clearly defined (Fraser et al., 2004; Posenato and Masetti, 2012). In the Trento Platform, *Lithiotis problematica* is common in the middle part of the Rotzo Fm (upper *Orbitopsella* Zone) during a prevailing mesotrophic regime, although its occurrence in the upper part of the Formation (*Lituosepta compressa* Zone) cannot be excluded (e.g., Contrada Dazio section). Frequently, *L. problematica* accumulations overlie rhynchonelliform brachiopod beds, larger foraminifera and solitary corals, which suggest fully marine and well oxygenated conditions (Posenato and Masetti, 2012). *Cochlearites loppianus* thrives in the upper part of the Formation, marked by oligotrophic setting with more stable nutrient supply (Fugagnoli, 2004; Posenato and Masetti, 2012). The greater surviving capability in lower oxygenated muddy substrates of *Cochlearites* compared to *Lithiotis* is suggested by the larger body cavity and pallial surface (Posenato and Masetti, 2012). Furthermore, *Cochlearites* accumulations generally overlie megalodontid coquinas. These latter bivalves, indicating very shallow, euhaline to slightly hyperhaline and warm waters, suggest that *Cochlearites* inhabited these environments (Posenato and Masetti, 2012). This latter phase, with *Cochlearites*-dominated accumulations records the maximum lateral and vertical lithiotid development.

Lithioperna is considered the most eurytopic lithiotids adapted to low oxygenated environments too. In the Southern Alps, it is the first lithiotid genus to appear after the end of the Early Pliensbachian C-isotope perturbations and the short-term warm-humid climatic phase registered by *Eomiodon* horizon (Posenato et al., 2013b; Franceschi et al., 2014a). *Lithioperna* thrived in shallower and more stressed marine environments in comparison to *Lithiotis* and *Cochlearites* (Posenato et al., 2000). This genus is very common in the Trento Platform and it ranges throughout the Rotzo Fm (e.g., Posenato and Masetti, 2012), frequently within *Cochlearites*- or *Lithiotis*-dominated accumulations.

The maximum proliferation of lithiotids occurred during the late Pliensbachian, both in the Tethyan and Panthalassa regions (Fig. 2.2). The dispersion has been related to the opening of Hispanic Corridor (Nauss and Smith, 1988; Franceschi et al., 2014a), which connected the Tethys and Paleo-Pacific oceans (e.g., Aberhan, 2001).

Although there is not a full agreement on the timing of the opening of the Hispanic Corridor (Franceschi et al., 2014a, and references therein), this marine connection promoted the dispersion of lithiotids along the Panthalassa and Tethyan coasts. This diffusion was allowed by the onset of more stable meso-oligotrophic conditions after the S–P Event (Franceschi et al., 2014a).

The lithiotid extinction occurred during a new global environmental and biotic stressed phase related to the early Toarcian Anoxic Event (e.g., Fraser et al., 2004; Trecalli et al., 2012; Franceschi et al., 2014a; Posenato et al., 2018; Brame et al., 2019).

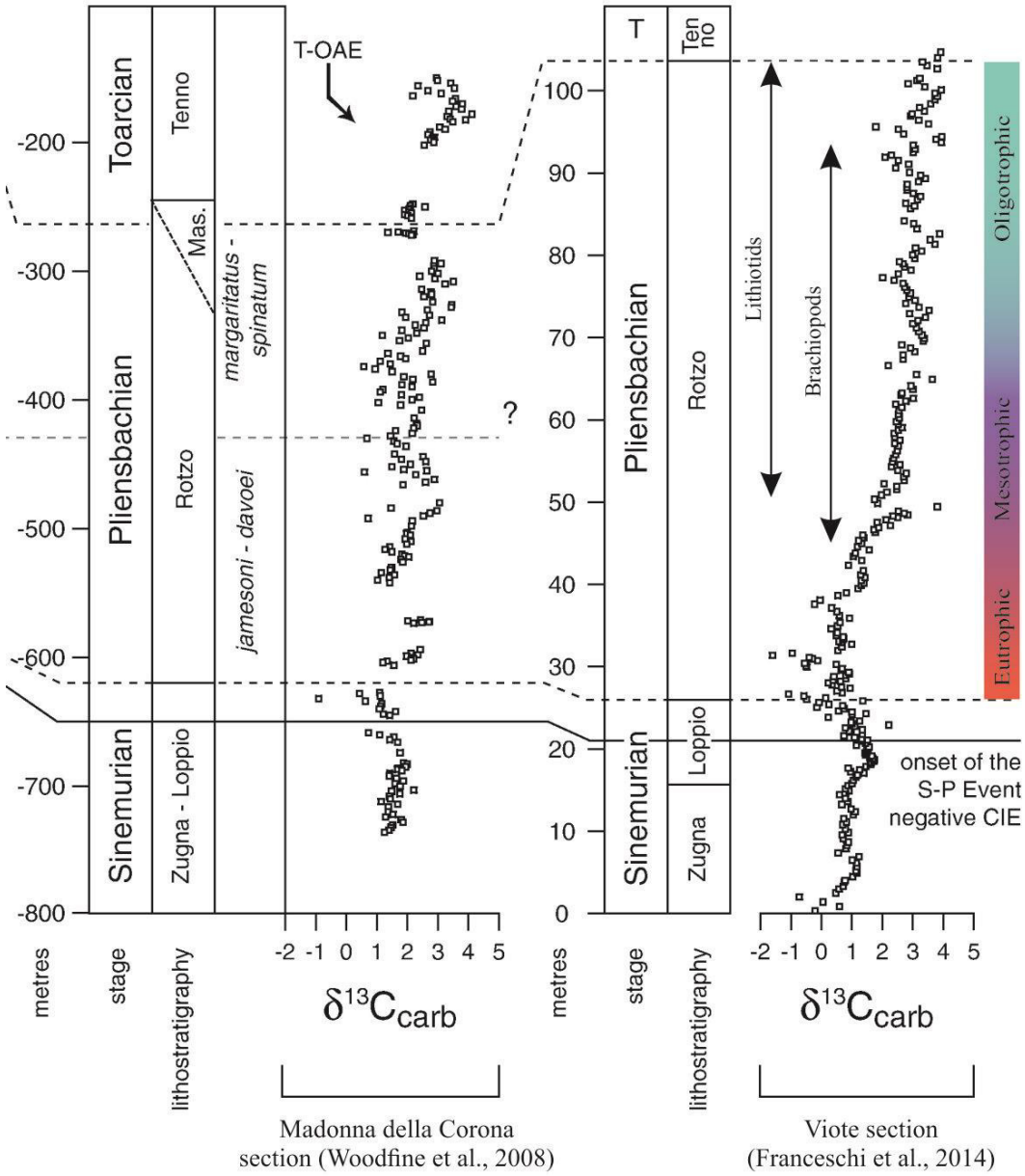

Figure 2.4. Chemostratigraphic correlation of Viote and Madonna della Corona sections (from Franceschi et al., 2014a, modified). Trophic regime in Viote section from Fugagnoli (2004) and Franceschi et al., 2014a. The correlation with the ammonoids bio-chronostratigraphy of Madonna della Corona derived by the comparison of $^{87}Sr/^{86}Sr$ data (Woodfine et al., 2008). Mas., Massone; T, Toarcian. See text for further details.

Chapter 3

Distinguishing core and flank facies based on shell fabrics in Lower Jurassic lithiotid shell beds

This chapter has been published in Palaeogeography, Palaeoclimatology, Palaeoecology, v. 526, 2019, p. 1–12.
Supplementary data can be found online at https:// doi.org/10.1016/j.palaeo.2019.04.010.

3.1. Introduction

The lithiotid bivalves, *Cochlearites*, *Lithiotis* and *Lithioperna* had similar ecologies included the ability to be framework builders in the shallow-water lagoon. *Cochlearites* and *Lithiotis* were suspension-feeders, which developed a semi-infaunal mode of life within low energy, soft substrates (Chinzei, 1982; Seilacher, 1984). These taxa were cemented in the early life stage to hard substrates. *Lithiotis* and *Cochlearites* shells are rarely found as bouquet-like aggregates suggesting that their life position was basically up-right (Göhner, 1980; Chinzei, 1982; Posenato et al., 2018). Their accumulations are characterized by a mud-supported core with a loosely packed shells fabric with embedded congregation of forms (constratal *sensu* Skelton et al., 1995) and few shells in vertical position. These accumulations, lacking a wave-resistant rigid framework, have been defined as bivalve mounds (*sensu* Riding, 2002; Posenato and Masetti, 2012).

Lithioperna was suspension-feeder with an epifaunal to semi-infaunal mode of life. Two main morphotypes were recognized in adult shells (Seilacher, 1984): an orthothetic, mud-sticker (morphotype A of Broglio Loriga and Posenato, 1996), with a flat and thin shell contributing to crowded, vertically imbricated colonies, and a pleurothetic morphotype, cup-shaped recliner (morphotype B of Broglio Loriga and Posenato, 1996) with thick and roundish shells which lived in more sparse populations. The morphotype B had either heavyweight shells for bottom stabilization in skeletal supported substrates or corresponding lightweight strategies in mud-supported substrates (Broglio Loriga and Posenato, 1996).

Difficulties in distinguishing the lithiotids preserved in indurated limestone have hampered the detailed descriptions of their accumulations and related architecture (i.e., core and flanks), as well as the distinction of autochthonous and parautochthonous individuals. At the outcrop scale, randomly sectioned shells often do not show diagnostic characters at genus level.

Furthermore, the entire accumulation shape rarely crops out completely and architectural features (i.e., core, flanks as described by Posenato and Masetti, 2012) are poorly

known (e.g., Posenato et al., 2018). Although a suite of quantitative methods to describe rudist accumulations has been so far applied and discussed (e.g., Vilardell and Gili, 2003; Gili et al., 2016), little has been performed for the lithiotid accumulations as far as quantitative methodology is concerned (Posenato et al., 2018).

Various accumulations containing the monospecific taxa *Lithiotis problematica* Gümbel, 1871, *Cochlearites loppianus* (Tausch, 1890) and *Lithioperna scutata* (Dubar, 1948) from the Trento Platform are studied in detail in order to: (1) document different lithiotid accumulations with respect to taxonomic diversity of large bivalves, sedimentary fabric and taphonomy, (2) identify different accumulation types including cores and flanks by quantitative various sedimentary and taphonomic attributes, and (3) distinguish and interpret different systematic presence and preservation of autochthonous, parautochthonous or allochthonous bivalves within the architectural features of the accumulations.

3.2. Materials and methods

The studied lithiotid shell deposits are defined as accumulations to indicate bivalve deposits with no structural and dynamic implications (e.g., Riding, 2002). Eighteen lithiotid accumulations cropping out in the Verona, Vicenza and Trento areas (northeast Italy) were studied (Fig. 3.1; Tab. 3.1): one accumulation in the Vaio dell'Anguilla (Lessini Mts., Verona), seven accumulations in the Altopiano di Tonezza (Vicenza; six in the Toraro Mt. succession, one near Campoluzzo Mt.), five accumulations in the Altopiano di Asiago (Rotzo, Vicenza), an isolated outcrop near Passo Vezzena (Trento) with four lithiotid accumulations and a huge accumulation near Contrada Dazio (Folgaria, Trento).

The studied accumulations, characterized by the three most aberrant taxa (*Lithiotis*, *Cochlearites*, *Lithioperna*), occur in six different successions, within the Rotzo Formation and range from the *Orbitopsella* Zone to the *Lituosepta compressa* Zone (Fugagnoli, 2004; Fig. 3.1A; Tab. 3.1). These accumulations were selected for their distinctive characteristics which represent the suite of the larger bivalve accumulations. The Toraro Mt., Campoluzzo Mt. and Vaio dell'Anguilla outcrops, located in the middle-upper Rotzo Formation, show the accumulation shapes in which all lithiotid morphotypes occur (Figs. 3.2–3.4). The Rotzo accumulation case shows horizontally oriented shell accumulations, with no defined general shape. The largest accumulation occurs in Contrada Dazio outcrop (Göhner, 1980), where the lithiotid shells are chaotically arranged, while the Passo Vezzena outcrop has never been examined in detail.

The studied bivalve accumulations were described in terms of stratigraphic location, dominant lithiotid taxa, shell fabrics and taphonomic attributes. These attributes are (1) percentage of shell cover (% of area covered by shells), (2) shell density (number of individuals/400 cm^2 occurring in perpendicular sections to the bedding or on the bedding surface), (3) percentage of articulated and (4) complete shells, and (5) relative proportion of autochthonous/parautochthonous or allochthonous individuals.

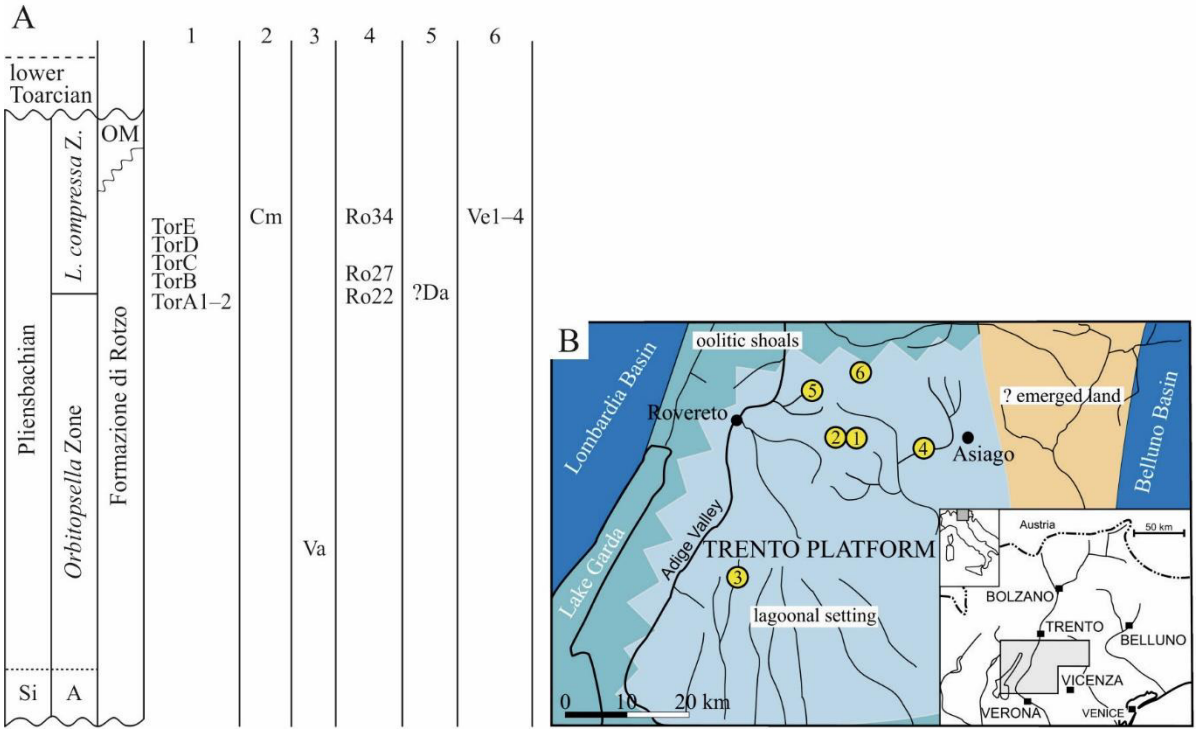

Figure 3.1. A) Schematic stratigraphic setting of the Rotzo Fm with the biostratigraphic location of the studied accumulations (TorA–E, Cm, Va, Ro22/27/34, Da, Ve1–4; Tab. 3.1). Numbers refer to the geographic areas of Fig. 3.1B. Si, upper Sinemurian; A, *Lituosepta recoarensis* Zone; *L. compressa* Z., *Lituosepta compressa* Zone; OM, Oolite di Massone. B) Geographic locations of the studied lithiotid accumulations in the Trento Platform, northern Italy. 1, Toraro Mt.; 2, Campoluzzo Mt.; 3, Vaio dell'Anguilla; 4, Rotzo; 5, Contrada Dazio; 6, Passo Vezzena. Palaeogeographic map modified from Posenato and Masetti (2012).

Stratigraphic section	**Accumulation**	**Distance from the base**	**Biozone**	**Total analysed quadrants**	**Areal extension for each quadrant**
Toraro Mt. (45°52'08.9"N, 11°16'20.2"E)	TorA1	~120 m	*Orbitopsella* Zone	15	400 cm^2
	TorA2	~120 m	*Orbitopsella* Zone	4	100 cm^2 (1), 56.25 cm^2 (3)
	TorB	160 m	*Lituosepta compressa* Z.	2	100 cm^2
	TorC	172 m	*L. compressa* Z.	42	400 cm^2
	TorD	177 m	*L. compressa* Z.	9	100 cm^2
	TorE	180 m	*L. compressa* Z.	26	400 cm^2
Campoluzzo Mt. (45°52'17.9"N, 11°15'34.4"E)	Cm	~1–2 m	*L. compressa* Z.	5	400 cm^2

Vaio dell'Anguilla (45°39'26.3"N 11°00'58.5"E)	Va	~15 m	*Orbitopsella* Z.	5	900 cm^2 (3), 400 cm^2 (2)
Rotzo (45°51'06.7"N, 11°22'15.8"E)	Ro22	~60 m	*Orbitopsella* Z.	3	400 cm^2
	Ro27	~68 m	*L. compressa* Z.	10	100 cm^2
	Ro34.1	~81 m	*L. compressa* Z.	1	400 cm^2
	Ro34.2	~82 m	*L. compressa* Z.	1	100 cm^2
	Ro34-section	~87 m	*L. compressa* Z.	1	400 cm^2
	Ro34-surface	~89 m	*L. compressa* Z.	10	400 cm^2 (9), 1600 cm^2 (1)
Contrada Dazio (45°55'40.1"N, 11°15'31.8"E)	Da	Isolated outcrop	? *L. compressa* Z.	4	900 cm^2
Passo Vezzena (45°57'05.1"N, 11°21'36.3"E)	Ve1	Isolated outcrop	*L. compressa* Z.	3	400 cm^2
	Ve2			6	1600 cm^2 (4), 400 cm^2 (1), 900 cm^2 (1)
	Ve3			2	400 cm^2 (1), 225 cm^2 (1)
	Ve4			1	900 cm^2

Table 3.1. Summary data of the studied lithiotid accumulations with the geographic and biostratigraphic locations, number of the total analysed quadrants and areal extension for each analysed quadrant. The distance of the studied accumulations from the base of the stratigraphic section refers to Coletta (2012; Toraro Mt., Campoluzzo Mt.), Posenato and Masetti (2012; Vaio dell'Anguilla) and Bosellini and Broglio Loriga (1971; Rotzo). Details of the shell accumulations in the text. Z., Zone.

The taxonomic identification of lithiotid bivalves at the outcrop scale is difficult because specific shell sections showing diagnostic characters are usually very rare (e.g., Posenato et al., 2018). The most recognizable characters are found in transversal sections of the dorsal body cavity (e.g., Berti Cavicchi et al., 1971; Chinzei, 1982; Broglio Loriga and Posenato, 1996). *Lithiotis* and *Cochlearites* have dorso-ventrally elongated shells, with a thick attached valve and a thinner free valve. In *Lithiotis*, the free valve is very thin and thus rarely preserved. *Cochlearites* is characterized by an umbonal area with a median large furrow on the thicker valve and a median ridge on the thinner valve. *Lithiotis* is distinguished from *Cochlearites* in having a body cavity with a sub-central ridge in the thicker valve and a furrowed median plate on the umbonal area. *Lithioperna* is characterized by large, flattened to concavo-convex shells with roundish to sub-rectangular outline. In longitudinal sections, the articulated shells of *Lithioperna* have a flattened shape with the lens-shaped articulated pair. Some representative randomly-sectioned shell specimens allowed for the taxonomic identification of the dominating bivalve taxa (see Posenato et al., 2018). Large rock samples were also sectioned and polished in order to identify enclosed specimens.

The sedimentary fabric and taphonomic attributes of the lithiotid accumulations were quantitatively assessed using field macro-photographs of exposed natural rock surfaces oriented

either parallel or perpendicular to the bedding and analysed by using the graphic software package AutoCAD 2016.

Each outcrop was mapped by quadrants (Fig. 3.2) in order to analyse the sedimentary and taphonomic attributes of the lithiotids within the accumulations. Whenever possible, representative quadrants were taken from the core and flanks of accumulations. In outcrops with undetermined accumulation architecture (i.e., Rotzo, Contrada Dazio), randomly distributed quadrants were taken from different parts of the accumulation. Depending on maximum shell size, quadrants ranging in size from 7.5 × 7.5 cm to 40 × 40 cm were analysed. In all, a total of 150 quadrants were analysed (Tab. 3.1) with the average values reported in Figs. 3.5–3.7.

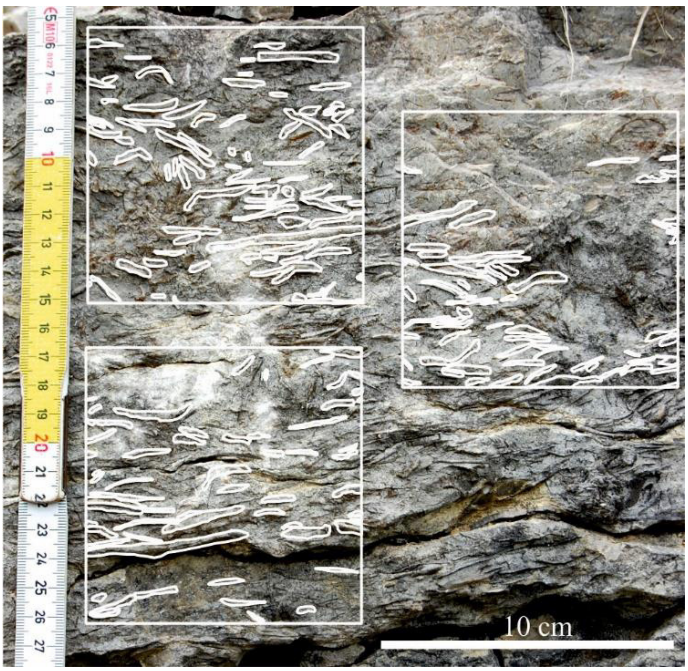

Figure 3.2. Example of quadrants within which the randomly sectioned lithiotid shells preserved within indurated limestone were traced (e.g., *Lithioperna*, TorD). In the digitally analysed photos sedimentary fabrics and taphonomic attributes such as percentage of shell cover, shell density, percentage of articulated and complete shells were calculated.

3.3. Results

3.3.1. Toraro Mt. accumulation A (TorA1 - A2)

Lithiotis characterizes two superimposed bivalve accumulations (TorA1, TorA2) consisting of peloidal-bioclastic rudstones/floatstones with a wackestone/packstone matrix containing rare undetermined lituolid larger foraminifera.

TorA1 accumulation is ca. 1 m high and ca. 10 m wide (Fig. 3.5A). The thick *Lithiotis* shells ranging from 5 mm to 25–30 mm in thickness and up to 30 cm high, are easily recognizable by the transversal sections of the body cavity of the attached valve. The free valve, thinner than the attached one, cannot be identified at the outcrop scale. Vertical and strongly inclined individuals are mostly preserved as moulds and casts due to aragonite dissolution (Posenato and Masetti, 2012, fig. 7g, k, l). In the TorA1 accumulation core the shell density is relatively low (7–15 ind./400 cm^2), but higher in the accumulation flanks (19–27 ind./400 cm^2;

Fig. 3.3B). The percentage of shell cover increases toward the accumulation flanks, where rare sponges, brachiopods, *Pseudopachymytilus*, *Opisoma* and solitary corals occur. The core is characterized by abundant autochthonous *Lithiotis* and brachiopod shells. The lithiotid shells have an inclination ranging from 25°–30° to 80°; some bouquet-like aggregates are also present (Fig. 3.3A). In the periphery of the flanks, the shells are sub-horizontal (at most inclined ca. 15°; Fig. 3.3B).

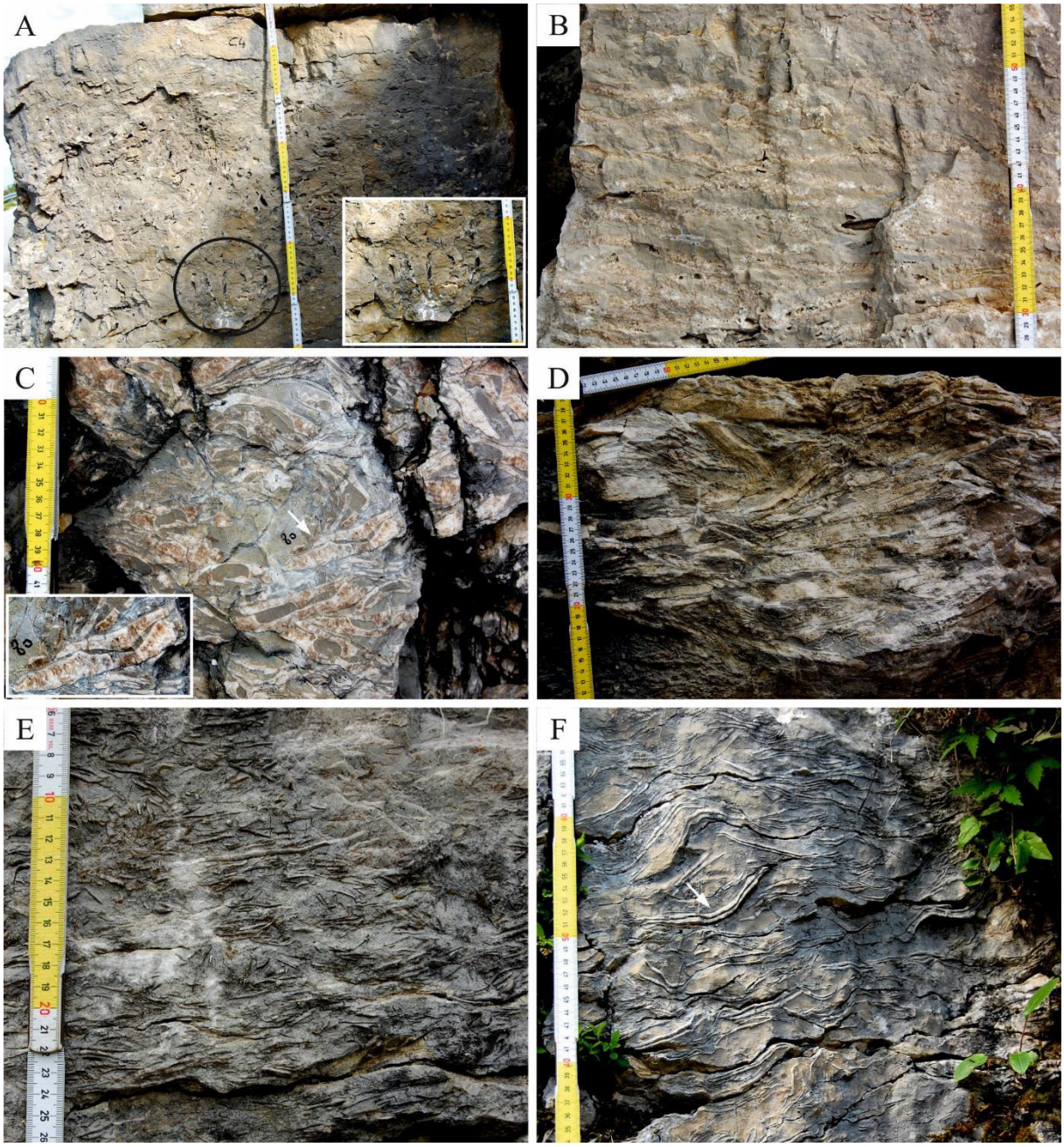

Figure 3.3. Examples of randomly-sectioned lithiotid specimens characterizing the studied accumulations. A–B, *Lithiotis problematica* (A, core with bouquet-like aggregate, magnified inset white rectangle; B, parautochthonous specimens in the accumulation flanks; TorA). C–D, *Cochlearites loppianus* (C, core; D, flanks; Passo Vezzena), white arrows points to a cross-section of an articulated shell showing the free right valve (RV) with the internal median ridge and the thicker left valve (LV) characterized by a median wide furrow (e.g., Chinzei, 1982). E–F, *Lithioperna scutata* (E, base of the accumulation, TorD; F, flank, Campoluzzo Mt.); white arrow points to an articulated specimen with the characteristic shape resembling a couple of lenses (e.g., Broglio Loriga and Posenato, 1996).

The smaller lens-shaped A2 accumulation (Figs. 3.4, 3.5A), ca. 4 m wide and 30 cm high, is dominated by wide, short and articulated *Lithiotis* shells (ca. 10 cm high and ca. 8 cm wide; Fig. 3.4). Subordinate components are represented by brachiopods, larger foraminifera, oncoids and peloids. The *Lithiotis* shells are sparse and sub-vertical in orientation.

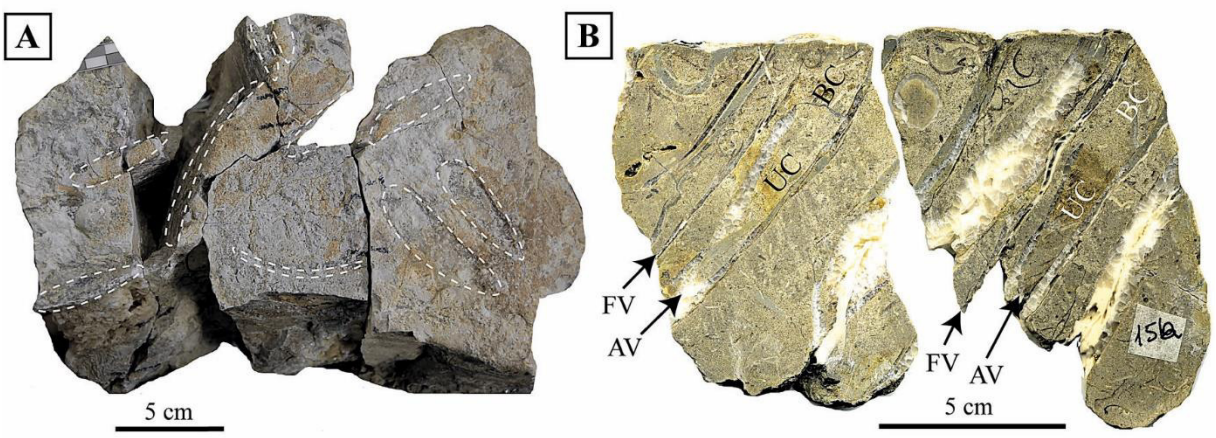

Figure 3.4. Two rock samples representing mostly articulated and autochthonous *Lithiotis problematica* specimens from the accumulation TorA2 (modified from Posenato et al., 2014). A) Upper bed surface with sub-transversal sections of the *Lithiotis* massive umbonal region. B) Polished surface of a perpendicular bedding section showing some articulated shells; two representative specimens are depicted with free (FV) and attached (AV) valves. BC, body cavity; UC, umbonal body cavity.

3.3.2. Toraro Mt. accumulation B (TorB)

This accumulation, 30 cm high in the core and ca. 10 m wide, consist of small *Cochlearites* shells (up to 10–15 cm in height) in a bioclastic wackestone sediment matrix (Fig. 3.5B). Locally few gastropods, rare solitary corals and rare thin-shelled bivalves are present (Posenato and Masetti, 2005; 2012, fig. 7o).

In the core, the *Cochlearites* shells show complete dissolution while those occurring in the accumulation flanks are recrystallised. The shells occur in sub-vertical position, with rare bouquet-like aggregates. In the core, due to poor preservation of the shells, articulated individuals were not recognized. The shell density ranges from 60 ind./400 cm^2 in the core to 100 ind./400 cm^2 toward the flanks (Fig. 3.5B). The flanks are characterized by a lower percentage of complete shells (24.2%) than in the accumulation core (44.4%).

3.3.3. Toraro Mt. accumulation C (TorC)

This tabular accumulation, lying on a storm deposit with thin-shelled bivalves and gastropods, is ca. 15 m wide and ca. 1.5 m thick. *Cochlearites*, up to 2 cm thick and 10–15 cm up to 30 cm in height, dominates. In the wackestone matrix, the shells are completely recrystallized. At the outcrop scale (about 5 m wide), this accumulation shows a tabular shape

(Fig. 3.5D). The accumulation flanks are not clearly detectable. The shell fabric varies within the accumulation and most of the individuals show an apparently chaotic arrangement with shell inclination ranging from few degrees to > 50°. Shell density and shell cover are highly variable (17–46 ind./400 cm^2 and 17–30%, respectively). Two bouquet-like aggregates were also identified. The morphoplasticity (i.e., ontogenetic shell adaptation to the substrate) of the shells is shown by autochthonous individuals, with the lowermost part of the shell sub-parallel and the uppermost part sub-vertical to bedding.

3.3.4. Toraro Mt. accumulation D (TorD)

This tabular accumulation occurs at the bottom of a lens-shaped *Cochlearites* accumulation, consists of decimetre-thick undulated packstone beds separated by erosional surfaces (Figs. 3.3E, 3.5C). Dominating *Lithioperna* occurs as small (up to 8 cm in size) fragmented and disarticulated shells. These are frequently iso-oriented and sub-parallel (10°) to the bedding. Low percentage of articulated (ca. 5%) and complete shells (2–17%) and high shell density (220–252 ind./400 cm^2) characterize this accumulation. Rare oncoids, brachiopods and gastropods are also present.

3.3.5. Toraro Mt. accumulation E (TorE)

This lens-shaped shell accumulation is dominated by recrystallized *Cochlearites* shells. In the central accumulation area these shells, up to 20 cm long, are apparently sub-horizontally arranged because they are transversally sectioned. Along the flanks the shells are longitudinally sectioned and show an inclination of > 30° (Fig. 3.6A). Locally, rare individuals of *Lithioperna* occur. Small brachiopods, rare solitary corals and gastropods are also present. The shell density increases toward the lateral areas (from 10 to 27 ind./400 cm^2). The same trend is followed by the percentage of shell cover (from ca. 10% to 36%; Fig. 3.6A).

3.3.6. Campoluzzo Mt. accumulation (Cm)

This accumulation is made up by *Lithioperna* morphotype A, with flattened, sub equivalve and slightly undulated shells (Figs. 3.3F, 3.6B). These are preserved as coarse calcitic prisms. Rare individuals of *Cochlearites* occur as very small, disarticulated and sub-horizontal shells. Rare brachiopods, gastropods and thin-shelled bivalves are also present.

Shell inclination varies from mainly sub-horizontal, to ca. 30° in the central part of the outcrop, up to 70° in its outermost part. The shell density ranges from ca. 39–66 ind./400 cm^2 in the central part to >100 ind./400 cm^2 in its periphery. The central area is characterized by

high percentage of articulated individuals (ca. 82%; even if recorded in some restricted areas) and the occurrence of some complete shells (8–25%). The abundant lithiotid fragments contribute, therefore, to the high shell density.

3.3.7. Vaio dell'Anguilla accumulation (Va)

The two lithiotid accumulations are located ca. 6 m and ca. 20 m above the base of the Formation (Posenato and Masetti, 2012, fig. 5). Both accumulations are dominated by *Lithioperna* morphotype A with densely packed vertically/sub-vertically arranged shells.

In the first accumulation, because the lower part is poorly preserved, the shell density and percentages of complete and articulated shells were tentatively calculated (Fig. 3.6C). In the middle to upper part of the accumulation, closely-packed, large shells are sub-horizontally arranged with a high percentage of articulated and complete individuals. The second accumulation is similar to the first with high shell densities (ca. > 30 ind./400 cm^2) and a high percentage of articulated and complete shells (ca. > 55% and > 30%, respectively; Fig. 3.6D). Rare shell fragments locally occur.

3.3.8. Rotzo accumulations (Ro)

In this succession, the lithiotid bearing outcrops are some tens of metres in width. The studied accumulations correspond to the Ro22, Ro27 and Ro34 units of Bosellini and Broglio Loriga (1971). These beds are characterized by *Lithiotis*, *Cochlearites* and individuals tentatively assigned to *Lithioperna* (Tab. 3.2).

The lower part of unit Ro22 contains *Lithiotis*, with a maximum shell size of ca. 20 cm long and up to 1 cm thick. Shell density (13 ind./400 cm^2) and shell cover (28.56%) are relatively low (Tab. 3.2). Shells are randomly arranged ranging from sub-horizontal individuals to inclined shells. Only larger individuals are articulated.

A tripartite subdivision is present in unit Ro27, 3 m in total thickness (Bosellini and Broglio Loriga, 1971). In the micritic lower subunit (1.5 m thick), *Cochlearites* dominates with subordinate *Lithioperna*. Rare gastropods are also present. The lithiotid shells are small in size (ca. 5–6 cm in height and only a few millimetres thick). Shell inclination ranges from 30°–40° in the lower part to sub-horizontal in the upper part. Shell density and shell size increase both laterally and vertically. The average shell density is high (112 ind./400 cm^2). The middle subunit (in total 1.45 m thick) consists of several lithiotid bearing layers intercalated with bioclastic micritic beds, about 20–40 cm thick with rare lithiotid shells. Each lithiotid layer is marked by undulated surfaces interpreted as synsedimentary erosional events. The uppermost

subunit (ca. 40 cm thick) contains highly concentrated, iso-oriented ?*Lithioperna* shells, with shell inclinations changing laterally from 25° up to horizontal. Taphonomic attributes are difficult to assess in the middle and upper subunits due to poor preservation.

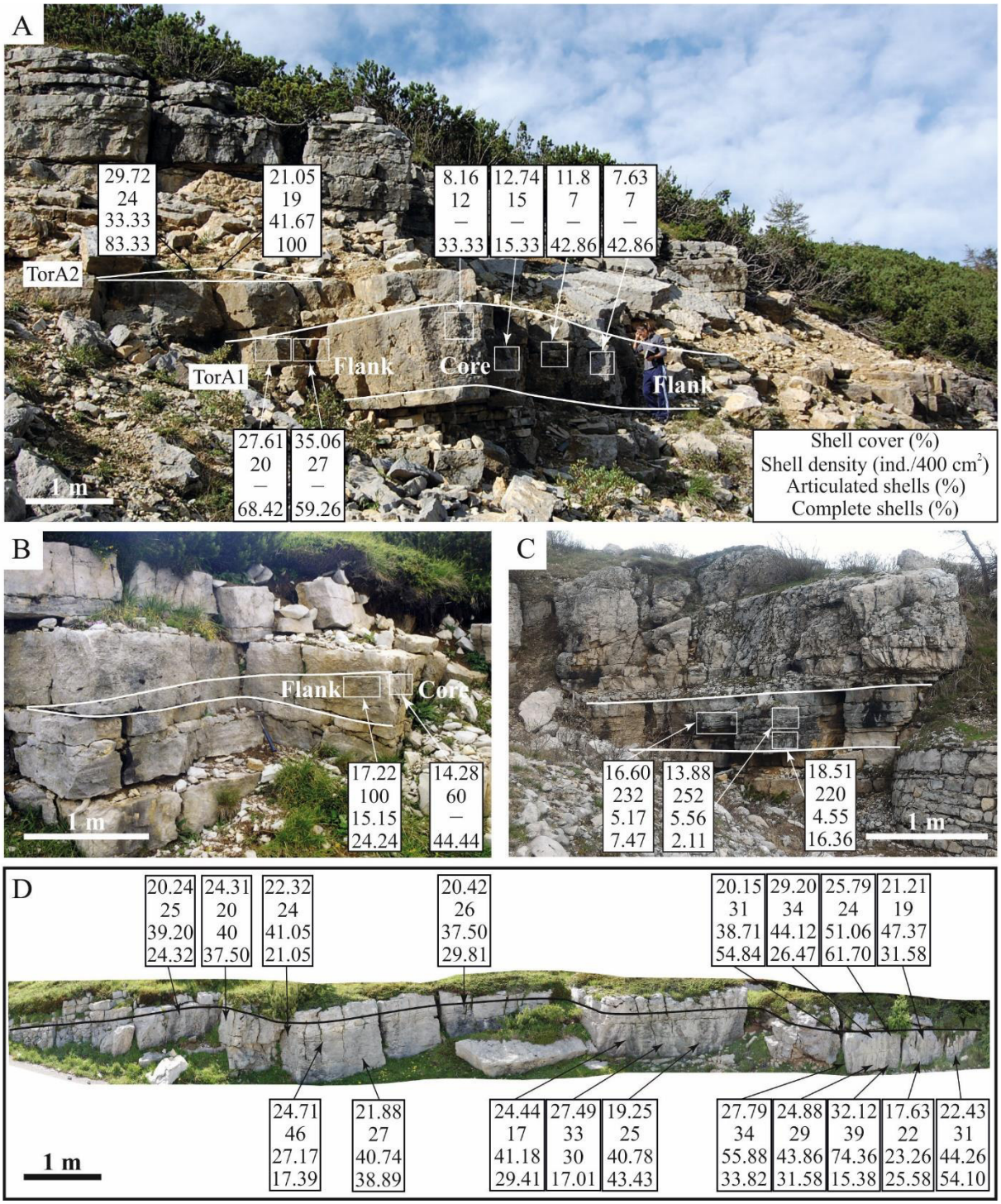

Figure 3.5. Distribution of distinguished features in the Toraro Mt. succession. The accumulations are marked by solid lines. A) TorA1–TorA2. B) TorB. C) TorD, characterized by *Lithioperna* shells, represents a tabular bioclastic, coarse-grained hard substrate for the overlying lithiotid accumulation. D) TorC.

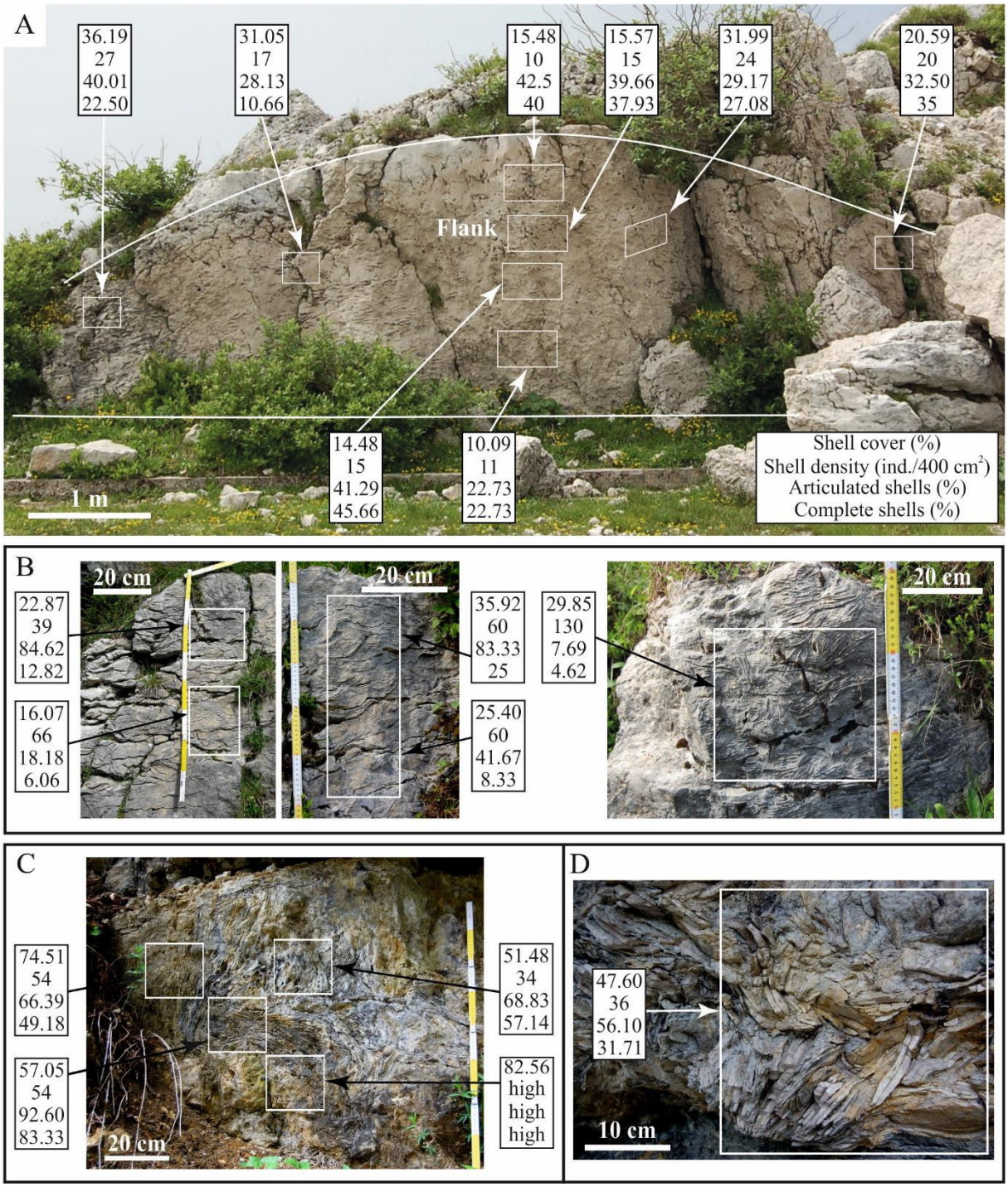

Figure 3.6. Distribution of distinguished features in the studied lithiotid accumulations in the Toraro Mt. (A, TorE), Campoluzzo Mt. (B) and Vaio dell'Anguilla (C–D) successions which are marked by solid lines. The studied TorE (A) represents a section of a *Cochlearites* accumulation passing only through the accumulation flank. The Campoluzzo Mt. (B) accumulation consists of parautochthonous *Lithioperna* individuals, while that of Vaio dell'Anguilla (C, D) consists of autochthonous *Lithioperna* individuals.

The Ro34 (ca. 10 m in thickness) was subdivided in four parts by Bosellini and Broglio Loriga (1971; Tab. 3.2). The unit consists of thick lithiotid accumulations with a micritic matrix (Bosellini and Broglio Loriga, 1971). The muddy intervals Ro34.1 and Ro34.2 (lower part) are dominated by *Cochlearites* with rare *Lithioperna*. The shell density is high (30–52 ind./400 cm^2; Ro34-section in Tab. 3.2) and the shells arrangement is chaotic. Sub-horizontal individuals

and rare bouquet-like aggregates are also present. Some bouquet-like aggregates were identified. Ro34-section and Ro34-surface show the same shell density (Tab. 3.2), while shell cover is biased by the poor shell surface preservation.

3.3.9. Contrada Dazio accumulation (Da)

In Contrada Dazio, lithiotid accumulation occurs in an extensive outcrop, ca. 30 m wide and high (Göhner, 1980). The analysed sedimentary body is wedge-shaped and only the lower 2 m, previously described (i.e., Interval A of Göhner, 1980), were studied in detail.

In this accumulation, the lithiotid shells are recrystallized and the core and flanks are not clearly distinguishable. *Lithiotis* dominates and is associated with subordinate *Cochlearites*. Both *Lithiotis* and *Cochlearites* are randomly arranged, with some individuals in an up-right position. Random shell sections and poor exposure conditions did not allow for the assessment of articulation. In the analysed quadrants, the percentage of complete shells does not show significant changes, while shell density increases toward the periphery (Da3–4; Tab. 3.2).

Shell beds	**Dominating taxa**	**Shell cover (%)**	**Shell density (ind./400 cm^2)**	**Articulated shells (%)**	**Complete shells (%)**
Ro22	*Lithiotis*	28.56	13	69.99	62.39
Ro27 (lower part)	*Cochlearites* (rare *Lithiop*)	52.95	112	16.24	21.44
Ro34.1	*Cochlearites* (rare *Lithiop*)	68.28	30	100	100
Ro34.2	*Cochlearites* (rare *Lithiop*)	61.41	52	83.33	36.67
Ro34-section	*Cochlearites* (rare *Lithiop*)	63.57	32	84.38	78.13
Ro34-surface	*Cochlearites* (rare *Lithiop*)	55.58	32	?	?10.56
Da1	*Lithiotis* (rare *Cochl*)	27.56	7	–	87.50
Da2	*Lithiotis* (rare *Cochl*)	22	11	–	87.50
Da3	*Lithiotis*	38.82	17	–	86.84
Da4	*Lithiotis*	31.95	17	–	86.84

Table 3.2. Dominating lithiotid genera and average values of shell bed characteristics and taphonomic attributes for the studied accumulations located in the Rotzo stratigraphic section (Ro) and Contrada Dazio (Da). The percentages of articulated and complete shells in the Ro34-surface are tentatively calculated (?) because the difficult in assessing articulated and/or complete individuals on bedding surface. In Da1–4 the articulated individuals cannot be identified at the outcrop scale. *Cochl*, *Cochlearites*; *Lithiop*, *Lithioperna*; −, no entry.

3.3.10. Passo Vezzena accumulations (Ve)

The studied lithiotid outcrop is located along the road connecting Asiago (Vicenza) to Lavarone (Trento; Fig. 3.1). The outcrop, about 20 m wide and 3 m high, is composed of four superimposed accumulations with packstone matrix dominated by *Cochlearites* (Ve1–4; Fig. 3.7A).

In Ve1 *Cochlearites* shells are chaotically to sub-vertically arranged (Figs. 3.3C, 3.7B). Rare gastropods are also present. The percentage of articulated and complete shells is relatively low (ca. 2.13% and 8.91%, respectively). Ve2 is characterized by vertical or slightly inclined *Cochlearites* shells. The estimation of the shell covered areas and the complete shells is highly influenced by the poor preservation of the outcrop (Fig. 3.7C). The shells are densely packed with complete, articulated individuals, up to 20 cm in height and up to ca. 1 cm in thickness. The *Cochlearites* dominated accumulations Ve3 and Ve4 show sub-horizontally and sub-vertically arranged large shells (up to 35 cm in height) with high percentage of complete, articulated individuals (> 40%). *Lithioperna* is subordinated. These last two accumulations are characterized by high densities of shells (ca. 48%; Figs. 3.3D, 3.7D–E).

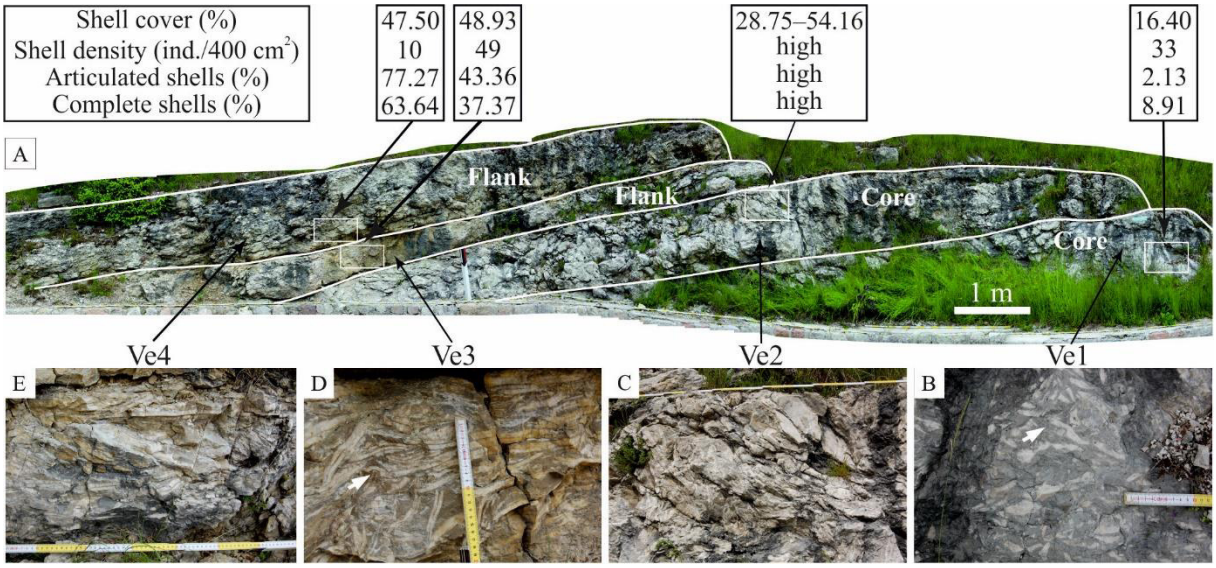

Figure 3.7. Distribution of distinguished taphonomic features in the studied lithiotid accumulations in the Passo Vezzena (A–E) outcrop. The accumulations are marked by solid lines. White arrows point to random sections of *Cochlearites* showing diagnostic characters (see e.g., Chinzei, 1982).

3.4. Discussion

Autochthonous *Cochlearites* and *Lithioperna* can occur both in the accumulation core and flanks while autochthonous *Lithiotis* only occurs in the accumulation cores (e.g., Figs. 3.3A, 3.5A; Tab. 3.3). Among the studied accumulations, TorA1–A2 represents the best example of an accumulation core where dominating autochthonous *Lithiotis* occurs in sub-vertical position

or in bouquet-like aggregates (Fig. 3.3A–B). The high percentage of complete *Lithiotis* shells (i.e., ca. 87%; Tab. 3.2) and their sub-vertical arrangement in the accumulation core of Contrada Dazio is also an indication for the autochthonous position of these bivalves.

Cochlearites typically occurs up-right within dense thickets and bouquets, whereby the commissure planes are oriented in various directions (Debeljak and Buser, 1998; Brame et al., 2019). Bouquet aggregates of *Cochlearites* were found in the cores of TorC, TorB and Ve1–2. These aggregates along with sub-vertical individuals are interpreted to be in life position (Chinzei, 1982; Seilacher, 1984). Similar as that described for rudists (Skelton et al., 1995), this arrangement suggests a relative sparse availability of suitable attachment substrates. The best examples of autochthonous *Cochlearites* shells are present in the Ve1–2 accumulations where they are complete, articulated and in a vertical or slightly inclined orientation (Fig. 3.3C–D). Sparse, small *Cochlearites* bouquets were also identified along the Ro34 accumulation flanks.

Autochthonous *Lithioperna* morphotype A showing the classic, highly-packed, vertically imbricated accumulations (e.g., Seilacher, 1984; Broglio Loriga and Posenato, 1996) were encountered in the core of the Vaio dell'Anguilla accumulation. The highly-packed aggregation together with the semi-infaunal life habits are highly conducive to burial and preservation and show corresponding high numbers of complete and articulated shells (Fig. 3.6C–D). This type of preservation is common in the Trento Platform (Posenato and Masetti, 2012) and in Apennine Carbonate Platform of southern Italy (Posenato et al., 2018).
In some cases, imbricated autochthonous shells acted as hard substrates for the larval settlement of *Cochlearites* (Posenato and Masetti, 2012, fig. 7c).

Inclined lithiotid shells found along the accumulation flanks are interpreted as parautochthonous shells which have been displaced from their life position. These shells are often correspondingly disarticulated and re-orientated, though they can remain complete (Tab. 3.3; Fig. 3.9). The displacement from the life position is likely due to a decrease of sedimentation rate and an increase in water energy before final burial (e.g., Chinzei, 1982; Seilacher, 1984; Posenato and Masetti, 2012). Sedimentation rates were high enough to hamper encrusting epifauna and bioeroding endofauna to develop. Very rare cases of bioinfestation are restricted to parautochthonous and allochthonous shells. The only detailed study on the occurrence of bioerosion in lithiotid fauna suggested seasonal or temporal mesotrophic conditions within an overall oligotrophic regime (Bassi et al., 2017).

In the Ve3–4 accumulations, parautochthonous *Cochlearites* and *Lithioperna* individuals are distinguished by high percentages of articulated shells along with large sizes and sub-horizontal positions (Fig. 3.7D–E). These occurrences are interpreted as the flanks of two accumulations whose cores are likely located lateral to the studied outcrop. The sub-

horizontally arranged *Cochlearites* of TorE are also interpreted as parautochthonous (Fig. 3.3E). In fact, if the accumulation core is surrounded by radially arranged parautochthonous shells, their transversal sections appear as sub-horizontal. The increase in parautochthonous specimens may, therefore, suggests a change in the above-mentioned environmental parameters, which influenced the shell stability on the muddy substrate.

Abundant parautochthonous forms are present in the accumulation flanks of the Campoluzzo Mt. accumulation (Fig. 3.6B). The shell density (> 39 ind./400 cm^2) and the flat and ventrally elongated shell morphology are characteristics of the *Lithioperna* morphotype A (Fig. 3.3F). This morphotype, which lived vertically in life position, was adapted to high sedimentation rates and contributed to very dense aggregates showing the typical vertically imbricated (book-like in Seilacher, 1984) or bouquet-like (e.g., Fraser et al., 2004) packing arrangement. Although shell inclination varies in the studied outcrops, the high percentage of articulated individuals lying sub-horizontally and the occurrence of fragmented and disarticulated shells (Tab. 3.3; Fig. 3.9) suggest that accumulation flanks could be subjected to a higher water turbulence and lower sedimentation rate than the autochthonous *Lithioperna* accumulations from the Vaio dell'Anguilla locality (Fig. 3.6C–D). A weaker substrate anchorage (byssate at the juvenile stage) with respect to the other lithiotids which are cemented as juveniles together with a reduced sedimentation rate could have allowed *Lithioperna* to grow sub-horizontally (e.g., Broglio Loriga and Posenato, 1996, fig. 4F) thus reducing the possibilities of preserving shells in an up-right position.

3.4.1. Taphonomic attributes of the lithiotid accumulations

The analysis of the studied lithiotid accumulations allowed taphonomic attributes of bivalves within the cores and flanks to be assessed. The lithiotid accumulations would have been exposed to processes of erosion, reworking and winnowing before final burial (e.g., Nauss and Smith, 1988; Posenato and Masetti, 2012). These parautochthonous/allochthonous accumulations show a high degree of spatial and temporal mixing, and thus represent within-habitat, time-averaged assemblages (Kidwell et al., 1986). Despite the fact that the taxonomic ascription of randomly sectioned specimens can be problematic, some general trends in preservation of these bivalves can be recognized. Furthermore, the Toraro Mt., Campoluzzo Mt., Passo Vezzena and Vaio dell'Anguilla accumulations show nearly entire accumulation shapes (with both core and flanks) and can thus be used as comparative models for the other outcrops such as Rotzo and Contrada Dazio which are not as well exposed. Distinctive

sedimentary fabrics as well as taphonomic features of the studied *Lithiotis*, *Cochlearites* and *Lithioperna* within the accumulation core and flanks (Tab. 3.3; Fig. 3.9) can thus be compared.

The lithiotid accumulations with a tabular shape (Fig. 3.5C–D) yield both reworked allochthonous shells (e.g., *Lithioperna*, TorD; Fig. 3.3E) as well as parautochthonous/autochthonous shells (e.g., *Cochlearites*, TorC). Allochthonous shell accumulations are characterized by low shell cover (< ca. 18%), high shell density (> 200 ind./cm^2) and very low percentages of articulated (< 6%) and complete bivalves (< 17%) suggesting physical reworking. This is the case for *Lithioperna* accumulation which represented a hard substrate for the settlement of cemented or byssally attached bivalves. The tabular *Cochlearites* accumulation (Fig. 3.5D) is comparable to those from the Apennine Carbonate Platform (Posenato et al., 2018).

Although adult specimens can also occur in the flanks, most lithiotid individuals in the core represent the largest-sized adults. In the *Lithiotis* accumulations, the core is mud-supported, with loosely packed shells of dominating autochthonous individuals (complete shells > 15%) associated with subordinate parautochthonous ones (e.g., Da, TorA1; Fig. 3.3A). The muddy flanks show higher shell cover and density, with well-preserved dominating sub-horizontal individuals (e.g., Ro22, TorA1; Fig. 3.3B). In the studied accumulation flanks, disarticulated *Lithiotis* shows a sub-horizontal to inclined orientation (Tab. 3.3). These are interpreted as parautochthonous because their interpreted life position was vertical to sub-vertical (e.g., Chinzei, 1982; Seilacher, 1984; Nauss and Smith, 1988).

The *Cochlearites* accumulation core and flanks show a high variability of shell fabrics and taphonomic attributes (e.g., Ve1–4; Tab. 3.3; Fig. 3.9). Only in the Passo Vezzena outcrop (Ve1–2; Figs. 3.3C, 3.7B–C), the core of the *Cochlearites* accumulation is well preserved, with individuals in life position (vertical/sub-vertical) with high shell densities. The flanks are characterized by inclined or sub-horizontal shells whose taphonomic attributes vary according to the distance from the core area (Ve3–4; Figs. 3.3D, 3.7D–E). As already noted in other localities (Posenato and Masetti, 2012), the flanks constitute the most conspicuous part of the accumulation. The peripheral area shows higher shell cover (> 20%; TorE) and shell density (ca. > 17 ind./400 cm^2; TorE; Fig. 3.6A) than the core area. In the *Cochlearites* tabular bodies (e.g., TorC; Fig. 3.5D), the shell arrangement and taphonomic attributes vary without a specific trend. In these bodies, sparse bouquet-like aggregates are present. With regard to the Rotzo accumulations, the Ro27 (dominated by *Cochlearites*) and the Ro34 (dominated by *Cochlearites*) are interpreted as the accumulation flanks because of their taphonomic attributes (Tab. 3.2). The studied *Cochlearites* are comparable to the records from southern Italy,

Slovenia, Morocco and western USA (Debeljak and Buser, 1998; Fraser et al., 2004; Posenato et al., 2018; Brame et al., 2019).

The single studied example of *Lithioperna* morphotype A accumulation core in the Vaio dell'Anguilla accumulation, is characterized by highly dense packed shells with sub-vertical/vertical arrangement. The accumulation core shows a high shell cover (ca. > 47%), a high percentage of articulated (ca. > 55%) and complete shells (ca. > 30%; Tab. 3.3; Fig. 3.9). In the Campoluzzo Mt., the *Lithioperna* accumulation flanks show high shell cover (> 15%) and density (h > 15 ind./400 cm^2), along with abundant parautochthonous individuals (Fig. 3.4F; Tab. 3.3). In both core and flanks, articulated shells occur in variable amounts (up to ca. 90%; Tab. 3.3; Fig. 3.9). *Lithioperna* accumulations described in the literature show generally a tabular shape (Posenato and Masetti, 2012; Posenato et al., 2018), which can be related to the *Lithioperna* life habit (e.g., weak bottom anchorage and shell instability), and environmental conditions (high hydrodynamic setting and low sedimentary rate; Debeljak and Buser, 1998; Posenato and Masetti, 2012).

Core	**Shell cover (%)**	**Shell density (ind./400 cm^2)**	**Articulated shells (%)**	**Complete shells (%)**	**Autochthonous individuals**	**Parautochthonous individuals**
Lithiotis	low	high–low	high	high	high	low
Cochlearites	high-low	high	high–low	high–low	high	low
Lithioperna A	high	high	high	high	high	low
Flanks						
Lithiotis	high	high	–	high	–	high
Cochlearites	high-low	high-low	high–low	high–low	low	high
Lithioperna A	low	high	high–low	low	low	high

Table 3.3. Distinctive taphonomic attributes for the core and flanks in the lithiotid accumulations. Autochthonous individuals were preserved in life position, while parautochthonous were reworked to some degree but not transported out of the original life habit (articulated or disarticulated but not in life position).
The obtained mean values differ among the dominating genera as follow (h, high): *Lithiotis*: shell cover, h > 25%; shell density, h > 17 ind./400 cm^2; articulated individuals, h > 35%; complete shells, h > 15%; *Cochlearites*: shell cover, h > 15%; shell density, h > 17 ind./400 cm^2; articulated individuals, h >35%; complete shells, h > 35%; *Lithioperna* A (morphotype *sensu* Broglio Loriga and Posenato 1996): shell cover, h > 40%; shell density, h > 17 ind./400 cm^2; articulated individuals, h > 35%; complete shells, h > 25%. h, high; l, low; –, no entry.

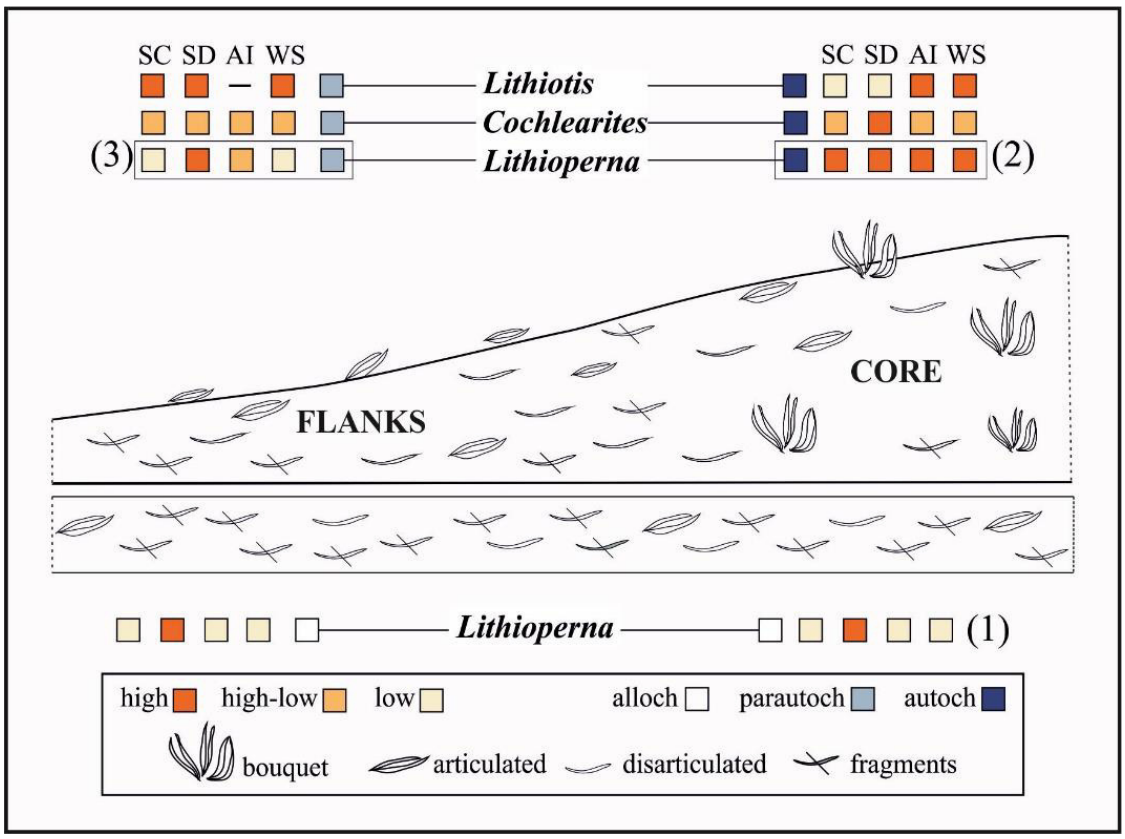

Figure 3.9. Schematic model of the studied lithiotid accumulations showing the dominant distribution of the assessed fabric and taphonomic attributes of autochthonous (autoch), parautochthonous (parautoch) and allochthonous (alloch) individuals. The tabular bioclastic hard-substrate (TorD), produced by physical reworking, is the representative study case made up of allochthonous *Lithioperna* shells (1; Fig. 3.6C). Autochthonous *Lithiotis* was found articulated in the level TorA2 overlying the TorA1, whereas parautochthonous *Lithiotis* characterize the accumulation flank (Fig. 3.6A). Autochthonous *Lithioperna* was recorded in the Vaio dell'Anguilla (2; Fig. 3.7C–D), while parautochthonous individuals of the Campoluzzo Mt. occur in the accumulation flank (3; Fig. 3.7B). Not to scale. Lithiotid shells are simply depicted and do not reflect the complex shell morphology. SC, shell cover; SD, shell density; AI, articulated individuals; CS, complete shells.

3.5. Conclusions

In the Pliensbachian shallow-water carbonate successions of the Southern Alps, northern Italy, different types of lithiotid constratal accumulations are present. Although the accumulations are often characterized by wide lateral extension, only a limited number of outcrops allow for the recognition of architectural features such as the core and flanks. A quantitative taphonomic analysis was performed in order to characterize these lithiotid accumulations and to explore the possibility of using sedimentary fabrics and taphonomic features to distinguish accumulation core and flanks.

Based on systematic composition, the accumulations can be dominated by a single lithiotid species or be composed of the three species (i.e., *Lithiotis problematica*, *Cochlearites loppianus*, *Lithioperna scutata*). When *Lithiotis* is the dominant taxon, it is rarely associated with subordinate *Cochlearites*. Dominant *Cochlearites* is associated with subordinate

Lithioperna. When *Lithioperna* dominates, it occurs only with flat and thin shells and is rarely associated with subordinate *Cochlearites*.

In the studied outcrops, autochthonous individuals in a vertical position or in a bouquet-like aggregates are recognizable in the accumulation core, while the flanks are characterized by high percentage of flat lying, toppled parautochthonous shells.

Shell bed characteristics and taphonomic attributes in the core and flanks vary according to the dominating lithiotid bivalves: 1) in the core, the shell cover is highest for *Lithioperna*, variable for *Cochlearites* and low for *Lithiotis*, while in the flanks these attributes show an opposite trend; 2) shell densities are high in the core for *Cochlearites* and *Lithioperna* and low for *Lithiotis*, while in the flanks it is high for all the taxa with more variability in *Cochlearites*; 3) articulated and complete shells vary conspicuously in both the core and the flanks; 4) *Cochlearites* shows the highest variability of taphonomic features; 5) a relative high percentage of articulated individuals (> 35%) of *Lithioperna* in the accumulation flanks suggests that autochthonous individuals also thrived in these areas.

Chapter 4

Paleoredox conditions and microbial role at the sediment/water interface in the lithiotid accumulations

4.1. Introduction

The Lower Jurassic lithiotid bivalves are well-known benthic components in tropical lagoon settings where they occur as larger shell accumulations (e.g., Posenato and Masetti, 2012). The lithiotid accumulation shape and size (up to 10 m high and several hundred meters wide), the prevailing muddy matrix along with the presence of sparse bacteria-like features in the lithiotid-bearing sedimentary successions (e.g., Scheibner and Reijmer, 1999; Fraser, 2002; Coletta, 2012; Gale, 2015; Franceschi et al., 2019) suggest a likely role of microbial activity and redox changes at the sediment/water interface in the bivalve-accumulation growth dynamics. Some indications regarding the possible bacterial activity in Morocco lithiotid accumulations refer to clotted texture interpreted as a microbial fabric (Brame et al., 2019). Previous studies suggest that the oxygenation level could vary during the lithiotid accumulation growth (e.g., Posenato and Masetti, 2012; Bassi et al., 2015). Pyrite framboids, a useful indicator of paleoredox conditions (e.g., Wignall and Newton, 1998; Wignall et al., 2010), have been already identified and associated to the demise of bivalve carpets in the Rotzo Formation (Bassi et al., 2015).

Calcified fossil bacteria, widespread from open sea, lagoon, and reef environments, play an important sedimentological role in building reefs and producing fine grained and fragmented sediments (Liu et al., 2017, and references therein). These calcified bacteria make biofilms which trap, bind and stabilize the sediments at the sediment/water interface (e.g., Riding and Toomey, 1972; Riding, 2000). In the modern coastal areas, the onset of oxygen-depleted water masses generally depends on the development of shallow stratified waters, high nutrient availability, and/or elevated seawater temperature (e.g., Breitburg et al., 2018). Several modern examples show a significant cyclic fluctuation in oxygen availability, oscillating from tidal to seasonal cycles, and longer-term periods (e.g., El Niño) whilst only long-term changes have been generally recognized in ancient environments (e.g., Oschmann, 1993). The evidences of concurrent occurrences of calcified bacteria, sulphur in depleted oxygen-setting and organic matter may be recorded in the lithiotid accumulations.

This study aims to 1) verify the occurrence of bacteria-like features to evaluate the microbial role in the accumulations; 2) evaluate the occurrence of pyrite shapes to assess the redox condition during the accumulation growth stages. Carried out on several lithiotid accumulations from five localities in the Trento Platform (Southern Alps), the study analyses in detail well-exposed lithiotid accumulations in terms of main skeletal and non-skeletal components, bacteria-like features, occurrence of pyrite and framboids.

4.2. Pyrite and framboids: historical background

Pyrite framboids are the most common iron-sulfide mineral in sedimentary rocks. The mechanism leading the formation of pyrite framboids included four steps: initial nucleation and growth of iron monosulfide; 2) reaction of monosulfide with greigite (Fe_3S_4) through disorder mackinawite and ordered mackinawite ($Fe_{1+x}S$); 3) aggregation of greigite microcrystals; 4) replacement of greigite with pyrite (Wilkin and Barnes, 1997). The formation of greigite constitutes a key phase in the framboids formation (Wilkin and Barnes, 1997). Greigite formation occurs only in weakly reducing conditions, which require hydrogen sulphide, ferrous iron and an oxidant such as oxygen, or elemental sulphur or dissolved polysulfide (e.g., Wilkin et al., 1996). The occurrence of sulphate-reducing bacteria producing hydrogen sulphide is essential even if they apparently do not influence the pyrite morphology (Wilkin and Barnes, 1997). The occurrence of this key components is confined immediately below to redox interface which separates oxygen-bearing from hydrogen sulphide-bearing waters (Wilkin et al., 1996). This interface is located just below or within the sediment-water interface. Only in few cases, for instance in restricted coastal basins, this interface occurs in the water columns (e.g., Black Sea; Wilkin et al., 1996). Raiswell and Berner (1985) divided framboids into two groups: syngenetic (those formed within the water column) and diagenetic (those formed within the sediments). Syngenetic pyrite is formed in ~3 days confirming the development of populations of small framboids in euxinic environments, where pyrite formation is influenced by advection and the Stoke's law (Rickard, 2019). Most sedimentary pyrite framboids are formed during the earliest stages of diagenesis and take about few days (~5 days) to form (Rickard, 2019). Rare larger pyrite framboids (up to 80 µm) can require few years.

Diagenesis can influence pyrite framboids with infilling or overgrowth. Nevertheless, the microcrystals are not affected by aggradation process. Observations on ancient black shale suggested that, once deposited, framboid size distribution is preserved over geological time

(Wilkin et al., 1996). Then, pyrite framboids with altered surface can be measured and included in the size distribution analysis.

Several iron oxides with spherical aggregates were identified in Holocene succession located in the Iberian Range (NE Spain; Mayayo et al., 2019). Based on crystals morphologies these spherical aggregates are the result of Fe-oxides replacement after pyrite framboids. Sulphur was not detected by EDS analyses therefore Mayayo et al. (2019) proposed that the pyrite oxidation occurs during the exposition of the floodplain with the implication of bacterial organisms (neutrophilic iron oxidizing bacteria and cyanobacteria) based on the association of Fe-oxides framboids with microbial features.

4.3. Materials and methods

Fourteen lithiotid accumulations outcropping in the Vicenza and Trento provinces (northern Italy; Fig. 4.1) were sampled: seven from the Toraro Mountain and one in the Campoluzzo Mountain (Altopiano di Tonezza, Vicenza), one accumulation in the Altopiano di Asiago (Rotzo section; Vicenza), one isolated outcrop near Passo Vezzena (Trento) with four lithiotid accumulations, and one accumulation near Contrada Dazio (Folgaria, Trento).

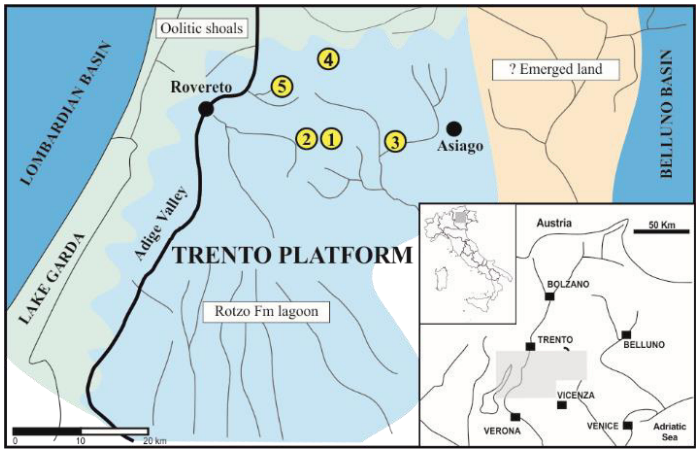

Figure 4.1. Geographical location of the studied lithiotid accumulations in the Trento Platform, northern Italy. 1, Toraro Mountain (Vicenza); 2, Campoluzzo Mountain (Vicenza); 3, Rotzo section (Vicenza); 4, Passo Vezzena (Trento) outcrop; 5, Contrada Dazio (Folgaria, Trento) outcrop. Palaeogeographic map from Posenato and Masetti (2012, modified).

The studied accumulations, selected for their distinctive accumulation architecture (i.e., lens-shaped with flanks/core or tabular geometry) and for their stratigraphic representativeness for the taxa distribution, occur in the middle and upper Rotzo Formation, ranging from the *Orbitopsella* biozone to the *Lituosepta compressa* biozone (Fugagnoli, 2004; Tab. 4.1). Lithiotid accumulations usually includes up to two genera (exceptionally three only

in the Contrada Dazio outcrop) one of which dominating (Chapter 3; Brandolese et al., 2019). Each accumulation was sampled according to the accumulation morphology in order to characterize the flanks-core, and the deposit which overlying the accumulation (here referred to as cover). Sometimes, lithiotid accumulations occur as tabular body, such as in the Toraro Mountain (e.g., TorC). In this case, due to the occurrence of bouquet-like aggregates (see Chapter 3 and Brandolese et al., 2019 for further details), the accumulation is considered as accumulation core.

A total of 142 thin sections (cut perpendicular to the bedding plane; Tab. 4.1) were analysed with optical microscope Leitz Diaplan using ×2.5 and ×4 magnifications. The standard size for the thin sections was 4×4 cm. Digital microphotographs were taken with a Canon EOS60D camera mounted on Leitz Diaplan binocular microscope. All thin sections are deposited at the Department of Physics and Earth Sciences, University of Ferrara, Italy.

					No. of analysed samples	
Stratigraphic section	**Studied accumulation**	**DLt**	**Distance from the base**	**Biozone**	**A**	**B**
Toraro Mt. (45°52'08.9"N, 11°16'20.2"E)	TorA1	*Lithiotis*	~120 m	*Orbitopsella* Z.	6	13
	TorA2	*Lithiotis*	~120 m		6	1
	TorB	*Cochlearites*	160 m	*Lituosepta compressa* Z.	5	5
	TorC	*Cochlearites* and rare *Lithioperna*	172 m	*L. compressa* Z.	6	21
	TorD2	Dominated by *Cochlearites*	177 m	*L. compressa* Z.	/	6
	TorE	Dominated by *Cochlearites* with rare *Lithioperna*	180 m	*L. compressa* Z.	11	17
	TorF	Dominated by *Cochlearites* with rare *Lithioperna*	180 m	*L. compressa* Z.	/	13
Campoluzzo Mount (45°52'17.9"N, 11°15'34.4"E)	Cm	*Lithioperna*	~1-2 m	*L. compressa* Z.	/	5
Rotzo (45°51'26.6"N, 11°22'25.5"E)	Ro	*Cochlearites*	~90 m	*L. compressa* Z.	/	10
Passo Vezzena (45°57'05.1"N, 11°21'36.3"E)	Ve1	Dominated by *Cochlearites* with rare *Lithioperna*	Isolated outcrop	*L. compressa* Z.	/	3
	Ve2				/	4
	Ve3				/	4
	Ve4				/	5
Contrada Dazio (45°55'40.1"N, 11°15'31.8"E)	Da	*Lithiotis* with rare *Cochlearites* and *Lithioperna*	Isolated outcrop	? *L. compressa* Z.	/	35

Table 4.1. Number of analysed samples for (A) pyrite and (B) skeletal and non-skeletal components in the studied lithiotid accumulations. The stratigraphic position (distance of the studied accumulations from the base of the referred stratigraphic section) refers to Coletta (2012; Toraro Mt., Campoluzzo Mt.) and Bosellini and Broglio Loriga (1971; Rotzo). DLt, dominant lithiotid taxon; Z., Zone; /, no entry.

Main skeletal and non-skeletal components (cortoids, peloids, oncoids) were distinguished. In the lithiotid accumulations the matrix textures follow Dunham's (1962) and Embry and Klovan's (1972) classifications. The term bioclast was used without genetic implications when the low preservation state hampered the certain identification. Cortoids and peloids follow the Flügel's (2010) definition. Cortoids are carbonate grains which exhibits a "*circumgranular non-laminated micritic rim commonly called micritic envelope*" (Flügel, 2010) and they were classified into two categories. Constructive cortoids resulted from the precipitation of microcrystalline calcite around and between filaments of endo- and epilithic algae and cyanobacteria; destructive cortoids give rise from the coexisting cyanobacterial microboring and filling boreholes (Flügel, 2010, and references therein).

Peloids are tentatively distinguished in microbial peloids, pelletoids (i.e., completely micritized grains) and fecal pellets (Flügel, 2010). For bad preserved non-skeletal components, the term peloid was used with no genetic implications.

Oncoids were subdivided in two types (Védrine et al., 2007). Type 1/2 oncoids have a micritic cortex with more or less regular concentric and continuous but barely visible micritic lamination. Type 3/4 oncoids are characterized by irregular cortex with more or less visible nucleus and lobate surface. The cortex varies showing few or no lamination with microencrusters-bearing organisms or microbial meshwork.

Recognized bacteria-like features are usually badly preserved so the term *genus*-like was adopted for their distinction.

Abundance of the components was assessed to as absent, rare, common and abundant. The different types of micrite were also considered in the analysis (i.e., very fine grained micrite, micrite, clotted peloidal micrite and microsparite). Eight representative thin sections were analysed by scanning electron microscope (SEM) with energy dispersive spectroscopy (EDS; University of Ferrara and University of Granada, Spain). Initially the observations were conducted in variable pressure mode (uncoated) and subsequently after coating with graphite.

The accumulations were sampled in their main architectural parts (core and flanks), and in the cover. For each part, skeletal and non-skeletal components were distinguished (bioclasts, small benthic foraminifera, larger benthic foraminifera, gastropods, brachiopods, *Palaeodasycladus* sp. (Pia, 1920) Pia, 1927, echinoderms, *Thaumatoporella parvovesiculifera* (Raineri, 1922), peloids, cortoids, fecal pellets, oncoids, bacteria-like features). Fecal pellets were considered as a distinct group because of their possible importance in the paleo-oxygenation analysis. The abundance (absent, rare, common, abundant) of the above-mentioned components was expressed as a percentage in the analysed thin sections (see

Appendix A.3 for further details). These data were plotted in schematic model according to the dominated lithiotid genus (i.e., *Lithiotis*, *Cochlearites*, *Lithioperna*). *Lithioperna* dominated accumulations are less frequent (Chapter 3; Brandolese et al., 2019) and only accumulation flanks were studied in detail (Campoluzzo Mt. outcrop). The accumulation core, outcropping in the Lessini Mts., shows high shell density and shell cover whilst the matrix is reduced (see Chapter 3 and Brandolese et al., 2019 for further details).

As in the TorA2 the original accumulation core matrix is preserved only in the lower restricted areas one thin section was analysed (Tab. 4.1). For further details on this accumulation see the Appendix A.4.

The analysis of redox condition focused on five accumulations outcropping in the Toraro Mt. (TorA1, TorA2, TorB, TorC, TorE). These accumulations are representative of the different lithiotid accumulation architecture (Chapter 3; Brandolese et al., 2019). No sample was analysed from *Lithioperna*-dominated accumulation (Cm) due to the higher water turbulence of the depositional setting (see Chapter 3 and Brandolese et al., 2019 for further details). The samples (about 2×2 cm) were polished, coated with graphite and observed with SEM in backscatter mode (using a FEI Quanta 400, located at the Centro de Instrumentación Scientifica, University of Granada, Spain). The photos of pyrite crystals and framboids were elaborated in order to measure and evaluate the pyrite morphology and the size distribution (S, total amount of framboids; md, mean diameter; MFD, maximum diameter; SD, standard deviation).

Altered pyrite showing framboidal-like shape was considered and measured as well as defined framboids. The results were plotted using “box-whiskers” diagrams, a useful tool to describe the size distribution of pyrite framboids in sedimentary deposits (e.g., Wilkin et al., 1997; Liao et al., 2017).

Even though the studied samples constitute limited, randomly selected surface area, the results can represent an approximation of the true framboid size distribution (e.g., Yang et al., 2016). The size-frequency distribution provides a practical criterion for identifying ancient euxinic/anoxic environments because it contrasts with the framboid populations in more oxygenated settings (e.g., Wilkin et al., 1996; Wilkin and Arthur, 2001). Both mean and maximum diameter size are good indicators of paleoenvironmental (Wignall and Newton, 1998). Irregular aggregates of discrete microcrystalline grains and undefined shapes of pyrite were also considered but not counted in the size distribution results.

Moreover, some alternative methods were tested in order to analyse the pyrite distribution in carbonate rocks. Their description is reported in the Appendix A.2.

4.4. Results

The results of the thin sections analysis are summarized in the Appendix A.3.

Chapter 3 deals with the taphonomic analysis of most of the studied lithiotid accumulations (see also Brandolese et al., 2019). In this study two accumulations were further added: TorD2 and TorF (Tab. 4.1). The TorD2 is *Cochlearites*-dominated accumulation overlying decametric-thick undulating beds with allochthonous *Lithioperna* shells (TorD; see Chapter 3 and Brandolese et al., 2019 for further details). The outcrop was sampled in order to evaluate the vertical evolution of the accumulation flank. The TorF lens-shaped accumulation, dominated by *Cochlearites* with subordinate *Lithioperna*, represents the accumulation flanks, as in TorE.

4.4.1. Non-skeletal components, bacteria-like features and microbial fabric

Constructive cortoids are rare to common and occur only in few samples (TorB, TorC, TorF, Campoluzzo Mt., Passo Vezzena accumulations; Plate 1). Cortoids with destructive envelope were observed in several samples (Plate 1; Appendixes A.5–A.15) but they are absent in TorA2, TorE and in Ro accumulations.

Peloids, fecal pellets and microbial peloids were easily distinguished whilst rare possible pelletoids were identified in several of the studied accumulations (Plate 2). The pelletoids always occur locally and are completely absent in TorA2, TorE, TorF and Ro accumulations. Longitudinal and transversal sections of isolated or aggregated fecal pellets, found in several samples (Appendix A.3), can be assigned to the ichnogenus *Favreina* Brönnimann, 1955 but their faint preservation state hampered the ichnospecies identification. Microbial peloids were found in several samples (TorB, TorC, TorE, TorF and Da accumulations), occurring in clusters and confined in interparticle shell porosity, like gastropods, bivalves or brachiopods (Plate 2). They are smaller (< 50 μm) than the fecal pellets and micritized grains and show faint outlines (e.g., Samankassou et al., 2005).

Oncoids were identified only in TorC (samples C-IO and C-OC). They are classified as type 3/4 oncoids (Plate 3). The size varies from few mm up to 10 cm. Calcimicrobial oncoid coatings were already reported in the Calcari Grigi Group (Cherchi and Schroeder, 2005).

Rare and well-preserved bacteria-like features constituted by sub-parallel, elongate, sinuous to irregular tangled tubular filaments of uniform diameter were recognised in TorF (Appendix A.11). Rare and not well-preserved features occur also in TorA1, TorD2, TorF and Contrada Dazio outcrop (Figs. 4.2–4.3; Plate 4). They can be ascribed to the genus *Girvanella* Nicholson and Etheridge, 1878. However, some of these features look like the Palaeozoic

genus *Subtifloria* Maslov, 1956, considered a sheath-calcified filament cyanobacterium like *Girvanella* (Feng et al., 2010, fig. 9). The bad preservation of these specimens hampered a certain systematic identification therefore they are indicated as *Girvanella*-like filaments. At least two types of *Girvanella*-like filaments are differentiated in the lithiotid accumulations: single tubules and rods. Single tubules are distinguished by micritic wall and spar-filled centre (Figs. 4.2–4.3; Plate 4). They are straight to slight curved and up to 700 µm in length and ~30–40 µm in diameter. They occur frequently isolated. Rods of uniform micrite are more difficult to distinguished (Figs. 4.2–4.3; Plate 4). They show the same length and shape of the tubules. The observed *Girvanella*-like filaments are very similar to those described from the upper Neogene of Sardinia (Italy; Saint Martin, 2010, fig. 3).

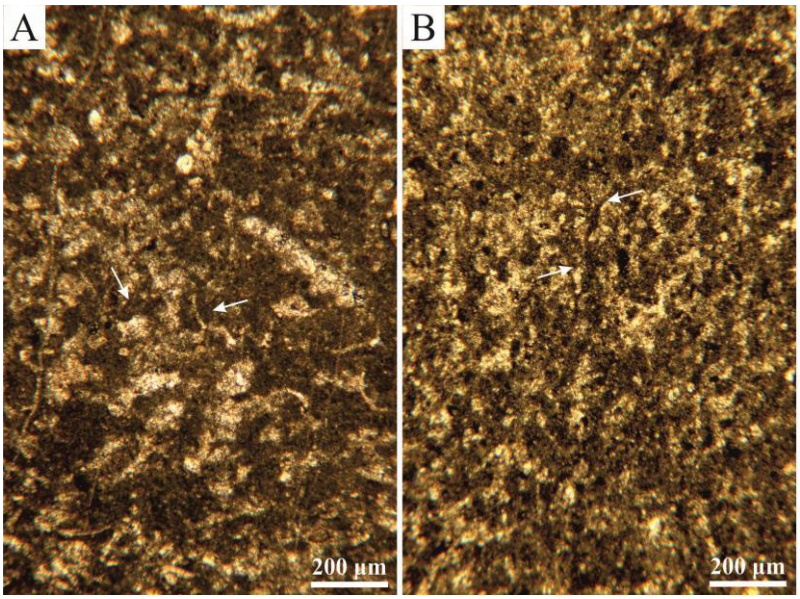

Figure 4.2. Photomicrographs of possible isolated *Girvanella* filament moulds preserved as micritic wall with spar-filled centre (A) and as micritic infilling (B). White arrows point to well preserved filaments. A) A1-10 (Toraro Mt.). B) A1-4 (TorA1, Toraro Mt.).

Rare *Rivularia*-like cyanobacteria (compare with *Cayeuxia* sp. Frollo, 1938 type) were observed in few samples of Contrada Dazio outcrop, TorA1, TorF and Ve3 accumulations (Plate 5). In the lithiotid-bearing successions, several authors reported the occurrence of *Rivularia*-like features usually assigned to the genus *Cayeuxia* (e.g., Fraser, 2002; Coletta, 2012; Gale, 2015; Franceschi et al., 2019). In the Toraro Mt., Coletta (2012) recognised *Cayeuxia*-like features in at least three samples (TO8 and TO19 in the *Orbitopsella* Zone and TO58 in the *Lituosepta compressa* Z.; Fig. 4.4). *Rivularia*-like cyanobacteria were also identified in the Lessini Mts. (Verona), in the Vaio dell'Anguilla (samples V14, V24 and V29 in *Orbitopsella* Z.; Borasio, 1999; Fig. 4.4) and in the Crespadoro/Campodalbero succession (sample U72, biozone not available; Borasio, 1999; Fig. 4.4). *Cayeuxia* Frollo, 1938 is a colonial organism constituted of loosely packed, radial tubiform filaments, asymmetrically bifurcated at irregular intervals. The branching angle is near 45° and the filaments are circular

in cross section with a diameter of ca. 30–40 µm (Liu et al., 2017). It predominantly occurs in lagoonal setting.

Bacteria-like features included also the dark clotted micritic features commonly found in several studied lithiotid accumulations. They show a typical dark colour in transmitted light, well-recognizable from the surrounding matrix, with maximum size < ~1 mm (Fig. 4.5; Plate 6).

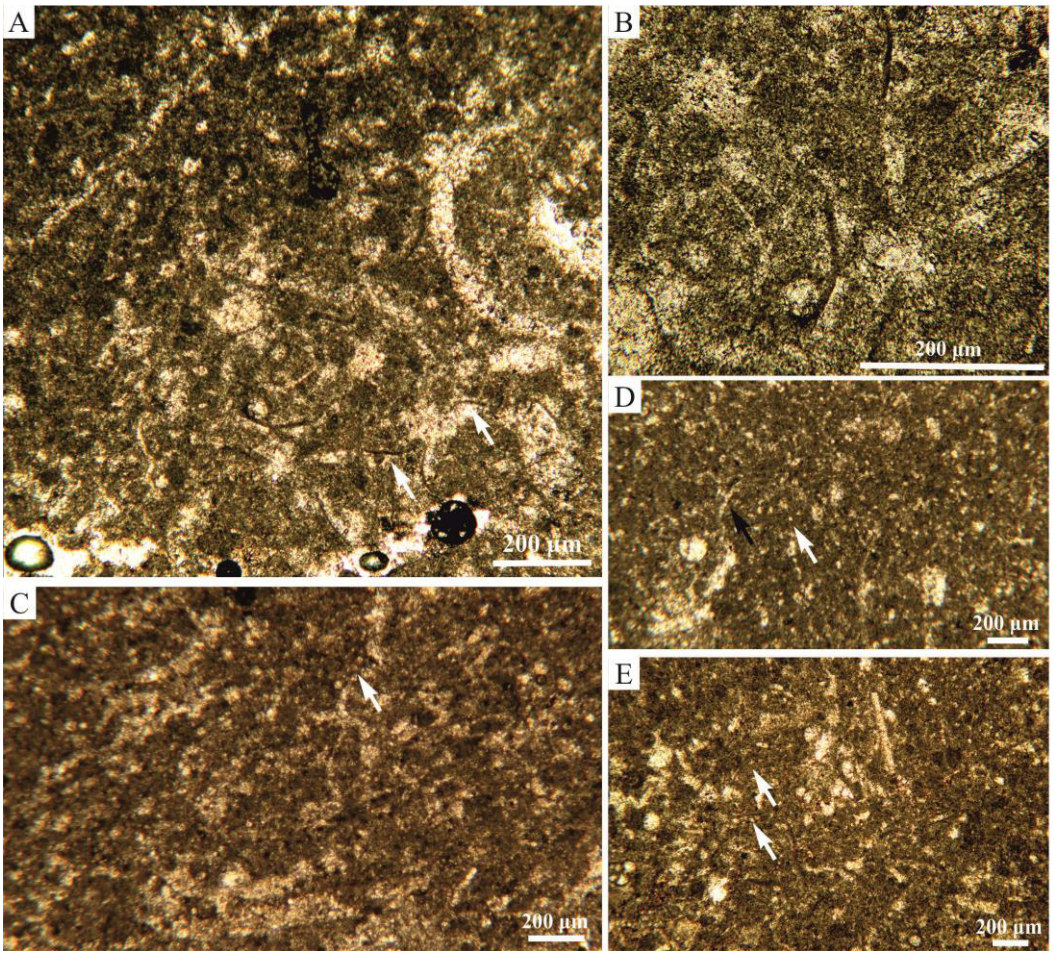

Figure 4.3. Several examples of *Girvanella*-like filaments. A, B, E) Rods of uniform micrite (white arrows in Fig. A and E). D, C) Transversal sections of single tubules distinguished by micritic wall and spar-filled centre (white arrows). Black arrow in Fig. D points to longitudinal section of single tubule distinguished by micritic wall and spar-filled centre. A) Sample F2-3 (TorF, Toraro Mt.). B) Detail of previous microphotographs, sample F2-3 (TorF, Toraro Mt.). C) Sample A1-11 (TorA1, Toraro Mt.). D) Sample Da-13 (Contrada Dazio outcrop). E) Sample F2-3 (TorF, Toraro Mt.). See text for further information.

The identified specimens do not show the "internal structure" which allow the taxonomic identification. The shape is usually undefined. In some cases, they show a dendritic/arborescent growth form with micritic branches appearing as tubules and a series of peloids (e.g., Figs. 4.5–4.6; Plate 6). Similar growth forms are often related to *Epiphyton-Renalcis* group (e.g., Riding and Toomey, 1972; Pratt, 1984; Coniglio and James, 1985). *Epiphyton* Bornemann, 1886 and *Renalcis* Vologdin, 1932 are small calcareous microfossils

with an unknown or uncertain systematic position (microproblematica), widespread and limited to Palaeozoic even if *Epiphyton*-like cyanobacteria were recognised also in Upper Jurassic reefs (Romania; Săsăran et al., 2014). Feng et al. (2010, figs. 13–5), reported the presence of the genus *Paraepiphyton* Wray, 1967 in Late Devonian carbonate sequences in southern China. The taxon is distinguished by dendritic mass of narrow micritic branched filaments. It differs from *Epiphyton* by its small size and less regular branching. *Paraepiphyton* was considered synonym of *Epiphyton* (Riding and Wray, 1972). This usually rare genus was recognized as one of upper Devonian key reef-components in south China (Zhang et al., 2007). The described *Paraepiphyton* specimens from China are very similar to those observed in the lithiotid accumulations. Pratt (1984) suggested that *Renalcis* and *Epiphyton* are actually "diagenetic taxa" formed soon after the algal death from the precipitation of calcite within coccoid-blue algal colonies. Few observed specimens show the same morphologies illustrated by Pratt (1984; p. 959, fig. 9c): "[…] *Clots attached to three branches on right side of tubular saccate form*" and "[…] *Squat, arborescent thallus showing variable chamber size*" (Fig. 4.6). The most representative studied specimens identified in thin sections were also observed at SEM, but no further information was obtained. Considering the highly morphological variability of this group and the pervasive taphonomic alteration of the specimens, their affinity with calcimicrobial association must be considered.

Among bacteria-like features, some analysed structures show a ring-shaped morphology (the so-called micritized ring-shaped bioclasts in Appendixes A.5–A.15) with a wide range of dimensions, including some specimens with smaller diameter that could be ascribed to *Decastronema* sp. (Plate 7). Transversal sections are characterised by thin micritic wall (dark in transmitted light) and central lumen (bright in transmitted light). Longitudinal sections are less frequent and can be confused with other microorganisms. No microstructure was distinguished. Some of the observed ?*Decastronema* sp. specimens are larger than those reported in literature (see Schlagintweit et al., 2015; Ćosović et al., 2008). *Decastronema* is poorly described in literature and often can be confused with other microfossils (Schlagintweit et al., 2015). In this case they could be interpreted as bioclasts. It might be also possible that some of these ring-shaped bioclasts are actually calcispheres. Calcispheres are usually refer to as hollow, spherical calcareous microfossils of various origins whose biological affinity remains uncertain (e.g., Berkyová and Munnecke, 2010). The observed specimens are in fact similar to those reported by Berkyová and Munnecke (2010, figs. 3–4). Moreover, calcispheres have been associated with micritization and peloid-derived lime mud (Berkyová and Munnecke, 2010).

In several lithiotid accumulations ?*Decastronema* sp. occurs in low density and is usually associated with *Thaumatoporella* sp. This association reminds the so-called "*Thaumatoporella-Decastronema* assemblage" often described in literature (see Schlagintweit et al., 2015 for further details).

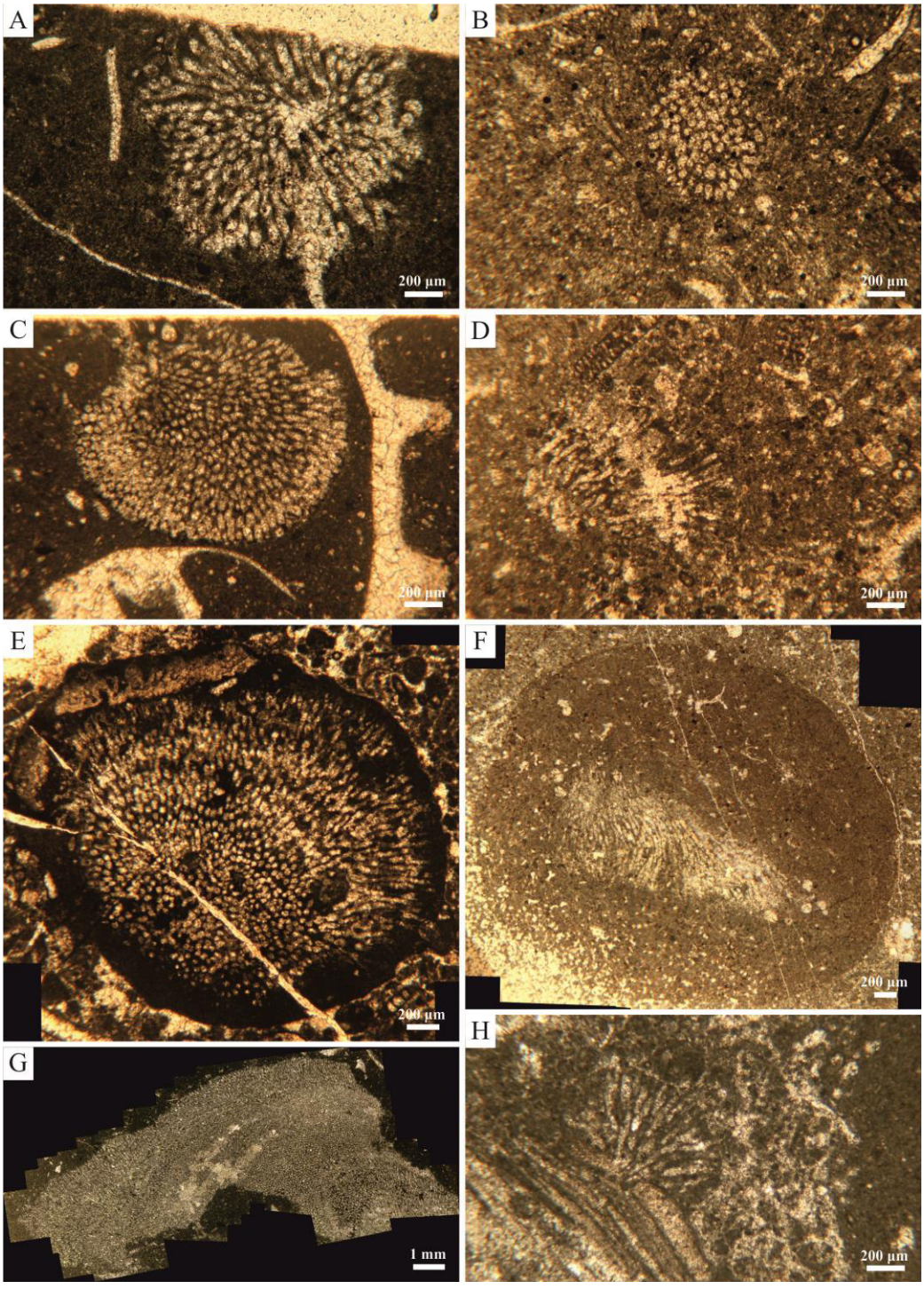

Figure 4.4. *Rivularia*-like specimens found in several locations of the Trento Platform. A) Vaio dell'Anguilla (Verona), sample V14 (Borasio, 1999). B) Vaio dell'Anguilla, sample V23 (Borasio, 1999). C) Vaio dell'Anguilla, sample V24 (Borasio, 1999). D) Vaio dell'Anguilla, sample V29 (Borasio, 1999). E) Crespadoro/Campodalbero section (Verona), sample U72 (Borasio, 1999). F) Toraro Mt. (Vicenza), sample TO8 (undeformed stitched micro-photo; Coletta, 2012). G) Toraro Mt., sample TO19 (deformed stitched micro-photo; Coletta, 2012). H) Toraro Mt., sample TO58 (Coletta, 2012).

Some authors interpreted *Thaumatoporella* and *Aeolisaccus* associations linked to the existence of sporadic restricted environment conditions (e.g., Tasli et al., 2006) or a "survival phase" dominated by disaster taxa (r-strategies organisms; e.g., Barattolo and Romano, 2005; Arriaga and Caus, 2014). Bosellini and Broglio Loriga (1971) reported the genus *Aeolisaccus* in the lower part of the unit27 in the Rotzo section along with Textularia and *Pseudocyclammina liasica*. The lower part of the unit27 included a *Cochlearites* bed (Chapter 3; Brandolese et al., 2019).

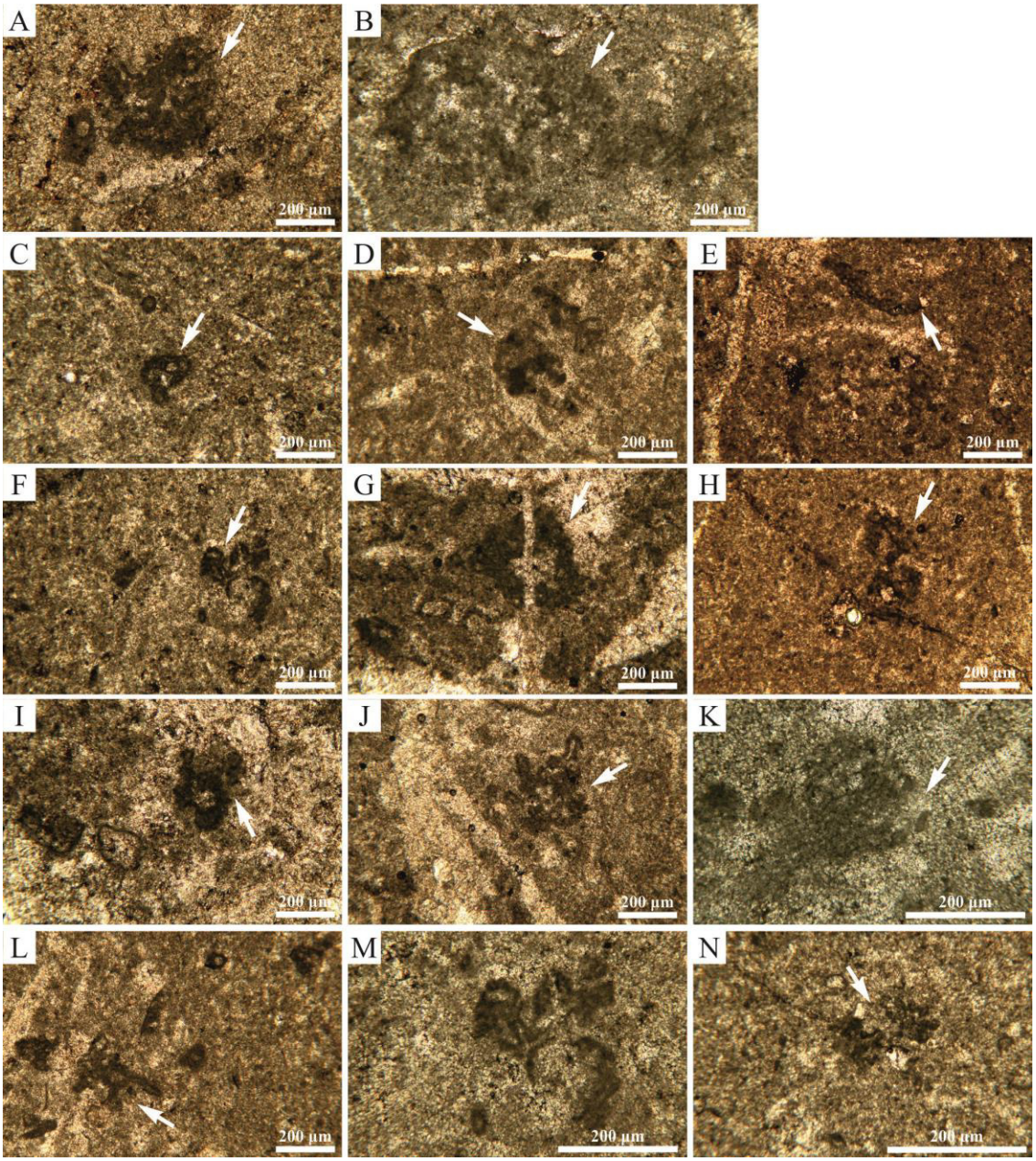

Figure 4.5. Thin section photomicrographs of dark clotted micritic structures (white arrows). A) Sample Ve1-3 (Passo Vezzena outcrop). B) Sample Ve3-15 (Passo Vezzena outcrop). C) Sample Da-32 (Contrada Dazio outcrop). D) Sample F1-1 (TorF, Toraro Mt.). E) Sample Da-10 (Contrada Dazio outcrop). F) Sample E-2C (TorE, Toraro Mt.). G) Sample Da-10 (Contrada Dazio outcrop). H) Sample Da-13 (Contrada Dazio outcrop). I) Sample E-1B (TorE, Toraro Mt.). J) Sample F1-4 (TorF, Toraro Mt.). K) Sample Ve3-15 (Passo Vezzena outcrop). L) Sample F1-1 (TorF, Toraro Mt.). M) Detail of photomicrograph F, sample E-2C (TorE, Toraro Mt.). N) Sample E-2C (TorE, Toraro Mt.). See text for further information.

In general, this taxon occurs in all the Rotzo Fm. The genus *Aeolisaccus* was assigned to the genus *Decastronema* (Cyanobacteria, order Nostocales, family Scytonemataceae; Golubic et al., 2006). The genus is widespread from the Cretaceous to Eocene and includes three species (*D. kotori*, *D. dunningtoni, D. barattoloi*). The type species *D. dunningtoni* Elliott, 1958, characterized by thicker tube diameter, has been attributed to pteropods (planktic gastropods), worm tubes, and foraminifera (e.g., Elliott, 1958; Brönnimann et al., 1972).

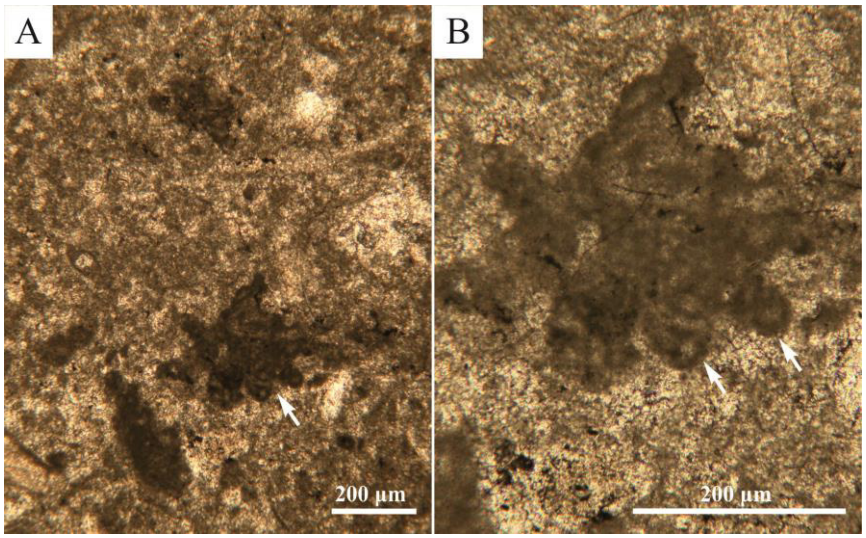

Figure 4.6. Dark clotted micritic structures with dendritic form (sample E-C5, TorE). White arrows point to circular subunits (e.g., Pratt, 1984). A) Zoom 4x. B) Zoom 10x.

Thaumatoporella parvovesiculifera occurs in several studied samples, often as free bended wall shapes with the typical porous wall (Plates 3, 8). These specimens likely correspond to broken fragments that originated from the erosion and breakage of original free and attached forms (Schlagintweit, 2013). In the studied materials, thaumatoporellaceans are rarely associated with "bacinellid" crusts showing two different morphotypes: 1) elongated attaching specimens with a thick wall with well-defined pores; 2) irregular lobate bubble-shaped morphologies (Schlagintweit et al., 2013; Plates 3, 8). Internal structures typically with thinner walls than the enclosing one were interpreted as daughter colonies (De Castro, 1988; 1990; Plate 3). The Mesozoic-lower Cenozoic *Thaumatoporella parvovesiculifera* (Raineri, 1922) is characterized by high morphological variability (Plates 3, 8), possibly related to original intraspecific differences, various preservation mode or life cycle stages (e.g., De Castro, 1990; 2002; Schlagintweit et al., 2013). One of more important proliferation periods (increased abundance, acme) corresponds to the Early/Middle Jurassic (Schlagintweit et al., 2013). This taxon is usually considered as an *incertae sedis* (or microproblematicum; e.g., Schlagintweit et al., 2013; 2015). Several forms were identified: fragments, irregular roundish specimens, encrusted morphologies (also within oncoids), cysts and daughter colonies forms (e.g., De Castro, 1990; 2002; Schlagintweit, 2013; Schlagintweit et al., 2013).

Three types of micrite were distinguished: clotted peloidal micrite, very fine-grained micrite and microsparite. When a detailed distinction was not possible, the generic term micrite was used (Fig. 4.7B). Aggrading diagenesis generally affected micrites obliterating the original fabric, therefore micrite (*sensu lato*) is the most abundant. Several samples show two different types of the distinguished micrite. Clotted peloidal micrite is characterised by changes in darkness, which reflects varying density and by changes crystal size between dark peloidal clots, likely rich in organic matter, and the white inter- granular areas that lack organic remains (e.g., Guido et al., 2011; Braga et al., 2019). Clotted peloidal micrite (Fig. 4.7A) was documented only in few samples of the TorA1 (both in the core, flanks and in the cover as well), in the flank areas of the TorD2, TorE, and TorF. Few samples were observed in Da and Cm accumulations. It is always restricted to limited areas and the variation towards the other two end-members is always gradual. Very fine micrite occurs essentially in Campoluzzo Mt. accumulation (in all the studied samples) and in TorD2 (5 samples on 6) (Fig. 4.7C). It was also recognized in the Rotzo accumulation, in the Contrada Dazio outcrop and in the TorB. Frequently it is limited to restricted areas. Microsparite is always limited to restricted areas.

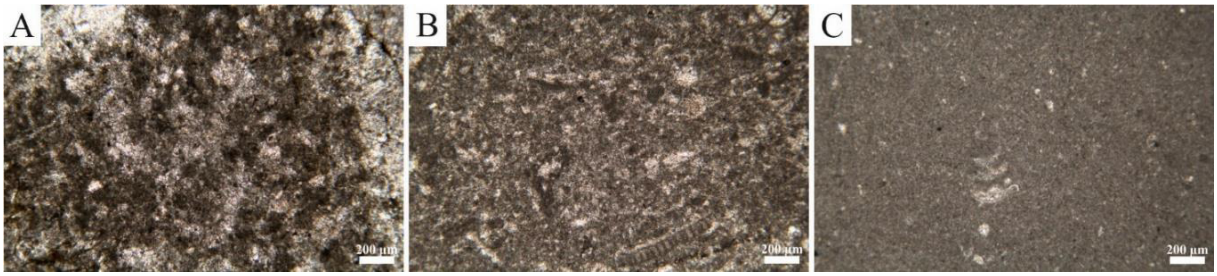

Figure 4.7. A) Clotted peloidal micrite, sample A1-13 (TorA1, Toraro Mt.). B) Micrite (*sensu lato*). Sample F2-2 (TorD2, Toraro Mt.). C) Very fine-grained micrite. Sample Cm1-1 (Cm, Campoluzzo Mt.).

The different types of micrite recognised with optical microscope were tentatively observed by SEM-EDS. A clear distinction between clotted peloidal micrite and micrite was not observed. Only few homogenous crystals were distinguished in limited areas (Fig. 4.8).

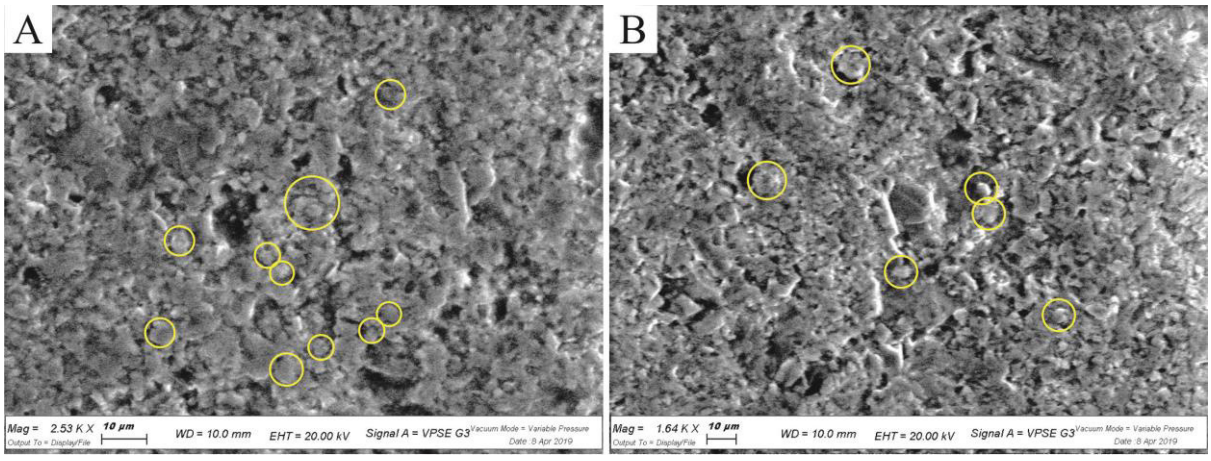

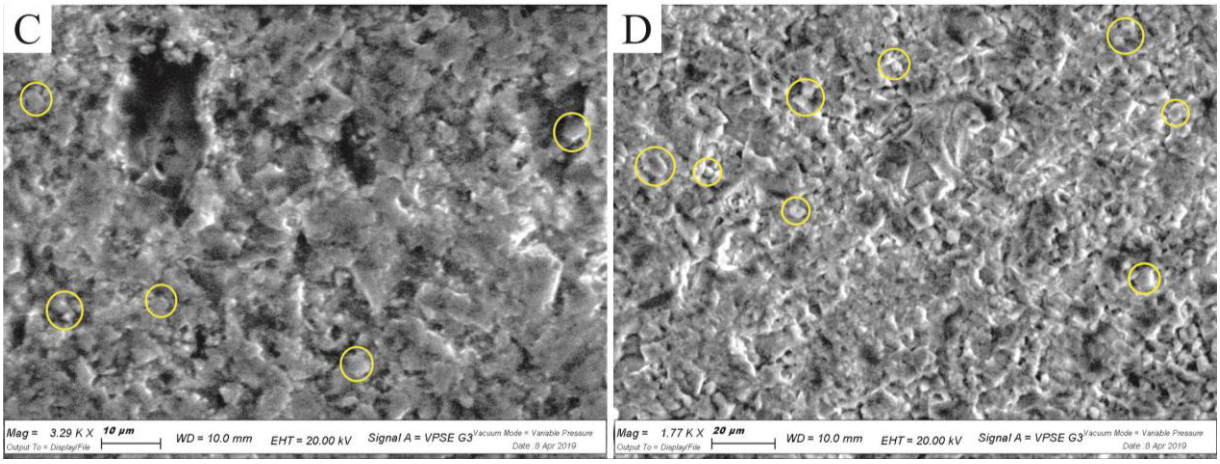

Figure 4.8. *continued*. SEM photos of micrite constituting the matrix of lithiotid accumulations. In all the images few homogenous crystals were observed. Yellow circles point to homogenous crystals which could be interpreted as residual automicrite. A) Sample E-C5 (TorE, Toraro Mt.). B) Sample E-C5 (TorE, Toraro Mt.).C) Sample E-C5 (TorE, Toraro Mt.). D) Sample A1-1 (TorA1, Toraro Mt.).

The EDS analysis carried out on roundish structures showed higher concentration of carbon (Figs. 4.9–4.10).

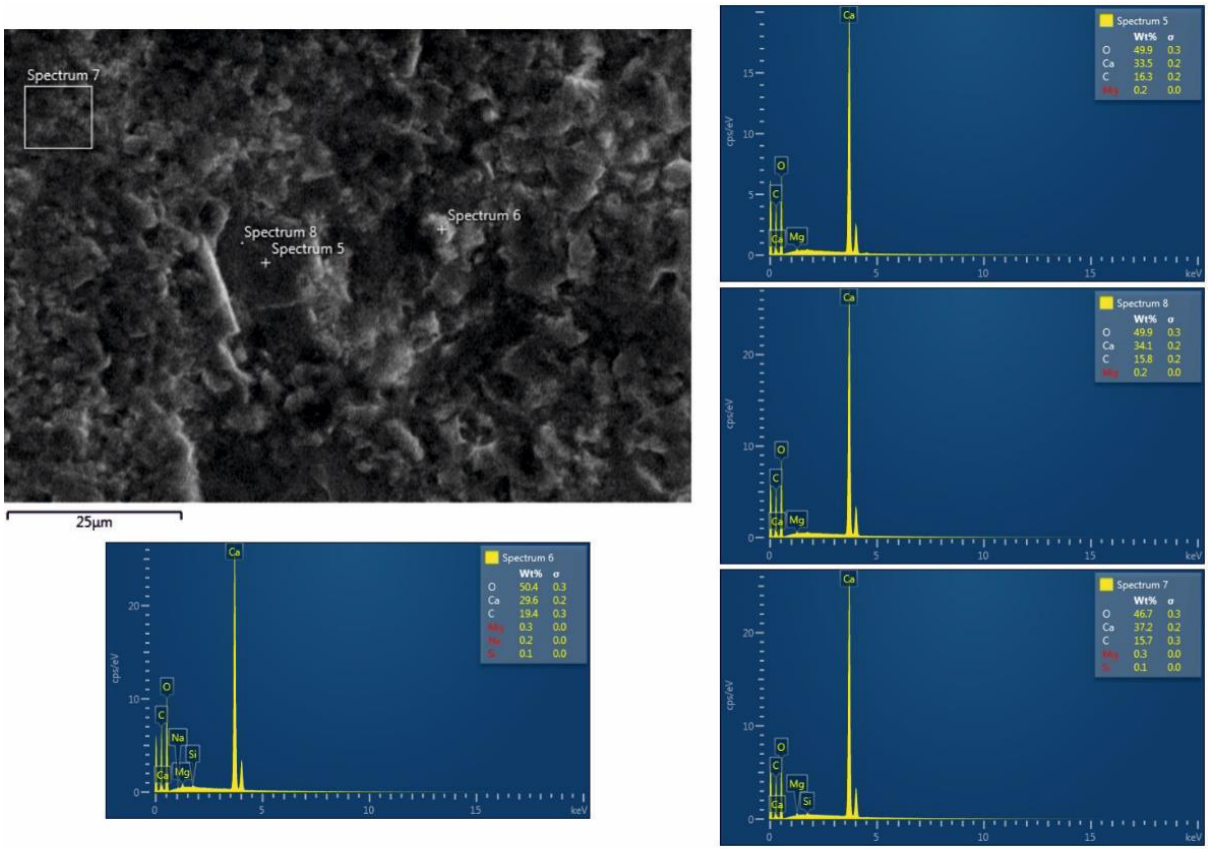

Figure 4.9. Semi-quantitative energy dispersive spectra (EDS) data obtained during SEM analysis of the various homogenous grain size particles described herein. Carbon exceeds in all the spectra and in particular in the spectrum 6 and 8. No significant indications of detrital micrite were observed.

The SEM-EDS could not be considered the best method to detect carbon content due to high external possible contamination. However, the stoichiometric comparison of these EDS spectra with purely carbonate grain spectra confirms the higher concentration of carbon.

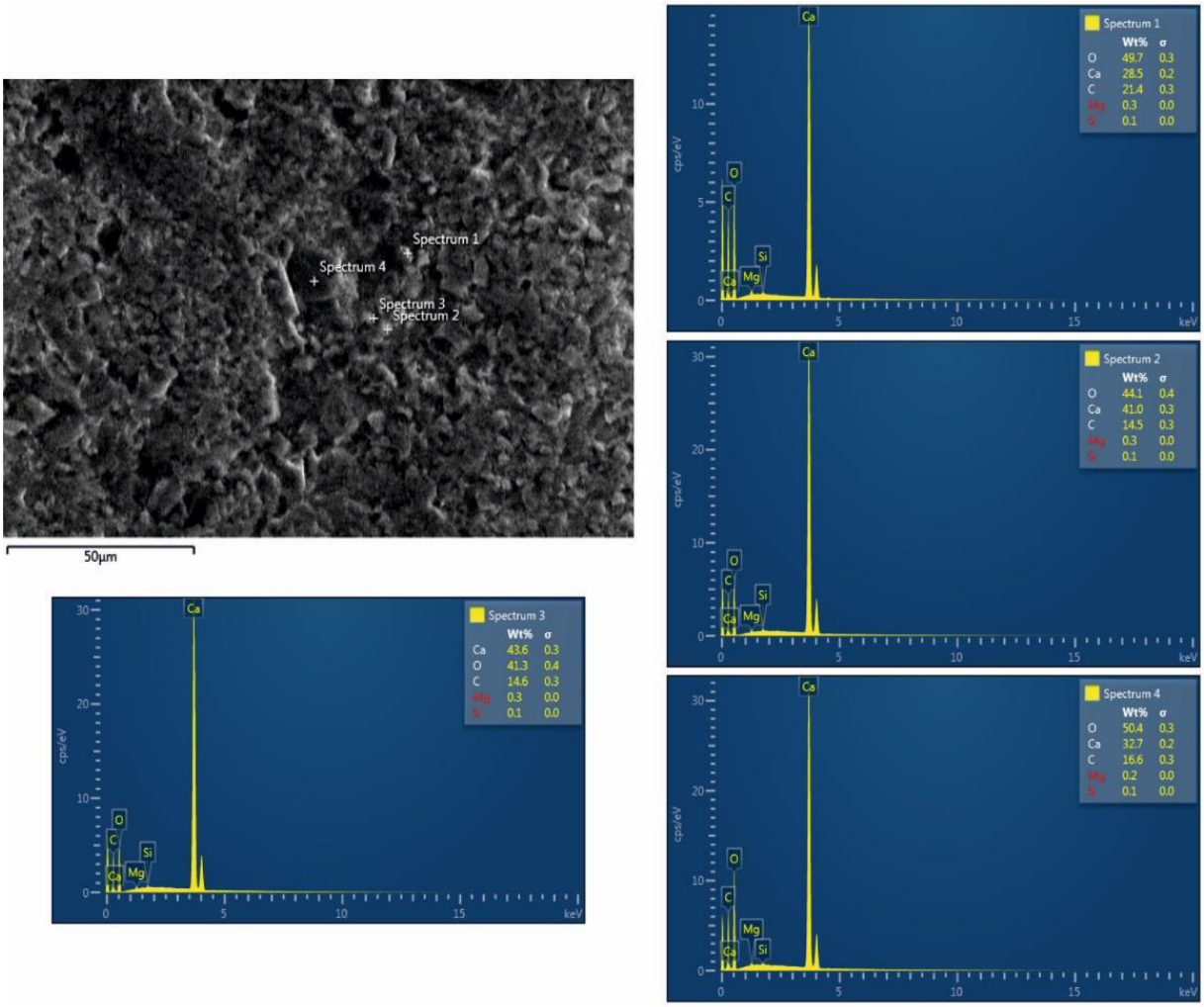

Figure 4.10. Semi-quantitative energy dispersive spectra (EDS) data obtained during SEM analysis of the various homogenous grain size particles observed in another samples. Carbon exceeds in all the spectra and in particular in the spectrum 4. No significant indications of detrital micrite were observed.

4.4.2. Pyrite and framboids

Pyrite shapes are documented in several studied samples (Tab. 4.1). Five types of pyrite were identified with SEM set in backscatter mode (Figs. 4.11–4.12): 1) unusual loose packed disc-shaped crystals, 2) altered pyrite framboids, 3) well preserved framboids, 4) euhedral crystals and, 5) undefined forms. Other minerals (e.g., barite $BaSO_4$, limonite $FeO(OH)\cdot nH_2O$ and iron oxides) were also recognised.

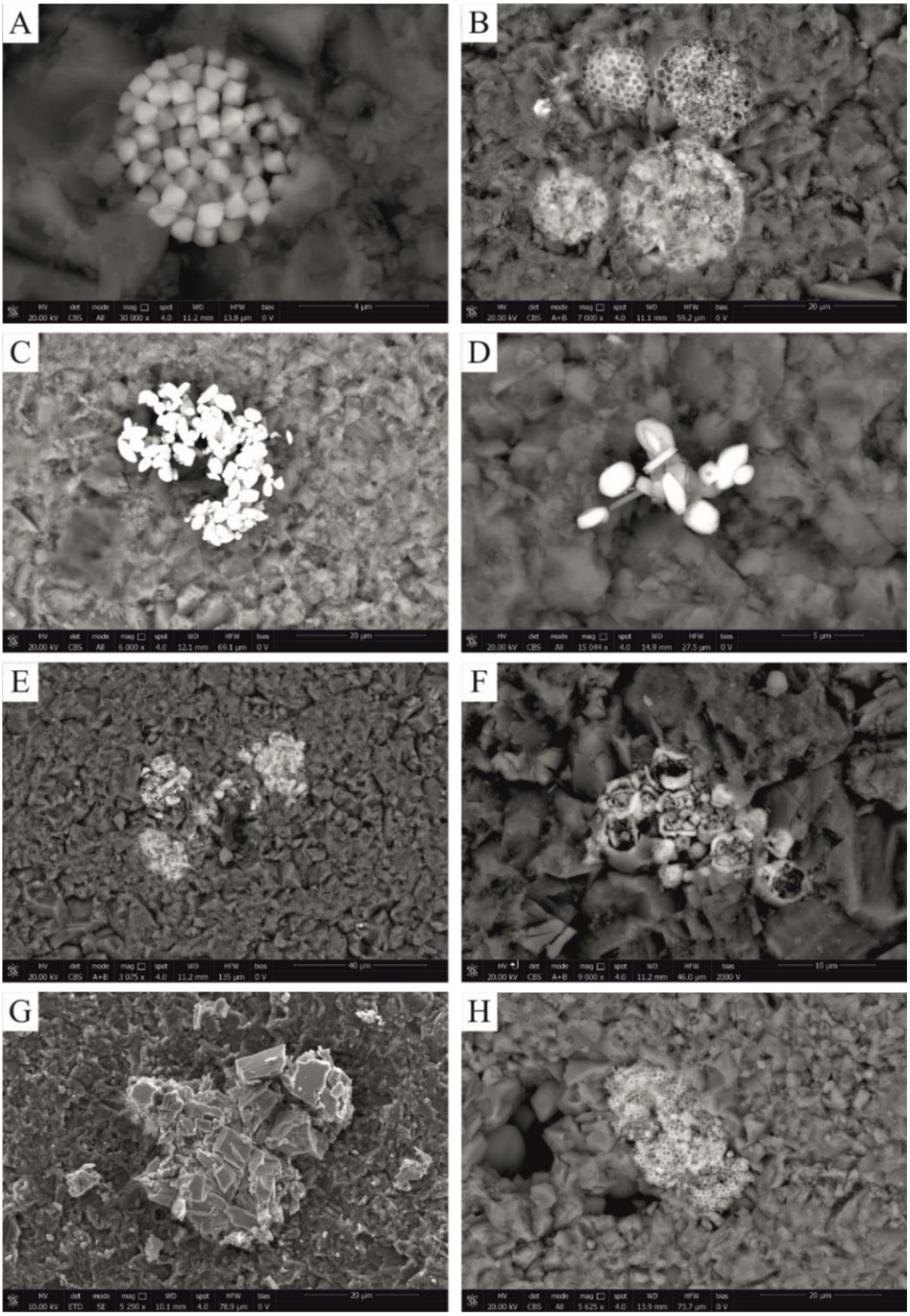

Figure 4.11. Backscattered electron images of pyrites occurring in lithiotid accumulations (Toraro Mt.). A) Well-defined pyrite framboid, sample TorC. B) Altered pyrite framboids, sample C-5B (TorC). C) Dense disc-shaped pyrite aggregate, sample C-1I2 (TorC). D) Loose disc-shaped pyrite aggregate, sample B-5 (TorB). E) Limonite, sample C-5B (TorC). F) Altered pyrite, sample C-5B (TorC). G) Barite crystal, sample E-1C (TorE). H) Fe-oxides, sample C-1CR (TorC). See text for further details.

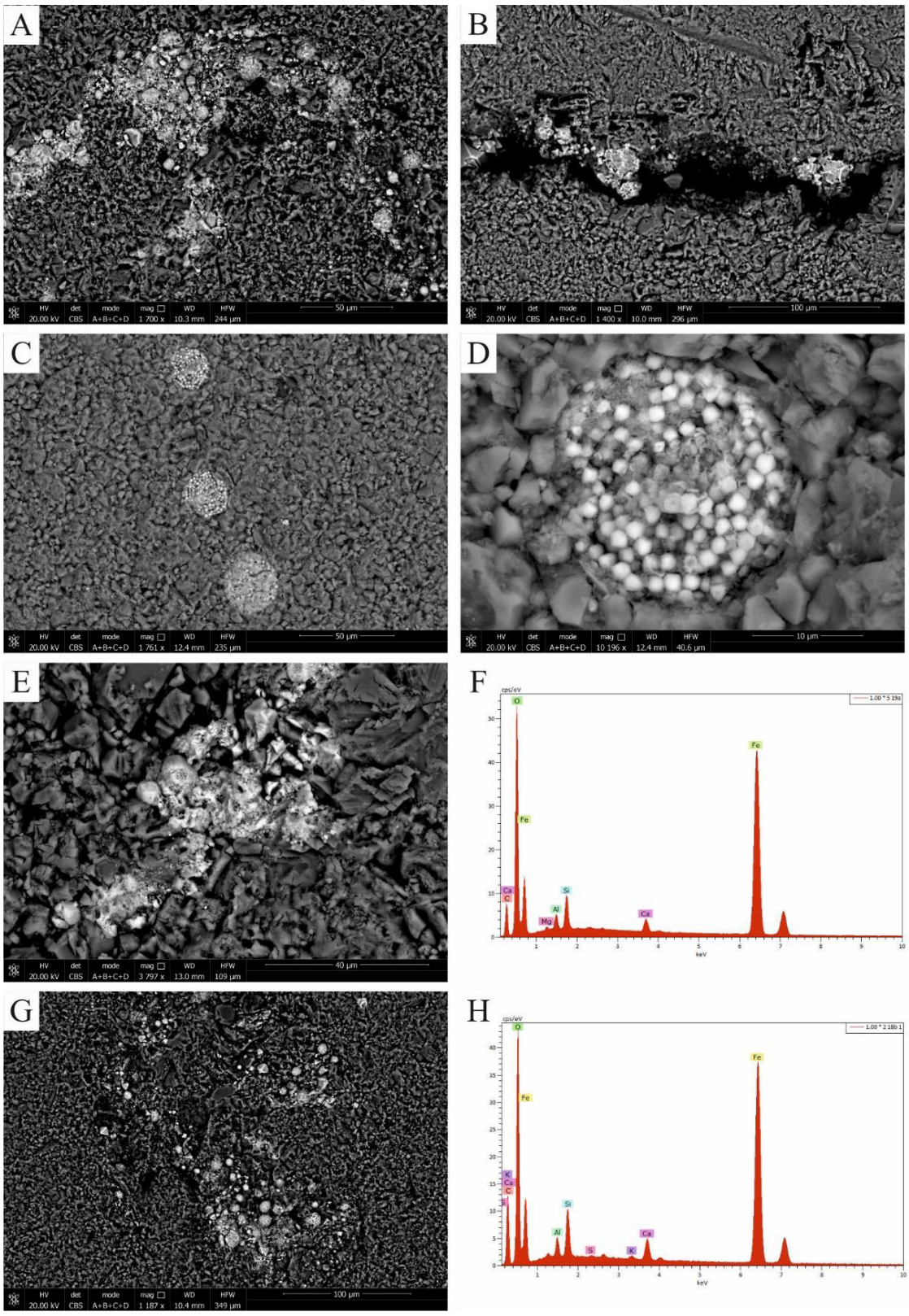

Figure 4.12. Backscattered electron images of pyrites from TorA2 lithiotid accumulation (Toraro Mt.). A) Framboids with altered surface, undefined shapes and not well-defined euhedral crystals, sample 18-block C upper part. B) Framboids with altered surface and not well-defined euhedral crystals, sample 18-block C lower part. C) Well-defined pyrite framboids, sample 22-block C (marl). D) Detail of previous photo, sample 22-block C (marl). E) Pyrite framboids with altered surface and isolated small crystallites and undefined (amorphous) forms, sample 19-block A lower part. F) SEM-EDS spectrum of iron oxides observed in the previous photo, sample 19-block A lower part. G) Framboids with altered surface, undefined forms and not well-defined euhedral crystals. H) SEM-EDS spectrum of altered pyrite observed in the previous photo, sample 18-block C upper part. See text for further details.

4.4.3. Distribution in the lithiotid shell accumulations

The abundance of skeletal and non-skeletal components was evaluated according to the dominating genus and their distribution in the lithiotid accumulations (Fig. 4.13). The sampling location and the pyrite/framboid distribution in the studied accumulations are reported in Figs. 4.14–4.18.

In the *Lithiotis*-dominated accumulations (TorA1, TorA2, Contrada Dazio outcrop), *Thaumatoporella parvovesiculifera* and the bacteria-likes structures are more common in the core than in the flanks. *Rivularia*-like features were observed both in the flanks (TorA1) and in the core (Contrada Dazio). On the contrary, peloids and fecal pellets are rare in the flank areas, even if they can be locally common/abundant in the accumulation core. Cortoids occur basically only in the flanks. The lithological difference between core and flanks is not sharp and varying between wackestone to wackestone-packstone (Appendix A.3). Locally wackestone-mudstone occurs in the accumulation flanks (see Appendix A.3).

The *Cochlearites*-dominated accumulations are characterised by an increase in occurrence of bacteria-like structures (included *Rivularia*-like organisms) and non-skeletal components in the flanks than in the core. Only fecal pellets are more common in the core. Rare *Palaeodasycladus* sp. were locally found both in the core (Ve3) and in flank areas (TorF). The Rotzo accumulation is particularly distinguished by the occurrence of rare encrusting organisms (likely foraminifera) associated with micritic laminae recognised in several samples. Commonly, the *Cochlearites*-dominated accumulation core is distinguished by mudstone-wackestone, while in the flanks the lithology varies from wackestone to wackestone-packstone (Appendix A.3).

The mudstone-packstone cover deposits overlying *Lithiotis*- and *Cochlearites*-dominated accumulations show different composition (Appendix A.3). On the *Lithiotis* accumulations the cover is constituted by wackestone and wackestone-packstone with rare peloids and locally *T. parvovesiculifera*. In the *Cochlearites* accumulations, the cover is characterised by cortoids, fecal pellets, bacteria-likes features; oncoids are also present.

Only *Lithioperna* accumulation flanks were analysed showing a clear difference in respect to the former lithiotid accumulations. Abundant fecal pellets locally occur with frequent-to-rare peloids and rare cortoids, whilst bacteria-like features and *T. parvovesiculifera* are absent. The lithology is similar to that recognised in *Cochlearites* accumulations flanks (Appendix A.3). A general increase in frequency were registered also for bioclasts.

Matrix is highly variable between both core-flank and lithiotid genus-dominated accumulations. Clotted peloidal micrite locally occurs in all lithiotid accumulation flanks, whilst it was identified only in the *Lithiotis* accumulation core and in the cover.

Pyrite was analysed in five accumulations outcropping in the Toraro Mt. section.

In TorA1, pyrite was found only in three samples located at the top of the accumulation (A1-1, A1-4) and in the flank areas (A1-11; Fig. 4.14A). In the sample A1-1 undefined shapes were recognised. Only one framboid is well defined (12.01 µm in diameter) while the altered pyrite shows framboid-like shape. In the sample A1-1, considering all framboidal forms, the measured parameters are: S= 14, md= 8.95 µm, MFD= 22.33 µm and SD= 5.5 µm. Because the sample A1-4 is constituted by solely altered shapes these are not considered in the size distribution analysis. The sample A1-11 is distinguished by S= 8 (including well- and less well- preserved), md= 7.89 µm, MFD= 12.01 µm and SD= 2.57 µm. Few undefined pyrite (maximum size 30 µm) was also recognised.

In TorA2 accumulation, the analysed samples were collected from the upper and lower part of two blocks (Fig. 4.15). Pyrite was abundant in all the observed samples. Rarely pristine pyrite was observed. Framboids are usually altered in iron oxides. In the lower part of block A, altered framboidal structures were identified (iron oxides) with undefined shapes (maximum size 88 µm). The measured iron oxides framboids (S= 10) show md= 8.87 µm, MFD= 13.06 µm and SD= 1.99 µm. In the upper part undefined shapes (max size 135 µm) and pyrite framboids occur (S= 74, md= 14.06 µm, MFD= 34.98 µm, SD= 5.28 µm). Block C was analysed in two distinct portions. In the first block (polished slab 18; Fig. 15), the upper part is distinguished by undefined shapes (maximum size 15 µm), euhedral crystals, and iron oxides framboids (S= 86) with md= 6.55 µm, MFD= 14.32 µm and SD= 2.56 µm. The same elements characterise the lower part, where the measured framboids are S= 35 with md= 16.44 µm, MFD= 29.73 µm and SD= 6.66 µm, while undefined shapes are up to 40 µm in length. In the second block (polished slab 22; Fig. 15), no framboids were identified in the lower part. In the upper part several framboids occur: S= 47 with md= 8.17 µm, MFD= 16.14 µm and SD= 3.1 µm. In the marl, limonite and larger iron oxides framboids were recognised (S= 3, md= 25.83 µm, MFD= 31.23 µm, SD= 4.69 µm).

In TorB, well-defined pyrite framboids were found in the cover deposit (sample B-1; Fig. 4.14B). The well-defined framboids (S= 23) show a md= 12.93 µm, MFD= 22.51 µm and SD= 4.43 µm. Altered pyrite framboids and undefined shapes dominate the accumulation flanks (sample B-2 and B-4). The measured parameters are S= 21, md= 6.94 µm, MFD= 15.33 µm and SD= 3.51 µm and S= 13, md= 6.08 µm, MFD= 10.07 µm and SD= 2.24 µm,

respectively. Disc-shaped pyrite (each crystallite varies from ~1.36 to ~3.4 µm in diameter) along with altered pyrite framboids occurs towards the accumulation core.

In TorC, pyrite occurs as altered framboidal and undefined shapes (Fig. 4.16A). Limonite was found at the base of the accumulation, corresponding to the bioclastic packstone-grainstone (sample C-B5). Disc-shaped pyrite occurs locally, at the top of the accumulation (sample C-1I2), as well as iron oxides with undefined morphologies. Altered pyrite framboids were locally recognised with no distinction between the different part of the accumulation. At the base of the outcrop (sample C-5B) the measured parameters are: S= 6, md= 10.14 µm, MFD= 16.88 µm and SD= 4.24 µm. In the periphery (sample C-1CR): S= 5, md= 8.10 µm, MFD= 10.77 µm and SD= 2.63 µm. In the middle area two points were analysed. In the sample C-3CL the measured parameters are: S= 9, md= 14.33 µm, MFD= 19.95 µm and SD= 2.45 µm, while in the sample C-1CL S= 2, md= 6.19 µm, MFD= 8 µm and SD= 2.56 µm.

In the analysed samples (No. 11) of the TorE, pyrite was not found (Fig. 4.16B), while barite microcrystals are frequent.

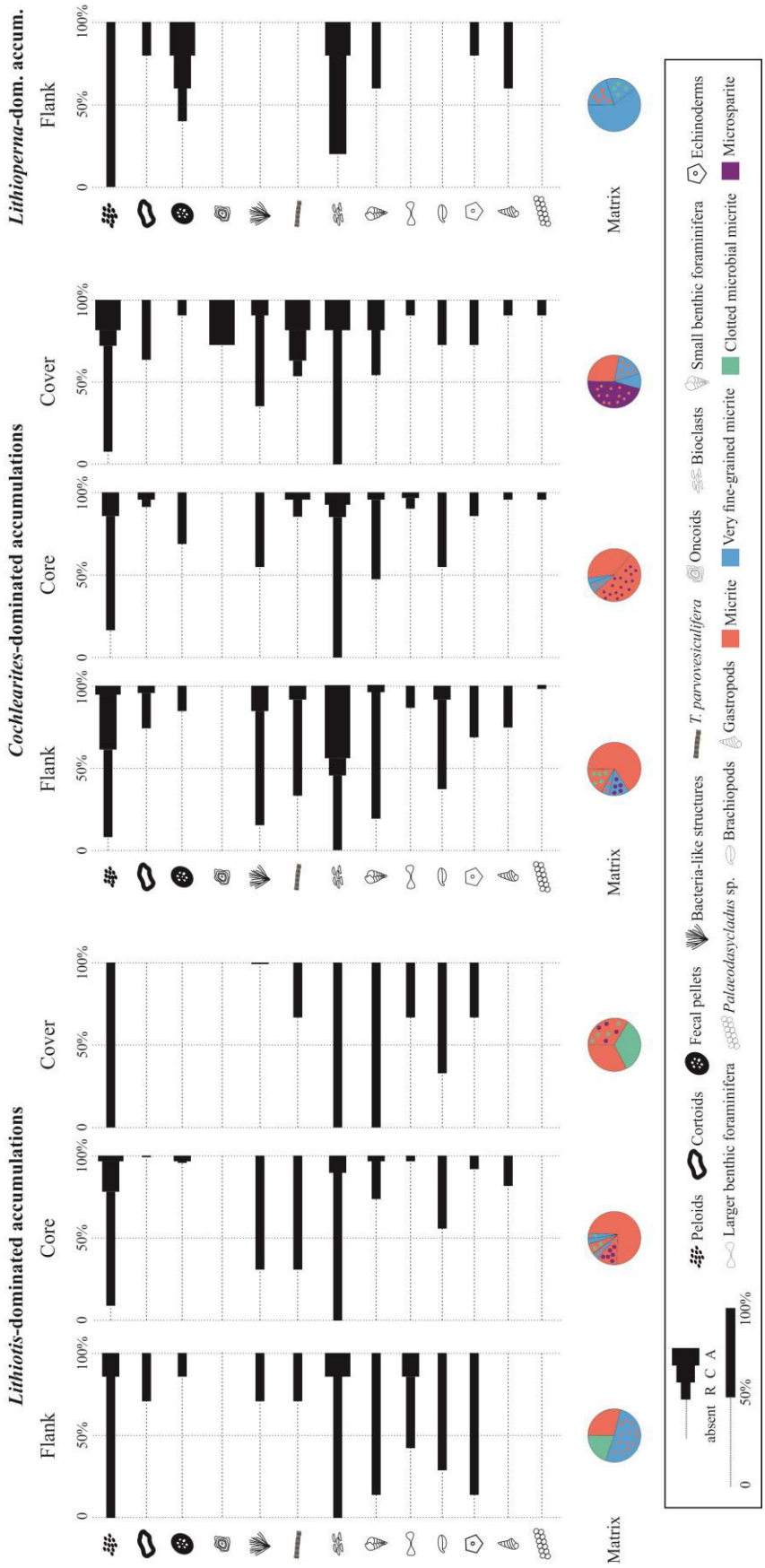

Figure 4.13. Skeletal and non-skeletal components distribution in the analysed accumulations according to the dominating lithiotid genus. The cover constitutes the deposit overlying the lithiotid accumulation. Terms as flank, core and cover do not mean proximal or distal locations in the accumulation. The analysed data are included in Appendix A.3. See text for further details. R, rare; C, common; A, abundant.

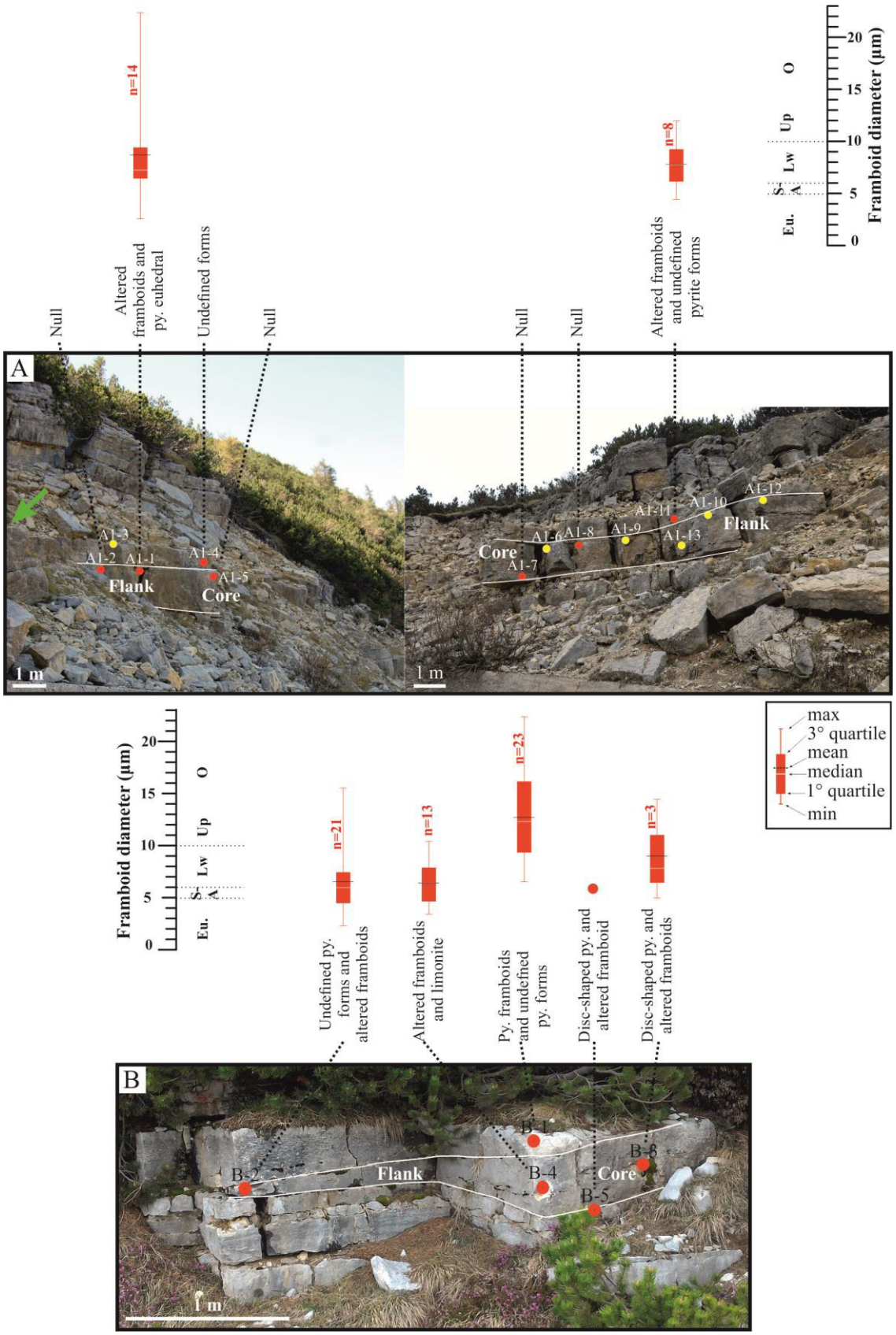

Figure 4.14. A) TorA1. B) TorB. Sampling scheme and the corresponding "Box-and-whisker" plots for the diameters of pyrite framboids in the lithiotid accumulation compared with the inferred water-column redox conditions (Eu, euxinic; S-A, suboxic-anoxic, Lw, lower dysoxic; Up, upper dysoxic; O, oxic; Wignall et al., 2010). Red points indicate the samples studied for pyrite framboids and thin section analysis. Yellow points show the samples collected only for thin section observations. In the Fig. A, the green arrow indicates the approximate position of TorA2. Py., pyrite.

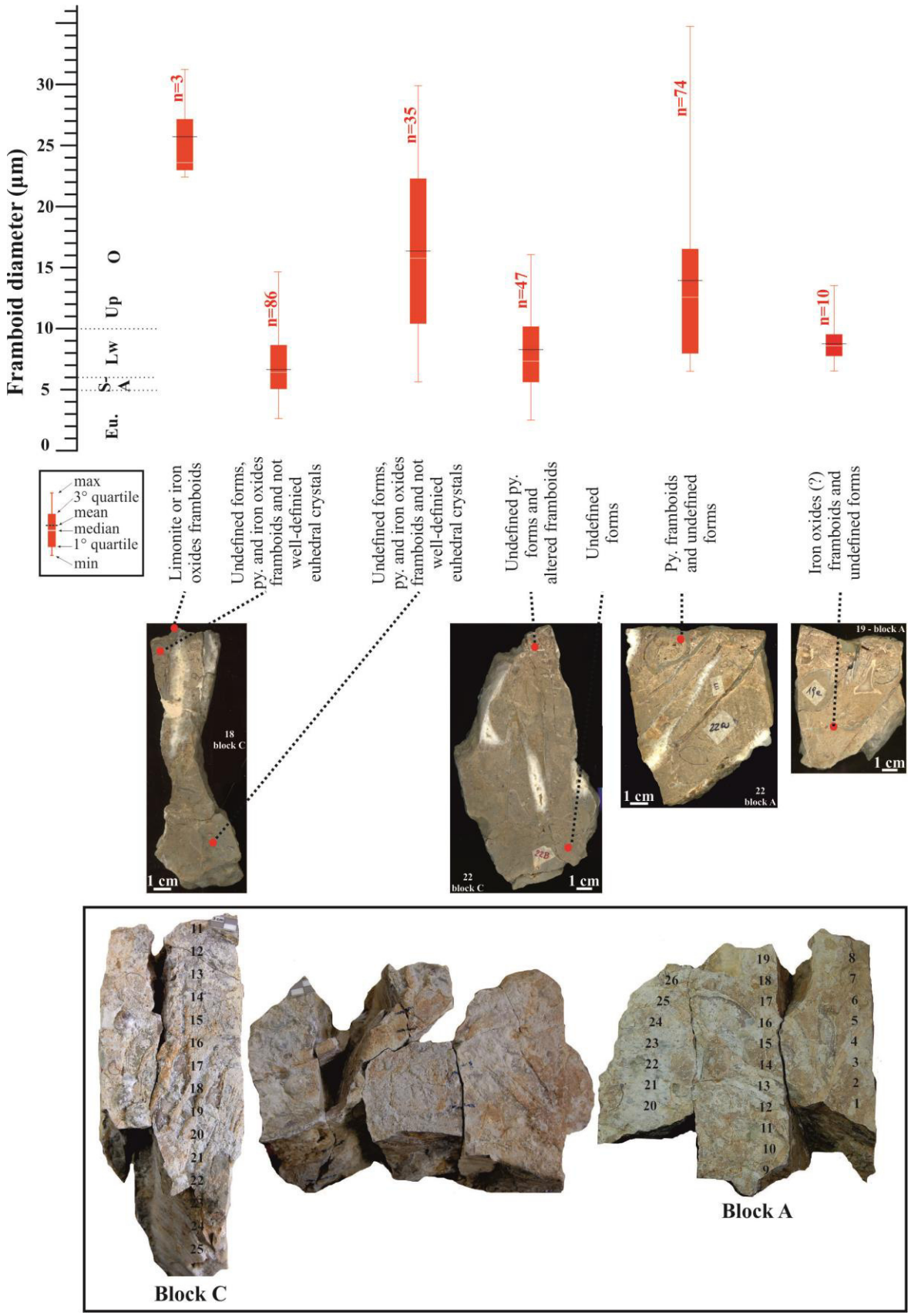

Figure 4.15. TorA2. Sampling scheme and the corresponding "Box-and-whisker" plots for the diameters of pyrite framboids in the lithiotid accumulation compared with the inferred water-column redox conditions (Eu, euxinic; S-A, suboxic-anoxic, Lw, lower dysoxic; Up, upper dysoxic; O, oxic; Wignall et al., 2010). Red points indicate the samples studied for pyrite framboids. The single studied thin section is made from polished slab 22 block C. Py., pyrite.

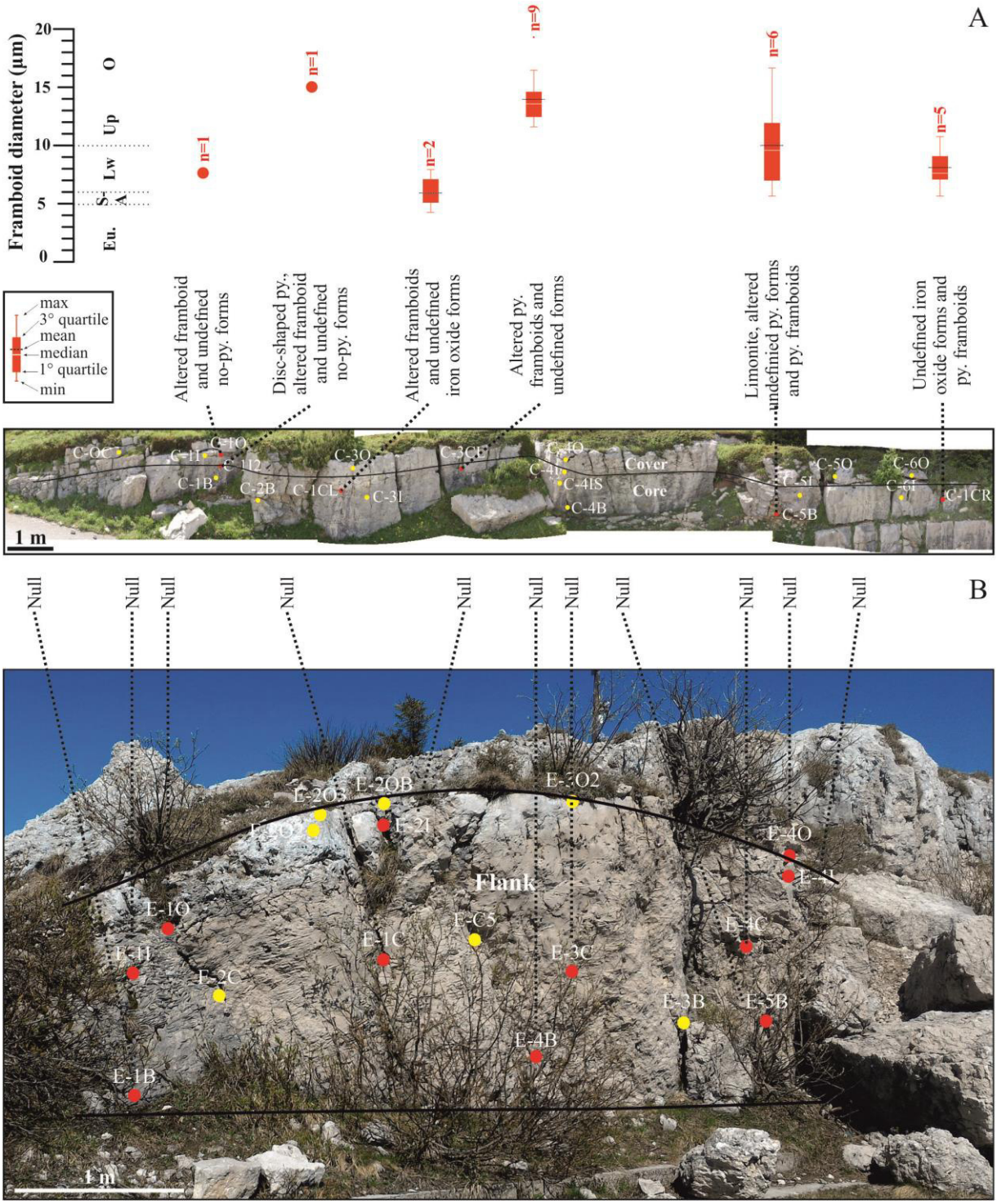

Figure 4.16. A) TorC; B) TorE. Sampling scheme and the corresponding "Box-and-whisker" plots for the diameters of pyrite framboids in the lithiotid accumulation compared with the inferred water-column redox conditions (Eu, euxinic; S-A, suboxic-anoxic, Lw, lower dysoxic; Up, upper dysoxic; O, oxic; Wignall et al., 2010). Red points indicate the samples studied for pyrite framboids and thin section analysis. Yellow points show the samples collected only for thin section observations. Sample C-3CL and E-1I were studied only for pyrite analysis. Py., pyrite.

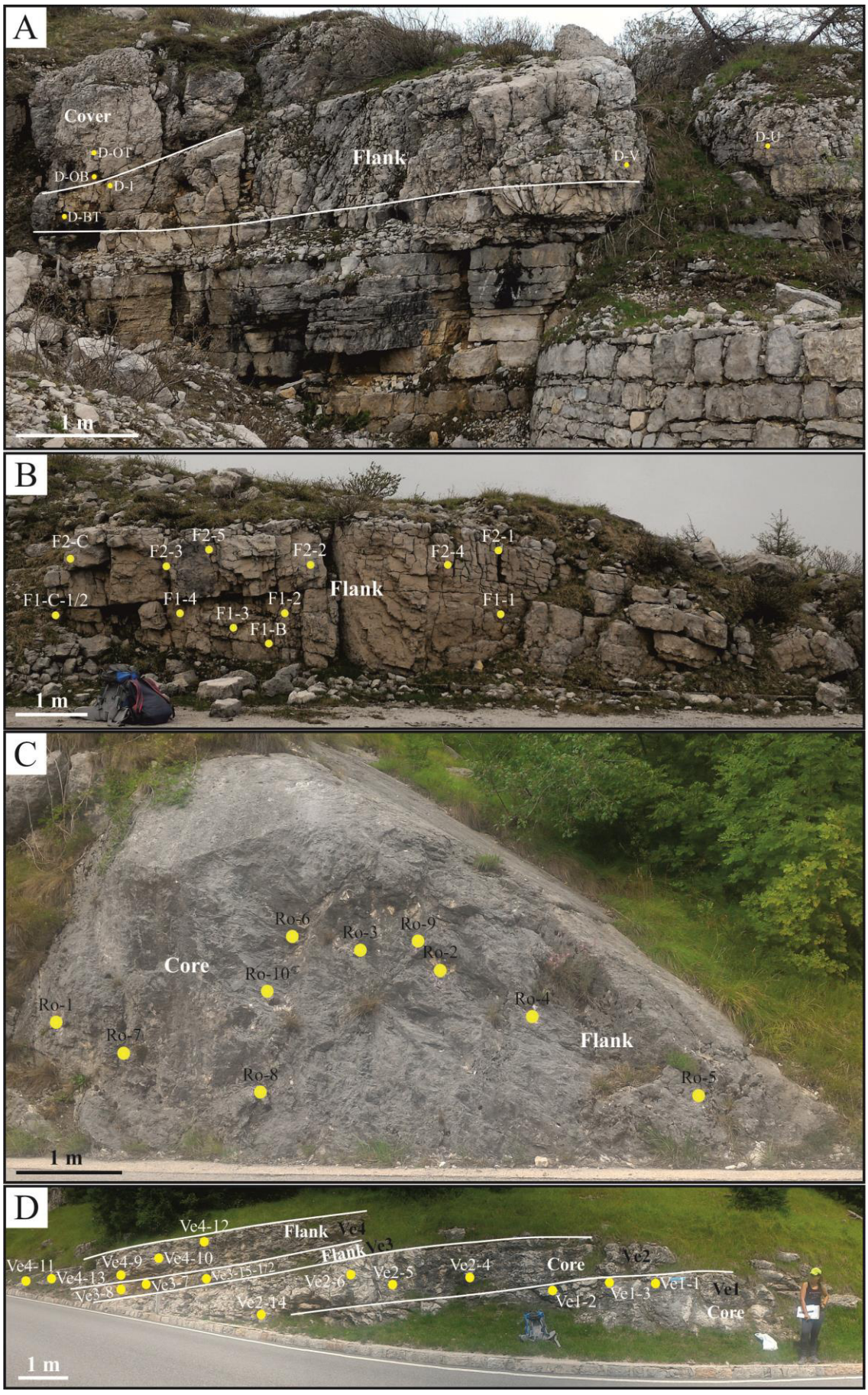

Figure 4.17. Locations of the samples analysed in thin sections. A) TorD2 (Toraro Mt.). B) TorF (Toraro Mt.). C) Rotzo accumulation. D) Passo Vezzena outcrop. Yellow points show the samples collected for thin section observations.

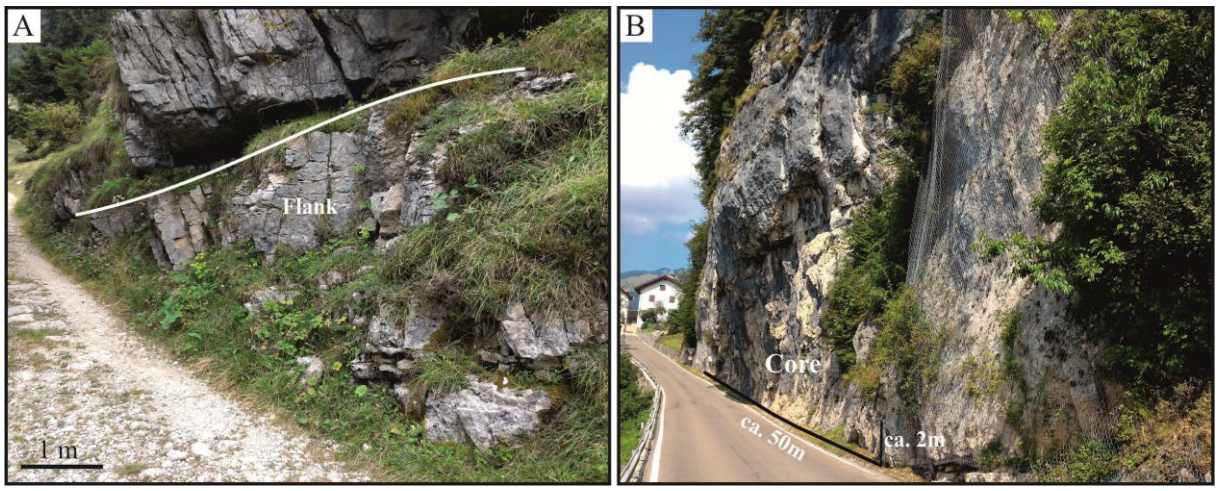

Figure 4.18. Isolated outcrops with lithiotid accumulations. A) Campoluzzo Mt. outcrop (Cm; Tonezza del Cimone, Vicenza). B) Contrada Dazio (Da; Folgaria, Trento). In Cm accumulation, samples for thin section observations were randomly collected. In Da outcrop a 2-m thick succession was sampled.

4.5. Discussion

4.5.1. The microbial role on the substrate/water interface

Occurrence of peloids, bacteria-like features and clotted micrite fabric provides evidences of microbial activity on the sediment/water interface (e.g., Riding, 2000).

In the lithiotid accumulations matrix peloids are the most frequent components associated with bioclasts. The likely origin of most of them as pseudo-faeces is related to bivalve occurrence. In modern shallow water environments, the contribution of suspension-feeding bivalves in biodeposit producing pseudo-faeces is considerable (e.g., Kooijman, 2006). A similar contribution was already suggested for Pliensbachian bivalve carpets where autochthonous micrite was produced by the gregarious lithiotids along with microbial colonies (Bassi et al., 2015). Peloids can also be directly related to microbial origin. Coniglio and James (1985) suggested that the calcified algal contribution in the micrite production ranges from well-defined algal particles (colonial individuals) to less identifiable particles that would be classified as peloids. For instance, *Girvanella* preservation could varies from tubules with micritic wall and spar-filled centre to rods of uniform micrite (e.g., Schmidt, 2006; Figs. 4.2–4.3). The fragmentation of *Girvanella* sheets infilled by micrite, contributed to the production of silt-size peloids.

The occurrence of microbial activity is confirmed by the presence of several types of bacteria-like features, associated with cortoids, pelletoids and oncoids. Microbial peloids were locally recognised in few samples from Contrada Dazio outcrop, TorB, TorC, TorE and TorF accumulations. Their fuzzy outlines and the occurrence in clusters point to a microbial origin (e.g., Macintyre, 1985; Chafetz, 1986; Riding, 2000; Samankassou et al., 2005). Locally, rare

pelletoids (micritized grains) were identified. They are directly linked to micritization which rarely affects the bioclasts in the studied accumulations. Slightly difference in the frequency and abundance occurs between core and flanks both in *Lithiotis*- and *Cochlearites*-dominated accumulations (Fig. 4.13). The rare peloids occurrence in *Lithioperna* flanks could be associated with the higher water turbulence as confirmed by common occurrence of bioclasts and abundant parautochthonous bivalve shells (Chapter 3; Brandolese et al., 2019).

Destructive cortoids are common in the studied samples, while constructive cortoids are rare. Cortoids are related to micritization (destructive envelope) and encrustation (constructive envelope). Their distribution, restricted to specific accumulations, could be indicative of micritization/encrustation rate. The cortoid occurrence is also related to algal and microbial activity (e.g., Flügel, 2010). Their rare occurrence in both *Lithiotis* and *Cochlearites* accumulation cores suggests a rapid burial in these areas as confirmed by the occurrence of autochthonous lithiotid individuals (see Chapter 3 and Brandolese et al., 2019 for further details) instead of lower bacterial activity (Fig. 4.13).

Seven out of ten studied samples from the Rotzo accumulation show thin micritic laminae (Plate 1). They encrusted lithiotid shells and occur with encrusting foraminiferal-like tests. These thin micritic laminae are related to microbial activity and lower sedimentation rate. Rare bioerosion traces in the lithiotid shells support this interpretation. Usually, the level of bioerosion and encrustation on lithiotids is unexpectedly low, due to their semi-infaunal mode of life (e.g., Chinzei et al., 1982; Bassi et al., 2017; Brame et al., 2019). The reduced bioerosion rate in lithiotid bivalves could depend on high sedimentation rate in oligotrophic regime, which reduces the proliferation of bioeroding organisms (e.g., Bassi et al., 2017). The unusual occurrence of these encrusting organisms and borings can be associated to local variations from oligotrophic to mesotrophic regime (e.g., Fugagnoli, 2004; Bassi et al., 2017).

In the studied lithiotid accumulations the recognised common clotted peloidal micrite is interpreted as automicrite (organomicrite *sensu* Reitner and Neuweler, 1995). Even if clotted peloidal micrite was limited to restricted areas (e.g., Fig. 4.19) its occurrence cannot be underestimated. This micrite type is well documented in *Lithiotis*-dominated TorA1 accumulation, where it was recognised in several samples. It was also identified in Contrada Dazio outcrop and in *Cochlearites*-dominated accumulation TorD2, TorE and TorF. Because of its common occurrence in the *Lithiotis*- and *Cochlearites* accumulations, the lack of clotted peloidal micrite in the other studied accumulations depends on diagenetic alteration, rather than no-primary deposition.

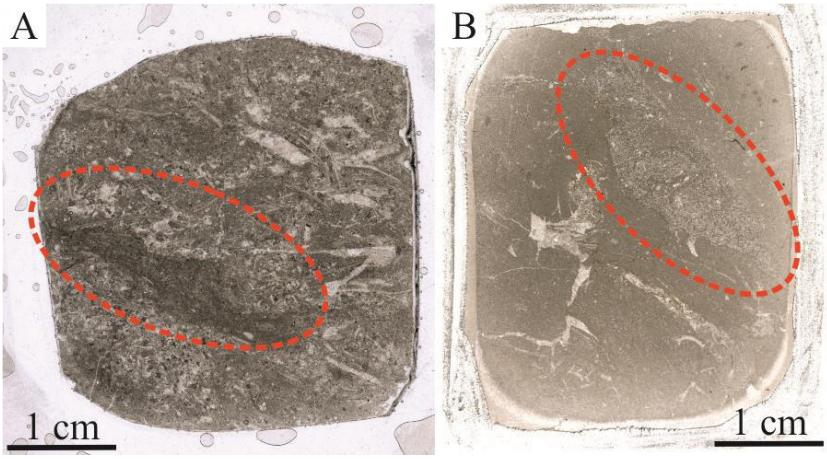

Figure 4.19. Preserved clotted peloidal micrite (automicrite) limited to small area (red circles). A) Sample E-C1 (TorE). B) Sample A1-8 (TorA1).

Assessment of the sedimentological role of the bacteria-like features must be considered related to the muddy matrix and skeletal and non-skeletal components. The likely role of microbial colonies is not limited to the production of carbonate mud but also in the stabilization of the soft substrate. Posenato and Masetti (2012) suggested the occurrence of microbial mats as stabilizing factors in high-steeped lithiotid accumulation flanks (30–40°). The muddy-substrate stabilization is favoured by the frequent occurrence of the microencruster *Thaumatoporella parvovesiculifera* in the *Lithiotis*- and *Cochlearites*-dominated accumulations. *T. parvovesiculifera*, recognised in several samples of the Toraro Mt., Rotzo and Contrada Dazio accumulations, occurs as (1) elongated encrusting thick-walled specimens and (2) irregular lobate bubble-shaped morphologies. The morphotype 1 can be interpreted as forming on the crust surface; the morphotype 2 can be interpreted as a diagenetic alteration of sediment-dwellers forms (Schlagintweit, 2013). The role of *T. parvovesiculifera* as microencruster and their occurrence in microbial facies is well known (e.g., Shiraishi and Kano, 2004; Spalluto, 2011; Graziano, 2013).

The microbial occurrence seems to be more frequent in the *Cochlearites* accumulations than in the *Lithiotis* one (Fig. 4.20). A key factor in cyanobacterial sheath calcification is the carbonate saturation state (e.g., Pentecost, 1981; Kempe and Kazmierczak, 1994; Saint Martin, 2010). During the Phanerozoic, periods with bacteria abundance broadly correspond to intervals when seawater carbonate saturation state is estimated to have been elevated (Riding and Liang, 2005). The occurrence of sparse bacteria individuals is not exceptional in the Rotzo Formation (Fig. 4.4). *Rivularia*-like individuals (i.e., *Cayeuxia*) are reported by several authors in Italian and Moroccan outcrops (Borasio, 1999; Coletta, 2012; Brame et al., 2019; Fig. 4.4). The relative more frequent occurrence of bacteria-like features in the upper part of the Rotzo Formation (i.e., Toraro Mt. succession) could be explained with general decrease in runoff which increments the marine water saturation state. The

widespread of larger lithiotid accumulations, dominated by *Cochlearites,* has been associated with the onset of oligotrophic ecosystem, characterized by low and stable nutrient supply, a general lowest water turbidity and enhanced water turbulence (Fugagnoli, 2004; Fig. 4.20). Reduced terrestrial influx can also be hypothesised along with an antiestuarine water circulation which could favoured the development of this large-scale sedimentary bodies (e.g., Fugagnoli, 2004). In the upper part of the Formation, the onset of fully marine condition evidenced by high diversity in larger foraminifera (Fugagnoli, 2004) is also confirmed by the presence of type 3/4 oncoids (TorB; Védrine et al., 2007) and by the higher occurrence of *T. parvovesiculifera.* In particular, *T. parvovesiculifera* is generally absent/very rare in the TorA1 (*Lithiotis*-dominated accumulation) where bacteria-like structures are less frequent, whilst in Contrada Dazio outcrop (occurring towards the *L. compressa* Z.; Chapter 3; Brandolese et al., 2019) and generally in *Cochlearites*-dominated accumulations (*L. compressa* Z.) its abundance increases, confirming the correlation between these forms and the onset of fully marine conditions (Fig. 4.20). The assemblages, including *Thaumatoporella parvovesiculifera* and moderately diversified assemblage of foraminifera and associated microfossils, are in fact typical of a shallow-marine, lagoon setting within normal salinity and clear water (Hughes, 2013). The development of more stable marine conditions is even confirmed by the occurrence of rare fragmented *Palaeodasycladus* sp. in Passo Vezzena outcrop and in TorF (Toraro Mt.; Fig. 4.20).

The relative higher microbial activity both in *Cochlearites* and *Lithiotis* accumulations can be related to shell density. Where shell density is lower or variable (see Chapter 3 and Brandolese et al., 2019 for further details), as in the *Cochlearites* flanks (TorF and TorE) or in the *Lithiotis* core (i.e., Contrada Dazio), the occurrence of bacteria-like features is higher. *Lithiotis* core and *Cochlearites* flanks are the more developed conspicuous accumulation parts. These are distinguished by high mud occurrence suggesting the likely role of microbial colonies in the micrite production. The relatively higher shell density in *Cochlearites* accumulation core and in *Lithiotis* accumulation flanks suggests better ecological conditions for the bivalve development. Abundant fecal pellets indicate a stable nutrient supply and good oxygen level on the bottom (e.g., Martínez et al., 2014).

In the *Lithioperna*-dominated accumulation (Campoluzzo Mt. outcrop), abundant and well preserved fecal pellet aggregates occur, while small benthic foraminifera are rare and less frequent. In the accumulation flanks, characterised by higher abundance and occurrence of bioclasts respect to the core, the high density of parautochthonous lithiotid shells could be subjected to a higher water turbulence and lower sedimentation rate (Chapter 3; Brandolese et al., 2019) which favoured the *Lithioperna* life on the bottom, increasing the fecal pellet

production. The well-known *Lithioperna*-dominated accumulations, located in the *Orbitopsella* and *Lituosepta compressa* Zone (Posenato and Masetti, 2012), are distinguished by tabular geometry with densely packed shell-supported cores (e.g., Posenato and Masetti, 2012; Brandolese et al., 2019; Chapter 3). These accumulations, distinguished by a rigid framework, grew in higher hydrodynamic conditions than the other accumulations (e.g., Posenato and Masetti, 2012; Brandolese et al., 2019; Chapter 3) likely hampering the occurrence of bacteria-like structures and *T. parvovesiculifera*.

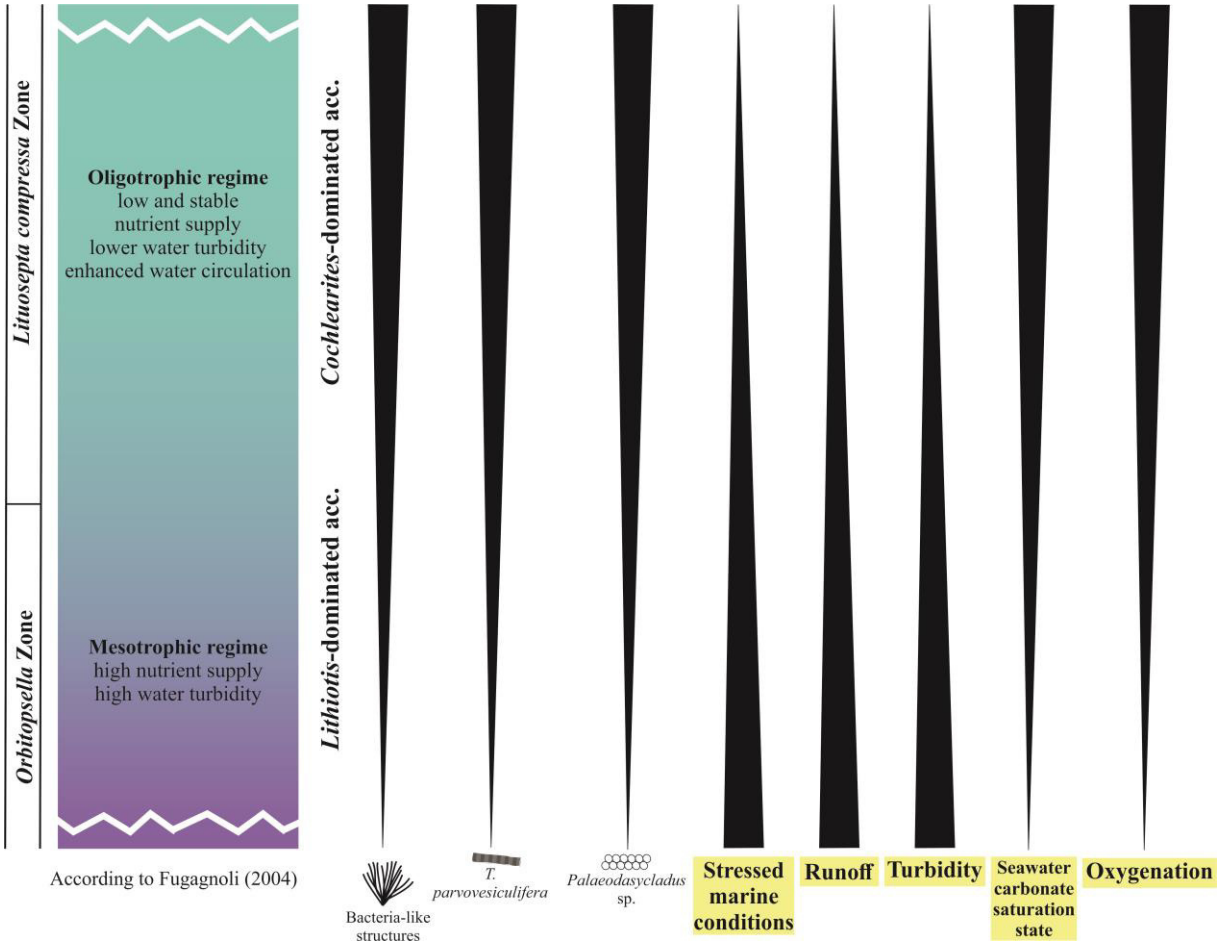

Figure 4.20. Summary of some skeletal and non-skeletal component distribution in the Rotzo Formation. The frequent occurrence of microbial features and *T. parvovesiculifera* confirms the onset of more stable marine conditions in the *Lituosepta compressa* Z. The fully development of lithiotid accumulations is registered in this biozone. The others studied microcomponents do not follow a specific trend. The ecological model suggested by Fugagnoli (2004) is reported on the left side. The evolution of most important environmental parameters is illustrated on the right side. See text for further details. In the *Lithioperna*-dominated accumulations bacteria-like structures and *T. parvovesiculifera* are completely absent.

The rarity of small benthic foraminifera (ubiquitarians r-strategies; Fugagnoli, 2004) in *Lithioperna* flanks and in the *Cochlearites* and *Lithiotis* core area is related to the higher water turbulence and lower sedimentation rate. The occurrence of opportunistic *Glomospira*-

textulariid assemblage (Plate 9) with lithiotids is also reported from the Tibet Region in the high-energy facies (Wignall et al., 2006).

The cover deposit shows slightly difference in skeletal abundance and frequency between *Lithiotis* and *Cochlearites* dominated accumulations (Fig. 4.13). The oncoidal packstone with type 3/4 oncoids observed in TorB along with a general increase in bacteria-like features and *T. parvovesiculifera* suggest fully marine conditions. The occurrence of abundant bioclasts could be associated with more intense transport events.

4.5.2. Paleoredox conditions: evidences from pyrite occurrences

Excluding TorA2, the studied samples yielded few pyrite specimens (< 25 specimens; Figs. 4.14–4.16; Appendix A.1).

The limonite founded in several samples represents oxidized or replaced pyrite framboids (e.g., Wilkin and Barnes, 1997; Figs. 4.14–4.16; Appendix A.1). The oxidation of pyrite framboids could occur with a general increase and extension of oxic conditions in the upper sediment layer. The role of bacteria in the pyrite framboid oxidation cannot be completely excluded (e.g., Mayayo et al., 2019). The alteration of pyrite framboids, including oxidation, during post-diagenetic phases could be included.

Other pyrite shapes, which cannot be related to paleoredox conditions, were identified in the studied lithiotid accumulations (Figs. 4.14–4.16). This is the case of the disc-shaped pyrite, never illustrated in literature. Disc-shaped pyrite occurs locally only in TorB and TorC, always in aggregates constituted by several microcrystals (Appendix A.1). Because SEM analyses of this disc-shaped pyrite revealed pyrite composition, pyrrhotite or other minerals, showing a similar shape, can be ruled out. The pyrite shape depends on the condition under it was formed. Two hypotheses can be considered. Wignall and Newton (1998) suggested that pyrite lump forms with their elongate, oval outline can be reminiscent of bacterial cells. The average size of these forms fit well with the measured disc-shaped pyrite. Biological influence was been considered in the other minerals formation, such as barite, resulted in similar size and morphologies (e.g., Griffith and Paytan, 2012). Considered the small size (~2–3 µm) and its shape, disc-shaped pyrite could be also ascribed to the initial phases of euhedral microcrystal precipitation. However, it cannot be considered as the initial phase of pyrite framboids because the size of each elements exceeds the usual framboidal microcrystallites. In fact, one of the distinct characteristics of pyrite framboids is the uniformity of their microcrystals (e.g., Rickard, 1970). The size of each microcrystallite is less than 1 µm, providing to the particles a colloidal behaviour. The looser packing which characterises the

disc-shape pyrite aggregates could be related to the lower volume/surface ratio. The volume/surface ratio is responsible of the free energy which is associated with the aggregation phase in pyrite framboids. The uniform size of each particle is likely due a single nucleation event, as in pyrite framboids. However, in the former case the larger size is likely due to a longer phase in which the solute ions concentration remains high, favouring the nucleation and the growth by diffusion. In fact, Wang and Morse (1995) reported that the morphology of pyrite crystals, formed at room temperature, is primarily controlled by the degree of supersaturation in the solution from which pyrite is precipitated. With the increasing supersaturation, pyrite morphology changes in the following order: cube - octahedron - spherulite. Some studied crystals show octahedral-roundish shape. Wilkin and Barnes (1997) reported also that poorly development of octahedral grains of pyrite is related to slower rates of pyritization.

Pyrite euhedral microcrystals were rarely observed in few samples (Figs. 4.14–4.16; Appendix A.1). Probably they have been formed by the direct precipitation of pyrite within the sediment at slower rate than framboids, becoming progressively more important in later diagenesis (e.g., Wignall et al., 2010). In this condition the sulphide has more time to react with the precursor mineral to form pyrite (Roychoudhury et al., 2003).

In rare samples (TorA1) few framboids exhibits granular and amorphous pyrite overgrowth (according to Morse and Cornwell, 1987; see Appendix A.1).

Small isolated and abundant crystallites were observed in few samples of TorB, TorC and TorA2 (Appendix A.1). Their occurrence can be related to insufficient time for nucleation and growth or hydrodynamic instability instead of reduced oxygen conditions.

In several studied samples, pyrite occurs as undefined morphologies, frequently with altered surface. The relatively higher occurrence of euhedral and undefined forms (called also "*nondescript solid masses*" by Wilkin et al., 1996) greater than 10 μm is common for dysoxic/oxic environments (Wilkin et al., 1996). On the contrary, this feature is never described for euxinic environments.

Most of the measured framboids are larger, indicating oxic conditions (Fig. 4.21). Few isolated samples from TorA2, TorC and TorB show more restricted (dysoxic) conditions (Fig. 4.21).

In TorA1 (Fig. 4.14A) pyrite framboids occur only close to the upper limit of the bivalve accumulation indicating lower dysoxic conditions. Anoxia or insufficient water oxygenation could be the causes for the demise of bivalve accumulations as in the southern Lessini Mts., where lithiotid accumulations occur in shallow and restricted lagoon or marsh

environment (Posenato and Masetti, 2012). In the TorA1, the reduced inferred water redox conditions were likely not enough negative for the demise of the accumulation.

The TorA2 is distinguished by higher abundance of pyrite forms. In the lower part the occurrence of larger framboids suggests oxygenated conditions even if locally decrease of oxygen level occurs (Fig. 4.15). The occurrence of well-defined euhedral crystals points to a diagenetic origin (see Appendix A.4 for further details). More reduced oxygen conditions were instead registered in the upper part of the accumulation. In the overlying marls (Fig. 4.15) the pyrite shapes point to more oxygenated conditions. The redox-condition changes registered by pyrite shapes is strictly associated with the accumulation dynamics (see Appendix A.4 for further details).

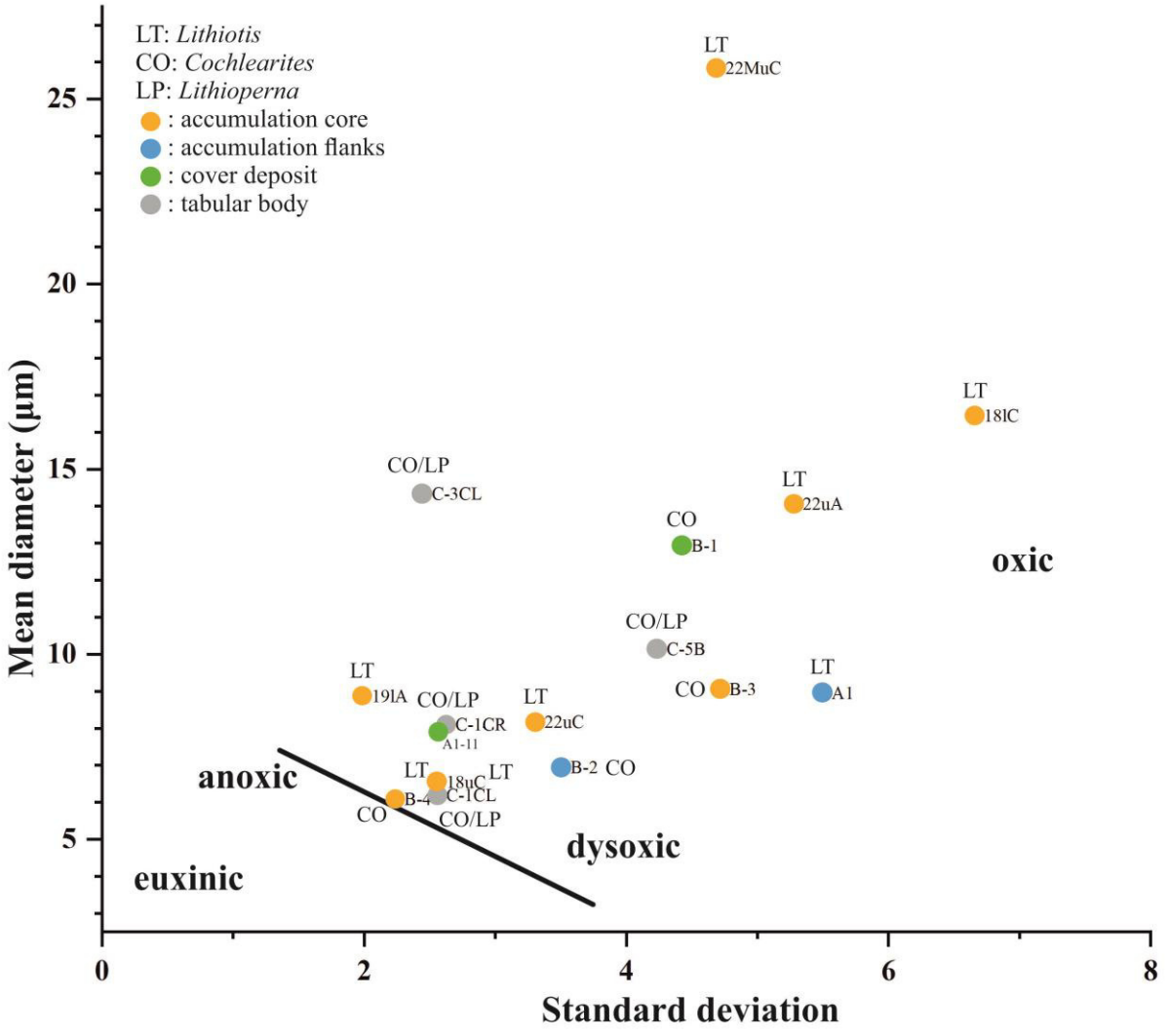

Figure 4.21. Mean diameter *versus* standard deviation plot of the studied samples. TorA1, A1 and A1-11; TorA2, 18uC, 18lC, 22uC, 22MuC, 19lA, 22uA; TorB, B-1, B-2, B-3, B-4; TorC, C-1CL, C-1CR, C-3CL, C-5B. Boundary between oxic-dysoxic and euxinic conditions according to Wignall and Newton (1998). For each sample the dominated genus is also reported. CO/LP points to *Cochlearites*-dominated accumulation with subordinate *Lithioperna* shells. Further details in text and in Appendix A.1.

In TorB lower dysoxic conditions were recorded both in the accumulation flank and core areas (Fig. 4.14B). The cover deposit, characterised by high fragmentation and disarticulation of the bioclasts, yielded larger pyrite framboids indicating more oxygenated conditions and high-water energy. TorB accumulation is constituted by unusual small-sized *Cochlearites* shells. The shell density is relatively high both in the flanks and in the core (Chapter 3; Brandolese et al., 2019). The reduced size of lithiotid shells could be associated with strongest spatial competition (higher shell density) and the occurrence of low dysoxic condition. This accumulation registered the earliest *Cochlearites* appearance in the Toraro Mt. section therefore the reduced shell size could be also related to evolutionary reasons (Posenato and Masetti, 2012).

In tabular accumulation (TorC) the analysed samples suggest locally changes in redox conditions (Fig. 4.16A). These changes could depend on the laterally extension of the bivalve accumulation. In fact, reduced oxygen conditions indicated by smaller pyrite framboids, were detected only in few portions and these conditions did not influence the bivalve growth itself (up-right life position; e.g., Kershaw et al., 2018) rather the life in/on the sediment/water interface. In fact, no small benthic foraminifera and no bacteria-like features were found in this accumulation. The absence of pyrite in the cover deposit is probably due to the onset of more oxygenated conditions as confirmed also by the occurrence of more small benthic foraminifera, bacteria-like structures and *T. parvovesiculifera*.

The total absence of pyrite in the TorE can be associated with the decrease (or complete absence) of the factors promoting the pyrite formation such as organic matter, sulphate and highly reactive iron. According to the results on skeletal and non-skeletal components distribution, decrease in terrestrial influx could be suggested in the upper part of the Rotzo Fm contributing to the reduction of organic matter and reactive iron supply. The low occurrence of organic matter can also be confirmed by the light colour of the limestone even if the major constrain in the pyrite crystallization can be the absence of iron. In fact, in the TorE abundant barite was identified (Fig. 4.11G). Barite microcrystals precipitated in several oceanic settings and at least four general modes of barite formation were recognised (Griffith and Paytan, 2012). According to microcrystal size and morphology, barite occurring in TorE is diagenetic or hydrothermal. Diagenetic barite precipitates during post-deposition diagenetic processes usually through a dissolution-reprecipitation process. The dissolution of barite mediated by sulphate reduction in sediments provides barium (Ba) for the following re-precipitation of barite when the Ba-rich pore fluids interact with pore water rich sulphate at the redox boundary within the sediments (Griffith and Paytan, 2012). Hydrothermal barite precipitates from Ba-rich fluids associated with volcanic hydrothermal activity. Due to

extensional fault and fractures, these hydrothermal fluids reached the sea floor where they mix with seawater, enriched in SO_4^{2-} precipitating barite (Griffith and Paytan, 2012). No evidences of coeval hydrothermal activity were observed in the studied area. Barite formation can confirm the likely lowest occurrence of iron (highly reactive iron) responsible for the pyrite formation. Even if SO_4^{2-} is abundant in seawater, its presence can be associated also to the decay of organic matter after burial.

Gradients in oxygen levels could be also reflected by changes in benthic foraminiferal assemblages as already proposed for the Rotzo Formation (Fugagnoli, 2004). However, some points must be taken into consideration in order to use fossils benthic foraminifera as paleoredox and in general as paleoenvironmental indicators.

Several taphonomic processes, such as transport, test destruction and dissolution, bioturbation, and life processes could affect the composition and preservation of fossil benthic foraminiferal record (see review in Murray, 2006). These processes can be responsible for the decrease of absolute number of tests and of the species diversity (Smith et al., 1987).

Moreover, fossil assemblages contain time-averaged signals, which could mostly be driven by contrasts in (short-term) environmental variations (Nguyen et al., 2009, and references therein).

In the studied accumulations, the larger benthic foraminifera are sometimes fragmented and abraded suggesting a transport, even weaker, which could hamper a complete separation between flanks and core. Excluding *Orbitopsella* sp., which is the dominating genus in the middle part of the Rotzo Fm where *Lithiotis* accumulations flourished allowing an easy identification, the low preservation state frequently hindered the taxonomic identification.

However, comparing *Lithiotis*- and *Cochlearites*-dominated accumulations (without distinction between flanks and core) slightly differences were noted (Fig. 4.13). Higher abundance of *Orbitopsella* sp. in *Lithiotis*-dominated accumulations is not unexpected since the taxon was highly adapted to mesotrophic regime with higher nutrient supply and higher water turbidity (e.g., Fugagnoli, 2004; Appendix A.5; Plate 10). Therefore, the relatively higher rate of micrite sedimentation and water turbidity which distinguished lithiotid accumulations could be only partially limiting factors in the development of the *Orbitopsella* assemblage. In *Cochlearites*-dominated accumulations, instead, the diversity of foraminiferal assemblages seems to be higher, as already proposed for the upper part of the Rotzo Fm (i.e., oligotrophic regime, lower water turbidity and enhanced water circulation; Fugagnoli, 2004; Appendixes A.7–A.13, A.15; Plate 10) while their abundance is reduced (Fig. 4.13).

However, further considerations should be ruled out due to above-mentioned taphonomic processes.

Regarding small benthic foraminifera, the observed taxa can be included in the *Glomospira/Planiinvoluta* spp. assemblage (see Fugagnoli, 2004 for further details) both in *Lithiotis*- and *Cochlearites*-dominated accumulations (Plate 9). These forms are very tolerant genera which occur in both high diversity foraminiferal assemblages as well as in oligospecific assemblages (r-strategies forms; Fugagnoli, 2004, and references therein). Even if slightly differences in small benthic foraminifera occurrence were registered between the lithiotid accumulation parts (i.e., core, flanks and cover; Fig. 4.13), their ubiquity and low occurrence hinder a clear definition of the ecological limiting factors.

However, further detailed investigations are necessary in order to understand the taphonomic processes affecting the foraminiferal faunal assemblages with the aim to use them in the paleoenvironmental interpretation.

4.6. Conclusions

This study (a) verified the occurrence of bacteria-like features to evaluate the microbial role in the geometry of the lithiotid accumulations and early mud stabilization, and (b) examined the occurrence of pyrite shapes to assess the redox conditions during the lithiotid accumulation growth. Well-exposed lithiotid accumulations were analysed in detail in terms of main skeletal and non-skeletal components, bacteria-like features, occurrence of pyrite and framboids.

The abundant peloids characterising the accumulations were pseudo-faeces in origin, related to bivalve occurrence. Only in *Lithioperna* accumulation flanks peloids are rare. This is related to the higher water turbulence of the depositional setting.

In *Lithiotis* and *Cochlearites* accumulations rare micritization and high sedimentation rate are evidenced by the rarity of pelletoids (micritized grains) and of destructive and constructive cortoids (destructive envelope for micritization; constructive envelope for encrustation). Consequently, the bivalve shells were prone to be rapidly buried.

The microbial activity produced coated grains and thin micritic laminae which stabilised the soft substrate on which the lithiotids grew. This activity seems to be more frequent where the shell density is lower, namely in the *Cochlearites* accumulation flanks and in the *Lithiotis* accumulation core. The microbial activity was able to produce an earlier stabilization of the mud facilitating the accumulation growth with respect to the surrounding area. Unlike the latter genera, *Lithioperna* generates tabular bodies.

Pyrite occurs with low number of specimens (<25) per samples. Altered pyrite, limonite, disc-shaped pyrite, barite and Fe-oxides were also recognised.

In the *Cochlearites* accumulation core the sediment/water interface was lower dysoxic to oxic. The *Lithiotis* accumulation core grew in fully oxic conditions.

The accumulation flanks for both taxa record oxic-dysoxic conditions. The deposits overlying the lithiotid accumulations formed under oxic conditions.

The relative increase in occurrence of bacteria-like features and calcareous green algae (*Thaumatoporella parvovesiculifera* and *Palaeodasycladus* sp.) upwardly in the Rotzo Formation points to a general decrease in water runoff and an increase in marine water saturation state.

In the studied areas the stratigraphic distribution of the lithiotid accumulations in the Rotzo Formation shows that the *Lithiotis* accumulations decrease in occurrence upwardly, while the *Cochlearites* ones increase. This trend reflects a paleoecologically gradient from more stressed marine conditions to fully marine oxygenated settings, where the benthic assemblages flourished.

4.7. Plates

Plate 1

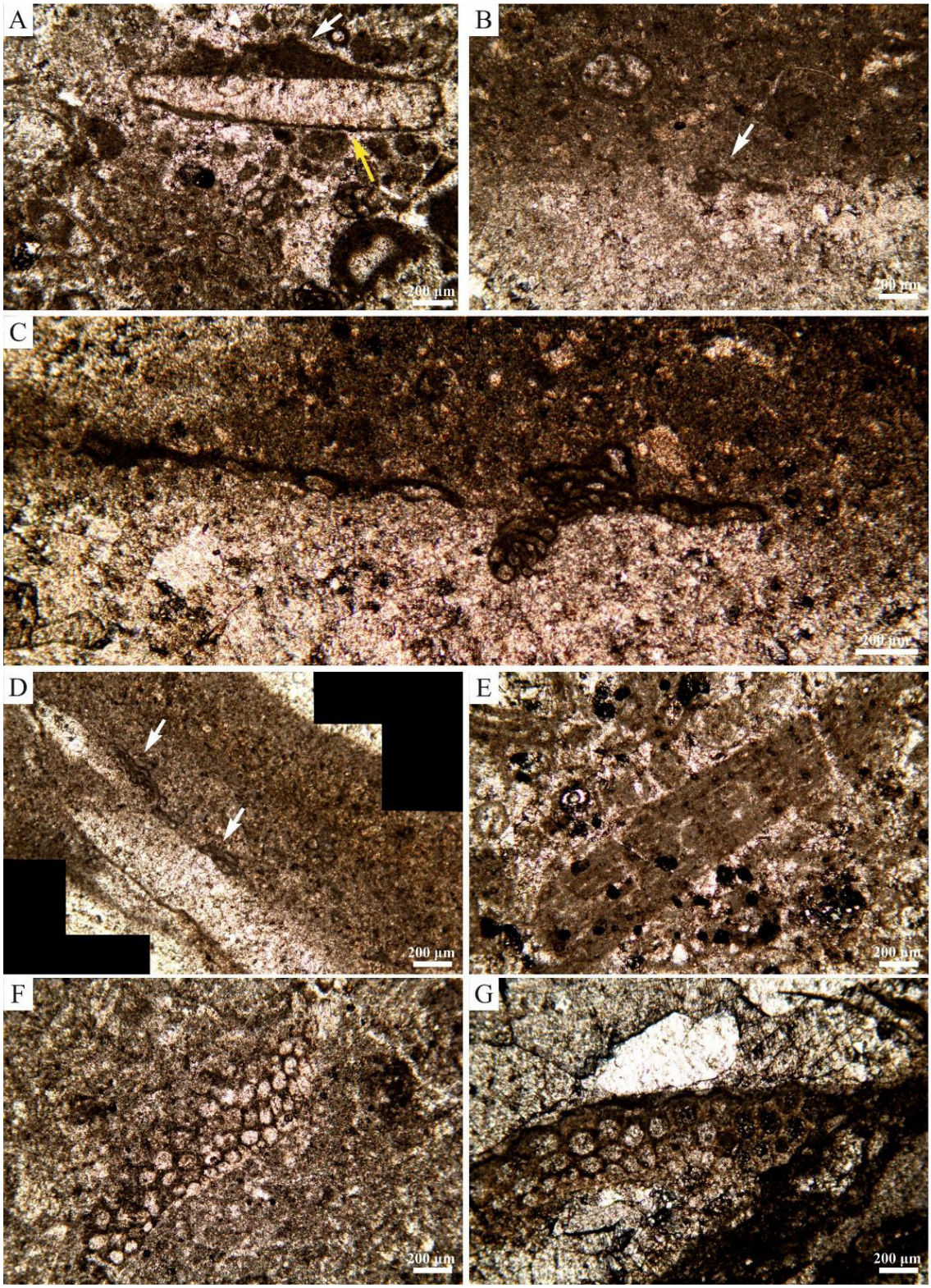

A) Cortoid with constructive (white arrow) and destructive envelope (yellow arrow). Sample C-1B (TorC). **B)** Encrusting organism (white arrow). Sample Ro-9 (Rotzo). **C)** Encrusting foraminifer and superimposed micritic laminae on lithiotid shell (distort stitched microphotograph). Sample Ro-9 (Rotzo). **D)** Encrusting foraminifer (white arrows; distort stitched microphotograph). Sample Ro-7 (Rotzo). **E)** Longitudinal section of a coprolite. Sample C-1B (TorC). **F)** Fragmented *Palaeodasycladus* sp. (Pia, 1920) Pia, 1927. Sample F1-1 (TorF). **G)** Fragmented *Palaeodasycladus* sp. (Pia, 1920) Pia, 1927. Sample Ve3-14 (Ve3).

Plate 2

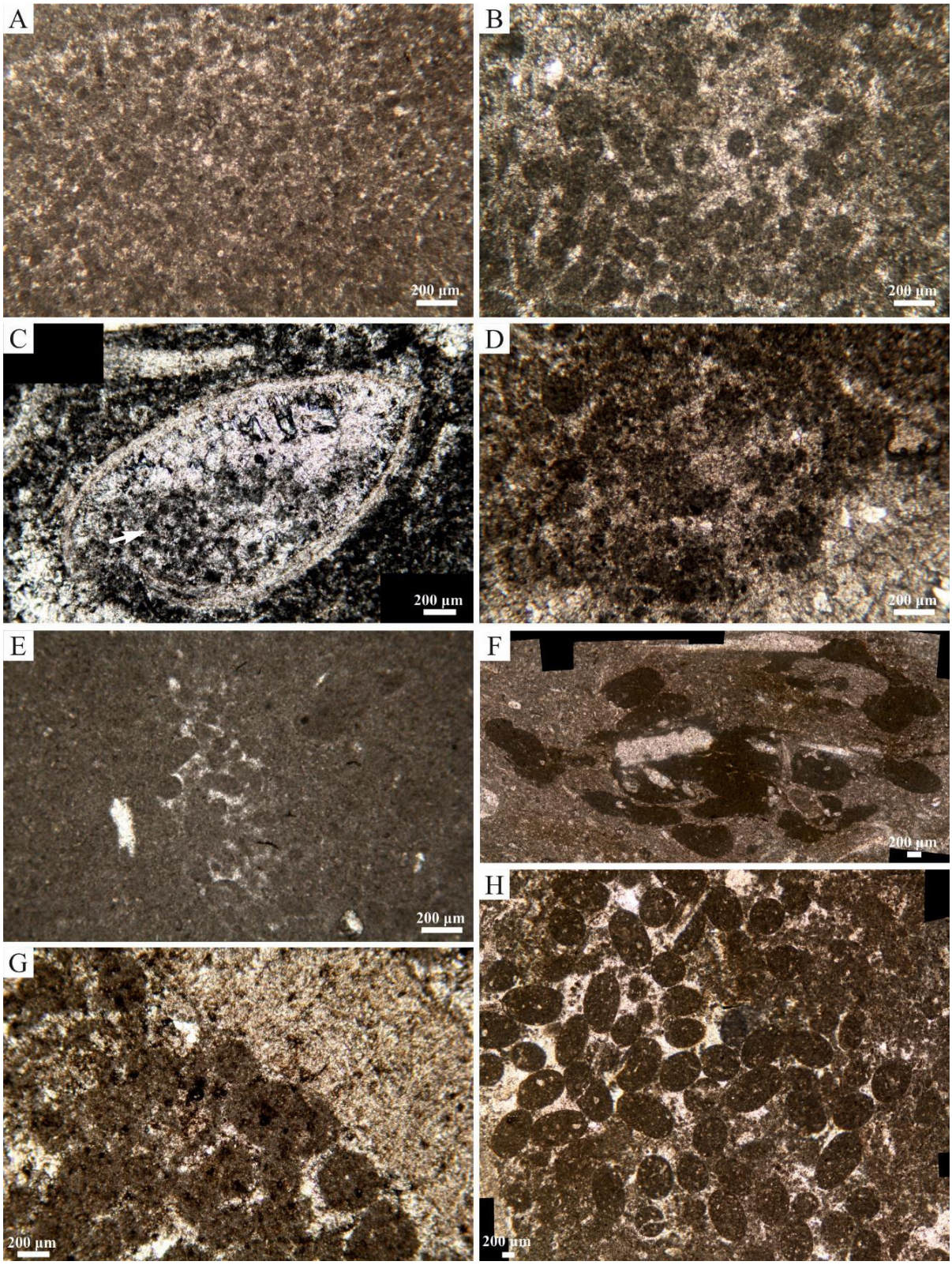

A) Peloids. Sample A1-7 (TorA1). **B)** Fecal pellets. Sample Da-8 (Contrada Dazio). **C)** Microbial peloids with fuzzy outlines in intraskeletal cavity (white arrow; distort stitched microphotograph). Sample E-C5 (TorE). **D)** Small clotted peloids. Sample Da-15 (Contrada Dazio). **E)** Fecal pellet aggregate (distort stitched microphotograph). Sample D2-BT (TorD2). **F)** Larger dark peloids: fecal pellets or pelletoids? Sample Ve3-8 (Ve3). **G)** Larger peloids: fecal pellets (undeformed stitched microphotograph). Sample E-C5 (TorE). **H)** Fecal pellets aggregate (undeformed stitched microphotographs). Sample Cm-1-1 (Campoluzzo).

Plate 3

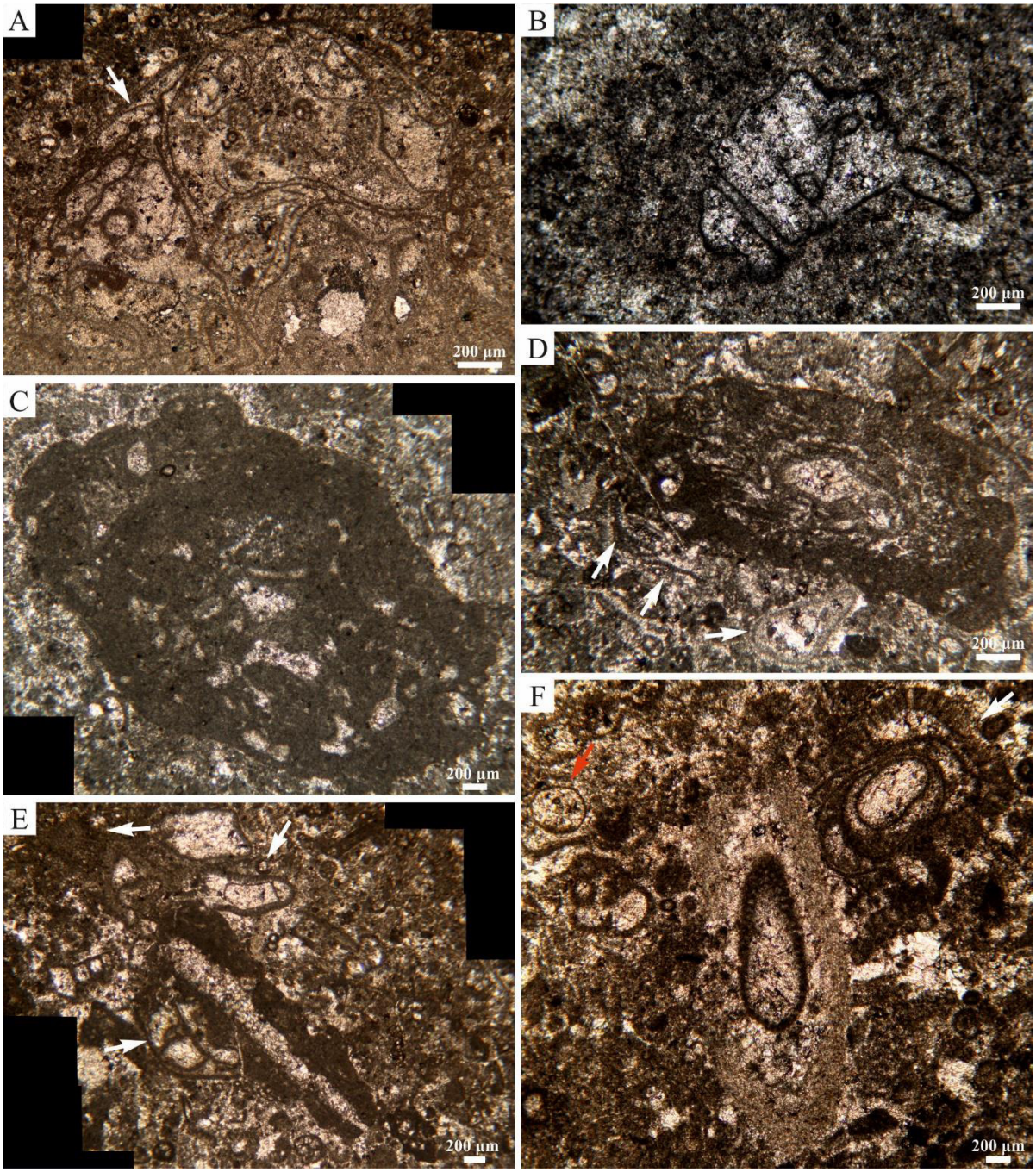

A) *Thaumatoporella parvovesiculifera* (Raineri, 1922), irregular roundish specimen with daughter colonies (white arrow; undeformed stitched microphotographs). Sample C-OC (TorC). **B)** *T. parvovesiculifera* (Raineri, 1922), irregular roundish specimen with daughter colonies. Sample Da-2 (Contrada Dazio). **C)** Oncoid type 3/4, with a nucleus not well defined (distort stitched microphotograph). Sample C-OC (TorC). **D)** Oncoid with meshwork-like structure as cortex (type 3/4). White arrows point to *T. parvovesiculifera* and irregular roundish specimen. Sample C-OC (TorC). **E)** Oncoid type 3/4. Fragments and irregular roundish specimen with daughter colonies of *T. parvovesiculifera* (Raineri, 1922) (white arrows) (distort stitched microphotograph). Sample C-OC (TorC). **F)** Oncoid not well-defined (distort stitched microphotograph). The white arrow points to an irregular roundish specimen while the red one to a cyst of *T. parvovesiculifera* (Raineri, 1922). Sample C-OC (TorC).

Plate 4

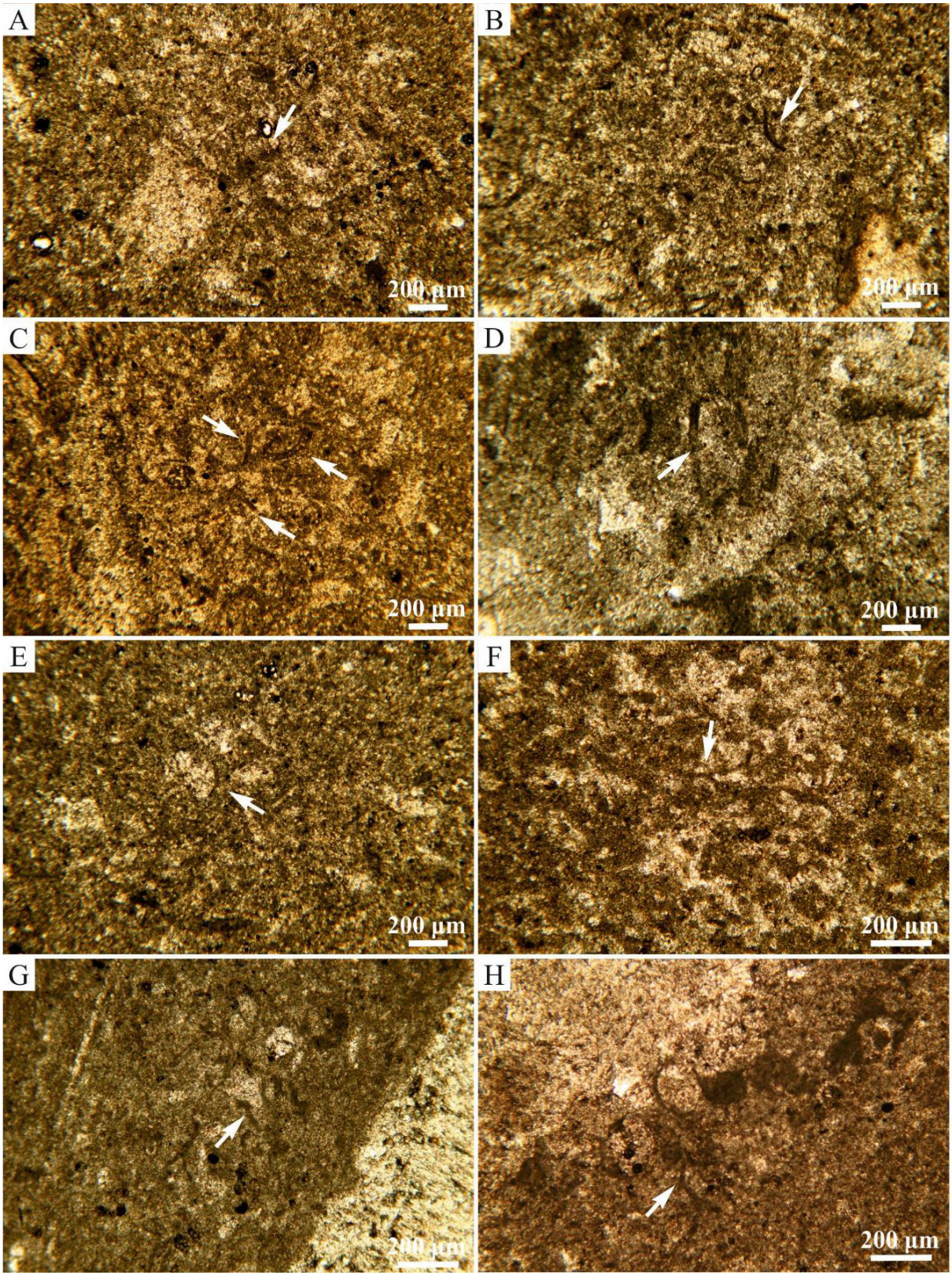

Girvanella-like organism variability (white arrows). **A)** Sample Da-19 (Contrada Dazio). **B)** Sample Da-32 (Contrada Dazio). **C)** Sample D2-BT (TorD2). **D)** Sample Da-2 (Contrada Dazio). **E)** Sample Da-18 (Contrada Dazio). **F)** Sample A1-4 (TorA1). **G)** Sample D2-1I (TorD2). **H)** Sample Da-20 (Contrada Dazio).

Plate 5

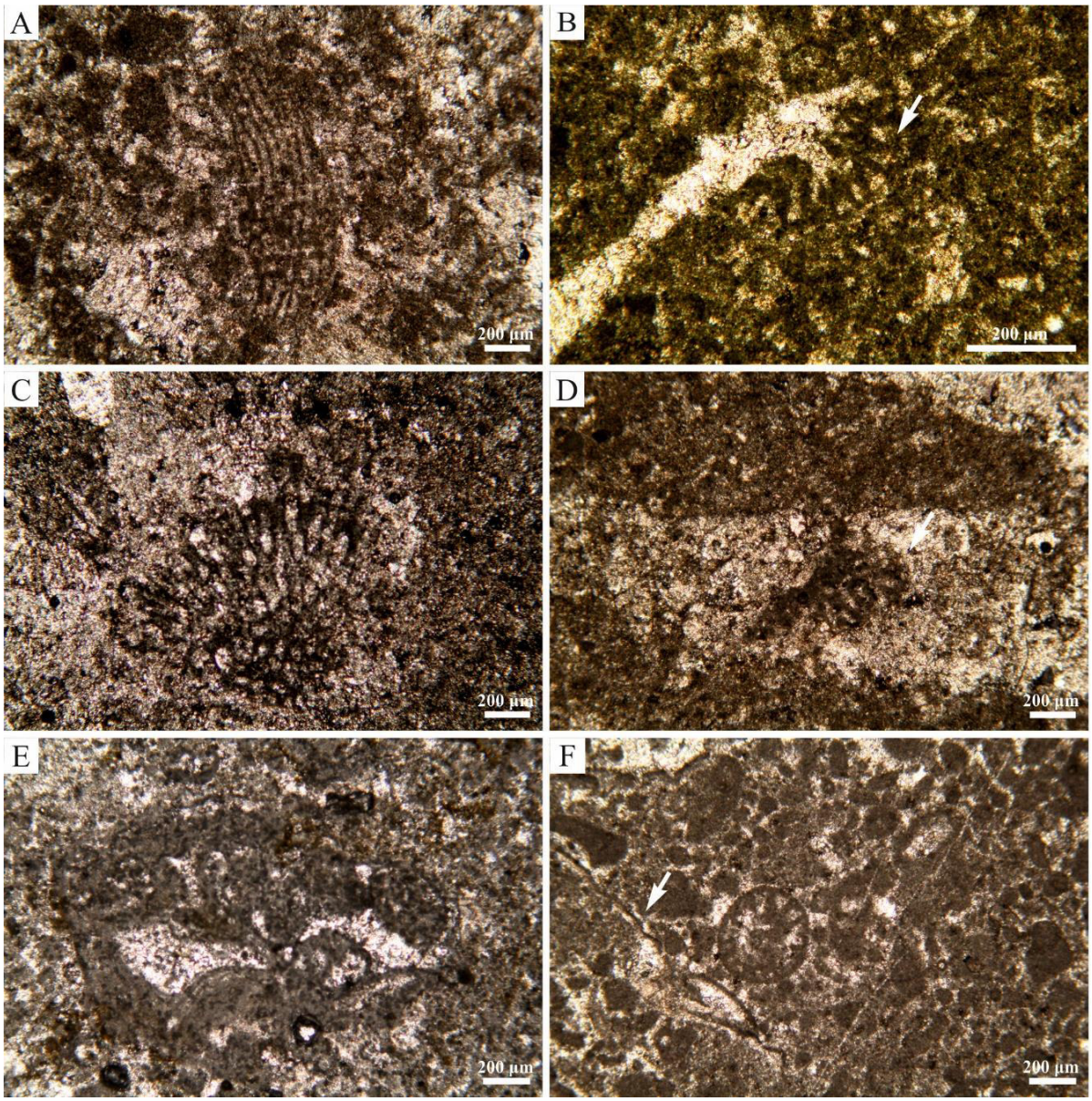

A) *Rivularia* like-structure. Sample A1-9 (TorA1). **B)** *Rivularia* like-structure (white arrow). Sample F2-3 (TorF). **C)** *Rivularia* like-structure. Sample Da-16 (Contrada Dazio). **D)** *Rivularia* like-structure (white arrow). Sample A1-1 (TorA1). **E)** Bacteria-like feature, likely *Tubiphites*-like organism distinguished by internal cavity, pear-shaped, filled with cement and a thick envelope of micritic not well-defined lamination. Sample C-1O (TorC). **F)** Micritic laminae (white arrow). Sample D2-BT (TorD2).

Plate 6

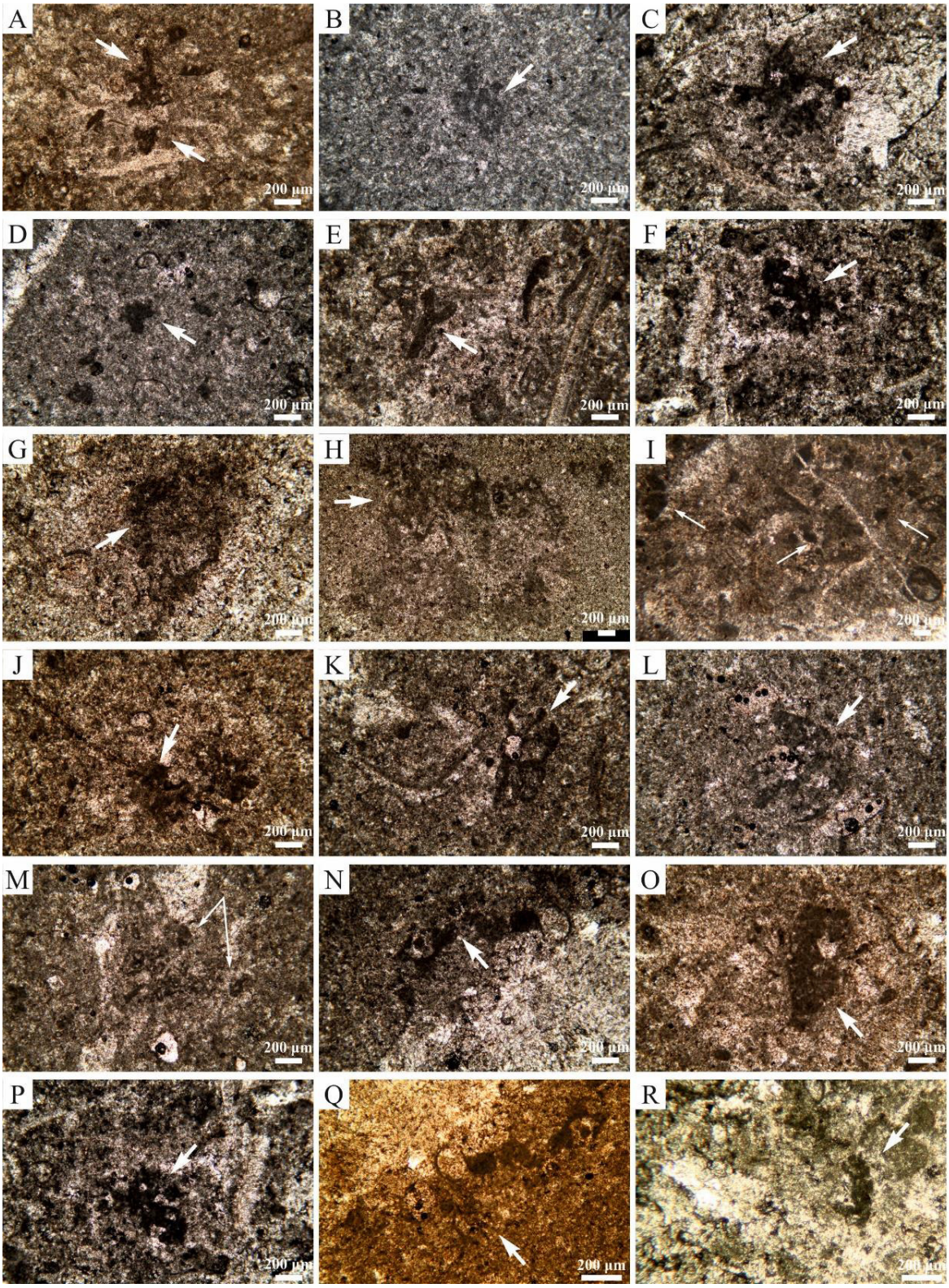

Dark micritic clotted structures variability (white arrows). Several specimens show a dendritic shape, likely bacteria-like organisms. **A)** Sample F1-1 (TorF). **B)** Sample F1-2 (TorF). **C)** Sample E-1C (TorE). **D)** Sample F1-2 (TorF). **E)** Sample D2-BT (TorD2). **F)** Sample E-1C (TorE). **G)** Sample Ro-8 (Rotzo). **H)** Sample Ve2-4 (Passo Vezzena). **I)** Sample Ve1-3 (Passo Vezzena). **J)** Sample Da-32 (Contrada Dazio). **K)** Sample Da-34 (Contrada Dazio). **L)** Sample Da-19 (Contrada Dazio). **M)** Sample Da-13 (Contrada Dazio). **N)** Sample Da-20 (Contrada Dazio). **O)** Sample Da-32 (Contrada Dazio). **P)** Sample E-1C (TorE). **Q)** Sample Da-20 (Contrada Dazio). **R)** Sample E-C5 (TorE).

Plate 7

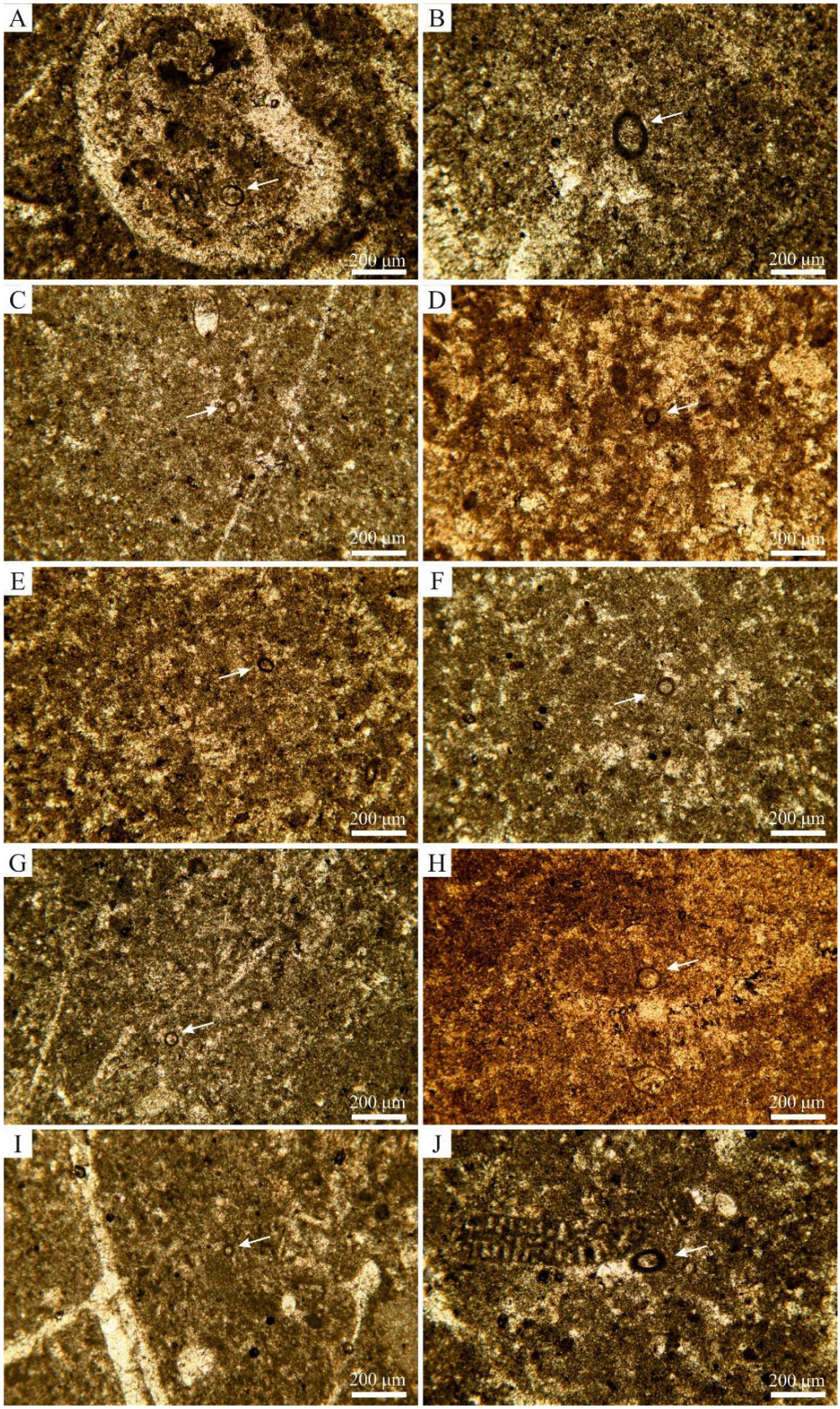

Ring-shaped micritized structures variability (white arrows). **A)** Sample Da-10 (Contrada Dazio). **B)** Sample Da-2 (Contrada Dazio). **C)** Sample A1-8 (TorA1). **D)** Sample A1-8 (TorA1). **E)** Sample A1-4 (TorA1). **F)** Sample A1-8 (TorA1). **G)** Sample F2-2 (TorF). **H)** Sample A1-8 (TorA1). **I)** Sample F1-4 (TorF). **J)** Sample A1-8 (TorA1).

Plate 8

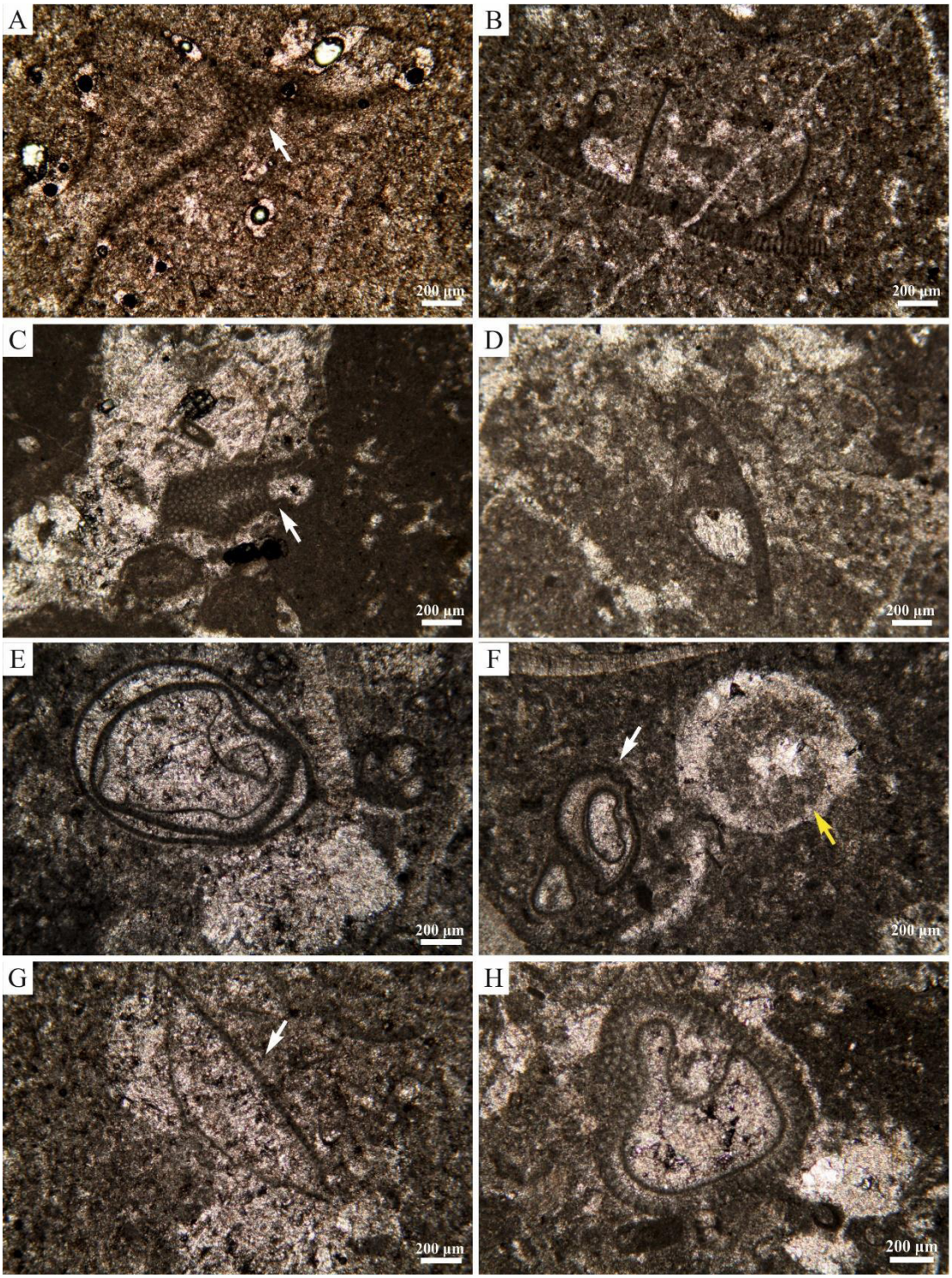

A) *Thaumatoporella parvovesiculifera* (Raineri, 1922), fragment (white arrow). Sample Da-28 (Contrada Dazio). **B)** *T. parvovesiculifera* (Raineri, 1922), fragments with well-defined perforate external wall. Sample F1-1 (TorF). **C)** *T. parvovesiculifera* (Raineri, 1922), fragments (white arrow). Sample C-B1 (TorC). **D)** *T. parvovesiculifera* (Raineri, 1922), fragments with well-defined perforate external wall. Sample F2-1 (TorF). **E)** *T. parvovesiculifera* (Raineri, 1922), irregular roundish specimen with daughter colonies. Sample D2-OB (TorD2). **F)** *T. parvovesiculifera* (Raineri, 1922), irregular roundish specimen with daughter colonies (white arrow). Yellow arrow points to microbial clotted peloids with fuzzy outlines in intraskeletal cavity. Sample F1-1 (TorF). **G)** Attaching specimen (*Thaumatoporella* ladders *sensu* Schlagintweit, 2013) with well-recognised perforated wall (white arrow) and thin, aporate, basal layer (see Schlagintweit, 2013 for further details). Sample E-2O2 (TorE). **H)** *T. parvovesiculifera* (Raineri, 1922), irregular roundish specimen with well-defined perforate external wall (distort stitched microphotograph). Sample C-OC (TorC).

Plate 9

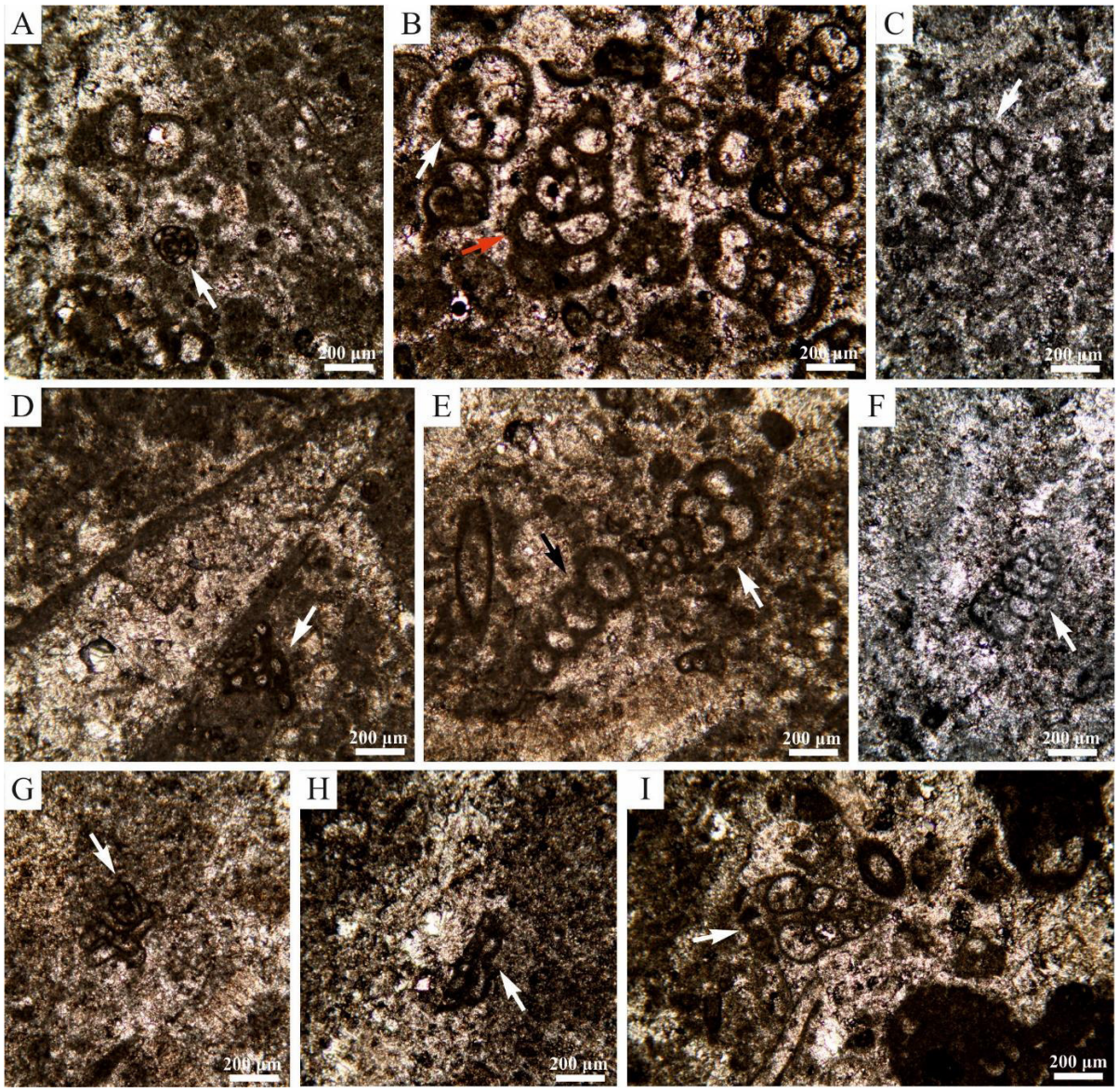

A) *Glomospira* sp. Rzehak, 1885 (white arrow). Sample C-OC (TorC). **B)** Textulariids (red arrow) and Valvulinids (white arrow). Sample C-OC (TorC). **C)** *Duotaxis metula* Kristan, 1957 (white arrow). Sample D2-BT (TorD2). **D)** ?*Planiinvoluta* sp. Leischner, 1961 (white arrow). Sample C-OC (TorC). **E)** *Textulariidae* (white arrow) and ?*Ammobaculites* sp. Cushman, 1910 (black arrow). Sample Ve1-1 (Ve1). **F)** Valvulinids (white arrow). Sample E-1B (TorE). **G)** *Planiinvoluta* sp. Leischner, 1961 (white arrow). Sample E-1O (TorE). **H)** *Meandrovoluta asiagoensis* Fugagnoli & Rettori, 2003 in Fugagnoli et al. (2003; white arrow). Sample E-2OB (TorE). **I)** *Siphovalvulina variabilis* Septfontaine, 1988 (white arrow). Axial section. Sample C-B1 (TorC).

Plate 10

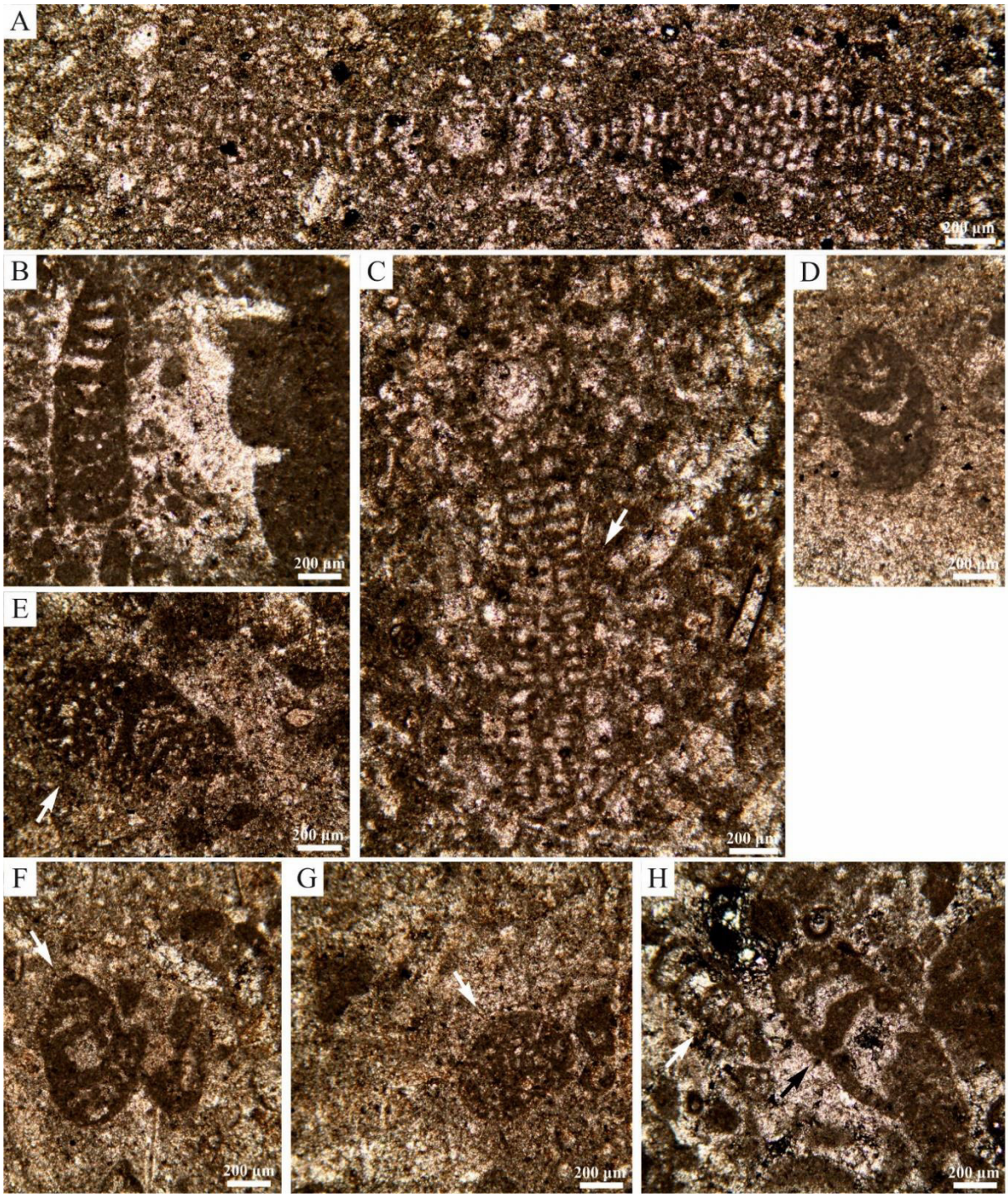

A) *Orbitopsella* sp. Munier-Chalmas, 1902 (distort stitched microphotograph). Sample A1-12 (TorA1). **B)** ?*Haurania deserta* Henson, 1948. Transverse/oblique section. Larger bioerosion traces on the right side. Sample Ve1-1 (Ve1). **C)** *Orbitopsella* sp. Munier-Chalmas, 1902 (stitched microphotograph; white arrow). Sample A1-4 (TorA1). **D)** ?*Amijiella amiji* (Henson, 1948). Longitudinal-oblique section. Sample Ve1-3 (Ve1). **E)** Unrecognizable larger benthic foraminifera (white arrow). Sample Ve1-1 (Ve1). **F)** Unrecognizable larger benthic foraminifera (white arrow). Sample Ve1-1 (Ve1). **G)** Unrecognizable larger benthic foraminifera (white arrow). Sample Ve1-1 (Ve1). **H)** ?*Haurania deserta* Henson, 1948 (black arrow). Transverse/oblique section. ?*Ammobaculites* sp. Cushman, 1910 (white arrow), equatorial to oblique section. Sample C-B1 (TorC).

Chapter 5

Lithiotid sclerochronology: assessment of growth patterns and paleoenvironmental implications

5.1. Introduction

Bivalves constitute a sensitive, high-resolution archive of past climatic and environmental changes (e.g., Jones, 1983; Marchitto et al., 2000; Richardson, 2001; Schöne and Surge, 2012; Schöne and Gillikin, 2013). Their shells record information on seasonal or inter-annual fluctuations of temperature, salinity, food availability and water quality as geochemical proprieties and variable growth rates (Kennish and Olsson, 1975; Jones et al., 1986; Wefer and Berger, 1991). These rates are the subject of sclerochronology, which includes studies on growth patterns in skeletal hard parts of corals, molluscs, and fish otoliths (e.g., Davenport, 1938; Clark, 1968) and biogeochemical variations (e.g., Gröcke and Gillikin, 2008).

Stable isotope geochemistry has become a key tool in paleoclimate and paleoenvironmental reconstruction (Gillikin et al., 2007). The oxygen isotope composition ($\delta^{18}O$) have been used to reconstruct both sea surface temperature and salinity (e.g., Jones et al., 1989; Weidman and Jones, 1994; Ingram et al., 1996; Dettman et al., 2004) while carbon isotope composition ($\delta^{13}C$) can theoretically give information on the dissolved inorganic carbon (DIC) and salinity (e.g., Mook and Vogel, 1968; McConnaughey and Gillikin, 2008).

Lithiotids were already a subject of sclerochronological (e.g., Accorsi Benini and Broglio Loriga, 1977; Chinzei, 1982; Accorsi Benini, 1985) and geochemical analyses (Fraser, 2002; Killam, 2018). In particular, Fraser (2002) focused on the lithiotid growth rate (*Lithiotis*, *Cochlearites* and *Lithioperna*), while Killam (2018) focused on *Cochlearites* and on the lithiotid calcification rate in order to verify the occurrence of symbiosis, as suggested in the past literature (e.g., Broglio Loriga and Neri, 1976; Accorsi Benini and Broglio Loriga, 1977).

The main three lithiotid genera, *Lithiotis*, *Cochlearites* and *Lithioperna*, show different geographic and stratigraphic distribution possibly related to different constraining ecological factors still unclear (e.g., Posenato and Masetti, 2012).

This chapter presents the results obtained from stable isotope ($\delta^{13}C$ and $\delta^{18}O$) and sclerochronological analyses performed on some extraordinarily preserved specimens of lithiotids (*Lithiotis problematica*, *Cochlearites loppianus* and *Lithioperna scutata)* along with some specimens of *Opisoma excavatum* and *Pachyrisma* (*Durga*) *crassa*, which are

frequently associated with the former ones. Accurate investigations on the bivalve growth pattern and geochemical variations allow to discuss the paleoenvironmental and paleoclimatic changes recorded locally by each studied specimen from the Pliensbachian part of Rotzo Formation.

5.2. Sclerochronology: general features

The bivalve growth is controlled by a combination of environmental, physiological and endogenous rhythms (e.g., Schöne and Surge, 2012; Schöne, 2013).

The periodic growth pattern is constituted by growth lines which separate the growth pattern into time slice of potentially equal duration, known as growth increments, and expression of fast growth (e.g., Schöne and Surge, 2012). The formation of growth lines requires a gradual decrease of biomineralization rates as well as a change in chemical and crystallographic proprieties (Schöne and Surge, 2012). When an organism cannot tolerate environmental stress (e.g., temperature), its growth ceases or decreases forming growth lines. Growth line formation is related to a higher amount of organic content relative to calcium carbonate.

The physiologic mechanism which drives the growth line formation is not still known but is associated with variations in the relative rate of formation of organic matrix and calcium carbonate. The main proposed hypothesis on the production of growth lines (e.g., Lutz and Rhoads, 1980) is related to the periodic dissolution of shell surface associated with the anaerobic respiration. This occurs when the valves are closed and produce acids which are neutralized by the dissolution of shell calcium carbonate. The insoluble organic matrix associated with dissolved carbonate is left as a residual sheet.

The growth increment thickness and deposition rhythm change as effect of physiological (e.g., reproduction, ontogeny) and environmental factors (tidal cycle, water temperature, storm events and food availability) which are frequently species-specific (e.g., Aubert et al., 2009, and references therein). Tides constitute one of the strongest factors regulating growth periodicity in intertidal and subtidal bivalves (Pannella, 1976). The rhythmic tidal fluctuations in sea level influenced water depth, food supply, mechanical agitation, pressure, temperature and light, all parameters whose variations affected the bivalve growth pattern (Pannella, 1976). The most frequent tidal periodicity of bivalve shells is represented by semi-diurnal, diurnal, weekly, fortnightly, monthly, semi-annual and annual growth increments (see Pannella, 1976 for further details). The occurrence of fortnightly bundles (~14 microgrowth increments) and monthly (~28 microgrowth increments) are

considered to reflect tide-controlled shell growth and consequently suggesting the daily accretion of shell carbonate (e.g., Walliser et al., 2018, and references therein). The annual growth increments are distinct by thick growth lines which usually are produced during prolonged intervals of slowed shell accretion and can potentially provide information on the inter-annual climate variability (e.g., Walliser et al., 2018).

5.3. The oxygen isotope record and water paleotemperatures

The oxygen isotope value of the shell carbonate is the most common proxies for water paleotemperature in bivalve sclerochronology. The $\delta^{18}O_{shell}$ is a function of the stable oxygen isotope composition of the ambient sea water ($\delta^{18}O_{seawater}$) and the temperature by which the shell was precipitated (Urey, 1948). In coastal areas, $\delta^{18}O_{seawater}$ varies geographically and seasonally and these variations often exceed the variability caused by temperature changes (Mook, 1970; LeGrande and Schmidt, 2006). This variability is driven by freshwater runoff and evaporation which cause $\delta^{18}O_{seawater}$ to correlate with salinity variations (de Winter, 2019).

Considering the paleoenvironmental setting of the Lower Jurassic Rotzo sedimentary succession (e.g., Clari, 1975; Posenato and Masetti, 2012), the main parameter that should be considered is the salinity fluctuations. In the tropical lagoon areas frequently characterized by large salinity fluctuations associated with variations of $\delta^{18}O_{seawater}$, the paleotemperature reconstruction could be particularly complicated (Gillikin et al., 2005). The freshwater is enriched of ^{16}O and consequently the $\delta^{18}O$ values in the shells would be lower. Salinity changes of 2‰ would correspond to a shift in the oxygen values of ~0.5‰ (Fairbanks et al., 1997) which corresponds to about 2–3°C. Moreover, the variability in the reconstructed temperature excursions would be amplified (Crippa, 2015). This situation is accentuated in monsoonal climate where the warm season shows strong rainfalls leading to a decrease in surface salinity (lower $\delta^{18}O$ values), while the cold season is comparatively dry with a higher salinity (higher $\delta^{18}O$ values) (e.g., Alberti et al., 2017). This climate regime, which was also suggested for the Rotzo sedimentary succession (e.g., Bassi et al., 1999; Posenato et al., 2013b; Neri et al., 2017), could therefore lead to an overestimation of the seasonality (Brigaud et al., 2008).

The role of evaporation seems more negligible due to the occurrence of coal lens in the studied area (Fig. 5.1; Posenato and Masetti, 2012). In fact, coal deposits represent the most unequivocal evidence of humid weather because their formation required persistent wet

ground condition suggesting year-round rainfall and/or low evapotranspiration rates (Hallam, 1984; Parrish et al., 1982).

Ideally, if shells are formed in normal marine salinity conditions, temperature assessing is based on the oxygen isotope composition of ambient water during shell formation. For ancient environments, $\delta^{18}O$ of seawater is not always available and therefore standard values are used. Considering that $\delta^{18}O_{seawater}$ varying during the Phanerozoic the oxygen isotope composition trend is not linear but instead a band (Veizer et al., 1999). Nevertheless, since the Jurassic is considered as ice-free period, $\delta^{18}O$ of Jurassic seawater ($\delta^{18}O_{seawater}$) is estimated as -1‰ VSMOW (Shackleton and Kennett, 1975). This value might be a considerable simplification, considering the latitudinal gradient of $\delta^{18}O_{seawater}$ in modern oceans (LeGrande and Schmidt, 2006). A similar scenario was also supposed for the Jurassic (Roche et al., 2006; Alberti et al., 2019a). In fact, the average $\delta^{18}O_{seawater}$ value of -1‰ could be higher for the equatorial and lower for higher latitudinal areas (e.g., Alberti et al., 2019a). Consequently, the proposed paleotemperature would be shift towards higher values if, for instance, the temperature would be calculated with the $\delta^{18}O_{seawater}$ of 0‰ (ca. 4°C). In the tropical area the strong evaporation might be slightly higher at low latitude, increasing the reconstructed temperatures of few degrees. Martin-Garin et al. (2010) used a $\delta^{18}O$ value of -1.2‰ for their studied material from Morocco (at a palaeolatitude of 15°N), producing a shift of ~1°C towards lower temperature. Besides, even altering the $\delta^{18}O$ value for water, the overall temperature trend would not change.

5.4. The carbon isotope record

$\delta^{13}C$ values of the water and shells are influenced by various processes (Alberti et al., 2019a), and even specimens of the same horizon can sometimes show a large range of values (e.g., McArthur et al., 2007). The carbon isotope composition of bivalve shell carbonates primarily depends on dissolved inorganic carbon (DIC) in seawater (Mook and Vogel, 1968; McConnaughey et al., 1997; Gillikin et al., 2006; McConnaughey and Gillikin, 2008; Owen et al., 2008; Poulain et al., 2010). A direct relationship is reported between $\delta^{13}C_{DIC}$ and primary productivity: when primary production is high, the carbon reservoir is depleted in ^{12}C, showing an increase in $\delta^{13}C$ in the carbonate materials (e.g., Mook, 1970; Mook and Tan, 1991; Hellings et al., 1999).

The influx of low-salinity water enriched in ^{12}C (e.g., riverine input) induced a shift in in $\delta^{13}C_{DIC}$ (Poulain et al., 2010). Fluvial DIC is often isotopically lighter than oceanic DIC, due to the input of CO_2 derived from the decomposition of terrestrial plants. As rivers enter

the ocean, mollusc shells pick up the mixture of fluvial and marine DIC, and $\delta^{13}C$ shell reflects the mixture (e.g., Mook and Vogel, 1968; Gillikin et al., 2006).

Nevertheless, a disequilibrium between $\delta^{13}C_{shell}$ and $\delta^{13}C_{DIC}$ was observed in some bivalves (e.g., *Mytilus edulis*, Vander Putten et al., 2000). Vander Putten and co-workers suggested that this disequilibrium could be caused by kinetic and/or metabolic isotope fractionation effects (the so-called "vital effect"). As discussed by McConnaughey (1989a, b), the kinetic isotope fractionation effect is due to the simultaneous depletion of ^{18}O and ^{13}C associated with carbon and oxygen isotope fractionation during CO_2 hydration and hydroxylation kinetic effects generally affect both $\delta^{18}O$ and $\delta^{13}C$ and result in a good correlation between them (McConnaughey, 1989a,b). The metabolic isotope fractionation effect is translated in the decrease of $\delta^{13}C_{shell}$ as a consequence of an increase of respiration rate. In some bivalves, the increase in the respiration rate corresponds to the breeding period, and it followed by a decrease in $\delta^{13}C_{shell}$ after spawning. Furthermore, the minimum $\delta^{13}C_{shell}$ can be linked with maximum food availability, which induced a higher respiration rate. The influence of bivalve physiology on $\delta^{13}C_{shell}$ was already suggested in the past (Dillaman and Ford, 1982; Tanaka et al., 1986; McConnaughey et al., 1997; Lorrain et al., 2004; Gillikin et al., 2006; 2007; 2009; McConnaughey and Gillikin, 2008) as well as the incorporation of isotopically light metabolic carbon, derived from food into shell carbonate (e.g., Tanaka et al., 1986; McConnaughey et al., 1997; Wanamaker et al., 2007; Owen et al., 2008; Gillikin et al., 2006; 2007; 2009). However, the processes of metabolic carbon incorporation into the shell remain poorly known, and the estimation of metabolic carbon contribution to the shell appears highly variable between studies (Poulain et al., 2010, and references therein). For instance, in deep-sea molluscs, *Pecten maximus* and *Mytilus edulis* metabolic carbon contribution is lower than 10% (McConnaughey et al., 1997; Lorrain et al., 2004; Gillikin et al., 2006) while in freshwater unionid shells and in shallow marine *Mercenaria mercenaria* is between 25 and 40% (Gillikin et al., 2007; 2009). However, in some bivalves, as the giant clams of the genus *Tridacna*, $\delta^{13}C_{shell}$ sometimes remains relatively constant for decades (McConnaughey and Gillikin, 2008, and references therein; Yamanashi et al., 2016).

5.5. Materials and methods

Bivalve shells were collected from different localities and stratigraphic levels of the Rotzo Formation in the Trento Platform (Fig. 5.1). The analysed specimens come from the Lessini Mounts (Verona and Vicenza) and they were collected from marlstones beds, where

easy isolation of shells from the rocky matrix was possible. The studied material is deposited at the "Piero Leonardi" Museum of the University of Ferrara.

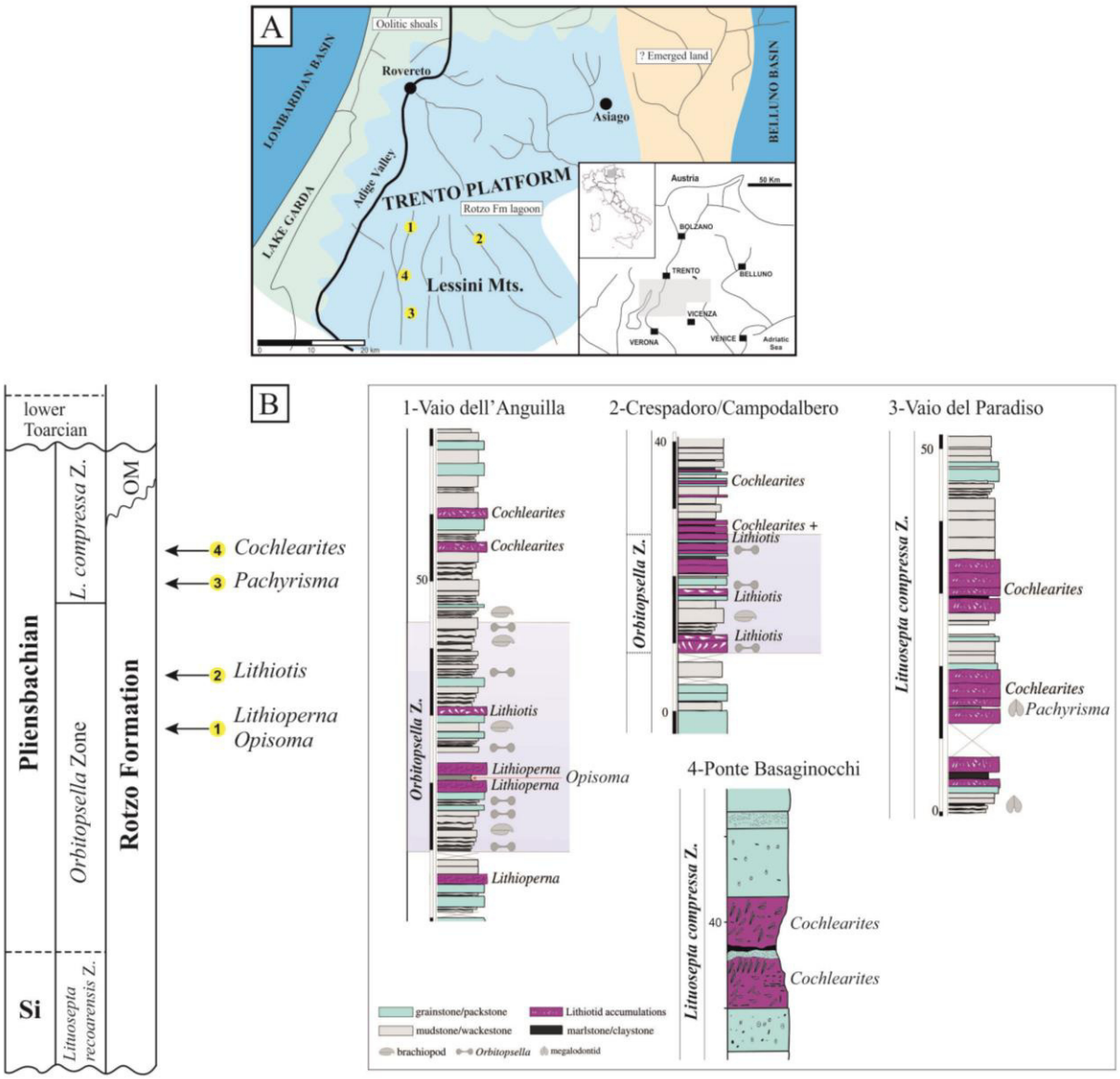

Figure 5.1. Geographic (A) and stratigraphic location (B) of the collected specimens in the Trento Platform (northeastern of Italy). 1, Ponte dell'Anguillara (Vaio dell'Anguilla, Verona); 2, Crespadoro/Campodalbero (Vicenza); 3, Vaio del Paradiso (Verona); 4, Ponte Basaginocchi (Verona). Palaeogeographic map modified from Posenato and Masetti (2012). The stratigraphic sections are modified from Posenato and Masetti (2012; Vaio dell'Anguilla, Crespadoro/Campodalbero and Vaio del Paradiso) and Clari (1975; Ponte Basaginocchi). Z., Zone; *L. compressa* Z., *Lituosepta compressa* Zone; OM, Oolite di Massone; Si, upper Sinemurian.

For stable isotopic analysis, seven bivalve specimens were chosen: one specimen of *Lithioperna scutata* (LP3; with two sections in different parts of the shell), one specimen of *Opisoma excavatum* (O1), two specimens of *Lithiotis problematica* (LT6, LT7), one specimen of *Pachyrisma* (*Durga*) *crassa* (P1) and two specimens of *Cochlearites loppianus* (CO1, CO2). According to the unusual shell morphology (Fig. 5.2; Appendix B.1), *Lithiotis*, *Cochlearites* and *Lithioperna* shells were cut perpendicularly to the growth pattern in the

posterior and anterior wings (feather-like areas) detectable on the inner shell surface (Fig. 5.2). *Lithioperna* shell was also analysed in a nearly transversal section (profile *b* in Fig. 5.2). The shells of all the above cited taxa were not sectioned along the direction of maximum growth due to the pervasive diagenetic alteration which usually affects the inner shell portions. *Opisoma* and *Pachyrisma* were cut along the direction of maximum growth (Fig. 5.2). Because these last two specimens were fragmented and the ventral region was missing, the analysis focused on the cardinal area.

All the studied bivalves are characterised by the preservation of the original aragonitic shell. The reduced number of analysed individuals is due to the rare preservation of the original aragonite mineralogy during the diagenesis.

Before sampling and analysing for stable isotopes, diagenetic screening was conducted to evaluate the degree of shell preservation. The screening tests were SEM, cathodoluminescence and X-ray analyses. Even if these techniques sometimes do not work effectively (e.g., Fujioka et al., 2019, and references therein), applying multiple criteria could increase the significance of stable isotope results. Moreover, the correlation between the $\delta^{18}O$ and $\delta^{13}C$ values itself is a further indicator of diagenetic alteration.

Cathodoluminescence analysis (CL) was carried out on polished thin sections with cold luminescence microscope (Dipartimento di Fisica e Scienze della Terra, University of Ferrara). Carbonate luminescence depends on the molar ratio of iron and manganese (Fe/Mn). High Mn content in the calcite and aragonite lattice is an activator of luminescence, whereas Fe is a quencher (e.g., Garbelli et al., 2012). Mn is generally low in unaltered recent and fossil shells (e.g., Brand et al., 2003), where it could be preferentially incorporated during diagenesis (Brand and Veizer, 1980). The analysed thin sections were prepared following Mugridge and Young (1984).

Scanning electron microscope observations were performed with SEM Zeiss EVO 40 scanning electron microscope (CME of University of Ferrara) to verify the preservation of shell microstructures (see Appendix B.2). Small portions of each selected sample were polished and etched with HCl 5% for 15 seconds and coated with gold.

Fourteen powder samples for X-ray analyses were obtained using drill bits 1.8 and 0.5 mm in diameter. Usually, the outer whitish region largely corresponds to the pristine aragonite while the brownish inner region is represented by neomorphic calcite (e.g., Chinzei, 1982; Appendix B.3). The powder samples for the XRD analysis were collected both from the whitish and brownish part of *Lithioperna*, *Lithiotis* and *Cochlearites* shells in order to compare their preservation state (see Appendix B.3). Since *Opisoma* and *Pachyrisma* do not show any apparent evidence of diagenetic alteration, only one sample was collected from each

specimen (see Appendix B.3). The XRD analyses were performed with Phillips X'Pert-MPD PW3050 system at the Institute of Geology and Palaeontology, Tohoku University, Sendai, Japan.

Before sampling for isotope analysis, the selected specimens were washed with ultra-pure water and dried at room temperature for one night. Carbonate samples for the isotope analysis were drilled along a line of growth direction. Drill bits with diameters of 0.3 mm were used. A total of 23, 25, 56, 54, 45, 47, 212, and 102 powder samples were taken sequentially from the specimens LP3-a, LP3-b, O1, LT6, LT7, P1, CO1 and CO2, respectively. Stable isotope analyses of aragonitic shells were performed with a Thermo Scientific DeltaV Advantage mass spectrometer, coupled with a ThermoQuest Kiel III Carbonate Device, at the Institute of Geology and Palaeontology, Tohoku University, Sendai, Japan. Isotopic ratios were calibrated to the NBS-19 international standard relative to the Vienna Pee Dee Belemnite (VPDB). The analytical error of the instrument was ± 0.03‰ (1σ) for both carbon and oxygen isotopes based on replicate measurements of the laboratory references sample (JCp-1; Nakayama et al., 2008). Stable isotope values were reported according to distances from the origin (see Appendix B.4). Distances from the samples were measured from the centres of successive holes.

The most bivalves secrete the shell in oxygen isotopic equilibrium with the ambient water (e.g., Marchitto et al., 2000; Weidman and Jones, 1994). It is reasonable to assume that the same can be applied to the aragonitic shells of lithiotids. If so, the $\delta^{18}O_{shell}$ data can be used to calculate ambient temperature during growth using the following paleothermometry equation for biogenic aragonite of Grossman and Ku (1986) with a scale correction (from the VSMOW scale to the VPDB scale) of -0.27‰ (Dettman et al., 1999).

$$T\ (°C) = 20.60 - 4.34 * (\delta^{18}O_{shell} - (\delta^{18}O_{water} - 0.27))$$

Shell $\delta^{18}O$ and water $\delta^{18}O$ values are relative to the VPDB and VSMOW scale, respectively. The estimated palaeotemperature obtained from this equation requires knowledge of the $\delta^{18}O_{water}$ value during shell precipitation. For the ice-free period, like the Jurassic, the standard value -1‰ is typically assumed (Shackleton and Kennett, 1975). This standard value allows to compare our results to previous works. To evaluate the possible range paleotemperatures were also calculated for 0‰ and -1.2‰ (see Appendix B.4).

The growth pattern was observed in more specimens than those studied for geochemical analyses because the growth increments were not easily recognizable in all individuals (Appendix B.1). In fact, the analysis did not cover the entire shell sections, but it was focused on small shell portions showing distinct microgrowth lines (e.g., Walliser et al., 2018). In *Lithiotis*, *Cochlearites* and *Lithioperna*, the growth pattern was observed on shell

surface and in the posterior and anterior wings (Fig. 5.2; see also Appendix B.1). These features are less developed in *Opisoma* and *Pachyrisma*, hampered an accurate identification of growth increments on the external surface (see Appendix B.1). The bivalve shells were sectioned for sclerochronological analysis: perpendicular to the growth increments in the posterior and anterior wings (*Lithiotis*, *Cochlearites*, *Lithioperna*), and along the direction of maximum growth (*Opisoma*, *Pachyrisma*; Fig. 5.2). *Lithioperna* was also analysed on sections oriented perpendicularly to the inner shell surface (profile b in Fig. 5.2). To analyse shell growth increments, thin sections and acetate peels were made and observed in transmitted light with optical microscope Leitz Diaplan under 2.5x, 4x and 10x magnifications. Growth increment widths were measured on digital images of thin-sections and acetate peels using an image processing software. For *Lithioperna* the counted microgrowth increments exceed 180 units, which allow to implement spectral analysis in order to recognize periodic short-term growth dynamics. The analysis was conducted by continuous wavelet transformation set to Morlet wavelet (wavenumber = 6) using the PAST software (Hammer et al., 2001). In order to evaluate the 5% significance level (i.e., the 95% confidence interval) a univariate red-noise autoregressive lag-1 model was applied as a background spectrum (e.g., Walliser et al., 2018; Walliser et al., 2019).

The analysed samples are listed in Appendix B.1. The $\delta^{13}C$ and $\delta^{18}O$ data and inferred temperatures are listed in Appendix B.4.

The sclerochronological analysis was also conducted on the other two taxa, characterizing the Rotzo Formation: *Trichites* sp. and *Gervilleioperna* sp. These specimens were not included in geochemical analyses because only small fragments were available. Consequently, the results of the sclerochronological analysis are reported separately in Appendix B.5.

During the evaluation of preservation state (SEM observations) some articulated and well-preserved individuals of *Lithiotis problematica* allowed to analyse the occurrence and structure of the outer calcitic layer in this species and the free valve morphology. The comprehensive study is described in Appendix B.6.

Moreover, a juvenile specimen of *Lithiotis problematica* showed almost preserved internal shell corresponding to the likely chalky deposit. The detailed analysis of this individual is reported in Appendix B.7.

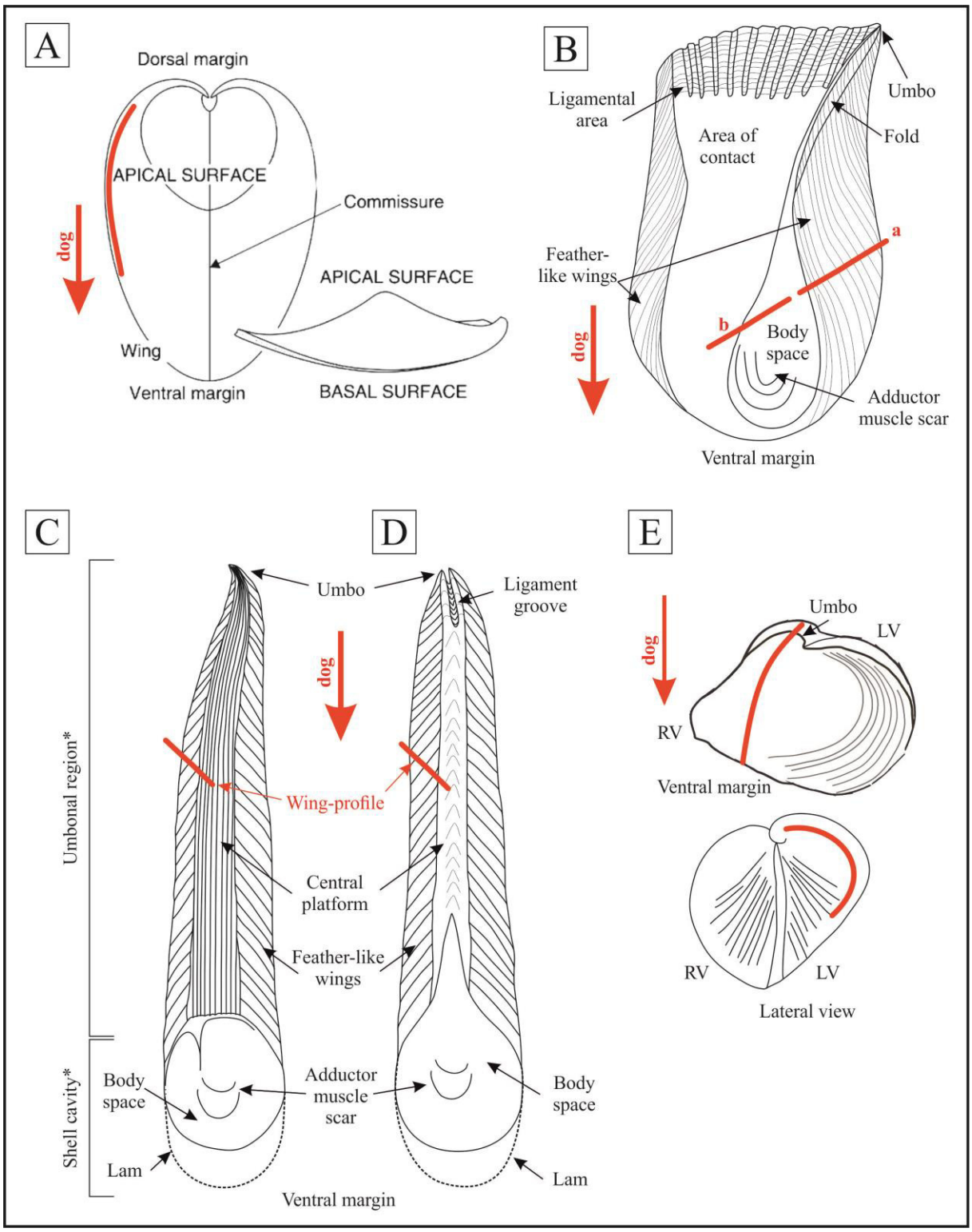

Figure 5.2. Illustrations of the studied materials along with terminology reported in the literature. The red lines indicate the cutting profiles used for sclerochronological and geochemical analyses. A) *Opisoma excavatum* (from Posenato et al., 2013a, modified). B) *Lithioperna scutata* (from Accorsi Benini, 1979). C) *Lithiotis problematica* (from Chinzei, 1982). D) *Cochlearites loppianus* (from Chinzei, 1982). E) *Pachyrisma (Durga) crassa* (from Tausch, 1890). * Terms used by Accorsi Benini and Broglio Loriga (1977). In *Lithioperna scutata*, *a* profile is referred to wing profile while *b* is the nearly transversal section (see text for further details). RV, right valve; LV, left valve; Lam, conchiolin-rich thin lamellae (Chinzei, 1982); dog, direction of growth.

5.6. Results

The main results of the stable isotope ($\delta^{13}C$, $\delta^{18}O$) analyses of the studied bivalves were reported in Table 5.1. Only acceptable $\delta^{18}O$ values (> -4‰) were considered in the seawater paleotemperature calculation for *Lithiotis* and *Cochlearites*. Details are discussed in paragraph 5.7.1.

Taxon	Specimen ID	No. Sample	$\delta^{13}C_{shell}$ Min [‰]	$\delta^{13}C_{shell}$ Max [‰]	$\delta^{13}C_{shell}$ Average	$\delta^{18}O_{shell}$ Min [‰]	$\delta^{18}O_{shell}$ Max [‰]	$\delta^{18}O_{shell}$ Average	T $\delta^{18}O_{shell}$ Min [°C]	T $\delta^{18}O_{shell}$ Max [°C]	T $\delta^{18}O_{shell}$ Average
Lithioperna scutata	LP3-a	25	4.93	6.21	5.37	-2.06	0.09	-1.33	14.68	24.03	20.84
	LP3-b	23	5.02	7.76	5.94	-1.97	-0.46	-1.18	17.08	23.62	20.22
Opisoma excavatum	O1	56	4.28	6.83	5.62	-1.80	0.48	-0.52	12.99	22.91	17.36
Lithiotis problematica	LT6	31 (54)	2.24	5.24	3.61	-3.76	-1.67	-2.63	22.33	31.39	26.52
	LT7	13 (45)	2.20	4.77	3.59	-3.97	-2.39	-3.38	25.48	32.33	29.74
Pachyrisma (Durga) crassa	P1	47	3.38	5.18	4.30	-1.86	-0.43	-1.16	16.94	23.15	20.12
Cochlearites loppianus	CO1	178 (212)	2.32	5.10	3.30	-4.00	-0.70	-2.08	18.14	32.44	24.12
	CO2	98 (102)	2.97	5.98	4.15	-3.96	-0.27	-1.87	16.26	32.29	23.19

Table 5.1. Carbon and oxygen isotope values of the studied bivalves with more positive than the diagenetic $\delta^{18}O$ threshold of -4.0‰ (details will discuss in paragraph 5.7.1). The total number of analysed samples for each specimen is reported in parentheses. In *Lithioperna scutata*, *a* profile is referred to wing profile while *b* is the nearly transversal section (Fig. 5.2). Temperatures were calculated assuming the $\delta^{18}O_{water}$ value of -1‰ (according to Shackleton and Kennett, 1975); for further details see text and Appendix B.4.

The correlation between the $\delta^{18}O$ and $\delta^{13}C$ values may represent another indicator of alteration. Both Spearman correlation coefficient (*rs*) and Pearson correlation coefficient (*r*) were used to evaluate a potential correlation between the $\delta^{18}O$ and $\delta^{13}C$ values in the present datasets (Tab. 5.2; Figs. 5.3–5.4). For the $\delta^{18}O$ and $\delta^{13}C$ values of *Lithiotis* and *Cochlearites*, the correlation coefficients were calculated both for the entire dataset and for the acceptable data ($\delta^{18}O$ > -4.0‰).

Taxon	All value		Only acceptable values	
	r	*rs*	*r*	*rs*
Lithioperna scutata (wing-profile) - specimen LP3	0.84	0.81	—	—
Lithioperna scutata (nearly transversal profile) - specimen LP3	0.29	0.49	—	—
Opisoma excavatum - specimen O1	0.20	0.12	—	—
Lithiotis problematica - specimen LT6	0.37	0.39	0.57	0.57
Lithiotis problematica - specimen LT7	0.30	0.16	0.54	0.45

Pachyrisma (*Durga*) *crassa* - specimen P1	0.27	0.30	—	—
Cochlearites loppianus - specimen CO1	0.17	0.21	0.38	0.39
Cochlearites loppianus - specimen CO2	0.46	0.44	0.36	0.37

Table 5.2. Correlation test between the $\delta^{18}O$ and $\delta^{13}C$ shell values; *r* (Pearson correlation coefficient); *rs* (Spearman correlation coefficient). Only acceptable values: $\delta^{18}O > -4.0‰$.

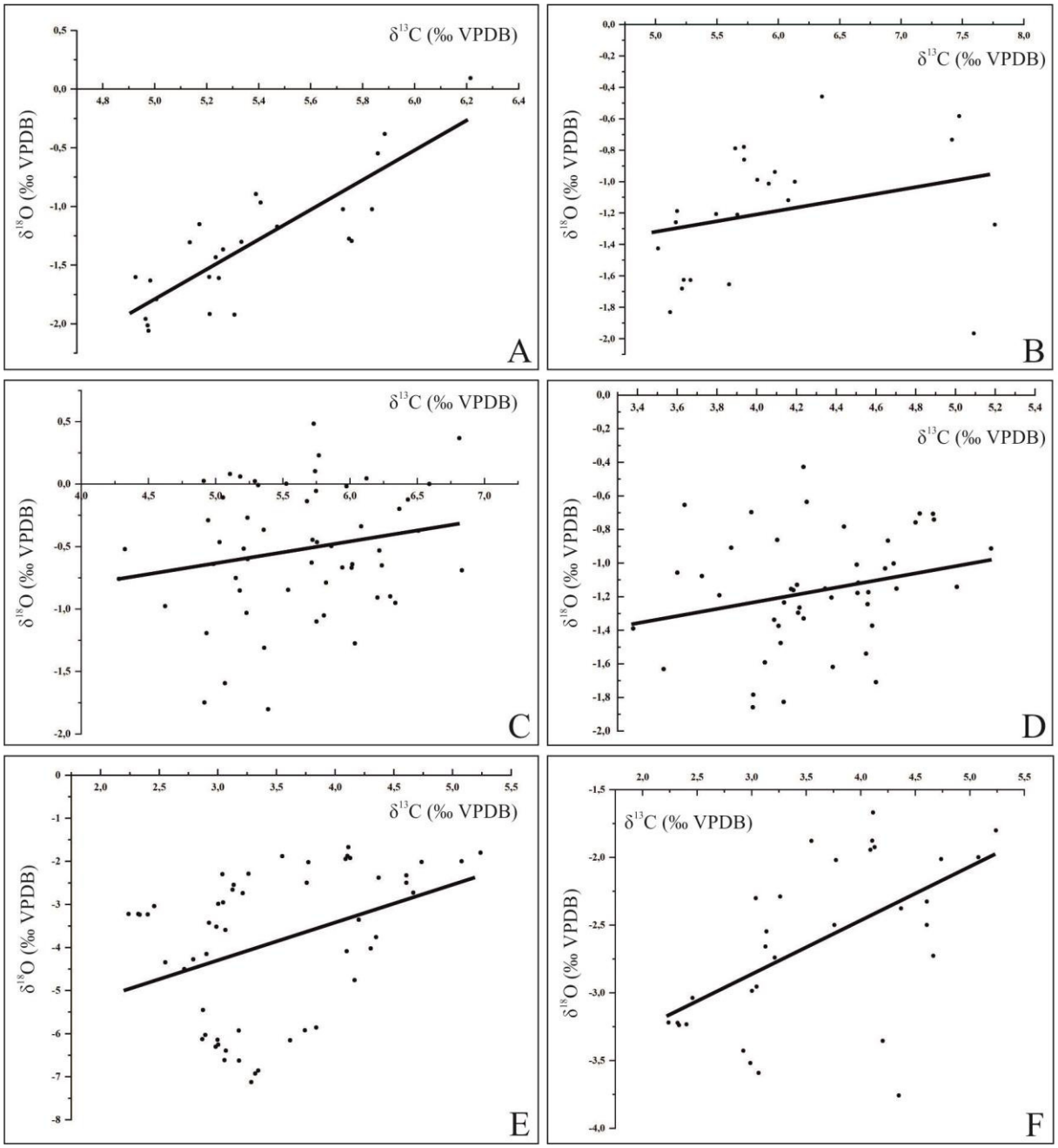

Figure 5.3. Cross plots of $\delta^{18}O$ and $\delta^{13}C$ data from the studied shells along with linear regression line. A) *Lithioperna scutata*, wing profile (specimen LP3). B) *Lithioperna scutata*, nearly transversal profile (specimen LP3). C) *Opisoma excavatum* (specimen O1). D) *Pachyrisma* (*Durga*) *crassa* (specimen P1). E) *Lithiotis problematica* (specimen LT6), all collected values. F) *Lithiotis problematica* (specimen LT6), only acceptable values ($\delta^{18}O > -4.0‰$).

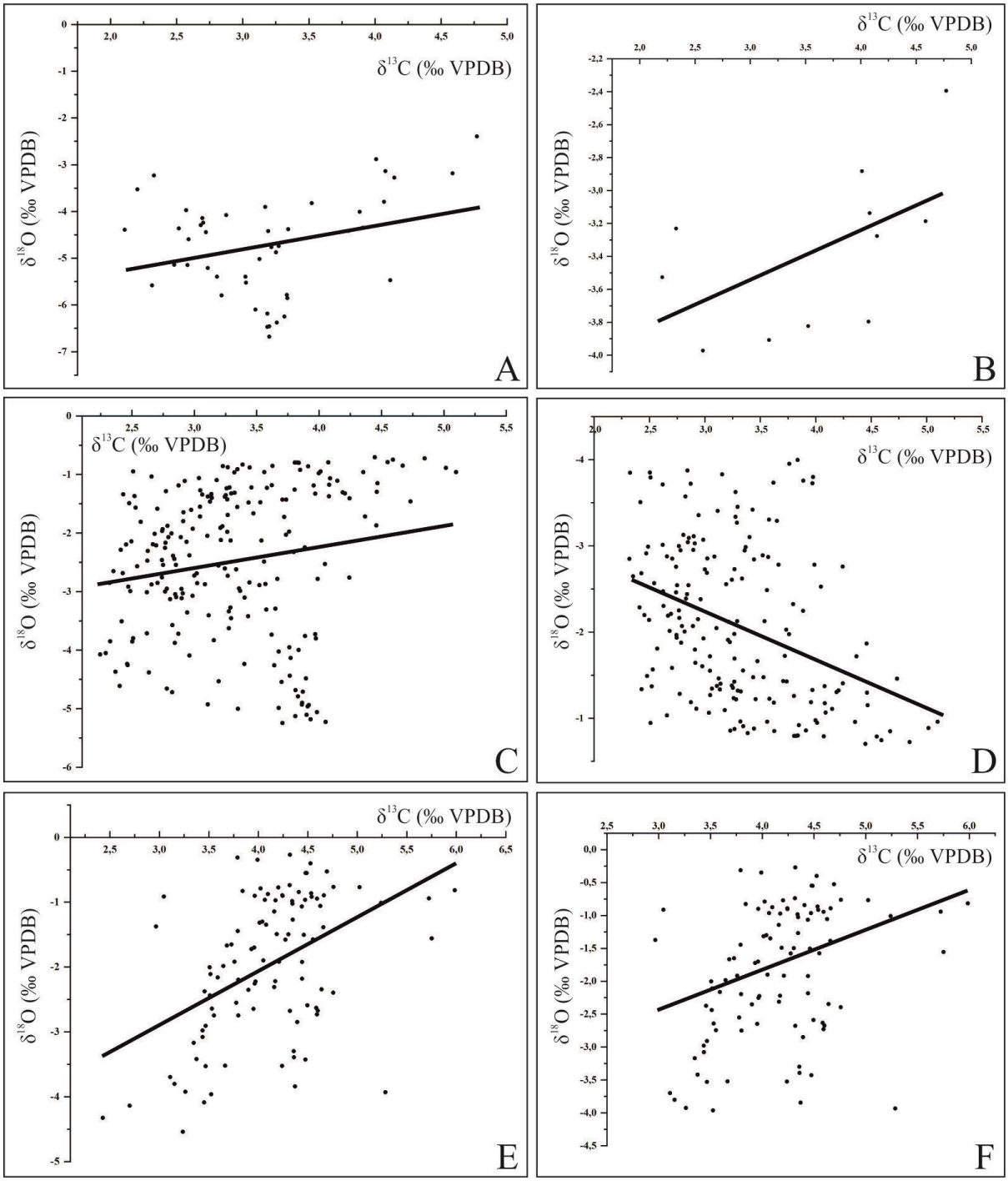

Figure 5.4. Cross plots of $\delta^{18}O$ and $\delta^{13}C$ data from the studied shells along with linear regression line. A) *Lithiotis problematica* (specimen LT7), all collected values. B) *Lithiotis problematica* (specimen LT7), only acceptable values ($\delta^{18}O$ > -4.0‰). C) *Cochlearites loppianus* (specimen CO1), all collected values. D) *Cochlearites loppianus* (specimen CO1), only acceptable values ($\delta^{18}O$ > -4.0‰). E) *Cochlearites loppianus* (specimen CO2), all collected values. F) *Cochlearites loppianus* (specimen CO2), only acceptable values ($\delta^{18}O$ > -4.0‰).

5.6.1. *Cochlearites loppianus* (Tausch, 1890)

Cochlearites is characterized by a predominant irregular fibrous prismatic aragonitic microstructure and nacreous wedges occurring in the wing regions. The inner part, usually recrystallized (brownish), was originally filled by the chalky deposit. The SEM analysis revealed the good preservation of both irregular fibrous prismatic and nacreous structures in the wing regions (Appendix B.2). The inner brownish area is altered in calcite, while in the whitish areas the original aragonite is well preserved (Appendix B.3). Frequently, with the increasing of diagenesis, in the wing areas narrow altered (calcite) bands substitute the original mineralogical phase (Appendix B.3). The CL analysis confirms these results, highlighting the occurrence of luminescent narrow calcite bands intercalated in the irregular fibrous prismatic layer (Figs. 5.17–5.18). The sclerochronological and geochemical analyses were conducted on the thicker attached valve.

In both *Cochlearites* specimens, the $\delta^{18}O$ and $\delta^{13}C$ profiles are characterized by a series of regular cycles of varying amplitudes and frequencies. In CO1 specimen (Fig. 5.5), the $\delta^{13}C$ curve fluctuates from 2.2 to 5.1‰ and from 2.3 to 5.1‰ (considering all and only acceptable values, respectively). The $\delta^{18}O$ values range from -5.3 to -0.7‰ (considering all values) while varies from -4.0 to -0.7‰ (considering only acceptable values). In CO2 (Fig. 5.6), the $\delta^{13}C$ curve ranges from 2.4‰ to 6.0‰ and from 3.0 to 6.0‰ (considering all and only acceptable values, respectively). The $\delta^{18}O$ values vary from -4.5 to -0.3‰ (considering all values) and from -4.0 to -0.3‰ (considering only acceptable values). In both specimens, the annual growth lines show not strictly relationship with the stable isotope extremes (i.e., minimum and maximum values). In the outer shell face, growth ribs are well-defined (Appendix B.1) and vary from 0.4 to 1.5 cm in thickness. A strong variation is registered with the ontogeny: in the juvenile stage, observed only in few individuals, the ribs are tight while in the adult stage are better define. The annual growth lines associated with the increments recognised in the shell surface were also observed in the cross-sectioned valve surface. The microgrowth pattern was recognised in detail only in few portions (Fig. 5.7). Daily microgrowth increments vary from ~15 to ~60 µm in thickness with an average value of ~30 µm. About 12–18 microincrements were grouped forming fortnightly (average thickness ~300 µm) and less defined monthly bundles (average thickness ~700 µm). Frequently, weekly clusters were also recognised. The nacreous wedges, identified in all the studied specimens (Appendix B.1), vary from ~100 µm to ~300 µm in thickness (e.g., Figs. 5.6–5.7). Their frequency varies between specimens.

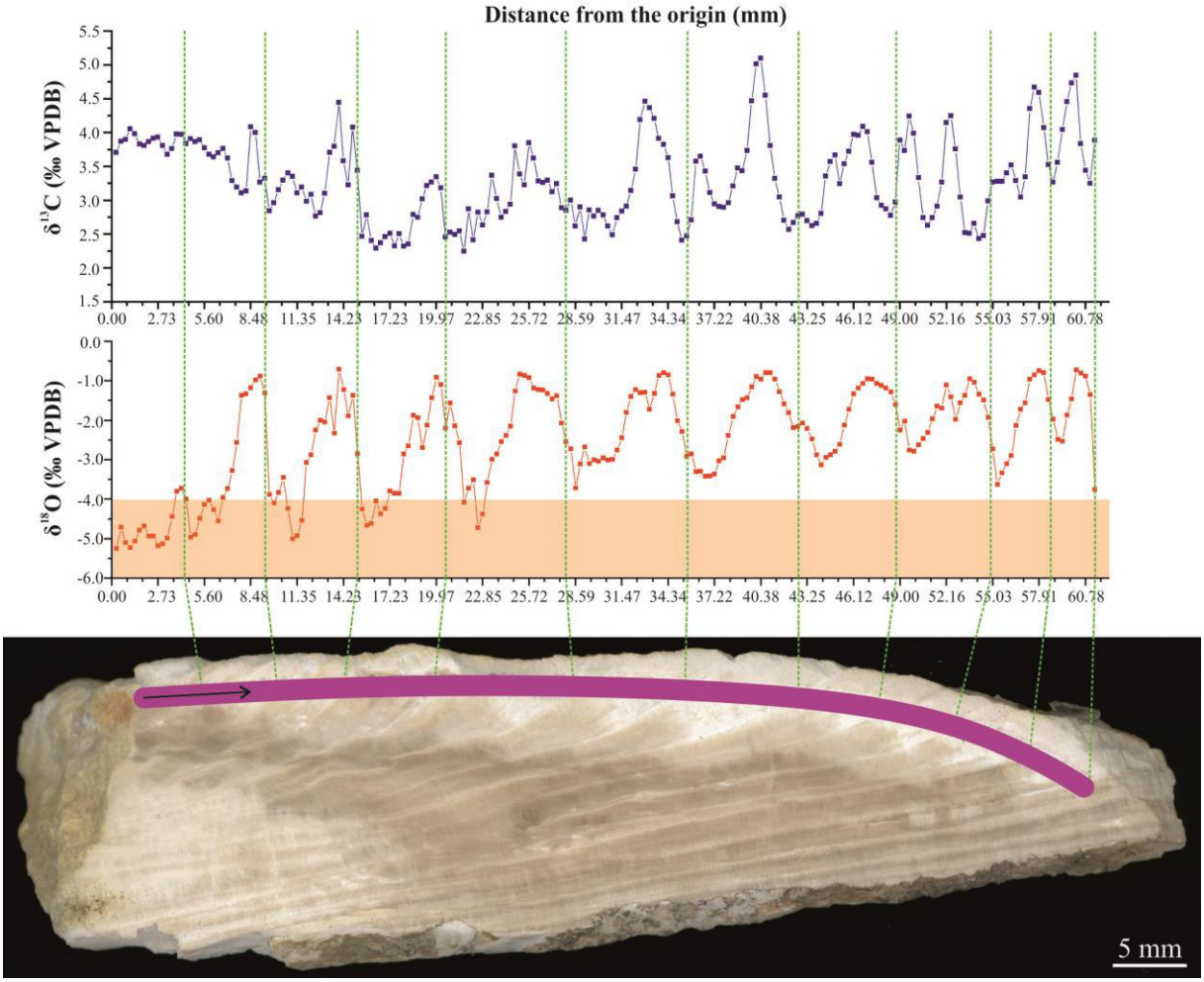

Figure 5.5. $\delta^{13}C$ and $\delta^{18}O$ profiles of *Cochlearites loppianus*, specimen CO1. The light orange band in $\delta^{18}O$ profile highlights the likely altered values ($\delta^{18}O$ < -4.0‰, see text for further details). Violet line indicates the sampled transect while black arrow the growth direction. Vertical green dotted lines show the position of annual growth lines. The origin of the studied transect is nearly the central platform (Fig. 5.2).

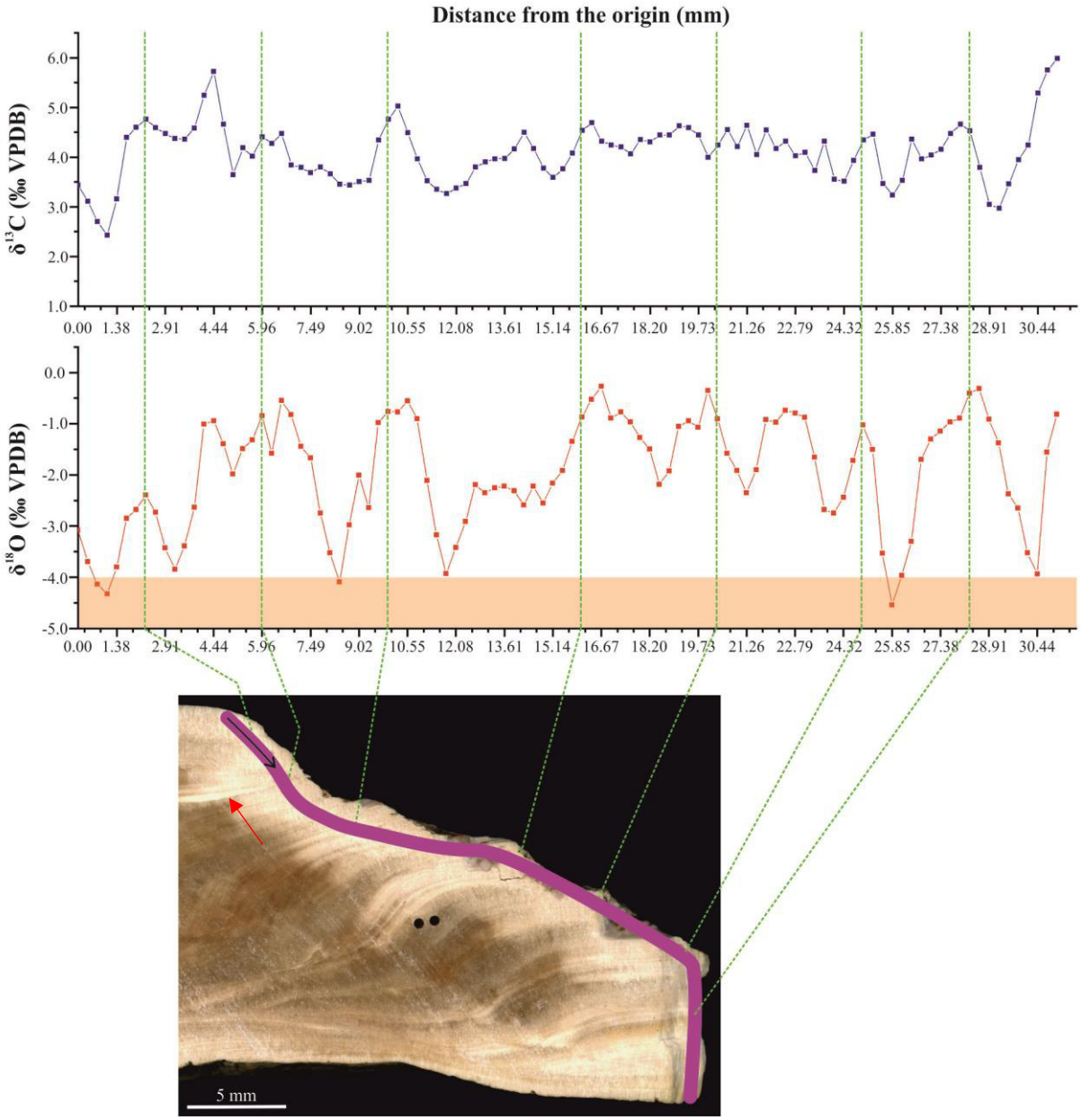

Figure 5.6. $\delta^{13}C$ and $\delta^{18}O$ profiles of *Cochlearites loppianus*, specimen CO2. The light orange band in $\delta^{18}O$ profile highlights the likely altered values ($\delta^{18}O$ < -4.0‰, see text for further details). Violet line indicates the sampled transect while black arrow the growth direction. Vertical green dotted lines show the position of annual growth lines. The red arrow indicates a well-defined larger nacreous wedge. The origin of the studied transect is nearly the central platform (Fig. 5.2).

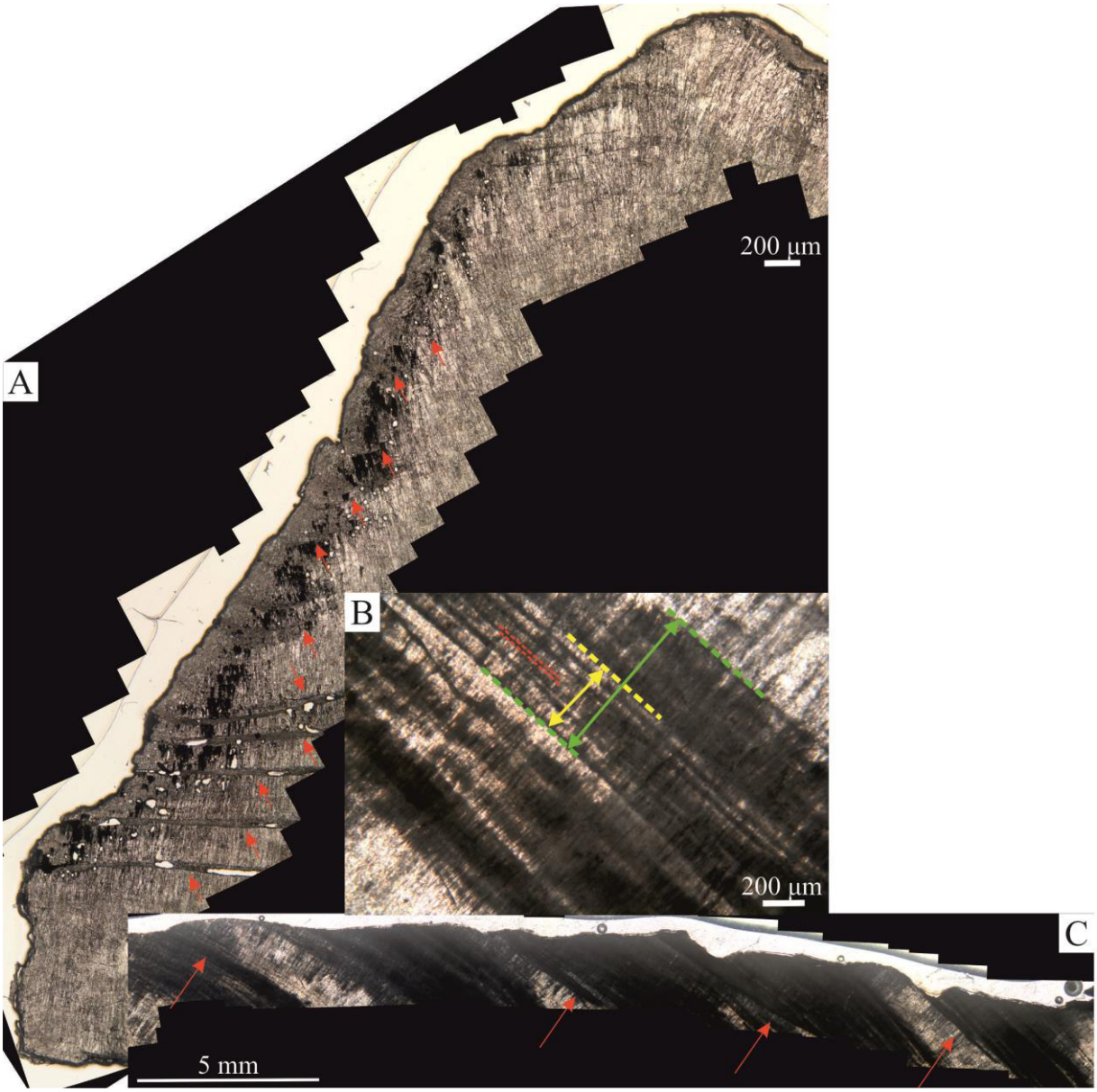

Figure 5.7. Growth pattern in *Cochlearites loppianus*. A) Specimen CO3. Stitched microphotographs of the entire shell where several nacreous wedges are recognizable (red arrows). The growth pattern is unclear. B, C) Specimen CO1. B) Detailed microphotograph of thin section showing daily growth increments grouped in fortnightly (yellow lines) and monthly bundles (green lines). C) Stitched microphotographs of the entire shell used for sclerochronological analysis. Nacreous wedges were recognizable (red arrows).

5.6.2. *Pachyrisma* (*Durga*) *crassa* Boehm, 1884

Pachyrisma is characterized by an aragonitic thick shell constituted, in the inner part, of irregular fibrous aragonitic prisms. The thin outer shell layer is not preserved. SEM, XRD and CL analyses revealed the good preservation of the studied specimen P1.

The $\delta^{13}C$ record of the *Pachyrisma* specimen P1 ranges between 3.4 and 5.2‰ and shows no clear seasonal trend (Fig. 5.8). The $\delta^{18}O$ record shows entirely defined seasonal cycles varying between -1.9 to -0.4‰ (Fig. 5.8). The juvenile area is more difficult to be distinguished than the adult growth stage, which is marked by more raised growth lines. The more marked growth lines, interpreted as annual, show no relation with the stable isotope extremes.

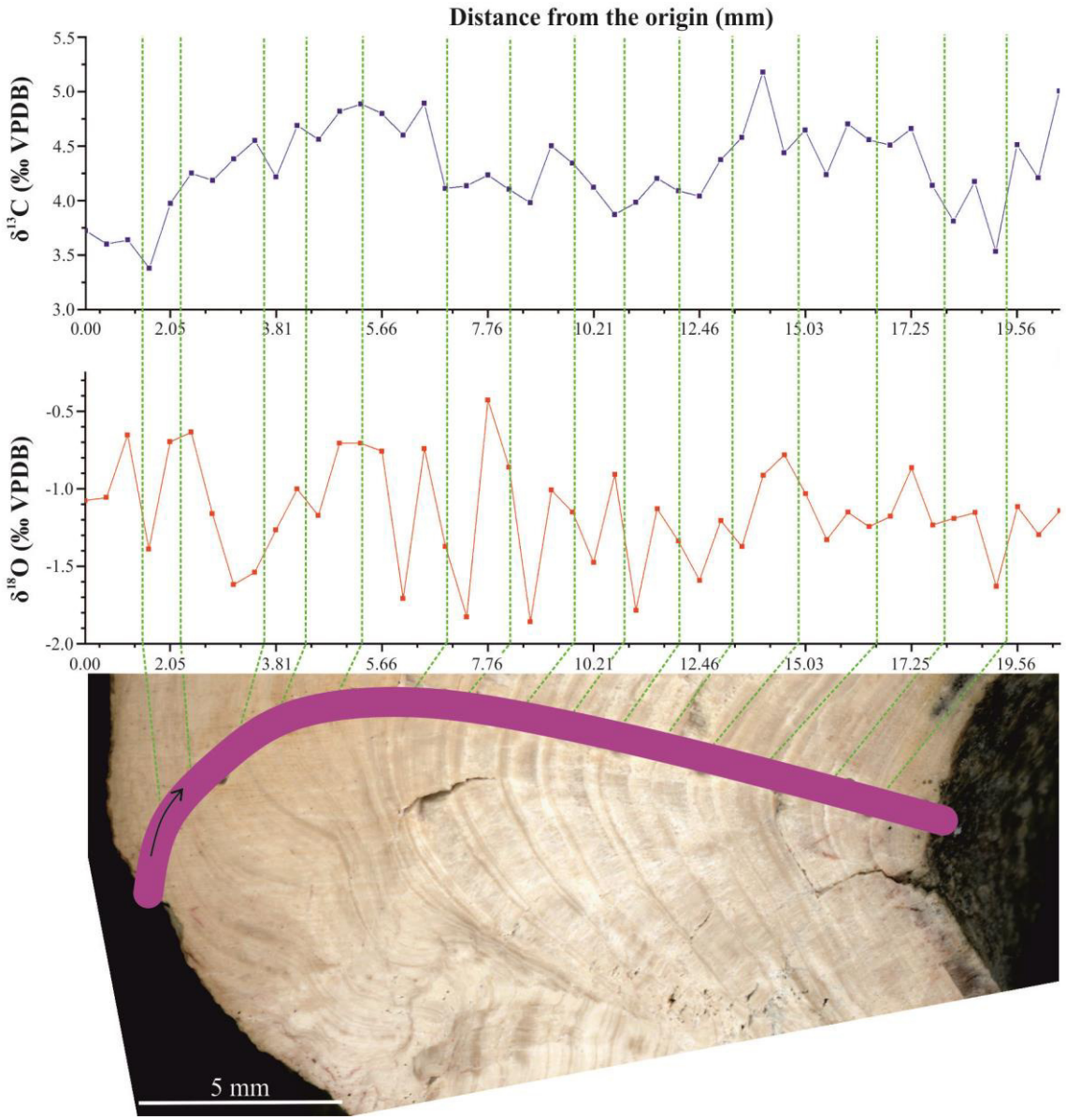

Figure 5.8. $\delta^{13}C$ and $\delta^{18}O$ profiles of *Pachyrisma* (*Durga*) *crassa*, specimen P1. Violet line indicates the sampled transect while black arrow the growth direction. Vertical green dotted lines show the position of the presumed annual growth lines. The origin of the studied transect is nearly the dorsal margin (Fig. 5.2).

Even though the analysed specimens are well preserved, in cross-sectioned shell the growth pattern is not well defined. The daily microincrements were tentatively identified only in small portions of the specimen P2 (average thickness ~7.5 µm; Fig. 5.9). About 14 microgrowth increments were grouped in fortnightly bundles. The annual growth increments are tentatively recognised in the polished-cross sectioned P1 shell (average thickness 1.2 mm; Fig. 5.8). SEM observations revealed a pervasive dissolution close to the growth lines (Appendix B.2).

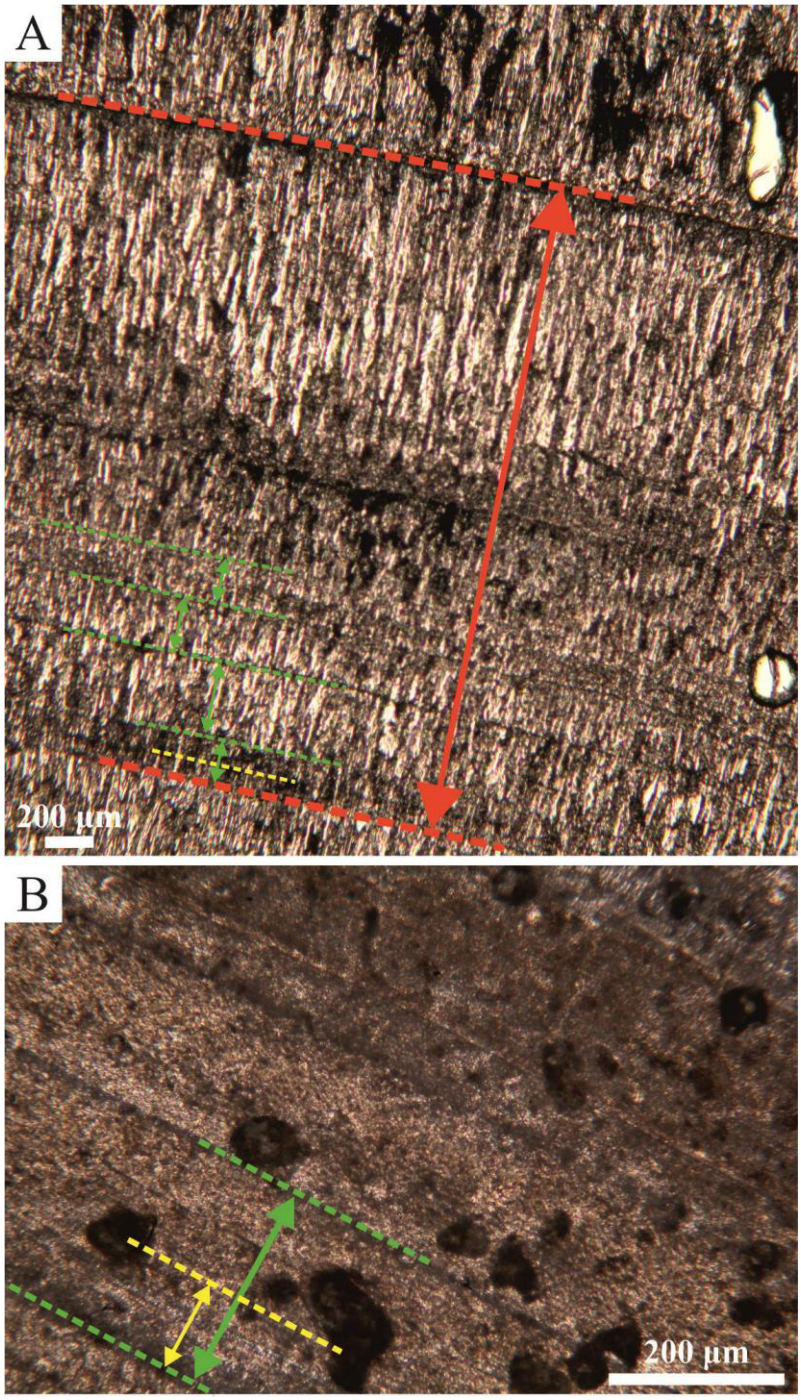

Figure 5.9. Growth pattern in *Pachyrisma* (*Durga*) *crassa*, specimens P1 and P2. A) Microphotograph of thin section showing likely monthly increments (green lines) and one fortnightly bundle (yellow line). Red lines highlighted annual growth increment; specimen P1. B) Detailed microphotograph of thin section showing daily growth increments grouped in fortnightly (yellow line) and monthly (green lines); specimen P2.

5.6.3. *Lithiotis problematica* Gümbel, 1871

Five specimens of *Lithiotis* were analysed in detail. Two of these specimens were chosen for geochemical analyses (Appendix B.1). Only the attached valve was analysed (see Appendix B.6 for further details). *Lithiotis* is distinguished by a prevailing aragonitic shell, which mostly consists of irregular fibrous prisms and nacreous wedges occurring in the anterior and posterior wings. The inner part is usually recrystallized (brownish in colour) and is characterized by granular-prismatic calcite, probably derived by the alteration of the original chalky deposit (e.g., Chinzei, 1982; see also Appendix B.7).

The analysed samples show a whitish outer cortex, which suggests the preservation of the pristine shell. SEM observations show well preserved irregular fibrous prisms, while nacreous wedges are rare. The XRD analysis reveals the contemporaneous occurrence of aragonite and calcite (~27% in specimen LT6 and ~34% in LT7; see Appendix B.3) while the CL image shows luminescent areas in the prismatic structure in the wing (Fig. 5.17). Note, however, that the shell profile used for XRD and CL analyses is opposite to that used for geochemical analysis since it is towards the inner shell part, usually more altered. The border between the preserved and altered areas is not sharp, excluding it as a good sampling for geochemical analyses. Consequently, the isotope results could be significantly influenced by diagenesis, and only few values are above the acceptable threshold ($\delta^{18}O < -4.0‰$; see Discussion below).

In specimen LT6 (Fig. 5.10), the $\delta^{13}C$ and $\delta^{18}O$ values vary from 2.2 to 5.2‰ and -7.1 to 1.7‰, respectively (considering all values). The acceptable values of $\delta^{18}O$ vary from -3.8 to -1.7‰, whilst the $\delta^{13}C$ values from the same samples range from 2.2 to 5.2‰. In the specimen LT7 (Fig. 5.11), the $\delta^{13}C$ values vary from 2.1 to 4.8‰, while the $\delta^{18}O$ values range from -6.7 to 2.4‰ (considering all values). The acceptable values of $\delta^{18}O$ vary from -4.0 to -3.4‰, whilst the $\delta^{13}C$ values from the same samples range between 2.2 and 4.8‰. In both analysed specimens, the annual growth lines show not strictly relation with the stable isotope extremes, even if they are proximal to lower oxygen values.

Regarding growth patterns, microgrowth increments were recognized only in restricted areas (Fig. 5.12). *Lithiotis* shows high variability, and the results could be slightly different among specimens. The thickness of daily microgrowth increments could vary from ~10 to ~60 µm (with average value ranges from ~15 to ~35 µm). Bundles of 12–17 microincrements were also documented, confirming the results obtained by Pecorari (2016). Monthly and weekly clusters were also recognized (Fig. 5.12). The annual growth increments, measured in cross-sectioned shells, vary from ~5 to ~10 mm. Comparable thicknesses of growth patterns were also obtained, considering the growth increments measured on the surface of anterior

and posterior wings (Fig. 5.12D). The nacreous wedges are less frequent respect to *Cochlearites,* but their size is up to ~500 µm in thickness.

The collected *Lithiotis* individuals are usually not complete, and the growth pattern on the inner shell surface can be observed only in small shell portions (see also Appendix B.1).

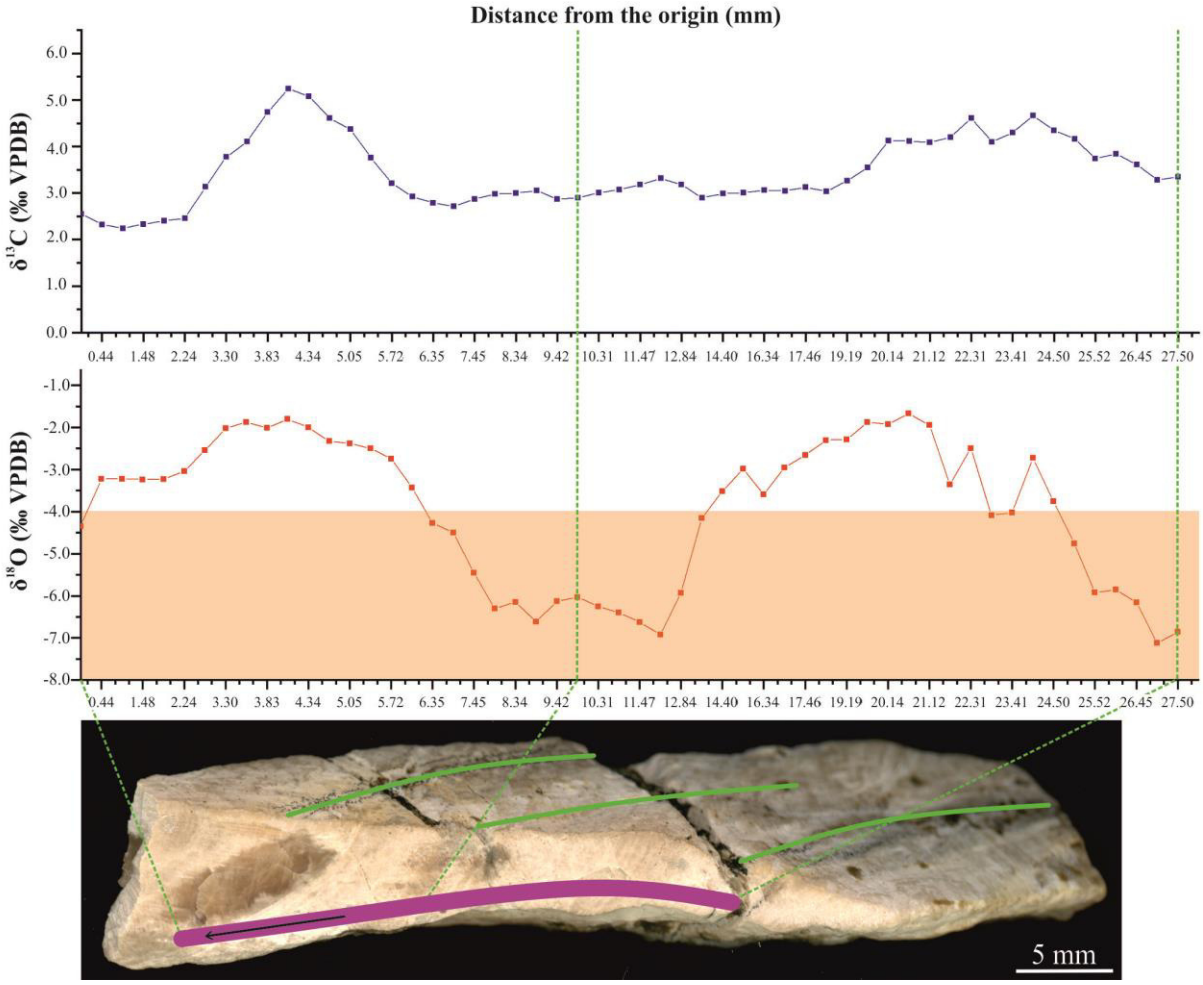

Figure 5.10. $\delta^{13}C$ and $\delta^{18}O$ profiles of *Lithiotis problematica*, specimen LT6. Violet line indicates the sampled transect while black arrow the growth direction. Vertical green dotted lines show the position of annual growth line, highlighted with green lines on the shell surface. The light orange band in $\delta^{18}O$ profile highlights the likely altered values ($\delta^{18}O$ < -4.0‰), see text for further details. The origin of the studied transect is nearly the first growth line (green line) in the left part of the photograph (see Appendix B.1 for further details).

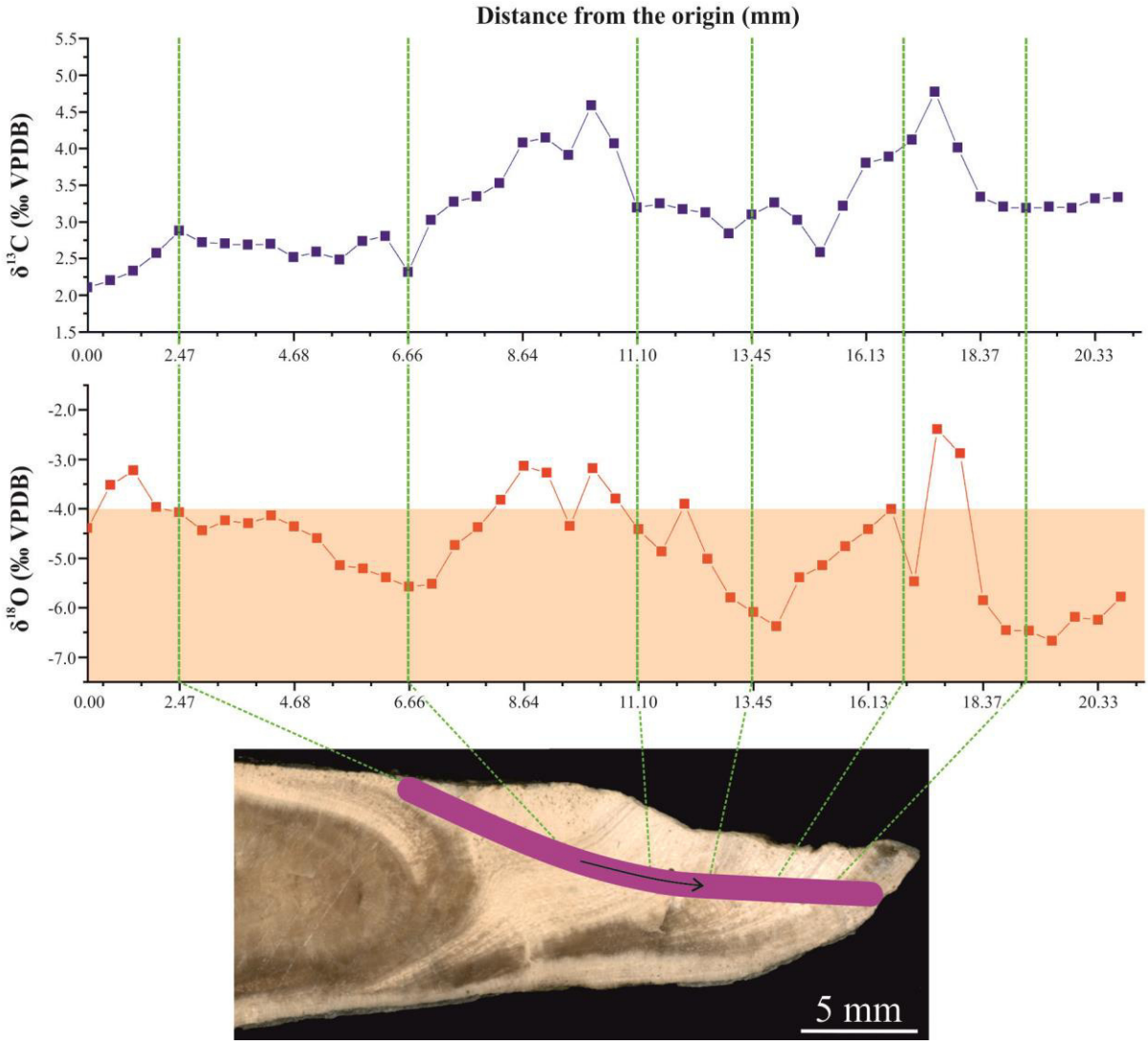

Figure 5.11. $\delta^{13}C$ and $\delta^{18}O$ profiles of *Lithiotis problematica*, specimen LT7. Violet line indicates the sampled transect while black arrow the growth direction. Vertical green dotted lines show the position of likely annual growth lines. The light orange band in $\delta^{18}O$ profile highlights the likely altered values ($\delta^{18}O$ < -4.0‰, see text for further details). The origin of the studied transect is nearly the central platform (Fig. 5.2).

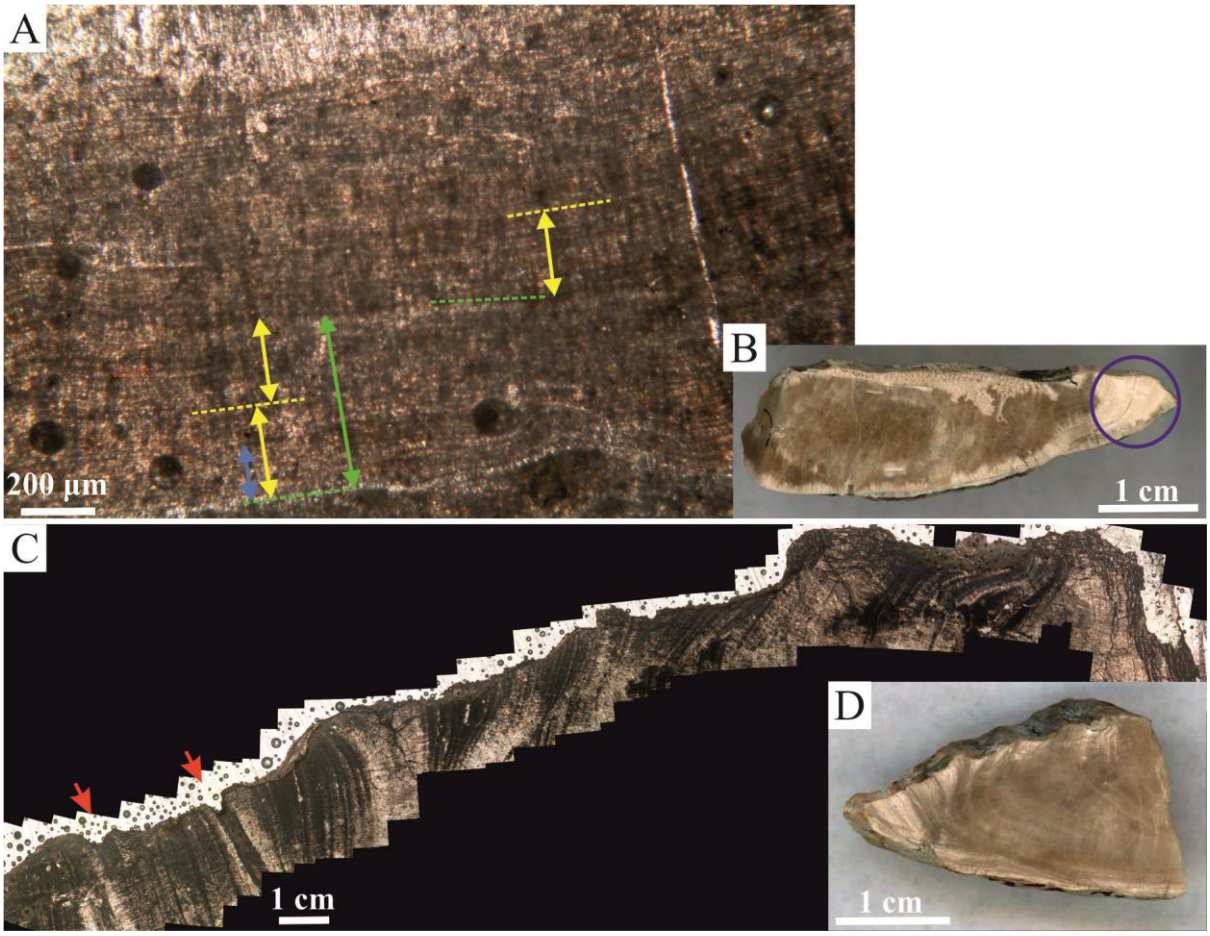

Figure 5.12. Growth pattern in *Lithiotis problematica*. A–B) Specimen LT6. A) Microphotograph of thin section showing daily growth increments grouped in fortnightly (yellow lines) and monthly bundles (green lines). Weekly clusters are also recognizable (blue arrows). B) Scan of the respective shell polished slab with the analysed area (blue circle). C, D) Specimen LT1. C) Stitched microphotographs of the entire shell margin analysed for sclerochronological study; rare nacreous wedges are recognizable (red arrows). D) Scan of the polished slab showing the likely annual growth increments.

5.6.4. *Opisoma excavatum* Boehm, 1884

A single specimen of *Opisoma* showed an optimal preservation state of the aragonitic microstructures as confirmed by SEM, XRD (see Appendixes B.2, B.3) and CL analyses.

The $\delta^{18}O$ curve shows well-defined cycles with slightly different amplitudes, while the $\delta^{13}C$ profile is distinguished by the less regular trend, even if distinct cycles are observable (Fig. 5.13). The carbon isotope values vary from 4.3 to 6.8‰ while oxygen ranges from -1.8 to 0.5‰. The annual growth lines seem to be related to seasonal oxygen isotope maximum values.

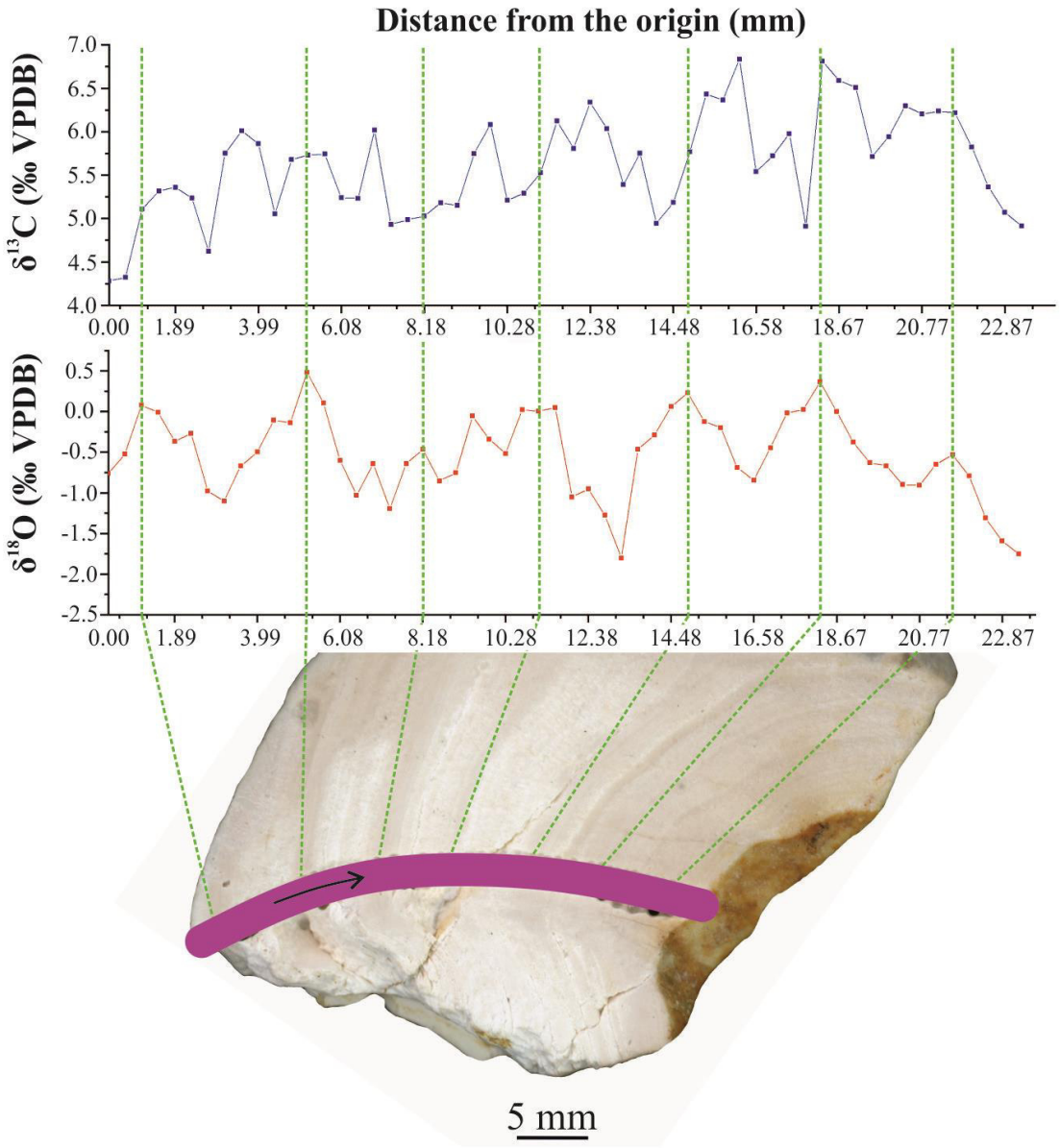

Figure 5.13. $\delta^{13}C$ and $\delta^{18}O$ profiles of *Opisoma excavatum*, specimen O1. Violet line indicates the sampled transect while black arrow the growth direction. Vertical green dotted lines show the position of annual growth lines. The origin of the studied transect is nearly the dorsal margin (Fig. 5.2).

Under an optical light microscope, no distinct microgrowth increments were recognized. According to stable isotope variations, only annual increments were tentatively distinguished in the polished cross-sectioned shell (Fig. 5.13), which varies from ~1.5 to ~4 mm (average value: ~3 mm).

5.6.5. *Lithioperna scutata* (Dubar, 1948)

Four specimens of *Lithioperna* were analysed. One of these was chosen for geochemical analyses (Appendix B.1). The diagenetic screening analyses (SEM, XRD, CL) revealed the good preservation of the aragonitic LP3 specimen in the nearly transversal cross-sectioned shell (Appendixes B.2, B.3). In the wing profile, instead, a low amount of calcite was detected by XRD analysis (Appendix B.3), assuming a negligible influence on isotope composition of the shell (Figs. 5.14–5.15; see Discussion below).

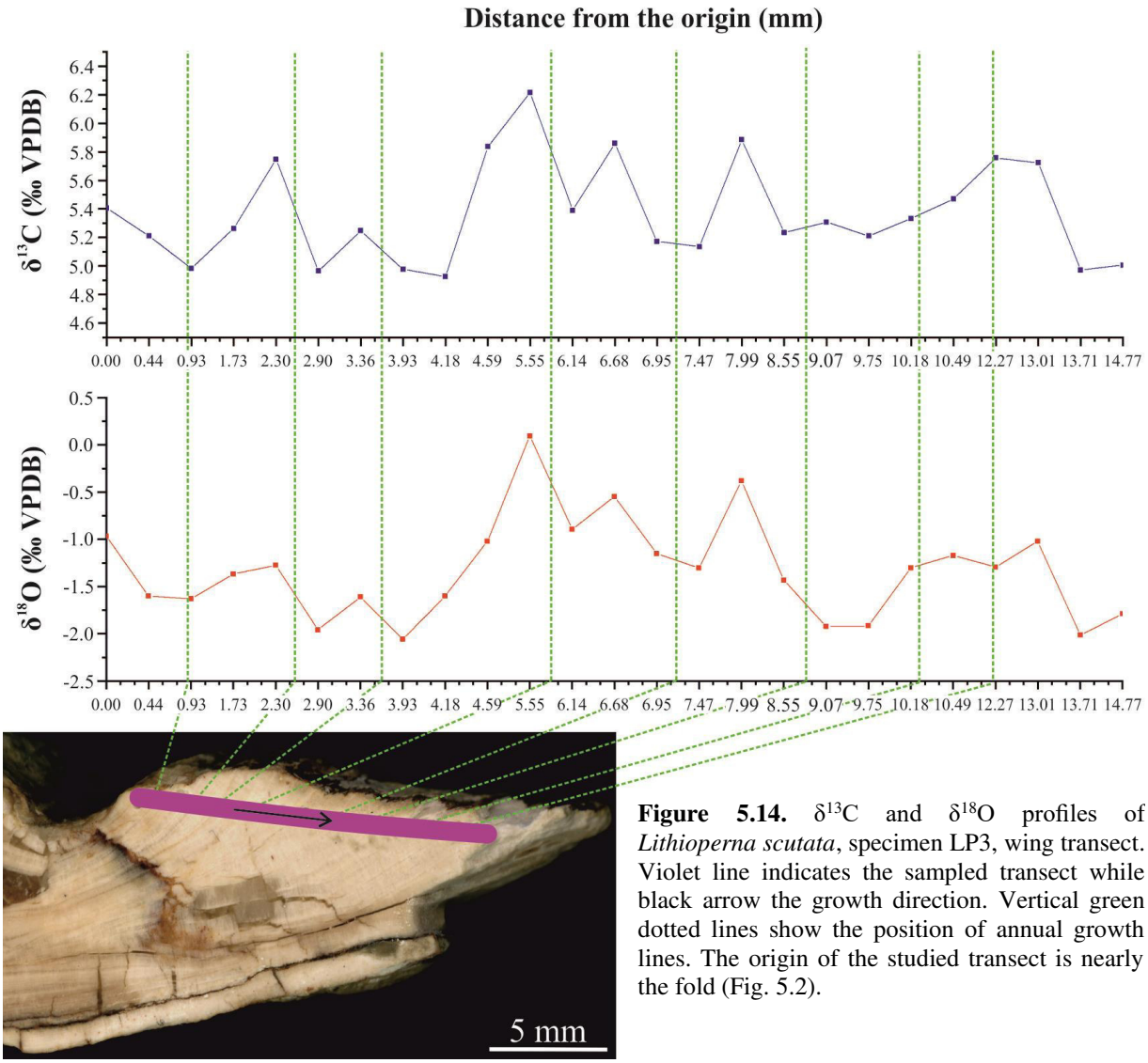

Figure 5.14. $\delta^{13}C$ and $\delta^{18}O$ profiles of *Lithioperna scutata*, specimen LP3, wing transect. Violet line indicates the sampled transect while black arrow the growth direction. Vertical green dotted lines show the position of annual growth lines. The origin of the studied transect is nearly the fold (Fig. 5.2).

In the wing profile (Fig. 5.14), the $\delta^{13}C$ and $\delta^{18}O$ values range from 6.2 to 4.9‰ and -2.1 to 0.1‰, respectively. In the nearly transversal cross-sectioned shell (Fig. 5.15), the $\delta^{13}C$ and $\delta^{18}O$ values vary from 5.0 to 7.8‰ and -2.0 to -0.5‰, respectively. Both $\delta^{18}O$ profiles show (similar) seasonal fluctuations, while the trend registered by the $\delta^{13}C$ is less regular. In both profiles, the annual growth lines show no relation with the stable isotope extremes (Figs. 5.14–5.15).

Regarding the growth pattern, microgrowth increments (daily) were recognized in the three studied specimens. The thickness of microgrowth increments varies within the same specimens and ranges from ~2 to ~10 µm. Fortnightly bundles are less defined as well as monthly clusters. Ghirardello (2015) reported the occurrence of monthly bundles in *Lithioperna* with similar microgrowth thicknesses. The annual growth increments are not easily recognizable even in the anterior and posterior wings (see Appendix B.1).

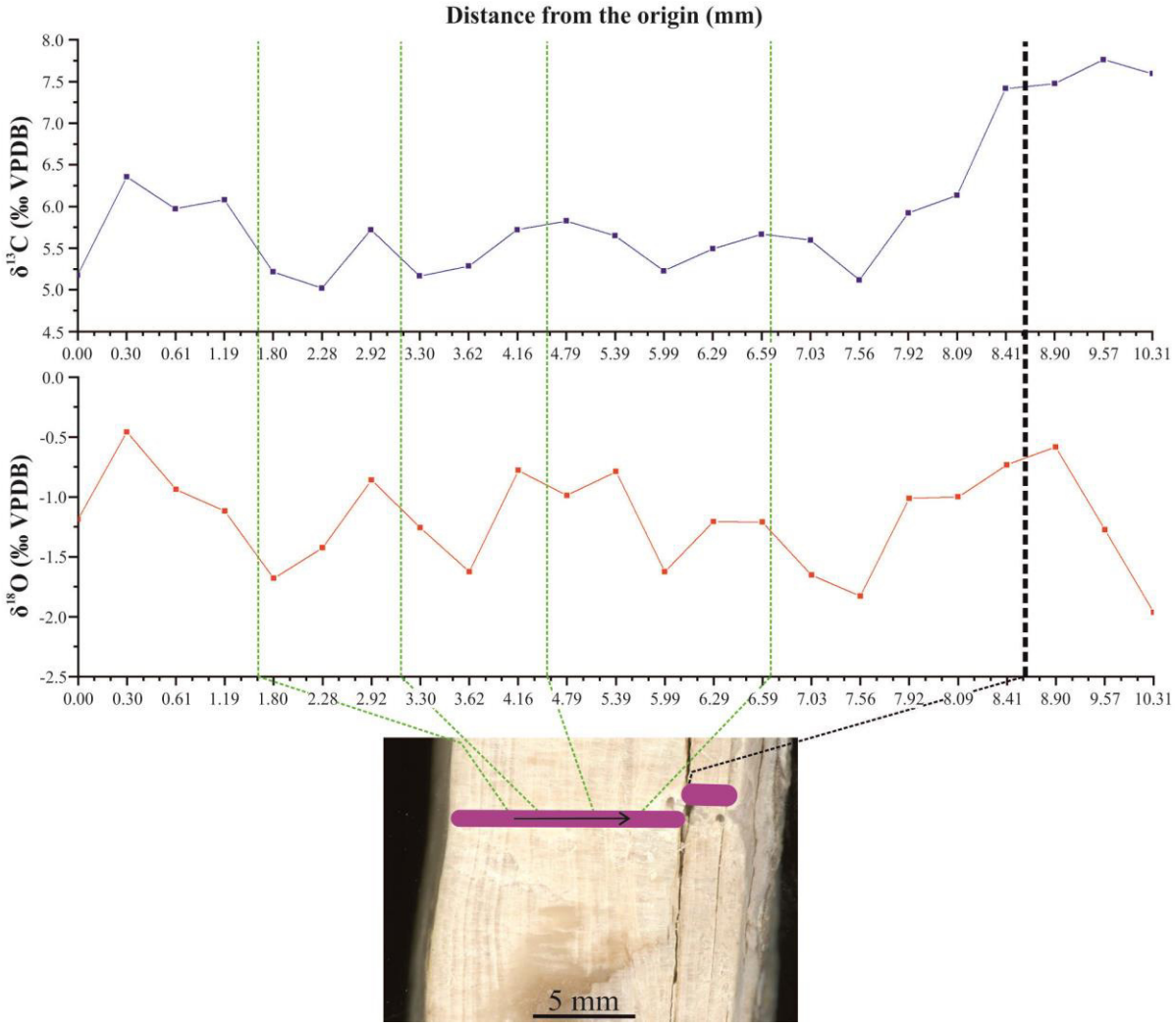

Figure 5.15. $\delta^{13}C$ and $\delta^{18}O$ profiles of *Lithioperna scutata*, specimen LP3, nearly transversal profile. Violet line indicates the sampled transect while black arrow the growth direction. Vertical green dotted lines show the position of annual growth lines while the black one the separated transect, just after the fracture. The origin of the entire studied transect is nearly the inner shell face.

A microstructural change was recognized in few samples (e.g., Fig. 5.16B–C): the annual growth line was followed by simple prisms that do not show microgrowth increments (see Discussion below). About 180 daily microgrowth increments along the nearly transversal cross-sectioned shell (specimen LP3) were counted, allowing to conduct spectral analyses. Continuous wavelet transformation spectra showed a signal at the period of ~16 increments (Fig. 5.16D).

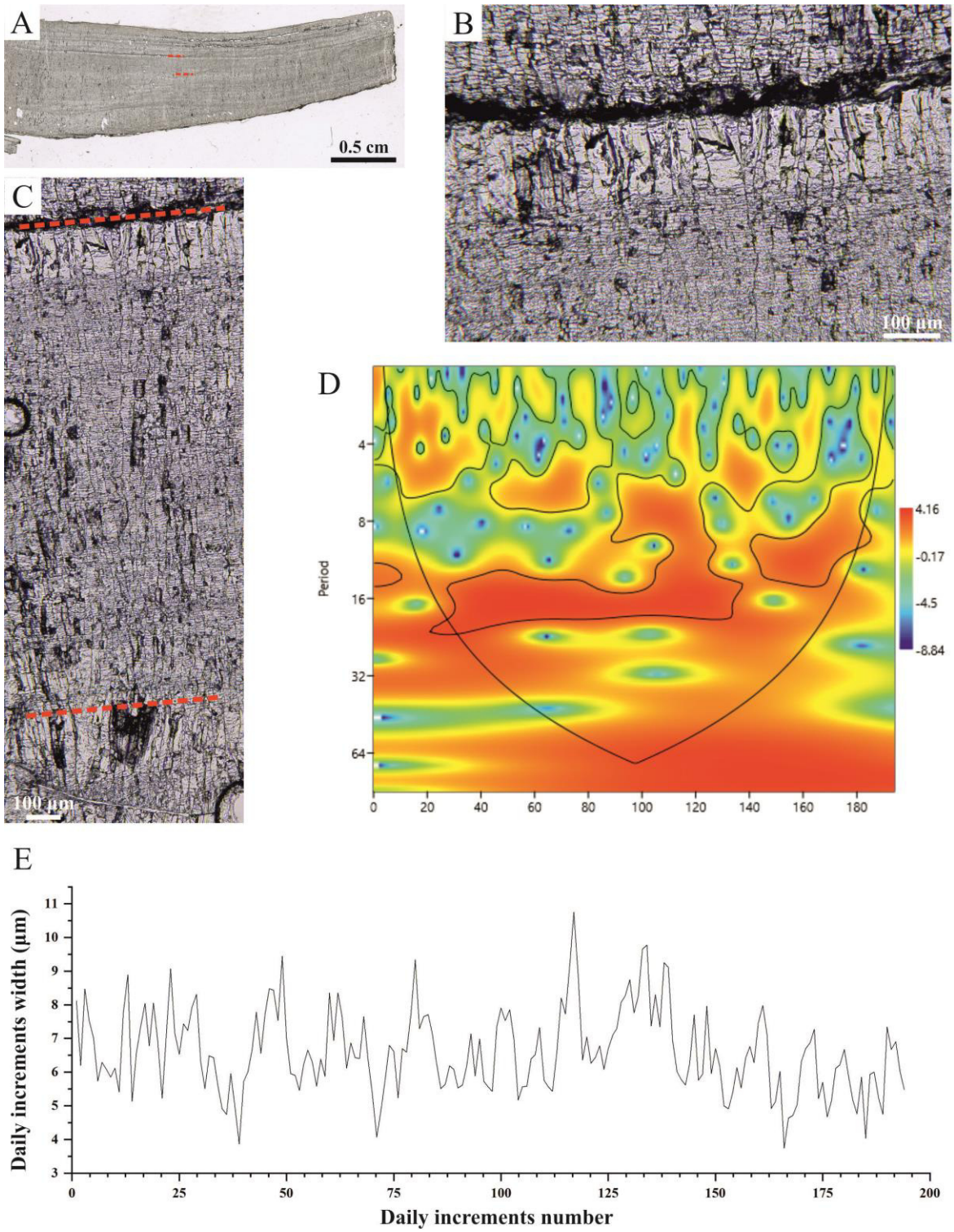

Figure 5.16. *Lithioperna scutata*, specimen LP3.

Figure 5.16. *continued*. A) Scanned acetate peel with likely annual growth increments (red lines). B) Microphotographs of acetate peel with well-defined daily microgrowth increments; the annual growth line is followed by thin prismatic layer with no microgrowth increments. C) Detailed microphotograph of annual increment (dotted red lines) with well-defined daily growth lines. D) Continuous wavelet transformation analysis; thick black contour lines display significant power (above the 5% significance level); the "cone of influence" shows the region where boundary effects are present (Hammer et al., 2001). E) Microgrowth increment width chronology. Assuming tide-controlled growth cycles, the chronologies represent ~180 days.

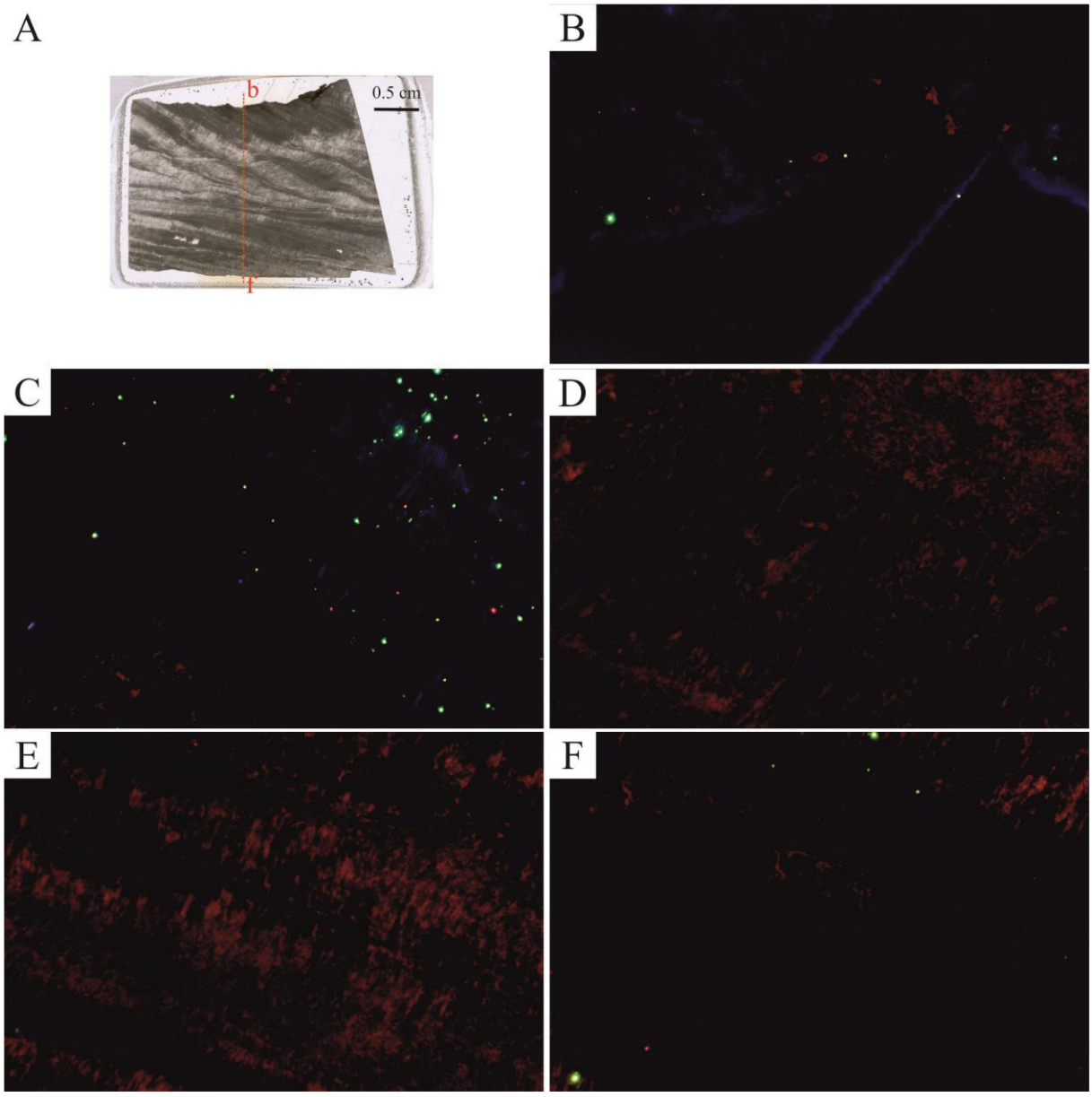

Figure 5.17. Thin section of *Cochlearites loppianus*, specimen CO1 under cathodoluminescence documenting different level of preservation. A) Scan of the studied thin section (slightly thicker) where red line shows the analysed profile with the respective position of the microphotographs. B–C) Non-luminescent irregular fibrous prismatic aragonitic area used for geochemical analysis (darker in scanned thin section). D, E) Luminescent areas in the inner part of the shell corresponding to calcite derived from alteration of inner aragonite chalky deposit (e.g., Chinzei, 1982; i.e., whitish in scanned thin section). F) Non-luminescent lower part of the thin section corresponding to the outer shell margin. The original irregular fibrous prismatic aragonitic shell is preserved.

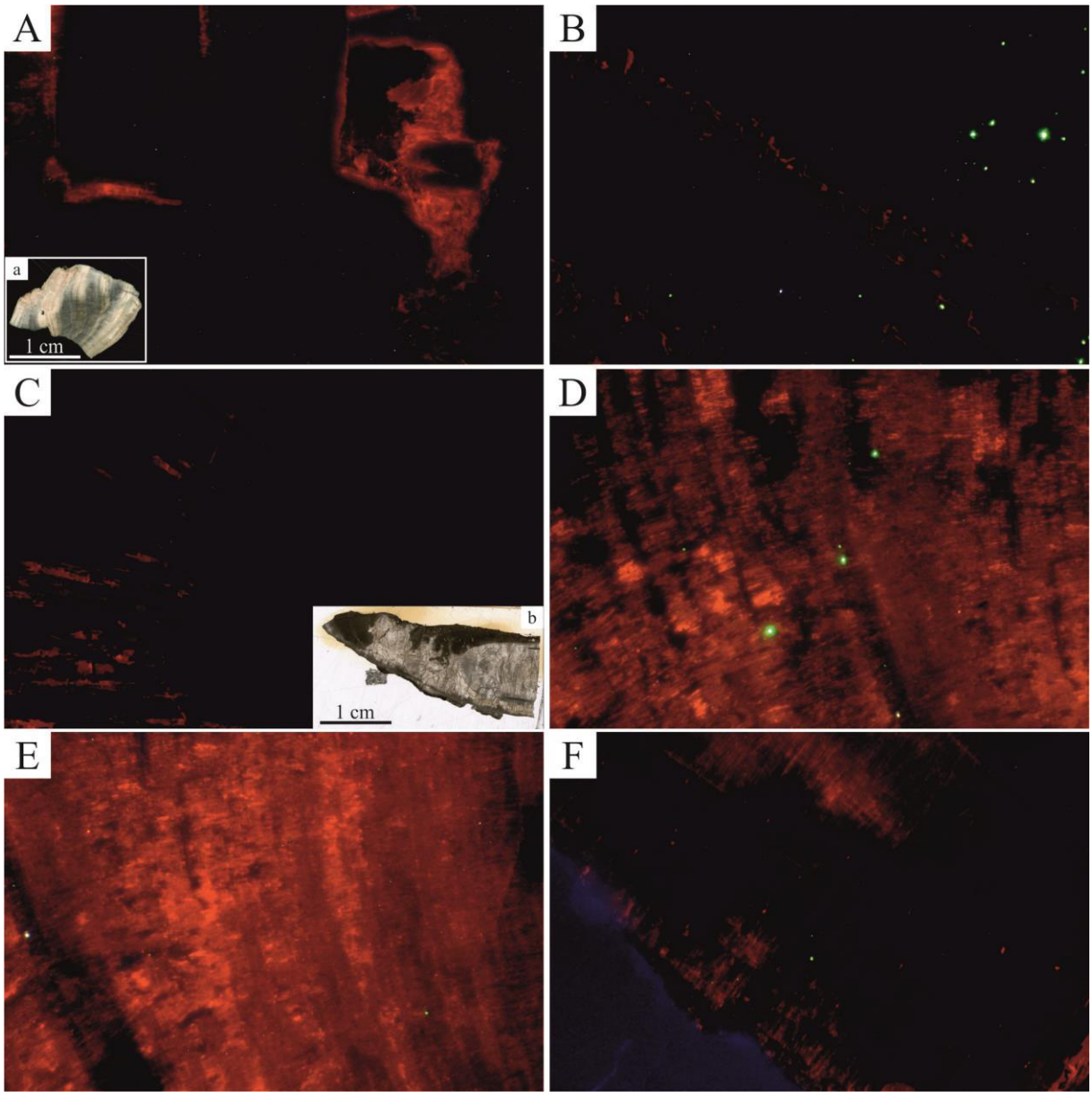

Figure 5.18. Thin section of *Cochlearites loppianus*, specimen CO2 and *Lithiotis* problematica, specimen LT6 under cathodoluminescence documenting different degrees of preservation. (a) Studied scanned CO2 thin section. A–B) Non-luminescent irregular fibrous prismatic aragonitic area used for geochemical analysis (darker in scanned thin section) with rare patchy luminescent areas towards the inner part of the shell. (b) Studied scanned LT6 thin section. C) No luminescent area corresponding to the darker region in thin section distinguished by irregular fibrous prismatic aragonite. D–F) Luminescent inner portions of *Lithiotis* shell, consisting of neomorphic calcite. F) Slightly luminescent areas in the irregular fibrous prismatic aragonite. The *Lithiotis problematica* specimen LT7 shows a similar luminescent trend towards the inner shell part.

5.7. Discussion

5.7.1. Preservation state

In order to use fossil shell materials for $\delta^{13}C$ and $\delta^{18}O$-based paleoenvironmental reconstructions, the evaluation of preservation state is compulsory. The alteration of the analysed materials could be evaluated also considering the correlation between the $\delta^{18}O$ and $\delta^{13}C$ values. Several authors reported lower $\delta^{18}O$ and $\delta^{13}C$ values for limestones and cements

than those for fossil shells suggesting that frequently these values depend on diagenetic alteration or on influence by meteoric waters (e.g., Hodgson, 1966; Hudson, 1977). The correlation between $\delta^{18}O$ and $\delta^{13}C$ values can occasionally be of primary origin (e.g., due to increased primary productivity at higher water temperatures; Alberti et al., 2019a; 2019b), therefore this correlation should be considered with caution.

In the analysed bivalve shells, $\delta^{18}O$ values are sometimes relatively lower considering other studies on well-preserved Jurassic fossils and altered shells as well as sediment and cement filling the shells (e.g., Alberti et al., 2017). The minimum $\delta^{18}O_{carb}$ reported for Pliensbachian seawater is ~ -4.0‰ (e.g., Dera et al., 2009; Korte and Hesselbo, 2011; Korte et al., 2015; Bougeault et al., 2017; Alberti et al., 2019b; Fig. 5.19). Hence, as acceptable oxygen isotope values the threshold of -4.0‰ was chosen.

The diagenetic screening (SEM, CL, and XRD analyses) performed in the present study suggested that *Opisoma* and *Pachyrisma* are well-preserved and useful for paleoenvironmental reconstruction. It is also confirmed by the reduced correlation coefficients between the $\delta^{18}O$ and $\delta^{13}C$ values (rs = 0.12 and rs = 0.3 for *Opisoma* and *Pachyrisma*, respectively; Tab. 5.2; Fig. 5.3) along with the occurrence of $\delta^{18}O$ values > -4.0‰.

The assessment of preservation state in *Lithioperna* seems to be more controversial. The analysed specimen LP3 shows well-preserved shell microstructure (Appendix B.2) and non-luminescent shell. Low amount of calcite in the wing region (Appendix B.3) was detected by X-ray analysis even if carbon and oxygen isotopes show acceptable values (< -4.0‰). In *Lithioperna* wing the higher correlation coefficient (i.e., rs= 0.81 for LP3-a and rs= 0.49 for LP3-b; Tab. 5.2; Fig. 5.3) could be due to the occurrence of lower calcite content even if a primary origin cannot be excluded. On contrary, *Lithioperna* nearly transversal profile (LP3-b) shows moderate correlation coefficients. Consequently, *Lithioperna* LP3-b profile provided consistent data whilst data from the wing-profile should be treated with caution.

Even if *Lithiotis* shell microstructure seems to be preserved (Appendix B.2), the analysed specimens LT6 and LT7 show slightly luminescent shells and X-ray analyses revealed the occurrence of lower amount of calcite (Fig. 5.18; Appendix B.3). The $\delta^{18}O$ profile shows lower values (< -4.0‰; Figs. 5.10, 5.11, 5.19) suggesting the likely influence of diagenesis. Surprisingly, in both analysed *Lithiotis* specimens the correlation coefficients obtained considering all the values (including altered points) are lower than those obtained considering only the acceptable values (Tab. 5.2). The same is obtained for *Cochlearites* CO1. This unusual result likely indicates a diagenetic close system. In this case, at least the general trend of stable isotope variations can be used as paleotemperature proxy. Another

explanation for this result should consider the lower number of analysed samples, but this limitation can be applied only to *Lithiotis* (number of acceptable samples for each shell: 31 and 13), not to *Cochlearites* specimen CO1 for which 178 powder samples were analysed. Note, however, that *Cochlearites* specimen CO1 shows well preserved shell microstructures, as revealed by SEM analysis, and non-luminescent shell.

Moreover, in all the studied shells the high resolution $\delta^{18}O$ isotope curves show cyclical patterns which argue that the isotopic composition of these specimens has not be completely diagenetically reset (e.g., Danise et al., 2020).

The *Cochlearites* specimen CO2 shows an increase of correlation coefficient when all values were considered (Tab. 5.2). In this case, the higher correlation is due to diagenetic alteration and the unacceptable values should be excluded.

Consequently, even if *Lithiotis* and *Cochlearites* show few portions with lower oxygen values (< -4.0‰), the general trend is evaluated but only the $\delta^{18}O$ > -4.0‰ data from the studied lithiotid shells should be discussed to assess the seawater paleotemperatures.

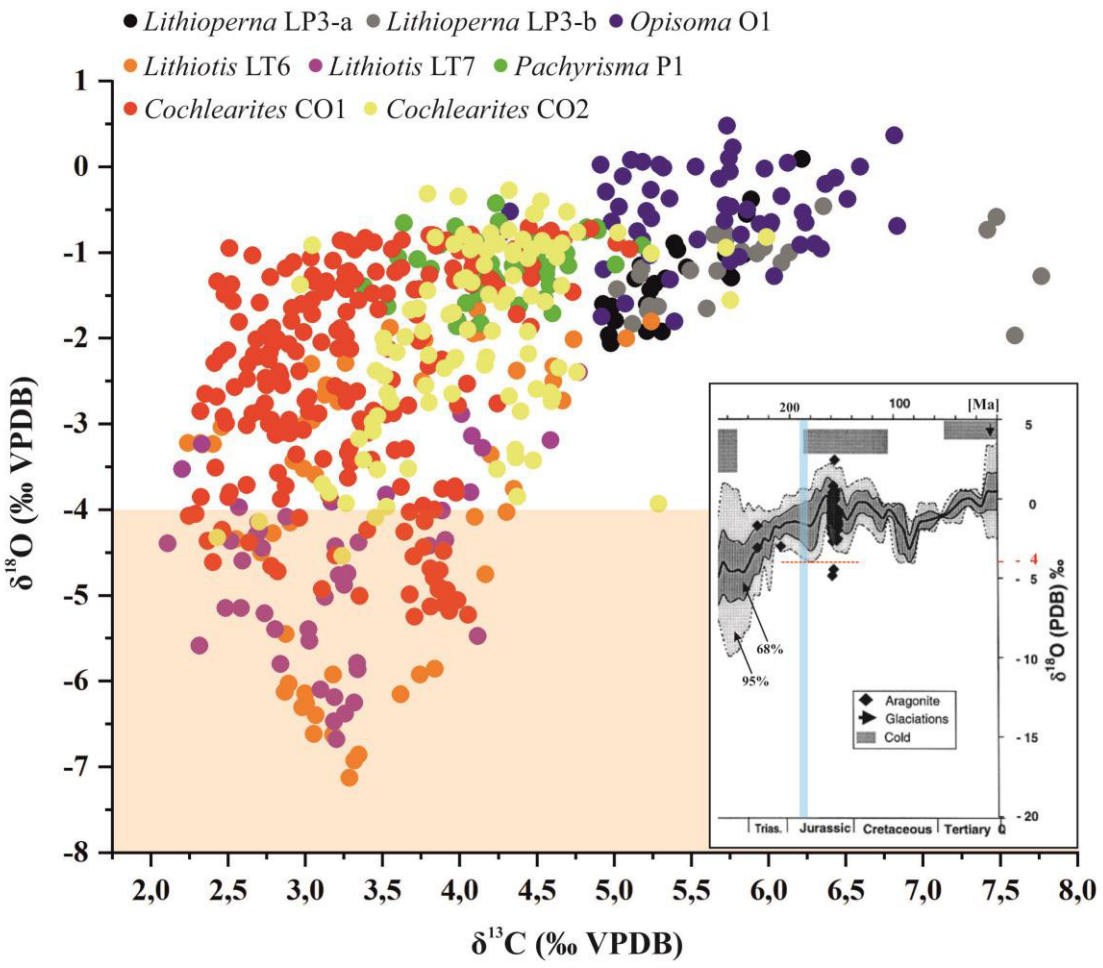

Figure 5.19. Cross plot of $\delta^{13}C$ *versus* $\delta^{18}O$ values of bivalve shell aragonite. Light orange band highlights not acceptable values ($\delta^{18}O$ < -4‰); see text for further details. On the right side, the Phanerozoic $\delta^{18}O$ trend compiled by Veizer et al. (1999). The shaded areas around the mean value (solid black line) include the 68% and 95% of all data (for further details see Veizer et al., 1999). Note that in Pliensbachian stage (light blue band) $\delta^{18}O$ trend doesn't show values < -4‰ (red line).

5.7.2. Growth pattern, seasonal changes in shell microstructures and longevity

In the studied bivalves, the growth pattern was analysed only in restricted shell portions were growth increments are well-recognizable.

A tidal influence is registered with fortnightly bundles in all the studied taxa, excluding *Opisoma excavatum*, whose growth pattern was not interpretable. It reasonable to state that *Opisoma* could live in deeper subtidal environmental setting (e.g., Posenato et al., 2013a). It is not unusual that microgrowth pattern is less defined in subtidal bivalves respect to those living in the intertidal area (e.g., Pannella, 1976). Frequently, the fortnightly bundles appear as two consecutive clusters, with thinner and thicker microgrowth. This pattern is associated with the alternating neap and spring tides (Kennish, 1980).

In the analysed specimens, the fortnightly bundles are distinguished by ~16 microincrements, as also observed with continuous wavelet transformation analysis in *Lithioperna* (Fig. 5.16). Recently, de Winter et al. (2020) have presented a sub-daily resolved chemical records of rudist shells showing that these bivalves precipitated 372 daily laminae per year. As predicted by astronomical models, and by bioarchives (see de Winter et al., 2020, and references therein), the length of day has increased in the geological Earth history. Therefore, the relatively higher number of microincrements (~16) forming fortnightly bundles in lithiotid bivalves should be argued considering the evolution of the length of astronomical cycles (i.e., diurnal, tidal and annual). However, further high-resolution analyses should be conducted in order to better estimates the length of astronomical cycles as well as the likely environmental change at higher (daily) temporal resolution.

No-periodic thicker growth lines were frequently recognised in the lithiotids (*Cochlearites*, *Lithioperna*, *Lithiotis*). Considering the growth line formation, their occurrence is strictly related to physiological stress after severe environmental changes. These stresses can be associated, for instance, to rapid short-term changes in water temperature (e.g., Kennish, 1980) and salinity (e.g., Richardson, 1987), or linked to spawning period. In the studied bivalves, the origin of these growth lines is not easily assessible due to the incomplete preservation of the growth pattern.

Regarding structural changes, in *Lithioperna*, the microstructural variations seem to be clear, even if slight differences occur within each shell and among individuals (as already observed by Accorsi Benini, 1979 and Accorsi Benini and Broglio Loriga, 1982). *Lithioperna* shell is essentially constituted by lenticular nacreous sublayers and irregular fibrous prismatic structures derived by the alteration of nacre (Accorsi Benini, 1979; Broglio Loriga and Posenato, 1996). The reciprocal arrangements of these two microstructures vary in the shell.

Along a nearly transversal section (Figs. 5.15–5.16), each annual interval is distinguished by prisms apparently with no growth increments followed by daily growth increments. Actually, the observed growth increments likely correspond to nacreous tablets. A similar pattern was recognised also in the feather-like transect even if the distinction of each year is less clear. The wavelet analysis showing fortnightly periodicity suggest a likely tidal influence in the tablets thickness.

The irregular fibrous prismatic level which immediately succeeding the annual growth line could indicate a stressed period which imply shell dissolution with the fusion of nacreous tablets (as already suggested by Accorsi Benini, 1979). Comparing with oxygen isotope values, the thick prismatic layer corresponds to lower oxygen value (higher temperature), which could be associated with more stressed conditions.

Recent studies showed that temperature constitutes one of the most important factors governing the microstructural changes in bivalves (e.g., Nishida et al., 2012; Milano et al., 2017). In bivalves of warm-water environments, seasonal microstructural changes are frequently represented by fibrous prismatic sublayers associated with extremely warmer summer temperature (Lutz and Rhoads, 1978). These fibrous prismatic sublayers are related with the anaerobic respiration which increases during the hot summer when oxygen solubility is reduced (Lutz and Rhoads, 1980). A similar behaviour could be applied to *Lithioperna*.
The irregular fibrous prismatic level should indicate a period of slow growth as also confirmed by higher correlation between $\delta^{13}C$ and $\delta^{18}O$ datasets which indicate a kinetic isotope fractionation effect. It is plausible to assume thus that the annual interval observed in the *Lithioperna* does not record the entire year.

Chinzei (1982) reported the occurrence of nacreous wedges both in *Lithiotis* and *Cochlearites*, highlighted that the wedges are usually more abundant in *Cochlearites* than in *Lithiotis*, likely due to diagenetic effects. Considering the analysed *Cochlearites* specimens the nacreous wedges occur with different size. In the specimen CO2 (Fig. 5.6), the nacreous wedges occur immediately before the annual growth lines, corresponding to the higher oxygen values (lower inferred temperature; see Discussion below). A similar trend was also recognised in the specimen CO1. The nacreous wedges recognised both in *Cochlearites* and *Lithiotis* show a columnar structure which has been associated with relatively high maximum rate of shell accretion (Carter, 1980). As observed in *Lithioperna*, the irregular fibrous prismatic microstructure could be associated with warmer temperature. However, in *Cochlearites* and *Lithiotis*, the irregular fibrous prismatic layer is thicker respect to *Lithioperna*. Even if the paleotemperature reconstruction using lithiotids could be uncertain due to the several and different environmental controlling factors on each taxon (see

Discussion below), a slight relationship can be observed between inferred temperatures and microstructures. In particular, the lower inferred temperatures in *Lithioperna*, correspondingly to nacreous microstructure is similar to that registered by *Cochlearites* in the nacreous wedges (minimum inferred temperature; Tab. 5.1; Appendix B.4). Nacreous microstructure (layer or wedges) could be correspond to the "normal" microstructure deposition while irregular fibrous prismatic structure could be related to stressed periods. The increase of this last microstructure in lithiotid bivalves (*Lithiotis* and *Cochlearites*) could be related with the onset of specific climate conditions (e.g., higher average temperature). It might also be possible that other parameters (i.e., salinity or food availability) slightly influenced microstructural changes, in particular when associated with temperature/seasonal changes.

This hypothesis should also consider the phylogenetic relation between these taxa and in any case further analyses should be conducted in order to clarify these aspects. Nevertheless, the occurrence of these wedges might interrupt the "normal" bivalve growth and, as a consequence of a diverse growth rate, the observed "annual" interval could not register the entire year.

Seasonal variations of $\delta^{18}O_{shell}$ and the identified annual growth pattern were used to reconstruct the growth curves and to evaluate bivalve life span. In particular, the suggested annul periodicity of the growth increments occurring in the feather-like wings of *Cochlearites*, *Lithiotis* and *Lithioperna* (e.g., Chinzei, 1982) was confirmed by the $\delta^{18}O$ profiles.

For *Opisoma*, due to the lack of information on sub-annually growth increments, the annual growth interval is delineated by maximum oxygen values. *Lithiotis* was not considered due to the lower-distinguished annual growth increments in the studied specimens LT6 and LT7 (2 and 3 increments, respectively). The growth curve representing shell thickness does not show similar shapes (Fig. 5.20). *Cochlearites* specimen CO1 shows two stages with high and low growth rates. These two stages likely represent the juvenile and senescent stages, respectively. The found trend is similar to that of tridacnids and brachiopods (e.g., Yamanashi et al., 2016, and references therein). In CO2 and O1 this trend is less recognizable. An early death before reaching the senescent stage cannot be ruled out. However, it might be possible that the diverse shell portions (i.e., cardinal area in *Opisoma* and wing regions in *Cochlearites*) were distinguished by no comparable growth rate. Similar conclusions can be draw for *Pachyrisma* whilst in LP3 the studied wing profile is uncomplete (Fig. 5.14). The studied bivalve profiles show that the *Cochlearites* growth rate is definitely higher than the other studied taxa, as confirmed by the average thickness of microgrowth increments observed in thin sections.

The best-preserved *Opisoma excavatum* specimens reported in literature (collected from Lessini Mounts; see Posenato et al., 2013a for further details) show essentially the massive cardinal region because the ventral region is generally fragile and commonly affected by abrasion and fragmentation (Aberhan and von Hillebrandt, 1999; Posenato et al., 2013a; Bassi et al., 2017). The estimated length for the preserved individuals is ~13 cm (Posenato et al., 2013a). Considering the average growth rate observed in the studied specimens, the individuals could live up to ~40 years. This slow growth rate could be related to apparently extreme environmental conditions (e.g., Accorsi Benini, 1985; see Discussion below).

Considering the $\delta^{18}O$ profile and the growth pattern observed in *Lithioperna*, the annual increments in the specimen LP3 vary up to ~2.5 mm in thickness. In other individuals, the annual growth increments observed in the inner wing surface vary up to 5 mm. Considering the high shell morphological variability that characterizes this taxon, *Lithioperna* individuals could live up to ~30 years.

According to the average annual growth thickness measured in the analysed *Lithiotis problematica* specimens and the maximum shell height (~30 cm; e.g., Accorsi Benini, 1985), this taxon could live up to ~30 years. Frequently, they likely did not exceed the ~15–20 years.

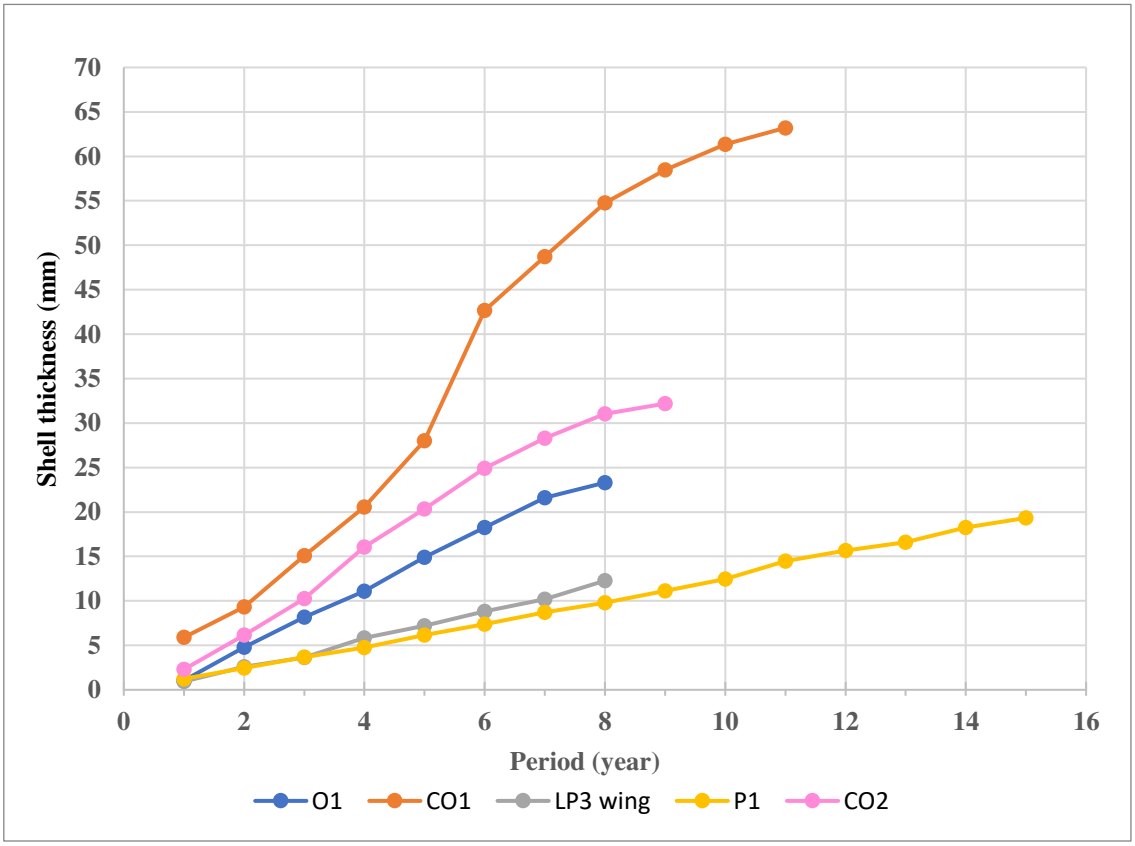

Figure 5.20. Comparison of the annual rate of shell thickening in the analysed bivalves. Each annual increment was measured perpendicular to growth lines/bands, considered also the $\delta^{18}O$ shell trend. O1, *Opisoma*; CO1, CO2, *Cochlearites*; LP3, *Lithioperna*; P1, *Pachyrisma.*

In *Pachyrisma* (*Durga*) *crassa*, the annual growth increments observed in thin sections and in polished slabs are about 2 mm in thickness. Based on the studied specimens, the taxon could live up to ~15 years.

Considering the analysed specimens, *Cochlearites* lived up to ~15–20 years. Since *Cochlearites* could be up to 70 cm in height (e.g., Posenato and Masetti, 2012), it is likely that this taxon could reach the ~40 years.

5.7.3. Oxygen isotope record and inferred paleotemperatures

The difference registered among the studied taxa could related with local environmental variations, instead of a stratigraphic trend (Fig. 5.21).

Cochlearites frequently overlies megalodontid accumulations which are associated with euhaline to slightly hyperhaline and warm waters (Posenato and Masetti, 2012). *Lithiotis* usually occurs close to rhynconelliform brachiopod beds, solitary corals and larger benthic foraminifera indicating fully marine and well-oxygenated conditions (e.g., Posenato and Masetti, 2012). The upper part of the Rotzo Formation is distinguished by higher water circulation and more opening marine conditions (e.g., Fugagnoli, 2004). According to these paleoenvironmental scenario, it can be assumed that the analysed *Cochlearites* and *Lithiotis* specimens thrived in a fully marine setting which was weakly influenced by salinity changes (i.e., due to river discharge). Therefore, oxygen isotope compositions could be used to reconstruct seawater paleotemperatures. Applying the equation of Grossman and Ku (1986) with a $\delta^{18}O$ value for seawater of -1‰ (Shackleton and Kennett, 1975), as the majority of studies on Jurassic stable isotope did, the inferred paleotemperatures from the two taxa are in fact similar varying from ~16°C up to ~32°C for *Cochlearites* and from ~22°C up to ~32°C for *Lithiotis*. Furthermore, *Cochlearites* is distinguished by higher stable isotope range (both oxygen and carbon; Tab. 5.1) which suggests more intense climatic extremes and consequently more seasonality (see Discussion below). According to the palaeolatitudinal position of the Lower Jurassic Trento Platform (see Chapter 2), the inferred climate is comparable to that occurring in modern costal lagoons at ~20° N or ~20° S latitude. Similar temperature gradients were also registered in these environments, such as in Brazil (~23°C to ~30°C, Açu lagoon; Chagas and Suzuki, 2005), in Yucatan, Mexico (~24°C to ~35°C, Celestun Lagoon; Herrera-Silveira, 1994) and in New Caledonia (SW Pacific; ~22°C to ~29°C; Ouillon et al., 2005). Actually, the minimum inferred temperatures in *Cochlearites* is quite lower than those reported for tropical costal lagoons. It is might be possible that *Cochlearites* slightly registered the influx of cold deep marine currents (i.e., seasonal upwelling). Costal upwelling is a complex phenomenon whose spatial and temporal

variability depends on several factors (e.g., geometry and bottom topography, costal winds) and produces highly heterogeneous environments (Strub et al., 1991). Upwelled water could be up to ~2–3°C colder than the surrounding waters (e.g., Ramanantsoa et al., 2018). Even if the upper part of Rotzo Fm registered more opening marine conditions (e.g., Fugagnoli, 2004), an intense upwelling of colder waters influx seems disputable to account for the low $\delta^{18}O$ values.

Another mechanism that can enrich seawater and thus bivalve shell aragonite in ^{18}O is the evaporation. Given that $\delta^{18}O_{shell}$ reflects surface water temperatures, evaporation of seawater would result in higher $\delta^{18}O_{shell}$ and thus "simulate" cold temperatures (e.g., Hornung et al., 2007). As previously discussed, an intense evaporation should be excluded in the Rozto Fm (i.e., occurrence of coal lens; see paragraph 5.3 for further details).

Note, however, that the higher $\delta^{18}O_{shell}$ could reflect a primary signal which indicate a decrease of sea water temperature.

In shallow water environments, feeble temperature variations (up to ~2°C) could occur with the deepening. It might be possible that *Cochlearites* occupied deeper water than *Lithiotis* even if a clear tidal influence is confirmed by sclerochronological analysis (see paragraph 5.7.2).

On contrary, *Opisoma*, *Lithioperna* and *Pachyrisma* occur in restricted shallow lagoon or marsh environments, as testify by the occurrence of silty marl with coal lenses and vertical roots (e.g., Posenato and Masetti, 2012). In these areas, the run-off input and consequently the salinity and nutrient fluctuations could be more relevant. Therefore, the oxygen isotope record could be not directly used for paleotemperature reconstructions and a comparison of all the analysed taxa should be excluded. Moreover, these taxa show similar values of oxygen isotope record and are distinguished by reduced range variations (Fig. 5.21).

5.7.4. Carbon isotope record

The carbon isotopic composition of bivalves varies in a more complex way and the origin of these changes is not fully understood (Lorrain et al., 2004). The controlling factors on bivalve $\delta^{13}C$ depend on several factors, such as the $\delta^{13}C$ of dissolved inorganic carbon, pH, food availability and seasonal changes in the calcification and metabolic rates (Titschack et al., 2010, and references therein). Moreover, all these processes vary in strength and time, complicating the interpretation of carbon isotope trend (Lorrain et al., 2004; Omata et al., 2005).

Although several authors observed that in numerous bivalves the stable carbon isotope decrease with the ontogeny (e.g., Kennedy et al., 2001; Keller et al., 2002; Lorrain et al.,

2004), in the studied specimens, $\delta^{13}C$ does not vary with the ontogeny. Lorrain et al. (2004) associated this trend with the increase of incorporation of respiratory CO_2 during growth, even if this model cannot be applied for all bivalves, as observed in tridacnids (e.g., Yamanashi et al., 2016, and references therein). Consequently, cannot be excluded that lithiotids don't show any ontogenetic trend. However, as illustrated in the Fig. 5.20, the lack of ontogeny trend could be also associated with the occurrence of incomplete shells (i.e., *Lithioperna* and *Cochlearites* specimen CO2; Fig. 5.20) or with the occurrence of juvenile individuals (i.e., *Opisoma* and *Pachyrisma*).

The $\delta^{13}C$ values of the studied specimens is relatively high (Tab. 5.1; Figs. 5.19, 5.21) and uncommon in most bivalves but similar values were reported for the modern *Isognomon* (Fraser, 2002), *Terebra areolata*, a gastropod common to nearshore tropical environments (Jones et al., 1986) and for some species of inoceramids (e.g., Walliser et al., 2018). More recently, Danise et al. (2020) observed higher $\delta^{13}C$ values in some bivalves (i.e., *Liostrea strigilecula*, *Gryphaea* sp., and *Deltoideum* sp.) collected from the Middle–Upper Jurassic Sundance Seaway (western United States).

These relatively higher carbon isotope values were obtained for all the studied bivalves, suggesting a specific trend. Note, moreover, that the $\delta^{13}C$ values in the analysed taxa can be considered a primary signal and don't relate to diagenetic alteration, which was excluded both by cathodoluminescence and SEM observations.

The data from the studied bivalves could reflect a regional carbon isotope trend, potentially linked with the dynamic setting of very shallow and restricted lagoon. In particular, *Opisoma, Lithioperna* and *Pachyrisma* which show the higher mean $\delta^{13}C$ values (Fig. 5.21) occur in marsh environments (e.g., Posenato and Masetti, 2012) where the amount of organic matter could be substantial. Therefore, the relative higher $\delta^{13}C$ values might be caused by burial of organic matter which produced the increase of the $\delta^{13}C$ value of DIC in the water.

Note, however, that the $\delta^{13}C$ values might be also influenced by species-specific vital effects (see Discussion below).

Following the hypothesis which suggests different controlling factors on the analysed bivalve species (i.e., strong riverine influence on *Pachyrisma*, *Opisoma* and *Lithioperna*), a direct comparison among all the studied bivalves as well as the definition of temporal trends in carbon and oxygen stable isotope ratios should be excluded (Fig. 5.21). Moreover, different metabolic contributions were observed in individuals of the same species collected from similar environments (e.g., *Mercenaria mercenaria*; Gillikin, 2005) and among different species. It might be possible that the stressed environments where these three genera occur

could induced a different fractionation (i.e., metabolic contributions) hinder the carbon isotope interpretation.

Therefore, these interpretations remain speculative until supported by further investigations.

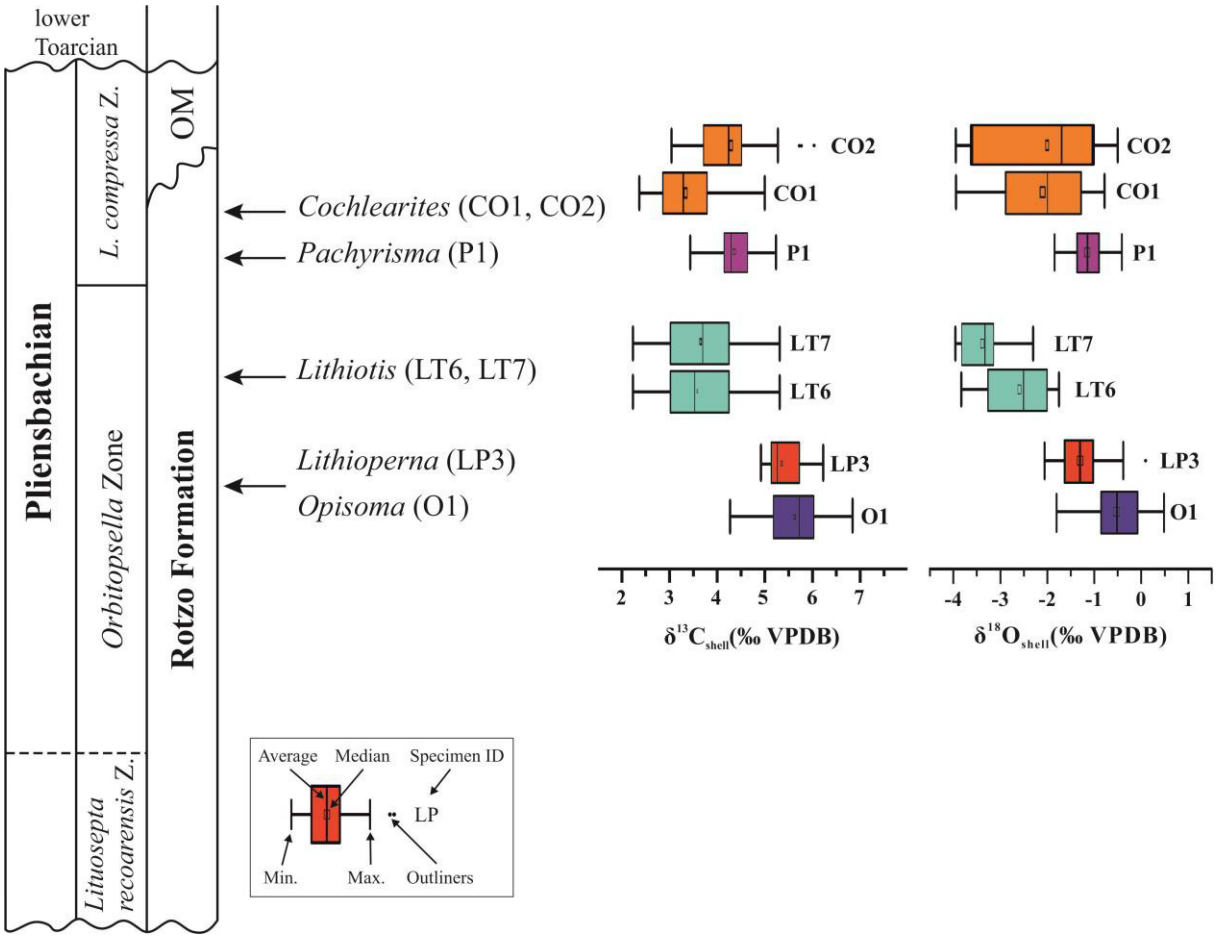

Figure 5.21. Summary of geochemical data with "box-and-whisker" plots of carbon and oxygen isotope values. *L. compressa* Z., *Lituosepta compressa* Zone; Z., Zone; OM, Oolite di Massone; Si, upper Sinemurian. A comparison of all the analysed taxa should be excluded to local environmental variations and species physiology (see text for further details).

5.7.5. Seasonality reconstruction

The analysed specimens show difference annual range of stable isotopes ($\delta^{18}O$ and $\delta^{13}C$), or seasonality, which could give information on past climate dynamics. In particular, oxygen isotopic data from serially sampled bivalve shells can provide an excellent record of paleoseasonality (Sessa et al., 2012). However, bivalves frequently could not register the entire range of climatic conditions (i.e., temperature; e.g., Kubota et al., 2017) due to each species physiology. Even if the evaluation of carbon and oxygen isotopes in bivalves can be argued, few general considerations can be drawn.

Cochlearites loppianus (specimen CO1) shows a $\delta^{18}O$ profile with well-defined seasonal cycles with slightly different amplitude. The major amplitude registered in the early

years is likely due to diagenetic alteration (orange band in Fig. 5.5). The annual growth lines recognised in the polished slabs occur, regularly, at the transition between the maximum and the minimum $\delta^{18}O$ values. The $\delta^{13}C$ values are more irregular in the early years while they seem to be more stable later, as testified by the occurrence of two (more or less) carbon cycles for each annual period (Fig. 5.22). Usually, the first smaller peak occurs with the onset of lower $\delta^{18}O$ value which is interpreted as corresponding to higher temperature or higher freshwater input. Considering that a monsoonal climate regime was already proposed for the Rotzo depositional setting (e.g., Bassi et al., 1999; Posenato et al., 2013b; Neri et al., 2017), in the second case an increase of run-off with fresh-water and nutrient input could correspond to the rainy season. In some monsoonal tropical lagoons, the rainy season is distinguished by decrease of water temperature (e.g., Reuter et al., 2013) which is opposite in the analysed oxygen isotope trend. Actually, in other regions (e.g., Li et al., 2014) the rainy season coincides with the warmest period. Since oxygen stable isotope could depend by either salinity or temperature changes as well as a mixing of these two parameters, in the analysed specimens a clear distinction between the two previous described scenarios is challenging. In any case, as can be observed in the other studied bivalves (see following Discussion), the alternation of two seasons, likely rainy and dry, is plausible (Fig. 5.22). In any case, lower salinity should induce a decrease in the $\delta^{13}C$ values as well as river input, which contains DIC enriched ^{12}C (Hellings et al., 2000; 2001). In addition, nutrient supply should continue for all the rainy season producing theoretically a more positive correlation.

As previously discussed, *Cochlearites* thrived in the upper part of the Rotzo Formation, which is distinguished by more stable marine conditions and oligotrophic regime (Fugagnoli, 2004). The influx of riverine input could be more negligible. Consequently, the increase of $\delta^{13}C$ could be associated with the primary production and therefore with proliferation of algal blooms. Moreover, the metabolic isotope fractionation effect on *Cochlearites* should be not negligible. The rapid decrease in $\delta^{13}C$ values is associated with the rise of respiration rate following the proliferation of algal blooms (higher food availability; e.g., Vander Putten et al., 2000; Fig. 5.22). Moreover, the $\delta^{13}C$ and $\delta^{18}O$ values show weak or no significant correlation (Tab. 2), excluding strong kinetic isotope fractionation effect (e.g., Yamanashi et al., 2016, and references therein). Note, however, that this first peak could be associated with spawning because it seems to be absent in juvenile stages of life and moreover, the inferred higher temperature could promote the reproduction (e.g., Lartaud et al., 2010).

Frequently, the second $\delta^{13}C$ peak corresponds to the higher $\delta^{18}O$ values and could be higher than the first one. Considering the temperature as the main controlling factor on $\delta^{18}O$,

this $\delta^{13}C$ peak occurs during lower inferred temperature. In this case, a fresh-water input might be excluded. This second peak could be related to outer lagoon upwelling event which could have an impact inside the lagoon (i.e., algal bloom) as observed in modern corals and in giant clams (Montaggioni et al., 2006; Aubert et al., 2009).

The illustrated trend is not well-recognizable in the specimen CO2 which is distinguished by frequently non periodic peaks and by less define annual growth pattern. These non-periodic points could be linked with the physiology (e.g., disease) and/or non-climatic stress (e.g., food availability).

No direct consistency between the maximum or minimum $\delta^{18}O$ values and the growth lines was identified for *Pachyrisma* (*Durga*) *crassa*. This is not so unusual for bivalve shells (e.g., Walliser et al., 2015) and may be due in part to low sampling resolutions in respect to growth increments (more time averaging of shell increments as in *Lithioperna*). The stable isotope curves do not show similarities each other. In restricted portions, the taxon shows the same trend registered by *Lithioperna* with the almost contemporaneous decrease of oxygen and carbon isotope (see Discussion below). *Pachyrisma* thrived in restricted and shallower lagoon habitats, similar to those reported for *Lithioperna* (Clari, 1975). Therefore, the controlling growth factors could be essentially associated with the seasonal increase in run-off and salinity changes.

For *Lithiotis problematica* the $\delta^{13}C$ increase corresponds to higher oxygen values while for the rest of the year shows no considerable variations (Fig. 5.10). As previously discussed, *Lithiotis* thrived in well oxygenated and fully marine conditions because it is frequently associated with brachiopods and larger foraminifera (e.g., Fraser, 2004; Posenato and Masetti, 2012). Because the influence of run-off should be minimal, the oxygen isotope could depend mainly on the temperature. As in *Cochlearites*, the single higher carbon peaks could be related to higher primary productivity (i.e., “winter algal bloom”).

Opisoma excavatum $\delta^{18}O_{shell}$ profile is characterised by defined regular cycles with slightly different amplitude. The apparent annual pattern recognised in the polished slab could be associated with highest oxygen values. If the temperatures should be the controlling factor on oxygen isotope, the growth lines formation would correspond with lower inferred temperature. Temperature likely constitutes the most important constrain factor in the bivalve growth. Each species shows a growth range based on optimum temperature interval. When the taxon-specific water temperature range is exceeded, biomineralization ceases and results in the formation of growth lines (e.g., Jones and Quitmyer, 1996; Schöne et al., 2002). As previously discussed, the analysed *Opisoma* specimen, collected from the Vaio dell’Anguilla section (Fig. 5.1), occurred in very shallow and restricted lagoon or marsh environments

(Posenato and Masetti, 2012). Therefore, the main controlling factor on *Opisoma* oxygen stable isotope could be the riverine input. Consequently, the growth line formation occurs likely during the season with run-off decrease which could be also associated with less food availability. In fact, aside temperature a variety of other factors are known to influence shell growth (i.e., reproduction, availability of food, tidal influences, storms, upwelling, and salinity; Sessa et al., 2012, and references therein). In the $\delta^{13}C_{shell}$ profile, weakly cycles were recognised, comparing with $\delta^{18}O_{shell}$ curve. For each oxygen isotope cycle, the carbon registered at least two shorts peaks with the minimum values slightly correspond to lower oxygen values (Fig. 5.22). Considering a monsoonal climate regime (i.e., alternation of rainy and dry seasons; Fig. 5.22), during the rainy season the fresh-water influx increased as well as the nutrient input involving a general decrease of $\delta^{13}C$. Actually, the higher nutrient input could favour phytoplankton blooms in tropical lagoons. Several authors have reported a relationship between $\delta^{13}C_{DIC}$ and primary production (e.g., Hellings et al., 1999). If the bivalve shell registered mainly the $\delta^{13}C_{DIC}$ signals, the $\delta^{13}C_{shell}$ should be distinguished by higher value. This scenario does not consider the likely metabolic contribution on $\delta^{13}C_{shell}$ values. In fact, in *Opisoma*, during the rainy season (lower oxygen values) $\delta^{13}C_{shell}$ shows different peaks, with no specific trend (Fig. 5.22). This absence of trend could be explained considering the metabolic and kinetic isotope fractionation effects of bivalve shell. For *Opisoma*, significant kinetic fractionation is ruling out due to the low correlation between $\delta^{18}O$ and $\delta^{13}C$ (Tab. 5.2; e.g., McConnaughey, 1989b). Regarding the metabolic isotope fractionation effect, the repetitive lower peaks of $\delta^{13}C_{shell}$ could be due to higher respiration rate which occur with the onset of algal blooms (higher food availability; e.g., Vander Putten et al., 2000; Fig. 5.22). Even if the repetitive small peaks cannot be associated only with spawning considering that bivalves span one or (at least) twice a year, lower $\delta^{13}C_{shell}$ peaks could be also associated with the reproduction phase distinguished by higher metabolic rate just after spawning (Vander Putten et al., 2000).

Lithioperna scutata stable isotope curves represent more time averaging of the shell increments as compared to *Opisoma*, *Lithiotis* and *Cochlearites*. Even if the nearly transversal profile (Fig. 5.15) is not the most suitable section to study the geochemical variations in bivalve shells, the obtained results were compared with the wing profile. The annual growth lines identified in thin sections (Fig. 5.16) were plotted to $\delta^{18}O_{shell}$ profile showing no direct correlation between the oxygen isotope extremes, as also found for *Cochlearites* and *Pachyrisma* (Figs. 5.5, 5.6, 5.8). Although $\delta^{18}O_{shell}$ curve shows possible seasonal cycles, the $\delta^{13}C$ curve is more variable and only in few yearly intervals some seasonal cycle can be distinguished. In these cases, the trend is more or less concordant (i.e., lower $\delta^{13}C$ value,

lower $\delta^{18}O$ value). In the Rotzo Fm, *Lithioperna* occurs also in restricted environments, with less water circulation (low oxygenation; e.g., Posenato and Masetti, 2012) and likely higher nutrient levels. In this case, the salinity could have been a stronger constrain for *Lithioperna* than for the lithiotids of the middle and upper part of the Rotzo Fm (i.e., *Lithiotis*, *Cochlearites*). In particular, the simultaneous decrease in $\delta^{18}O_{shell}$ and $\delta^{13}C_{shell}$ could be due to riverine input which implies a decrease of oxygen due to freshwater input and decrease of carbon due to lighter ^{12}C carbon input. The higher positive correlation between oxygen and carbon isotope could be linked to kinetic isotope fractionation effect (e.g., McConnaughey, 1989b).

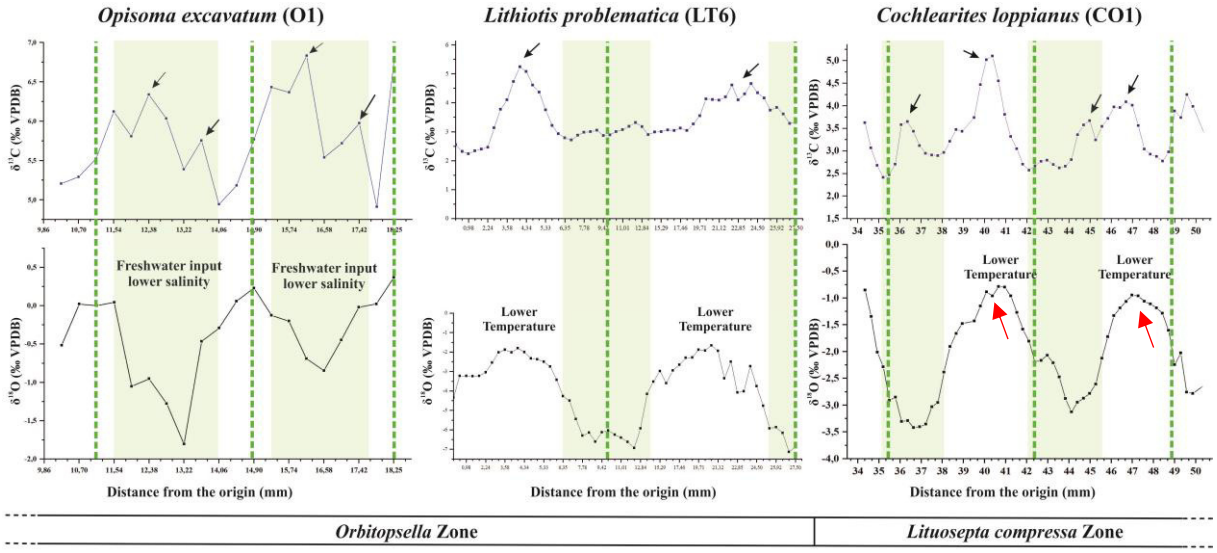

Figure 5.22. Comparison of $\delta^{18}O$ and $\delta^{13}C$ annual fluctuations in *Opisoma* (specimen O1), *Lithiotis* (LT6) and *Cochlearites* (specimen CO1). The dotted green lines indicate the annual growth lines. Black arrows point to higher carbon peaks discussed in detail in the text. In *Lithiotis*, $\delta^{18}O$ trend is acceptable (i.e., diagenetic closed system) even if includes values < -4.0‰; see text for further details. Note the seasonal variations both in $\delta^{18}O$ and $\delta^{13}C$ in all taxa. The alternation of two seasons (likely rainy and dry) is highlighted by white and light green bands. Red arrows highlight the position of nacreous wedges.

5.8. Conclusions

High resolution stable isotope ($\delta^{13}C$ and $\delta^{18}O$) analyses and growth-pattern investigations carried out on the lithiotid *Lithiotis problematica*, *Cochlearites loppianus* and *Lithioperna scutata* and other bivalves such as *Opisoma excavatum* and *Pachyrisma* (*Durga*) *crassa* highlight paleoenvironmental and paleoclimatic changes recorded by these Pliensbachian bivalves occurring in the Rotzo Formation.

The diagenetic screening (SEM, XRD, and cathodoluminescence analyses) indicated that the geochemical record of the studied bivalve shells has a good potential to be used as proxy of paleoclimatic changes in tropical lagoons.

Microstructural changes observed in *Lithioperna* as well as in *Lithiotis* and *Cochlearites* could be associated with temperatures changes even if further investigations are necessary to better define the controlling factors on microstructural variations. Moreover, these microstructural changes have to be considered possibly influencing the stable isotope profiles. These taxa could not register the full seasonal $\delta^{18}O$ and $\delta^{13}C$ amplitudes.

The inferred paleotemperatures from *Cochlearites* and *Lithiotis* are similar: ~16 – ~32°C for *Cochlearites* and ~22 – ~32°C for *Lithiotis*. *Cochlearites* recorded more intense climatic extremes and consequently more seasonality. *Opisoma*, *Lithioperna* and *Pachyrisma*, occurring in restricted shallow lagoon or marsh environment, are not prone to be used as paleotemperature proxy as far as oxygen isotope record is concerned.

The inter-annual variability was likely related to inter-annual changes in tropical climate and, in particular, was associated with rainy and dry seasons. During the rainy season, the intense riverine input could be associated with algal blooms as registered by *Opisoma* in the middle part of the Rotzo Fm. The water salinity could have been a stronger constraint for *Lithioperna*, *Opisoma* and *Pachyrisma* than for the other lithiotids (i.e., *Lithiotis* and *Cochlearites*). These bivalves, in fact, thrived in restricted lagoonal portions distinguished by less water circulation.

Lithiotis and *Cochlearites* seem to be less influenced by riverine input. They occur in the upper part of the Rotzo Formation, distinguished by amelioration of water circulation and the onset of fully marine conditions. In fact, their stable isotope profiles indicate more stable conditions.

In all the studied bivalves the growth pattern is characterized by fortnightly bundles confirming a clear tidal influence even in subtidal settings. This study confirms that the lithiotid bivalves could live up to ~40 years. *Lithiotis* grew for ~15–20 years, *Pachyrisma* (*Durga*) *crassa* and *Lithioperna* lived up to ~15 years. The largest sized *Cochlearites* showing the higher growth rate within this aberrant-bivalve group could reach the ~40 years.

Chapter 6
Conclusions

This thesis examined the paleoenvironmental and paleoclimatic constraints on the lithiotid distribution in the Lower Jurassic succession of the Trento Platform (Southern Alps). This bivalve group, which essentially includes *Lithiotis problematica*, *Cochlearites loppianus* and *Lithioperna scutata,* played a significant sedimentogenetic role in the Pliensbachian shallow-water carbonate lagoon.

Through taphonomic, palaeoecological and geochemical-sclerochronological analyses, the following main conclusions were achieved.

- The lithiotid accumulations can be dominated by a single lithiotid species or composed by all the three main species. Rarely, dominating *Lithiotis* is associated with subordinate *Cochlearites* whilst dominating *Cochlearites* is frequently associated with subordinate *Lithioperna*. When *Lithioperna* dominates, it occurs only with flat and thin shells and is rarely associated with subordinate *Cochlearites*. Autochthonous individuals (i.e., in life position or in a bouquet-like aggregates) are recognizable in the accumulation core, while the flanks are characterized by high occurrence of flat lying, toppled parautochthonous shells. The quantitative taphonomic analysis shows that (a) in the core, the shell cover is the highest for *Lithioperna*, variable for *Cochlearites* and low for *Lithiotis*, while (b) in the flanks these attributes show an opposite trend. Shell densities are high in the core for *Cochlearites* and *Lithioperna* and low for *Lithiotis*, while in the flanks the shell density is high for all the taxa with more variability in *Cochlearites*. Articulated and unbroken shells vary conspicuously both in the core and flanks. In particular, in the accumulation flanks a relative high percentage of articulated *Lithioperna* individuals (> 35%) suggests that autochthonous individuals also thrived in these areas.

- The geometry of lithiotid accumulations was probably controlled by the microbial activity and calcareous green algae (*Thaumatoporella parvovesiculifera*), which produced an early lithification of the muddy substrate allowing the bivalve accumulation raised with respect to the surrounding sea floor. In *Lithiotis*- and *Cochlearites*-dominated accumulations, the microbial activity seems to have been

more significant, in particular where the shell density is lower, such as in the *Cochlearites* accumulation flanks and *Lithiotis* accumulation cores. The microbial activity was not recognized in the *Lithioperna*-dominated accumulations, which are characterized by tabular bodies. The different shape of the *Lithioperna* accumulations can be related to the higher water turbulence of the depositional setting. The relative increase in occurrence of bacteria-like features and calcareous green algae (*Thaumatoporella parvovesiculifera*, *Palaeodasycladus* sp.) upwardly in the Rotzo Formation points to a general decrease in water runoff and an increase in marine water saturation state.

Regarding paleoredox conditions, the *Lithiotis* accumulation core grew in fully oxic settings. In the *Cochlearites* accumulation core, the sediment/water interface was low dysoxic. The accumulation flanks for both taxa record oxic to dysoxic conditions. The deposits overlying the lithiotid accumulations formed under oxic conditions.

- The inter-annual variability in the isotope profiles ($\delta^{18}O$ and $\delta^{13}C$) of some exceptional preserved shells was likely related to a tropical climate, with an alternation of rainy and dry seasons. However, different controlling shell growth factors seem influenced the analysed taxa. The water salinity could have been a stronger constraint for *Lithioperna*, *Opisoma* and *Pachyrisma*, whose stable isotope profiles suggest higher riverine input and strong seasonal algal blooms. These bivalves thrived in restricted environmental conditions with a sluggish water circulation. The stable isotope profiles of *Lithiotis* and *Cochlearites* suggest a decrease of riverine input influence and more stable conditions (i.e., less frequent seasonal algal bloom). The inferred paleotemperatures from *Cochlearites* and *Lithiotis* fit well with the modern tropical lagoon temperature even if *Cochlearites* recorded more intense climatic extremes and consequently more seasonality.

  The growth-pattern investigations confirm the tidal influence within a subtidal setting and the long life of some individuals (e.g., up to about 40 years old in *Cochlearites*) which distinguished this aberrant-bivalve group.